Springer Geophysics

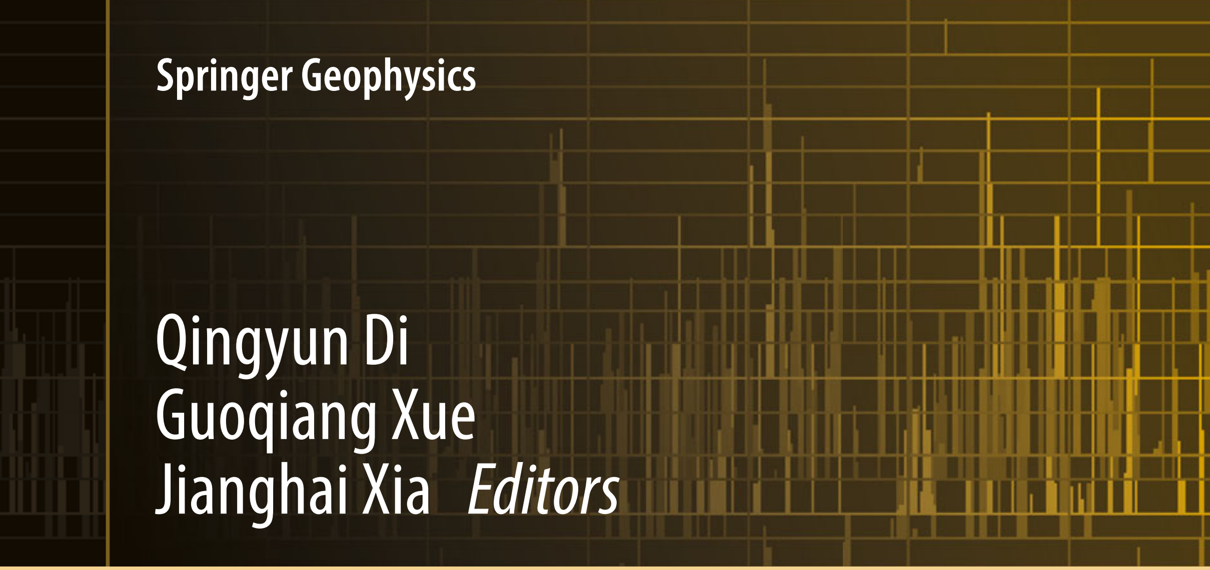

Qingyun Di
Guoqiang Xue
Jianghai Xia *Editors*

Technology and Application of Environmental and Engineering Geophysics

Selected Papers of the 7th International Conference on Environmental and Engineering Geophysics, ICEEG-Beijing 2016

Springer

Springer Geophysics

The Springer Geophysics series seeks to publish a broad portfolio of scientific books, aiming at researchers, students, and everyone interested in geophysics. The series includes peer-reviewed monographs, edited volumes, textbooks, and conference proceedings. It covers the entire research area including, but not limited to, applied geophysics, computational geophysics, electrical and electromagnetic geophysics, geodesy, geodynamics, geomagnetism, gravity, lithosphere research, paleomagnetism, planetology, tectonophysics, thermal geophysics, and seismology.

More information about this series at http://www.springer.com/series/10173

Qingyun Di · Guoqiang Xue
Jianghai Xia
Editors

Technology and Application of Environmental and Engineering Geophysics

Selected Papers of the 7th International Conference on Environmental and Engineering Geophysics, ICEEG-Beijing 2016

Springer

Editors
Qingyun Di
Institute of Geology and Geophysics
Chinese Academy of Sciences
Beijing, Chaoyang
China

Jianghai Xia
Zhejiang University
Zhejiang
China

Guoqiang Xue
Institute of Geology and Geophysics
Chinese Academy of Sciences
Beijing, Chaoyang
China

Springer Geophysics
ISBN 978-981-10-3243-1 ISBN 978-981-10-3244-8 (eBook)
DOI 10.1007/978-981-10-3244-8

Library of Congress Control Number: 2016957867

Printed on acid-free paper

This Springer imprint is published by Springer Nature
The registered company is Springer Nature Singapore Pte Ltd.
The registered company address is: 152 Beach Road, #21-01/04 Gateway East, Singapore 189721, Singapore

Contents

Application Research of Ant-Tracking Technology Based on Spectral Decomposition in Xingdong Mine

Jiangong Liu, Yanhui Wu, Peng Wang, Jia Song, Gouju Wang, Wentao Ma and Wei Wang

Abstract This work in Xingdong Mine 1200 Area is focused on use of the basic documents of seismic, logging and site disclosure and the results of comprehensive geological research. Based on Petrel geological modeling platform, applying the advanced spectral decomposition and Ant-Tracking technology, taking Xingdong Mine 1200 Area as an example, the large, medium and small-scaled discrete crack network models are established. It has also made reconstruction and realized the effective prediction of the fault system and Collapse-column, which provided a solid fundamental guarantee for the prediction of faults and complex geological body in other regions.

Keywords Spectral decomposition · Ant-Tracking · Modeling

1 Introduction

In coal mining process, collapse column, minor fault and fracture are the serious issues need to be addressed to avoid hydrogeological hazards. Especially for the mines under large mining depth and high confined situation in North China Type Coal Field, which coal seam floor bears high water pressure. 3-D seismic technology is rapidly expanded and applies in many mine areas for its advantage which is with less investment, high precision, quick results, and it has taken place of the traditional geological prospecting methods as an indispensable method in coal mine production. With the exploration of deep coal resource, the existing structure interpretation of seismic exploration becomes gradually unsatisfactory to the

---

J. Liu · Y. Wu · P. Wang · J. Song · G. Wang · W. Ma
Hebei Coal Research Institute, Xingtai, China

W. Wang (✉)
Institute of Geographic Sciences and Natural Resources Research,
Chinese Academy of Science, Beijing, China

Q. Di et al. (eds.), *Technology and Application of Environmental and Engineering Geophysics*, Springer Geophysics,
DOI 10.1007/978-981-10-3244-8_1

demand of control accuracy which is required by mine area production. This paper processes post-stack seismic data by spectral processing technique taking geological data, borehole data and on-the-spot exposure data as constraint conditions, to obtain discrete phase target data as the simple of Xingdong Mine 1200 Area. At the same time the study tries to use the Ant-Tracking to track target layer automatically and then verify the efficiency and applicability of comprehensive interpretation based on spectral decomposition and Ant-Tracking by summarized after mining.

2 Theory and Method

Theoretically, the high frequency component of seismic data is sensitive to micro-fault or micro-deflection. So we can explore the micro-fault or micro-deflection using high frequency component of seismic data. Spectral decomposition technology uses S-transform which can generate high resolution spectral decomposition image to calculate. Using spectral decomposition, the Ant-Tracking technique can automatically explore the small faults and fractures which is difficult to identify in the whole bandwidth seismic data [1].

2.1 Spectral Decomposition

Spectral decomposition is a seismic attribute technology based on time-frequency analysis [2]. It can process seismic data into frequency slice rather than time or depth slice, which can make the thin-layer reflection system produce complex resonant reflector. Fundamentally, spectral decomposition is the method to decompose the seismic data into seismic reflection frequency information. By choosing specific frequency, it is helpful for the interpreter to browse the selected frequency data, effectively identify and extract the concealed Strata and Structural Characteristics, adequately excavate connotative geologic information. Influenced by seismic resolution, the traditional seismic processing and interpretation has low accuracy to the fault less than 5 m. Using spectral decomposition can break through seismic resolution effectively and extrude geologic anomaly body better [3]. Spectral decomposition helps to show rock stratum forms and greatly increasing the recognition of micro-fault [4].

There are four common spectral decomposition techniques, namely, discrete flourier transform (DET), continuous wavelet transform (CWT), time and frequency continuous wavelet transform (TFCWT), S-transform (ST). We choose S-transform to process spectral decomposition, because it can generate high resolution spectral decomposition image [5], which has better application in removing the noise and analyzing thin interbed.

S-transform of function $h(t)$ can be expressed as:

$$S_f(t,f) = \int_{-\infty}^{\infty} \mathrm{h}(\tau)\ w(\mathrm{t}-\tau,\ f)\ \exp(-i2\pi f\tau)d\tau \tag{1}$$

$$w(t) = \frac{1}{k\sqrt{2\pi}}\exp\frac{-t^2}{2k^2} \tag{2}$$

So the blew can be obtained

$$S_f(t,f) = \int_{-\infty}^{\infty} h(\tau)\frac{|f|}{\sqrt{2\pi}}\exp\frac{-f^2(t-\tau)^2}{2}\exp(-i2\pi f\tau)d\tau \quad (f \neq 0) \tag{3}$$

where f is frequency, t is time, τ is the time on control the gauss window position on the timeline.

2.2 *Ant-Tracking*

Ant-Tracking is the algorithm to simulate the ants' foraging behavior based on computational intelligent. Following are its basic assumptions [6]:

The ants can communicate with each other by pheromone and surrounding environment. The characteristic reaction is made by every ant according to local environment, and only has a positive impact on its local environment.

The response to the environment is the Adaptability of the ant and is decided by its internal model.

For the individual ant, the choice is made by a single ant only according to local environmental independently; for groups ants, the behavior of a single is random, the highly ordered group behavior of the ants is formed through self-organization process.

Ant-Tracking has automatic seeking optimal mechanism. The ant finds path through the path' pheromone (Fig. 1), and establishments positive feedback mechanism to enhance the pheromone on the optimal the path. The ant takes pheromones as feedback carrier to determine the decision point, along with other path' pheromone decay over the time attenuation eliminate, when the optimal path appears barrier, it can find the other optimal path in time [7].

Tracking and interpreting the fracture of 3D seismic data by Ant-Tracking property module on Petrel geological modeling platform automatically, avoids interpreting seismic subjectively and solves the problem that the fracture producing in the interaction between structure and karst has the poor direction and is difficult to characterize [8], which improves the interpretation of the seismic profiles, and

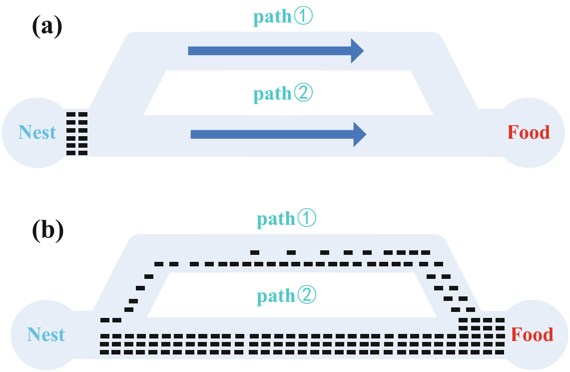

Fig. 1 The behavior of ants' foraging

shortens the time of manual interpretation, and a good result is obtained in identifying small scale structural anomalies.

2.3 *The Ant-Tracking Based on Spectral Decomposition*

- Processing seismic post stack data to generate the various frequency tuning cube by spectral decomposition technique.
- Analyzing spectral decomposition results and frequency trace gathers.
- Preprocessing the score frequency data by structure smoothing, median filtering method, and retain information of fault edge.
- Edge detecting by curvature cube or variance cube and attribute analysis and generating the ant tracing data.
- Reconstructing low frequency, intermediate frequency, high frequency to tracing the data by ant technology.
- Quantitative predicting and explaining the miniature fault and small fracture.

Through the spectral decomposition technique, we can generate suitable target attribute, and fast recognize target about the frequency division multiple attribute cube, and also interactively view trace gathers, horizon, log data, rock mass, which effectively reduces the reflection seismic anomalies of the detection of thin layer, fault and below abnormal.

3 Examples

XingDong mine is in North China Type Coal Field and 1200 area is very complex which has the large mining depth and a quantity of minor faults. Although a good result achieved in this area's conventional seismic interpretation, but it is a pity that the only one collapse column was not interpreted. This study takes geological site disclosure condition as constraints and used post stack data by Ant-Tracking Technology based on Spectral Decomposition to improve the discriminating capacity of geological condition and complicated geologic structure, and it's beneficial to develop seismic technology research in this area.

Within the scope of effective frequency band of seismic information, the Ant-Tracking Technology based on Spectral Decomposition was used in the whole work area [9]. By the increase of extract frequency, the features of complex geological body and minor faults become more distinct. The faults, mainly manifested as obscure or seismic event's distortion, which might lead to erroneous interpretation in case of conventional seismic section, but the response of weakly reflection and low energy were clearly displayed in the frequency-division section. This shows that the interpretation's accuracy is improved through the processing of the frequency-division section.

In order to exclude mutual interference, these technologies systematically used high image precision, improvement of resolution, average of frequency and noise elimination etc. As an effective method to reveal the hidden characteristics, the interpretation results are more reliable than the traditional interpretation results. The equifrequency cube data of 10 Hz interval from 40 to 90 Hz are extracted by using this technology. The revealed collapse column of 2# coal seam hasn't clearly morphologic change in the section of original data (Fig. 2). It shows that the short wavelength in long wavelength of the collapse column's structural characteristics has been hidden in the seismic data of the full frequency band. Both the low frequency cube and high frequency cube can make the X7, the only one collapse column in this area, and displays its location and type on account of the collapse column absorbing the high frequency components of seismic data, and the border

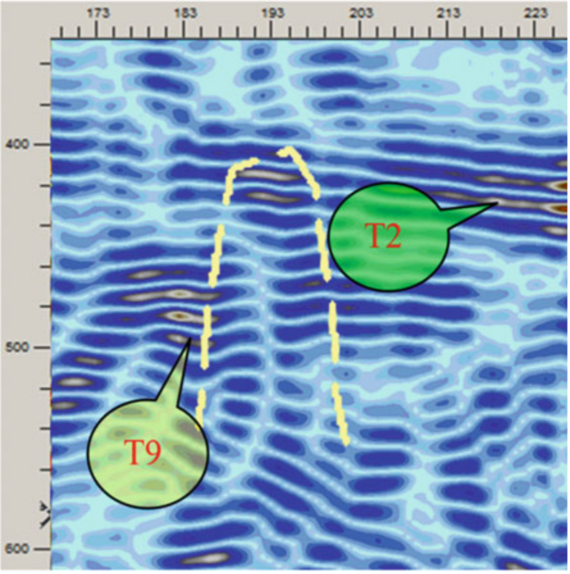

Fig. 2 The section of 30 Hz frequency cube

Fig. 3 The section of 50 Hz frequency cube

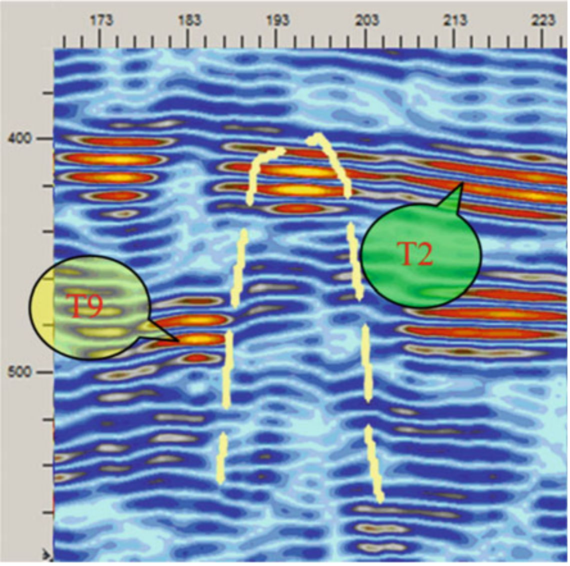

Fig. 4 The section of 70 Hz frequency cube

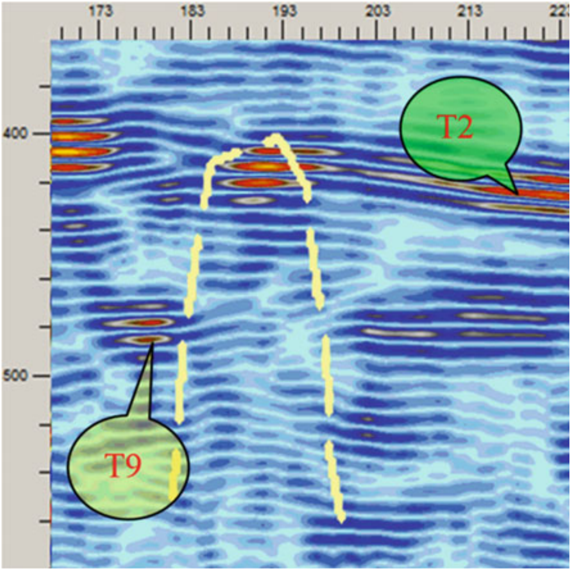

can be displayed by low frequency components (Fig. 3). But in 50 Hz frequency region (Fig. 4), the same as the section of original data, the opposite condition appeared since the spurious frequency may contain in relatively high frequency information (Fig. 5).

In order to identify faults quickly and effectively, the revealed faults as constraint condition to limit the dip angle and azimuth for search of ants. At first, the dip angle

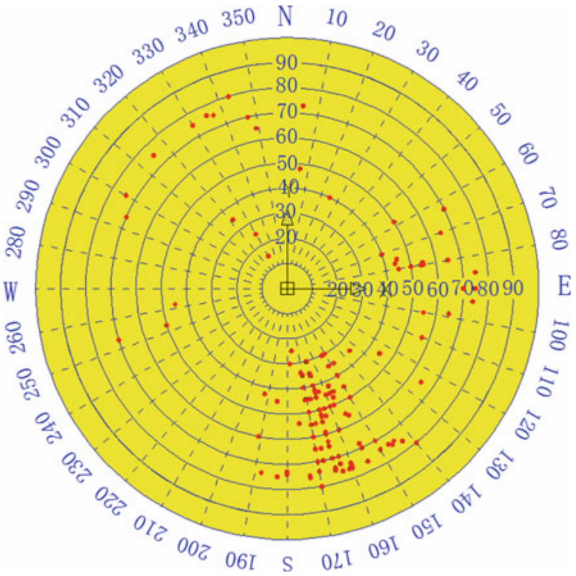

Fig. 5 Joint rose diagram

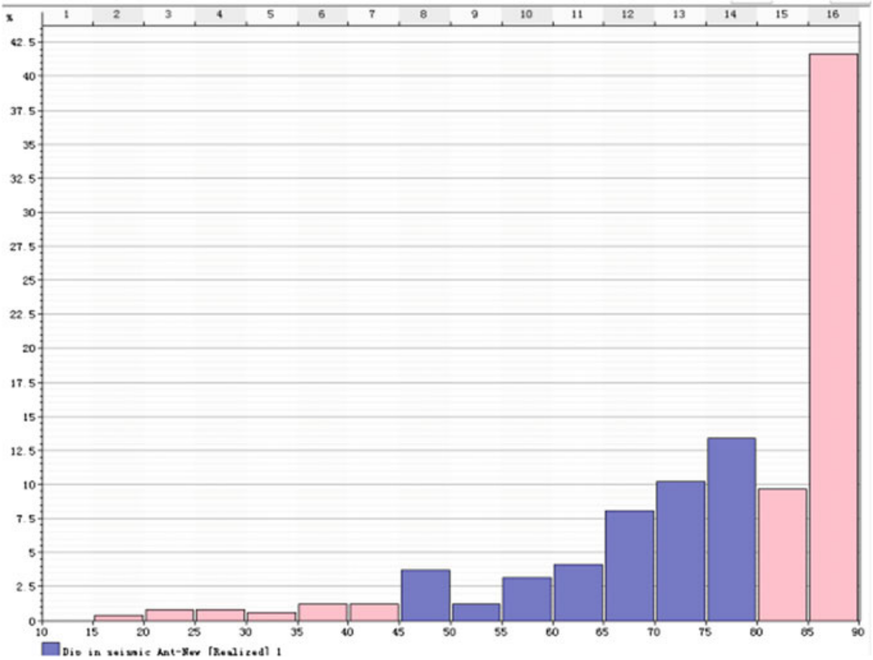

Fig. 6 Columnar statistical figure

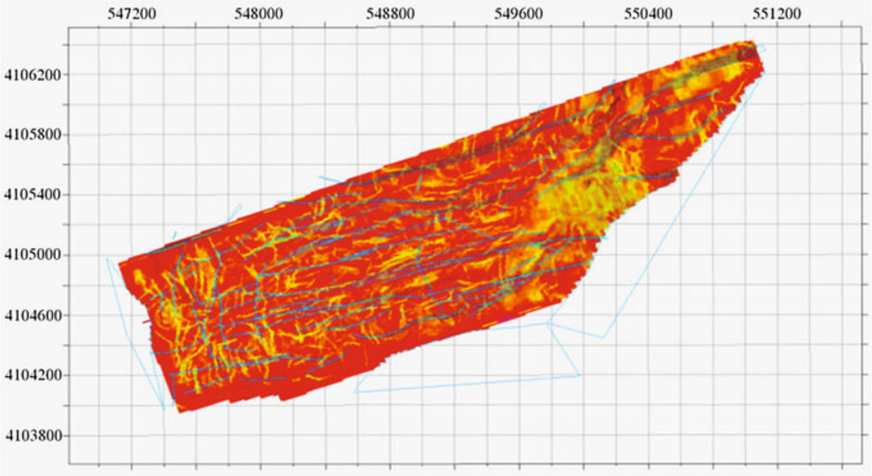

Fig. 7 The section of 20 Hz frequency cube based on Ant-Tracking tracing

and azimuth in this area are counted, and those points are taken to the rose diagram of joint (Fig. 6). At last, based on Petrel geological modeling platform to analyze the geological constraints, the red dot represents revealed faults, and the surrounding of those dots is the key searching area for ants. And the blue column means that those significant dip angle should be recorded (Fig. 7).

In order to achieve the micro-fracture and micro-fault automation interpretation of seismic data, firstly, we need select reasonable tracking and take advantage of aggressive mode tracing micro-fracture and micro-fault, through the tunnel to expose fault to verify its correctness. Secondly, through setting up reasonable parameters which include initial distribution of ants' boundary, step length and termination of the standard, we can extract micro-fracture effectively. Finally, knowing that screening and experimental parameters is the most relevant with practical fault, to improve the accuracy of the Ant-Tracking technology, we need correspond to a different constraint conditions combining with local geological structure.

Ants data cube in the whole frequency range and single frequency range reflect different details in the time slice. We using the dividing frequency data cube enable to fully exploit the Seismic Information to solve geological task. We using the low-frequency attribute volume track large scale fault characteristics, and using the medium-frequency attribute volume track for small scale faults characteristics, using the high-frequency attribute volume track fracture to provide some predictive information. By the ants tracking seismic attribute volume we can see the best effect of tectonic response in 50 Hz, because seismic exploration regional objects by geological relatively deep in the east, with high- frequency attenuation, the characteristics of the frequency is not obvious But we can obtain fault structure in 20 Hz

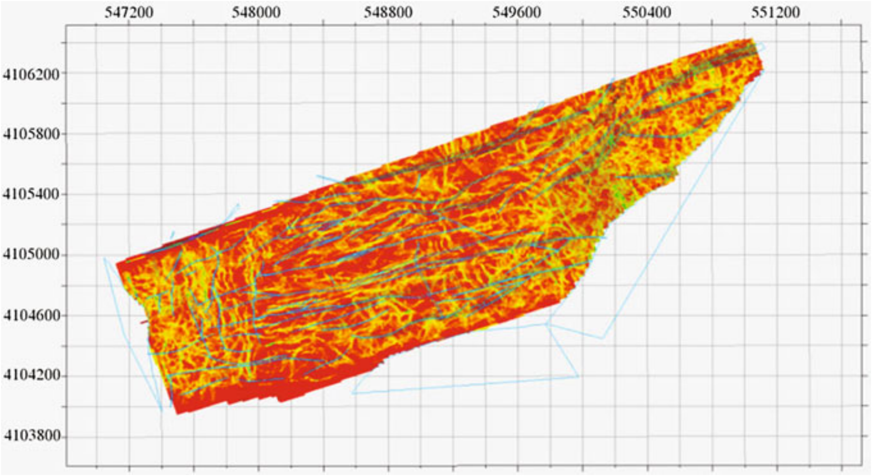

Fig. 8 The section of 80 Hz frequency cube based on Ant-Tracking

and obtain fracture in 80 Hz than ants data cube in the whole frequency range more effective. The blue solid curve represents the conventional interpretation of fault structure, and the yellow solid curve mark represents the Ant-Tracking of dividing frequency data cube interpretation results (Figs. 7, 8, and 9), and the white solid curve represents the whole frequency Ant-Tracking tracking results (Fig. 9).

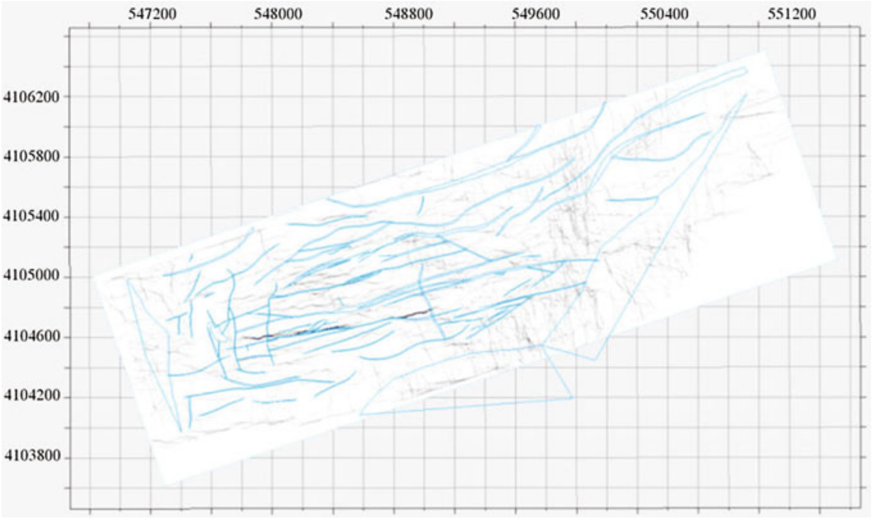

Fig. 9 The variance cube section of whole frequency based on Ant-Tracking Columnar statistical figure

4 Conclusions

The results suggest that the low frequency Multi-attribute seismic response obtained from spectral decomposition technology is consistent with practical data revealed The collapse column in Xingdong Mine 1200 Area is depicted effectively.

The Ant-Tracking can avoid interpreting seismic subjectively and can help understand the fault system in the studied area. Moreover, its practicability in coal mine is verified by the reveal geological information.

With the reveal geological information as constraints, through Ant-Tracking based on spectral decomposition, it is found that dividing frequency data cube have a better effect than the whole frequency data cube.

References

1. YuanZhiyun, Kong Ling hong and WangCheng lin, 2006, Application of spectrum decomposition in reservoir prediction: OGP, 41, 11–15.
2. Chang Suo-liang, Liu Da-meng, Lin Yu-cheng, 2009, Application of spectral decomposition for fine seismic structural interpretation in coal field and gas bearing property predication of coal seam: Journal of China Coal Society, 34, 1015–1021.
3. Peng S P, Gao Y F, Yang R Z, 2005, Theory and application of AVO for detection of coal bed methane A case from the Huainan coalfield: Chinese Journal of Geophysics, 48, 1475–1486.
4. LIU Chunyuan, WEI Xiucheng, ZHU Shengwang, JI Yuxin, 2008, Application of Spectral Decomposition in Carbonate Reservoir: ACTA GEOLOGICA SINICA, 82, 428–432.
5. Yu Hao, Li Jinsong, Zhang Yan, Xu Guangcheng, 2013, Spectral decomposition in fault and reservoir identifications: OGP, 48, 954–959.
6. Ma Xiaoyu, Wang Jun, Li Yonggen, Li Wenke, 2014, Prestack fracture prediction based on ant tracking: OGP, 49, 1199–1203.
7. Chen Zhaoming, Qing Chenggang, Zhou Jiangjiang, 2013, Application of ant-tracking in fracture detection in Paleogene Wenchang Formation of Huizhou: Oilfield. Journal of Yangtze University, 26, 71–74.
8. Wang Jun, Li Yandong and Gan Lideng, 2013, Fracture characterization based on azimuthal aniso-tropy of ant-tracking attribute volume: OGP, 48, 763–769.
9. Yuang Xiaoyu, Li Yingtao, Ye Ning and Zhang Shaonan, 2015, The Application of ant-tracking fracture detection based on Spectral decomposition in Yubei area. OGP, 50, 665–671.

Definition and Improved Algorithm of All-Time TEM Apparent Resistivity

Fei Li, Shangxian Yin, Demin Liu, Yong Han, Shuai Hua and Peng Chen

Abstract An improved TEM all-time apparent resistivity is proposed. Firstly, we give its definition. Its definition at time *t*(i) is the comprehensive resistivity of the zone from *Depth*(i − 1) to infinity, where, *Depth*(i − 1) is the maximum TEM field diffusion distance at time *t*(i − 1). Then, we give its algorithm based on the binary search algorithm. Finally, a half-space model and a whole-space model are constructed to test the proposed method. The traditional all-time apparent resistivity and the improved all-time apparent resistivity are calculated respectively by using the models built above. The results show that compared with traditional method, the improved all-time apparent resistivity is more fit to the theatrical model, and have higher precision and resolution.

Keywords Transient electromagnetic method · Algorithm · Half-space · Whole-space · All-time apparent resistivity

1 Introduction

Transient electromagnetic method (TEM) is widely applied in the mine groundwater disaster prevention and control. In the processing of TEM data, all-time apparent resistivity is an important parameter. However, influenced by the volume effect and equivalence problem, the calculation precision and resolution of traditional all-time apparent resistivity is low. Therefore, we proposed an improved all-time apparent resistivity, trying to improve the detection precision and resolution.

F. Li (✉) · S. Yin · D. Liu · Y. Han · S. Hua · P. Chen
Key Laboratory of Mine Disaster Prevention and Control, North China Institute of Science and Technology, Beijing 101601, China
e-mail: figo1@163.com

Q. Di et al. (eds.), *Technology and Application of Environmental and Engineering Geophysics*, Springer Geophysics,
DOI 10.1007/978-981-10-3244-8_2

2 Definition and Algorithm in Half-Space

The traditional definition of all-time apparent resistivity at time $t(\mathrm{i})$ is the comprehensive resistivity of the zone from depth zero to infinity. While the improved all-time apparent resistivity at time $t(\mathrm{i})$ is defined as the comprehensive resistivity of the zone from $Depth(\mathrm{i}-1)$ to infinity, where, $Depth(\mathrm{i}-1)$ is the maximum TEM field diffusion distance at time $t(\mathrm{i}-1)$.

The algorithm is based on the layered TEM forward modeling algorithm. We apply an i-layer model to calculate the improved all-time apparent resistivity at time $t(\mathrm{i})$. So the forward modeling equation can be expressed as:

$$B_z(\mathrm{i}) = f_{half-space}[X(i), t(i)] \tag{1}$$

where $f_{half-space}$ is the operator of layered TEM forward modeling; $B_z(\mathrm{i})$ is the magnetic induction intensity; $t(i)$ is the sample time; $X(i) = [\rho_1, \rho_2, \ldots, \rho_{i-1}, \rho_i, h_1, h_2, \ldots, h_{i-1}, h_i]$ is the model parameters, where, $\rho_1, \rho_2, \ldots, \rho_{i-1}, \rho_i$ are the resistivity of each layer, $h_1, h_2, \ldots, h_{i-1}, h_i$ are the thickness of each layer, h_i is infinite.

When we calculate the improved all-time apparent resistivity at time $t(\mathrm{i})$, $\rho_1, \rho_2, \ldots, \rho_{\mathrm{i}-1}, h_1, h_2, \ldots, h_{i-2}$ is known because they have been calculated at time $t(1) \sim t(\mathrm{i}-1)$, with only h_{i-1} and ρ_i is unknown. Firstly, we derive equation of h_{i-1}. The maximum TEM field diffusion depth at any time can be expressed as:

$$h = \sqrt{2t\rho/\mu_0} \tag{2}$$

Then, the diffusion velocity can be calculated as:

$$v = \partial h/\partial t = \sqrt{\rho/2\mu_0 t} \tag{3}$$

Furthermore, the thickness of h_{i-1} can be derived as:

$$h_{i-1} = \int\limits_{t(i-2)}^{t(i-1)} v dt = \sqrt{2\rho_{i-1}/\mu_0}\left(\sqrt{t(i-1)} - \sqrt{t(i-2)}\right) \tag{4}$$

By this time, only ρ_i is unknown in the model parameters $X(i)$. Because $B_z(i)$ is monotonic decreasing with resistivity ρ_i, ρ_i can be calculated by binary search algorithm when we bring the observation data to $B_z(i)$.

In the following, we give the detailed calculation steps:

(1) Given the initial search interval $[\rho_a, \rho_b]$, the minimum data misfit $\varepsilon_{\min}$ and the minimum interval length $\delta_{\min}$.
(2) Calculate the median resistivity $\rho_i = (\rho_a + \rho_b)/2$, and substitute it into equation $B_z(\mathrm{i}) = f_{half-space}[X(i), t(i)]$ to calculate the theoretical magnetic induction intensity $B_{zm}(\mathrm{i})$.

(3) Calculate the data misfit ε between the observed value $B_z(\mathrm{i})$ and the theoretical value $B_{zm}(\mathrm{i})$. If $\varepsilon < \varepsilon_{\min}$, then ρ_i is the improved all-time apparent resistivity, $h_i = \sqrt{2\rho_i/\mu_0}(\sqrt{t(i)} - \sqrt{t(i-1)})$, calculation ended; otherwise, go to step (4).

(4) If $B_z(\mathrm{i}) > B_{zm}(\mathrm{i})$, then $\rho_b = \rho_i$, otherwise, $\rho_a = \rho_i$. Calculate the length of search interval $\delta = \rho_a - \rho_b$. If $\delta < \delta_{\min}$, then ρ_i is the improved all-time apparent resistivity, $h_i = \sqrt{2\rho_i/\mu_0}(\sqrt{t(i)} - \sqrt{t(\mathrm{i}-1)})$, calculation ended; otherwise, go back to step (2).

3 Definition and Algorithms in Whole-Space

The definition and algorithm in whole-space can be obtained from that in half-space by two replacements. The two replacements are:

(1) Replace the half-space forward modeling equation $B_z(\mathrm{i}) = f_{half-space}[X(i), t(i)]$ with the whole-space forward modeling equation $B_z(\mathrm{i}) = f_{whole-space}[X(i), t(i)]$. In particular, due to the inseparability of the TEM field to the anomalies in roof and floor (or in front and rear), the mirror model [1] should be applied in constructing the model parameters $X(i)$.

(2) Replace h_{i-1} with $h_{i-1} \times \alpha$, where, α is the full-space response coefficient. A better result can be obtained when $\alpha = 0.3$ according to experience.

4 Synthetic Test

A half-space model with a low resistivity layer is constructed as shown in Fig. 1. The position of the low resistivity layer is in the depth of 60–80 m, with the resistivity of 1 Ω m. The resistivity of background is 10 Ω m. In Fig. 1, the dotted

Fig. 1 Results of a half-space model

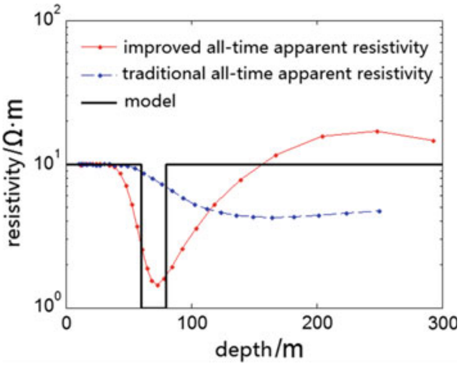

Fig. 2 Results of a whole-space model

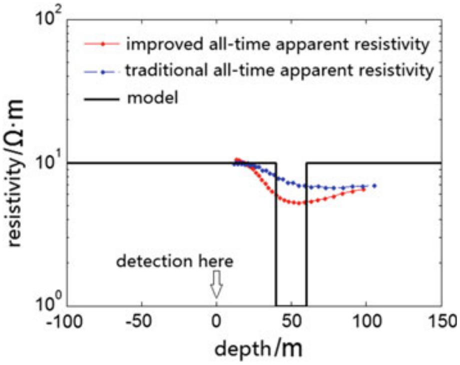

line represents the improved all-time apparent resistivity, and the pecked line represents the traditional all-time apparent resistivity. Figure 1 shows that as compared to traditional method, the improved all-time apparent resistivity achieves better results. The improved resistivity is more fit to the theatrical model, and have higher precision and resolution.

A whole-space model with a low resistivity layer is constructed as shown in Fig. 2. The position of the low resistivity layer is in the depth of 40–60 m, with the resistivity of 1 Ω m, and the resistivity of background is 10 Ω m. The detection position is located at zero on the x-axis. The dotted line represents the improved all-time apparent resistivity, and the pecked line represents the traditional all-time apparent resistivity. Figure 2 shows that as compared to traditional method, the improved all-time apparent resistivity achieves better results. The improved resistivity is more fit to the theatrical model, and have higher precision and resolution.

5 Conclusions

(1) We give the definition and algorithm of an improved all-time apparent resistivity. The improved all-time apparent resistivity at time $t(\mathrm{i})$ is the comprehensive resistivity of the zone from $Depth(\mathrm{i}-1)$ to infinity, where, $Depth(\mathrm{i}-1)$ is the maximum TEM field diffusion distance at time $t(\mathrm{i}-1)$. Based on the binary search algorithm, we give the detailed calculating steps.

(2) Synthetic test show that the improved all-time apparent resistivity is more fit to the theatrical model, and have higher precision and resolution.

Acknowledgment The research presented in this paper is supported by the Fundamental Research Funds for the Central Universities (No. 3142015019), Colleges and universities in Hebei province science and technology research project (No. ZC2016036, BJ201603) and Natural Science Foundation of China (Grand No. 51504097).

Reference

1. Li F, Tan Q, Liu DM, Zhang JG, et al., 2014, Whole-space inversion of mine transient electromagnetic method based on Mirror model: Journal of North China Institute of Science and Technology, 11, 15–19.

The Fast Imaging of Metal Pipe Exploration Using TEM Method

Zhaoqiao Zhang, Shucai Liu, Yong Zhang, Longjin Zheng and Lian Liu

Abstract The transient electromagnetic is one of the important geophysical methods, widely used in various fields, but there exist some problems when solving engineering geophysical problems. In response to this shortcoming, several methods are proposed for TEM imaging (dynamic multi-channel curves, Dynamic induced electromotive force contrast curve, dynamic apparent resistivity and dynamic resistivity depth map) to solve the problem of detecting at the scene quickly finding horizontal location and depth of metal pipe and other engineering problem in cities. And TEM has a relatively deep depth compared with metal pipe instrument and get more information about the features of subsurface. Finally, transient electromagnetic method proved quick detection the metal pipe problem through the detection experiments and several dynamic imaging method of metal tube.

Keywords Transient electromagnetic dynamic imaging

1 Introduction

Urban underground has a large number of pipeline but with the changing times, city disorderly repeated construction caused a large number of pipelines whose information missing buried in the underground. Unknown underground pipelines caused great trouble to the new construction. Such as road widening and construction of residential damage water pipes caused regional unsupplied water, gas pipeline damaged caused stop for gas, electricity cables or telecommunication cables dam-

---

Z. Zhang (✉) · S. Liu · Y. Zhang · L. Zheng · L. Liu
School of Resources and Geosciences, China University of Mining and Technology,
Xuzhou, China
e-mail: zhaoqiaozhang@sina.cn

Q. Di et al. (eds.), *Technology and Application of Environmental and Engineering Geophysics*, Springer Geophysics,
DOI 10.1007/978-981-10-3244-8_3

aged caused power and communications interrupted. In order to prevent damage to the unknown underground pipelines and bring production and construction huge economic losses, it is necessary to conduct geophysical exploration before construction.

DC1, VLF, Electromagnetic induction method, Ground Penetrating Radar2, Magnetic, Seismic and other methods are commonly used methods of pipeline detection. In the above-mentioned types of geophysical methods, Direct current method, Magnetic and Seismic imaging in the detection has low efficiency. The VLF and Electromagnetic induction for metal pipes have better detection results, which can not obtain electrical information of geotechnical structures at underground. However, Transient electromagnetic method have good results in the detection efficiency and access to underground electrical structure.

Urban Geophysical pay attention pragmatic issues, therefore the detection efficiency and detection effect has equal importance. Transient electromagnetic method has better detection results for shallow surface of metal pipes and cables. Induced secondary field around Anomaly body has a strong signal and noise ratio, suitable for solving the problem of urban underground pipeline detection. However, this is always true for transient electromagnetic detection equipment to display dynamic display information does not yet exist practical problems solved is not a small problem not with appropriate dynamic display information At the scene. In this paper, The dynamic transient electromagnetic imaging technology is expand discussed to solve the transient electromagnetic method detect metal pipeline and get dynamic feedback.

2 Imaging System

TEM Imaging System includes dynamic multi-channel curves, Dynamic induced electromotive force contrast curve, dynamic apparent resistivity and dynamic resistivity depth map. The dynamic image can show dynamic response of measurements on-site, rapid inferred metal pipe's location and depth of burial dynamic multi-channel curves: the induced electromotive force at the same delay time can be observed in the cross-section; Dynamic induced electromotive force contrast curve: Induced electromotive force attenuation curve by lifting and falling is observed for several adjacent measuring points; Dynamic apparent resistivity: Displays dynamic pseudosection apparent resistivity; Dynamic resistivity depth map: display resistivity depth profile (Fig. 1).

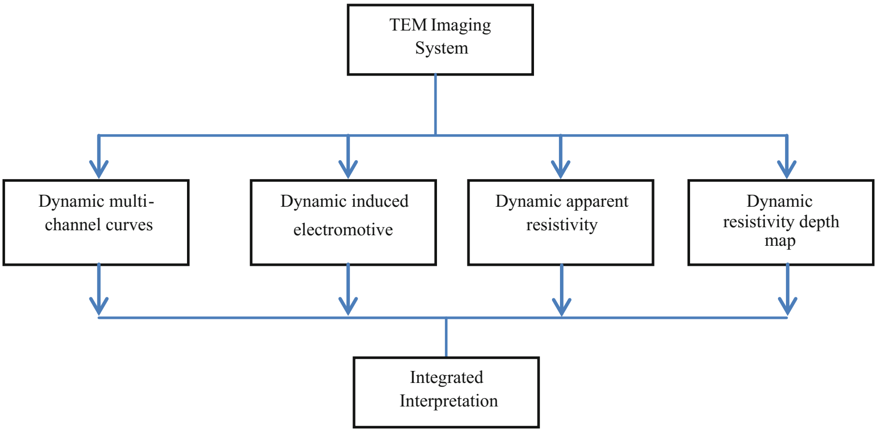

Fig. 1 TEM imaging system ace model

3 Setting Main Parameters

Probing shallow metal pipes, you must first select the appropriate sampling delay. Accord diffusion depth formula of TEM, The depth proportional to $\sqrt{\rho t}$. The half diffusion depth is usually taken as probing depth, giving the following formula to determine the sampling range

$$t_{\min} < 10^{-3} * h_{\min}^2 / \rho_{\max} \tag{1}$$

$$t_{\max} < 10^{-3} * h_{\max}^2 / \rho_{\min} \tag{2}$$

Late apparent resistivity formula

$$\rho = \frac{\mu_0}{4\pi}\left(\frac{2\mu_0 SNsn}{5}\right)^{\frac{2}{3}} t^{-\frac{5}{3}} \left(\frac{I}{V(t)}\right)^{\frac{2}{3}} \tag{3}$$

Time depth conversion formula

$$h = -0.5 * 2000 * \sqrt{\rho t} \tag{4}$$

Transmit coil use multiple small loop coil. Transmitter loop size 40 × 40 cm^2, turns 20 hit. In order to under the circumstances, the matching resistor prevent over-current for instrument and protect equipment burned. Receiving coil 40 × 40 cm^2, turns 40 hit.

For shallow metal pipeline detection, shallow surface soil is more complex filled. Original strata is destroyed, inversion methods has poor fitting effect obtaining information about the depth of metal pipelines, Inversion results has higher requirements for the parameters setting, which is not conducive to fast imaging and quickly obtaining depth information of the target body. In order to quickly obtain information about the depth of the target body, according to the depth of the diffusion equation, it is desirable half diffusion depth as the empirical formula of the depth conversion.

4 Dynamic Imaging Picture Show

Figure 2 represents dynamic multi-channel curves cross section, when N is 10, 20, 30, 65 points. When N = 10, voltage is gentle at the upper portion of figure, the downward electromagnetic waves uniform decay on the section; advanced induced voltage increases and lift upward along measuring point directions; N = 20, all induced electromotive force curve increases up at the figure describing measuring devices are close to underground metal pipe. N = 40, the measurement point pass through the top of the metal pipe, underground metal pipe produce induced eddy current, induced electromotive force measured overall increase. The induction potential first and decreased then. Dynamic multi-channel curves clearly reflect the position of the abnormal body in the horizontal direction of the cross section. When N = 65, Transient electromagnetic detection stop. multi-channel curves final display measurement results. Increased first voltage value decreased, a high regeneration process of decline. It can be seen that there are two extreme points in profile exception, immediately can determine the presence of two metal objects at underground.

Traditional measuring instruments can only be observed for the induced electromotive force curves in this case. When TEM detect urban metal pipe, Work experience requirements for equipment operator is higher. The inexperienced people is difficult to see the attenuation of induced electromotive force, the back

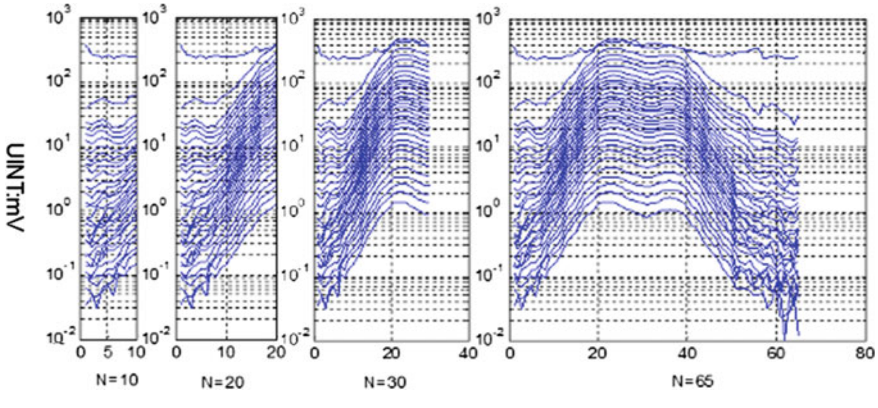

Fig. 2 Dynamic multi-channel curves

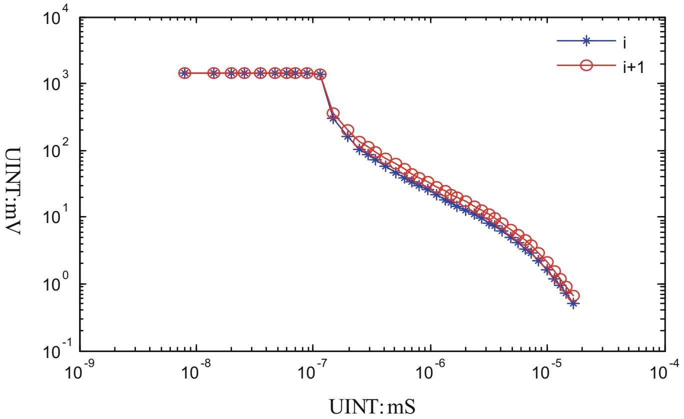

Fig. 3 Dynamic apparent resistivity figure

with the last collection can be displayed in Acquisition window and the induced electromotive force changing is easy to be observed as Fig. 3. The red curve represents the current data, the blue line represents curves back of collection. The change of induced electromotive force can be easily observed along the line direction, determined whether exists anomalies at underground.

Figure 4 is dynamic resistivity section figure. the each measuring point of the image is refreshed once, the cross-section update apparent resistivity changes. The figure selected N = 10, 30, 40, 65 measuring points. When N = 10, The point are away from the metal pipes. The early resistivity has good distribution layer which is affected by surface high resistance concrete pavement. N = 20, the measurement points close to the low resistivity anomalies the bottom of the resistivity overall upward slopping. N = 40, 2.2 and 3.5 m has two low resistivity body at

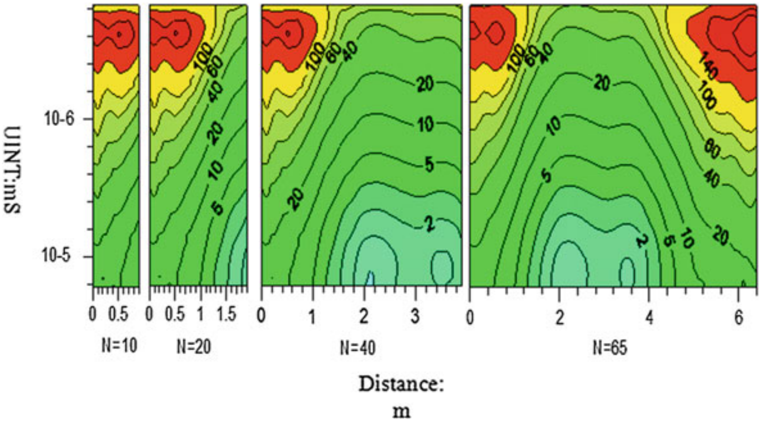

Fig. 4 Dynamic induced electromotive force contrast curve

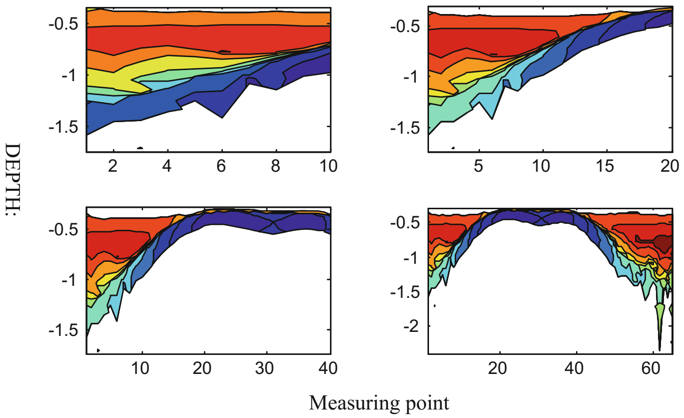

Fig. 5 Dynamic resistivity depth figure

cross-section, the left is more than the right of abnormal. When N = 65 cross-section measurements stop, we can quickly determine the existence of two low resistivity anomalies inferred cause by metal pipe from Fig. 4.

The above dynamic multi-channel curves and dynamic resistivity section can quickly determine the metal pipe in the horizontal direction of the position, but can not give roughly approximately buried depth of the metal pipeline. Transient electromagnetic method is more reliable interpretation of the one-dimensional transient electromagnetic inversion. However, the choice of inversion parameters is more trouble, the inversion work needs to spend more time. The time depth conversion is quickly realized to solve the engineering problems, the empirical formula is a good choice. It can quickly realize the dynamic display of deep profile. Four dynamic profile are N = 10, 20, 40, 65 points as Fig. 5. When N = 60 can be observed in the presence of two low resistivity anomaly zone in the section, abnormal centers located at (2.2, 0.4) and (3.5, 0.4). Therefore, Empirical formula infer depth of abnormal body that is a very effective and fast dynamic imaging method of metal pipe buried depth.

5 Conclusion

In the city of metal pipeline detection, TEM is a kind of efficient and advantageous method relative to other geophysical method. It can not only detect the location and depth of the metal line, but also can help in identification of leakage region near pipeline. Dynamic multi-channel can be used to quickly determine the position of the metal tube. Dynamic voltage curve can be easily observed abnormal rise, decrease on requirements for the operator's experience and ability dynamic apparent resistivity section can update change of the apparent resistivity, locking the abnormal range. The approximate depth of anomaly body can be inferred by dynamic resistivity depth map. The above several images can solve the transient electromagnetic method detect the problem of metal tube on site and other engineering geophysical problems. Fast dynamic imaging method combined with improved measuring device. TEM can be expected in the future which can has the high efficient in city geophysical exploration work.

Absorbing Quality Factor Attribute for Recognising Ordovician Cave and Underground River System in Tahe Oilfield

Yuxin Luo, Ruizhao Yang, Pengpeng Li, Duo Gao and Chao Liu

Abstract At Tahe Oilfield Ordovician strata, caves and underground rivers are the commonly developed geological structures…. Caves and underground rivers serve as connection pipes for different types of reservoirs, and are also an important part of a reservoir. This paper presents the researched carried out on a block of high resolution 3D seismic data from Tahe oil field. For the research, Absorption quality factor attribute (AQF) was tested with the aim of identifying the cave and underground river systems. In the AQF attribute sections, the caves were depicted clearly and some inconspicuous dot-like seismic reflection and some seismic reflection troughs were better displayed. In addition, the original seismic, similarity attribute data, body sculpting technology and drilling data successfully verified the caves which were predicted from the AQF data. Our research shows that AQF attribute identifies the caves and underground river systems very well. Hence, AQF attribute is useful in identifying and dividing caves and underground river systems.

Keywords Absorption quality factor · Tahe oilfield · Caves and underground river systems · Reservoir prediction

1 Introduction

Tahe Ordovician system carbonate reservoir development is closely related to that of Karst development. Karstification of the complex karst cave system constitutes the main reservoir space of carbonate reservoirs. Karst cave and underground river is an important part of reservoir space. Previous studies confirmed that Tahe ordovician strata of the Caledonian period have only experienced exposure three times. The massive supergene karst occurred in the Ordovician during the period of exposure. Multiple karstification formed the complex network of feather like cave

---

Y. Luo (✉) · R. Yang · P. Li · D. Gao · C. Liu
School of Geosciences and Surveying Engineering, China University of Mining
and Technology Beijing, Beijing, China
e-mail: Simonluo714@163.com

Q. Di et al. (eds.), *Technology and Application of Environmental and Engineering Geophysics*, Springer Geophysics,
DOI 10.1007/978-981-10-3244-8_4

system. And latter caves collapses, compaction, cementation, initially led to segmentation formation in the original cave system.

At Tahe Oilfield, more than 600 wells were drilled in Ordovician and well statistics show that unfilled medium-sized cave in the well data are nearly half. The largest unfilled cave is up to 37 m and the largest filling cave is up to 73 m [1]. Li [2] proposed that the formation of Tahe Ordovician carbonate system is mainly due to the Early Hercynian Weathering Crust Karstification, and that the system developed three other sub systems. They are underground river systems, karst caves, the corroded holes and fractures, where the underground river and karst cave system are based.

It can be seen that Tahe Oilfield Ordovician karst has a multi-stage history. The formation of karst caves and underground rivers has great reservoir space even though the entire cave system is very complex. Therefore, accurately identifying these caves and underground rivers is important for exploration at Tahe oilfield.

2 Theory and Method

2.1 Frequency Attenuation

Seismic waves propagation in underground media, which is not a completely elastic media of rock and wavefront diverging action will lead to continued weakening of the seismic wave amplitude. Many rock physics experiments shows that the existence of fluid will further strengthen the absorption of seismic waves, resulting in seismic wave velocity/frequency attenuation of wave field characteristic change. Mitchell [3] used energy absorption analysis to find natural gas in a channel sandstone and successfully applied the high-frequency absorption phenomena of seismic waves propagating in underground media. Korneev [4] used ultrasonic experiment to simulate seismic wave field characteristics of dry and water-saturated sand layer and he found that seismic wave field in water saturated sandstone has high frequency absorption and phase distortion phenomenon. According to this phenomenon, we can use the absorption quality factor attribute to reflect the subsurface seismic waves of high frequency absorption speed, thereby indicating subsurface media which contains fluid or having high porosity.

Formation of Tahe Oilfield Ordovician karst caves and underground river is related to epigenetic karstification. Qi Lixin et al. gave a statistic of 600 drilling wells which encountered Ordovician strata in Tahe Oilfield. The drilling data shows that even after the period of later cave collapse, during burial, compaction, filling and other geology effects, karst cave and underground river system still has a high porosity, and are filled with the underground liquid.

2.2 *Quality Factor*

Seismic waves attenuation properties of the medium in the ground are usually characterized by quality factor Q. Defined by the general formula below: When seismic wave propagation wavelength λ, the Q is equal to 2π times the ratio of previously stored energy E and energy consumption ΔE.

$$Q = 2\pi \cdot \frac{E}{\Delta E} \tag{1}$$

Both field and laboratory data show that quality factor is influenced by physical properties of the rock, fluid type, and the attenuation of the relevant fluid [5, 6]. The quality factor can be used to reflect the characteristics of reservoirs and hydrocarbon detection [7, 8].

In this paper, the Opendtect interpretation system launched by the Netherlands company GB was used to calculate the Absorption quality factor of seismic data. Absorption Quality Factor returns the area beyond the dominant frequency weighted by frequency. It shows how fast high frequencies are absorbed. It reflects the high-frequency absorption speed. Calculation of AQF is controlled by three parameters: The size of the window, the shape of the window, and window normalized. Normalization is used to enable comparison of absorption effects independent of seismic energy levels. AQF is especially useful in detecting hydrocarbon anomalies. Tahe Oilfield's caves and underground rivers system is not completely filled, mostly it contains underground fluid. So AQF attribute can be used to indicate any system composed of caves and underground rivers.

2.3 *Seismic Attributes*

Li [9] used finely coherence attributes of seismic data and discovered three ancient underground river karst pipeline systems at Tahe oilfield. Lu [10] used 3D visualization technology with amplitude attributes and coherence attribute to identify ancient river. And Wu [11] successfully applied amplitude attribute to describe the continuity of underground river reservoirs.

3 Example

In this paper, a block of 3D high-resolution seismic tests data in Tahe oilfield was researched. The test data covered an area of 72.9 km^2, and TVT time range of 3300–4500 ms. The seismic cube contained 2 major horizons: T4 and T6.

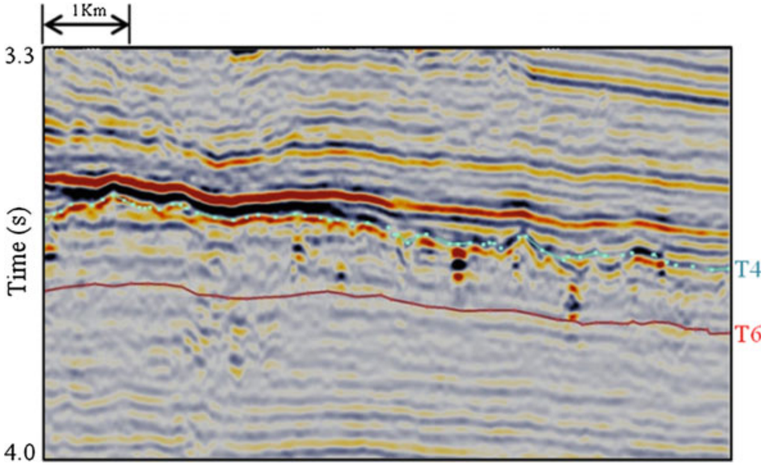

Fig. 1 Original seismic section

3.1 AQF Attribute Section

Figure 1 shows the original seismic profiles. Between T4 and T6 there are strong seismic reflection features just like beads. According to Lu Xinbian 2014, these beads feature is a reflection characteristics of ancient Karst. Figure 2 is AQF attribute section of the same position. In Fig. 2 these beads correspond to high value of AQF. Some inconspicuous beads like seismic reflection in Fig. 2 are outstanding. The area with this seismic reflection in Fig. 1 may represent fracture reservoir types.

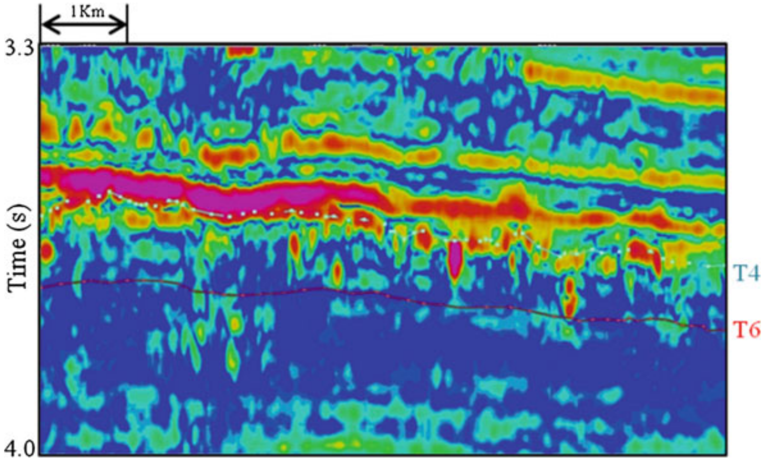

Fig. 2 AOF attribute section

3.2 Similarity and AQF

Figure 3 is a time slice of AQF attribute along T6 layer. High value areas of AQF was distributed over the slice. Figure 1 is Similarity time slice of T6 layer. It shows many rings of low similarity value region. According to Figs. 3 and 4, we can see that the AQF high value areas are always wrapped in low similarity attribute ring, which shows that the AQF attribute reflects the morphological characteristics of the ancient karst very well.

3.3 3D Carving Technology and Well Testing

Figure 5 is the high AQF value area obtained by using 3D carving technology. The figure shows the carved AQF attributes below 3750 ms. 7 wells were involved in the figure: 1 high yield well, 1 medium yield well, 4 low yield wells and 1 water well. All wells have hit the high value area of AQF attributes excepting No. 5.

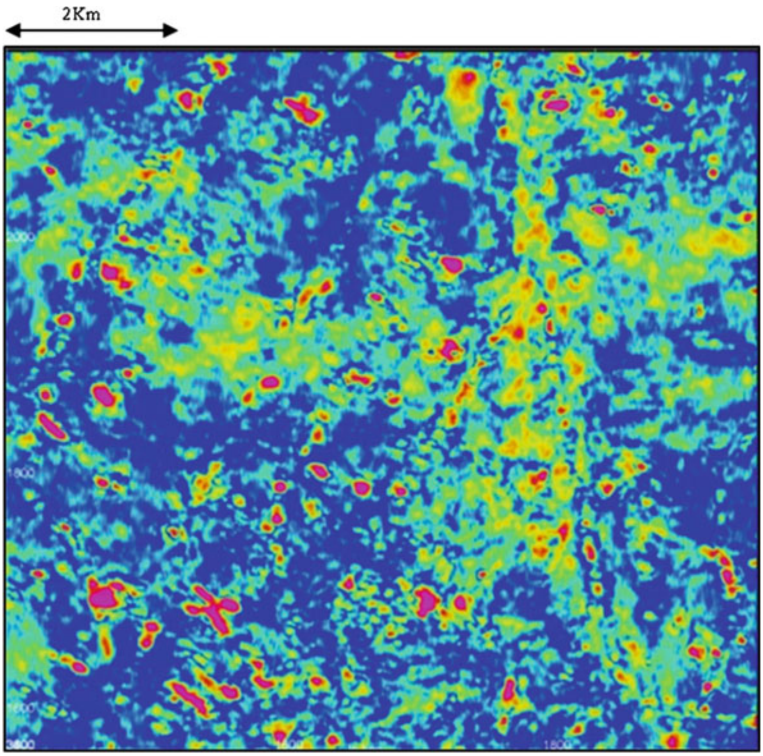

Fig. 3 AQF time slice along T6 layer

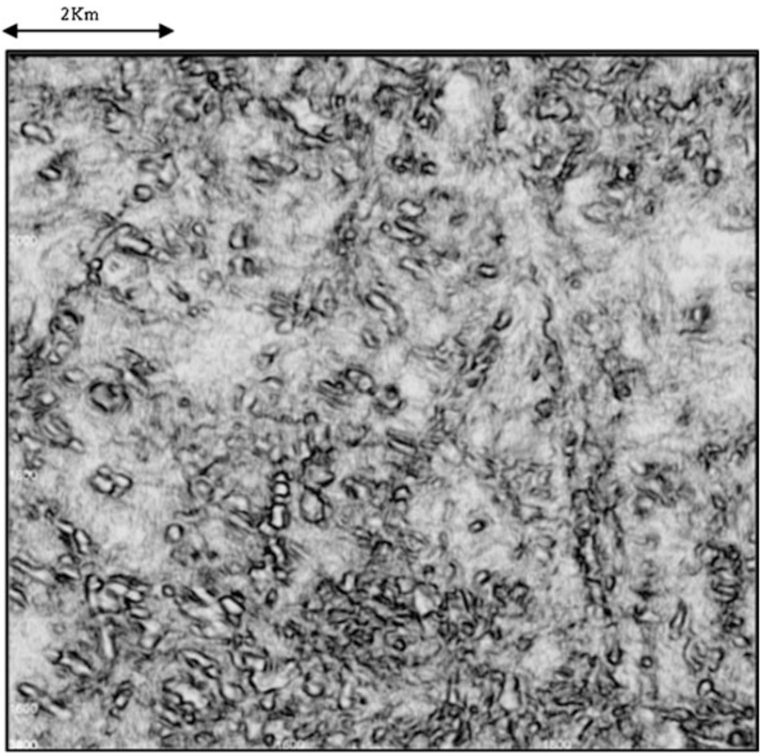

Fig. 4 Similarity time slice along T6 layer

Drilling data shows that No. 1/2/3/4/6/7 wells were encountered the ancient Karst. Hence, the drilling data proved the reliability of AQF on cave characterization. Figure 5 also shows that AQF attribute has a certain effect on the description of the karst system connectivity.

3.4 Prediction of Underground River

Figure 6 is Facies map of the caves and underground rivers taken from 3810 ms time slice of AQF attribute data. In the figure, red areas represent caves, green areas reflects underground channels. The figure shows the caves spots scattered, rivers dominated by patchy distribution.

Figure 7 is a partial view, along the prediction channel, two seismic sections and two AQF sections were extracted (Fig. 8).

In Fig. 8 AA′ and BB′ attribute sections at 3810 ms shows a strong continuous absorption feature, but in other areas of the facies map the phenomenon is not shown. Therefore, we have inferred that this anomalous response of AQF attribute reflects ancient underground channels.

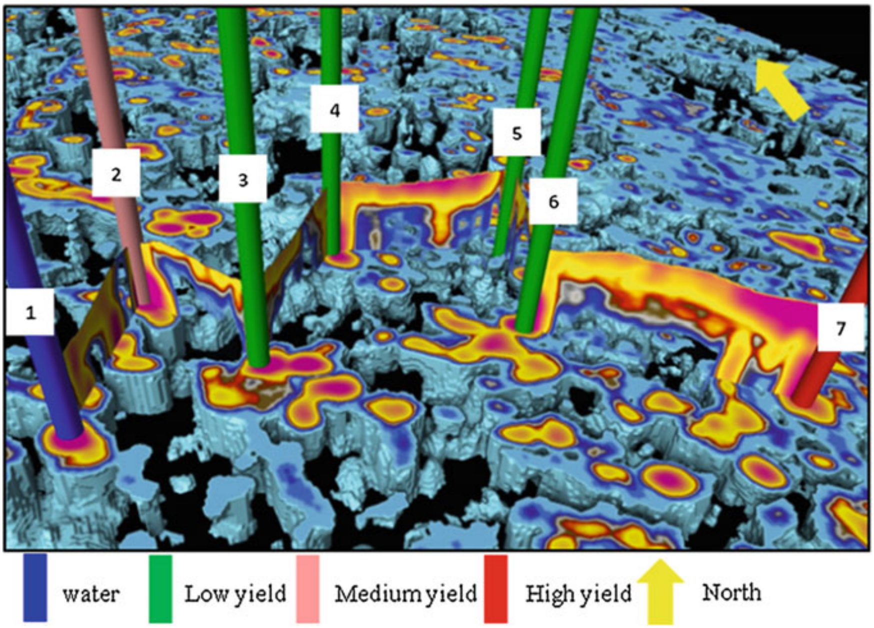

Fig. 5 Body sculptioning of AQF data and using well data

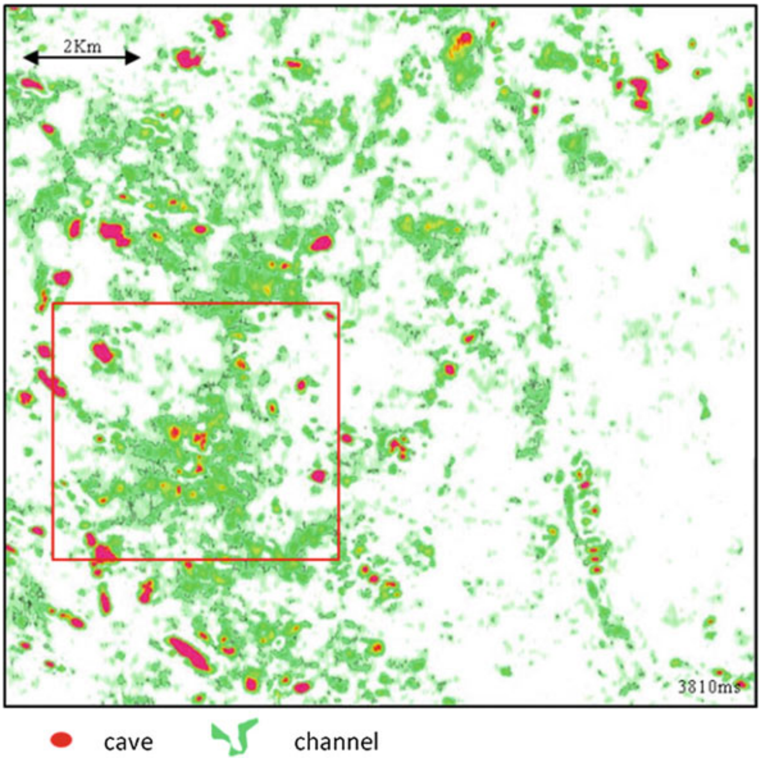

Fig. 6 Facies map of the cave and underground river

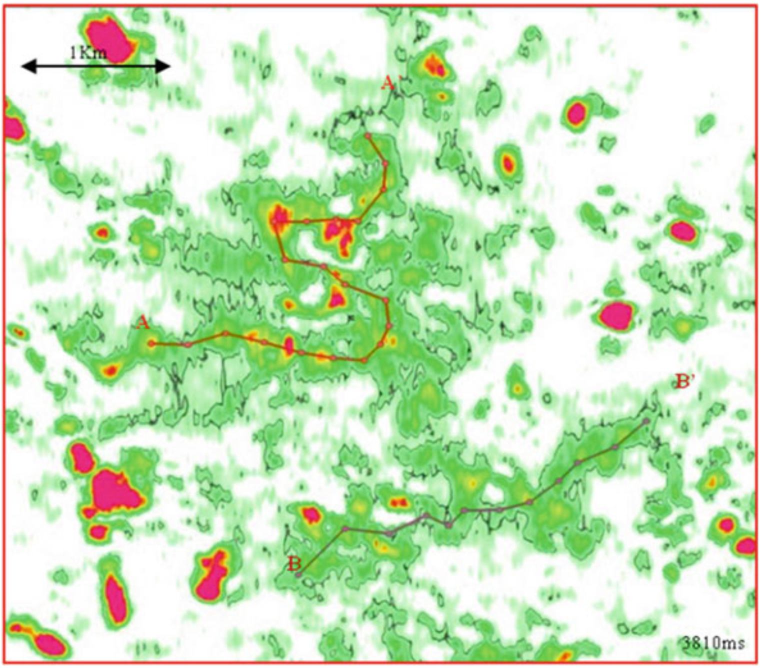

Fig. 7 Partial view of the facies map

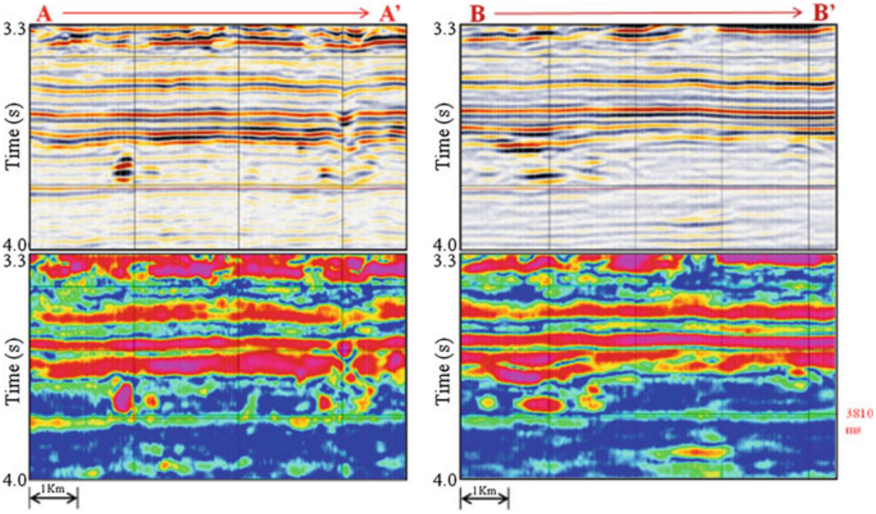

Fig. 8 Seismic sections and AQF section extracted along the prediction channel in Fig. 7

4 Conclusions

Combining seismic sections with similarity attributes, 3D carving technology and drilling data for AQF attribute, we were able to draw the following conclusions that:

- Absorbing quality factor attribute can highlight Tahe Ordovician cave's shape characteristics, especially the dot-like seismic reflection cave.
- Inconspicuous dot-like seismic reflection and some seismic reflection troughs, can be been better displayed in AQF attribute. And hence, AQF can be used in vuggy and fractured reservoir prediction.
- Absorbing quality factor as an attribute used for displaying seismic volume of oil and gas anomaly, can now be applied to identify caves and underground river systems and also to divide river systems in the future.

References

1. Qi Lixin, Yun Lu, "Development characteristics and main controlling factors of the Ordovician carbonate karst in Tahe oilfield," Oil & Gas Geology, 2010, vol. 01, pp. 1–12.
2. Li Yang, "The theory and method for development of carbonate fractured-cavity reservoirs in Tahe oilfield," Acta petrolei Sinica, 2013, vol. 01, pp. 115–121.
3. Mitchell, J Todd et al., "Energy absorption analysis: A case study," 66th Annual International Meeting 1996: SEG, Expanded Abstracts.
4. Korneev, Valeri A et al., "Seismic low-frequency effects in monitoring fluid-saturated reservoirs," Geophysics, 2004, 69(2), pp. 522–532.
5. Winkler K, Nur A.,"Seismic attenuation: effects of pore fluids and frictional sliding," Geophysics, 1982, 47, 1–15.
6. Sheriff, Robert E, Lloyd P Geldart, Exploration seismology. New York, CA: Cambridge University, 1995.
7. Toksöz, MN, DH Johnston, and A Timur, "Attenuation of seismic waves in dry and saturated rocks: I. Laboratory measurements," Geophysics, 1979, 44(4), pp. 681–690.
8. Frisillo, AL, and TJ Stewart, "Effect of partial gas/brine saturation on ultrasonic absorption in sandstone," Journal of Geophysical Research: Solid Earth, 1980, 85(B10), pp. 5209–5211.
9. Li Yang, Fan Zhihui, "Developmental pattern and distribution rule of the fracture-cavity system of Ordovician carbonate reservoirs in the Tahe Oilfield," Acta Petrolei Sinica, 2011, vol. 01, pp. 101–106.
10. Lu Xinbian, He Chengjiang, Deng Guangxiao, Bao dian, "Development features of karst ancient river system in Ordovician reservoirs, Tahe Oil Filed," Petroleum Geology & Experiment, 2014, vol. 03, pp. 268–274.
11. Wu bo, Rong Yuansuai, Liu Yao, Zhang zhenzhe, Deng Feng, "Exploration potential of oil and gas reservoirs of ancient underground river in Tahe Oilfield," Fault-Block Oil & Gas Field, 2015, vol. 06, pp. 702–704.

Research on Induced Polarization Relaxation Properties of Sand Sample

Qian Guo, Lichao Nie, Shucai Li, Bin Liu, Chuanwu Wang and Mingzhen Tian

Abstract The work discuss the main influencing factors of induced polarization effect including porosity, water content and current intensity from the analysis of induced polarization relaxation properties. The experimental device of induced polarization four-electrode method has been used to contrast three groups (particle size 0.6–1.18, 1.0–1.4, 2.36–4.72 mm) of aquifers sand sample. Different current has been supplied into each particle size group of sand simple with different water content (2–24%) to explore the impact of the relationship between aquifers sand sample and the induced polarization relaxation properties.

Keywords Induced polarization · Half-life time · Sand sample · Laboratory experiment

1 Introduction

Research on induced polarization relaxation properties of aquiferous sand sample is important for engineering applications like water quantity detection of rock and soil, induced polarization method in water source exploration, water-bearing structure quantitative detection of water and so on. Permeability coefficient and water content of rock sample or sand sample by induced polarization attenuation information have been determined [1–8] and the foundation of experimental and theory of quantitative detection of water has been established.

According to these analysis and experiment, influence characteristics between porosity, water content, current intensity and induced polarization relaxation

---

Q. Guo (✉) · L. Nie · S. Li · B. Liu · C. Wang · M. Tian
Geotechnical and Structural Engineering Research Center, Shandong University,
Jinan, China

Q. Di et al. (eds.), *Technology and Application of Environmental and Engineering Geophysics*, Springer Geophysics,
DOI 10.1007/978-981-10-3244-8_5

properties time have been researched by exploring the migrating rules of lon in sand sample as porous medium and a series of indoor test. Aquifers sand sample is porous medium with a large number of anisotropic hole which could be simplified as capillary model to research the migrating rules of lon in bearing water. The relationship between the secondary field of induced polarization and current intensity has been derived under the simplified model. Aquifers sand sample is porous medium with a large number of anisotropic hole which could be simplified as capillary model to research the migrating rules of lon in bearing water. The relationship between the secondary field of induced polarization and current intensity has been derived under the simplified model. It follows the main influencing factors of induced polarization effect are porosity, water content and current intensity from the analysis of induced polarization relaxation properties. According to the test data the induced polarization relaxation characteristics influenced by porosity, water content and current intensity has been analyzed coupled with microscopic mechanism.

2 Micro Mechanisms of Induced Plorization Relaxation Properties of Aquifers and Sample

Aquifers sand sample is porous medium with a large number of anisotropic hole which could be simplified as capillary model [9]. The wide or narrow pore of sand particle could be represented by the thin or thick capillary respectively. Pore system of sand sample is expressed as connected capillary model, as shown in Fig. 1.

The essential reason of the influence of the induced polarization effect is the different ionic concentration ratio of different thickness of the capillary when the aquifers sand sample is simplified as capillary model. Therefore, cation exchange capacity, concentration of pore water, the width of pore, the filling state of pore, and current intensity are the main influencing factors. The primary affecting Factors of induced polarization effect are porosity, water content and current intensity because of the cation exchange capacity and concentration of pore water have little difference in a certain geological unit area.

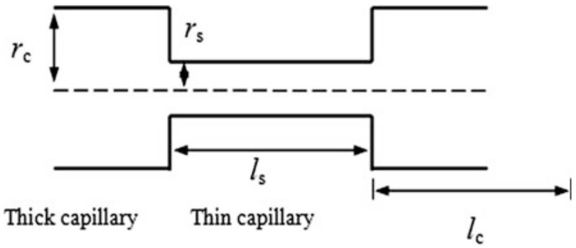

Fig. 1 Schematic diagram of capillary model

Fig. 2 Schematic diagram of ion diffusion

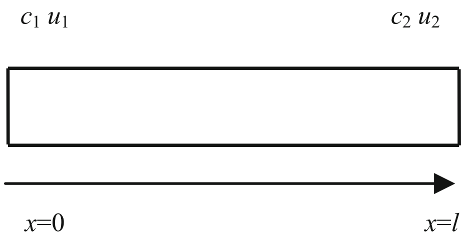

The number of capillary basic unit and wide pores will increase with an increase in porosity. The cross sectional area of pore water becomes large with the increase of water content in the similar sense. The amount of cation exchanges capillary and the difference of ionic concentration ratio of different thickness of the capillary increases with the increase of the pore width or the water content. It is obvious that the induced polarization effect is enhanced.

The following simplified model is built to explain the attenuation of secondary electric field of induced polarization for exploring the effect of current intensity on the half–life time of induced polarization. As Fig. 2 shows, in the one dimensional closed tube the concentration is c_1 and the space potent is u_1 at $x = 0$. The concentration is c_2 and the space potent is u_2 at $x = 1$. The Variety of concentration is analyzed according to the linear distribution of the initial concentration in the pipe is assumed.

There is following relationship between space potent and the ionic concentration, P is coefficient [9].

$$\frac{\partial^2 u}{\partial x^2} = P\frac{\partial^2 c}{\partial x^2} \tag{1}$$

The ionic concentration diffusion in one dimensional closed tube could be represented as the superposition of electric field force and electrochemistry imaginary force [6]. D is diffusion coefficient.

$$\frac{\partial c}{\partial t} = (P+D)\frac{\partial^2 c}{\partial x^2} \tag{2}$$

Above problem could be translate into definitive solution problem of Eq. (2). Set up c(x, t) = X(x)T(t), then:

$$\begin{aligned} &\begin{cases} X'' + \lambda X = 0 \\ X'(0) = 0 \qquad X'(l) = 0 \end{cases} \\ &T' + \lambda(P+D)T = 0 \end{aligned} \tag{3}$$

The general solution is as follow:

$$c(x,t) = \sum_{n=0}^{\infty} B_n \mathrm{e}^{\frac{-(P+D)n^2\pi^2 t}{l^2}} \cos\frac{n\pi x}{l} \quad n = 0, 1, 2, \ldots \tag{4}$$

The undetermined coefficient could be found out by Fourier series and initial conditions.

$$c(x,t) = \frac{c_1 + c_2}{2} + \sum_{n=2k-1}^{\infty} \frac{-4(c_2 - c_1)}{n^2\pi^2} e^{\frac{-(P+D)n^2\pi^2 t}{l^2}} \cos\frac{n\pi x}{l} \quad k = 1, 2, \ldots \tag{5}$$

The corresponding time is half-life time when the corresponding time between x = l and x = 0. The equilibrium concentration is $(c_1 + c_2)/2$ when t is infinite. The time t is as follow when the concentration at $x = 1$ is $(c_1 + 3c_2)/4$.

$$\begin{aligned} \frac{c_1 + 3c_{2\prime}}{4} &= \frac{c_1 + c_2}{2} + \sum_{n=2k-1}^{\infty} \frac{4(c_2 - c_1)}{n^2\pi^2} \mathrm{e}^{\frac{-(P+D)n^2\pi^2 t}{l^2}} \\ \frac{c_2 - c_{1\prime}}{4} &= \sum_{n=2k-1}^{\infty} \frac{4(c_2 - c_1)}{n^2\pi^2} \mathrm{e}^{\frac{-(P+D)n^2\pi^2 t}{l^2}} \\ \frac{\pi^2}{16} &= \sum_{n=2k-1}^{\infty} \frac{1}{n^2} \mathrm{e}^{\frac{-(P+D)n^2\pi^2 t}{l^2}} \end{aligned} \tag{6}$$

The half-life time is independent of the size of polarizability and supply current from formula (6), which is the linear phenomenon of induced polarization when the supply current is in a certain range. The voltage of induced polarization secondary field may increase linearly with the increase of the current and then changing slowly and tend to be saturated because of the overvoltage (Zeta voltage) increases non linearly. There is nonlinear phenomenon of induced polarization when the current passes which has been come up by He [10]. The value of coefficient P and the driving force of ion diffusion will decrease gradually when current increase to a certain degree. So the time t of reaching half concentration increases and the half-life time begins to change as the current increases by formula (6).

3 Experimental Method

Experimental device of induced polarization four-electrode method has been designed to measure the induced polarization effect of laboratory samples precisely which is shown in Fig. 3. The device (10 cm × 10 cm × 50 cm) which is made by

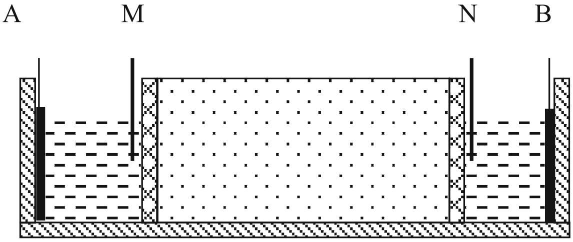

Fig. 3 Indoor test device of induced polarization

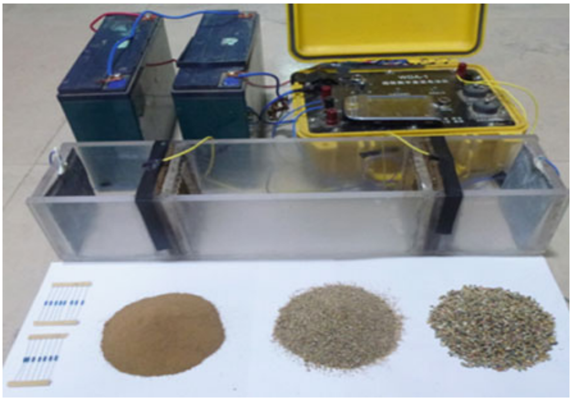

Fig. 4 Indoor test device and material

non metallic organic glass include is formed by two electrolyte compartments and one sample compartment. These compartments are separated by permeable plate. Supply electrode is lead plate (0.3 mm thickness) and measuring electrode is Ag/AgCl non polarized electrode. The over potential from electrode itself is suppressed to avoid the effect of metal electrode polarization.

Aquifers sand was used as sample. There were three groups of samples of different particle size (0.6–1.18, 1.0–1.4, 2.36–4.72 mm). The sand samples were screened according to the design size firstly and then be put into oven for drying under 90 °C. These sand samples were incorporated into water and 3% clay. The water content was 24–2% with 2% step (Fig. 4).

The sand sample of particle size 2.36–4.72 mm was picked to measure the half-life time in different current. Then the lager current and the small one were determined to measure the three groups sand sample in different water content.

4 Exploriment Result and Analysis

These three groups of sand samples were tested using 1 mA current to measure the half-life time separately. The half-life time test result is as shown in Fig. 5. The largest half-life time of belongs to the whole the group of particle size 2.36–

Fig. 5 Half-life time test result of three kinds of particle size

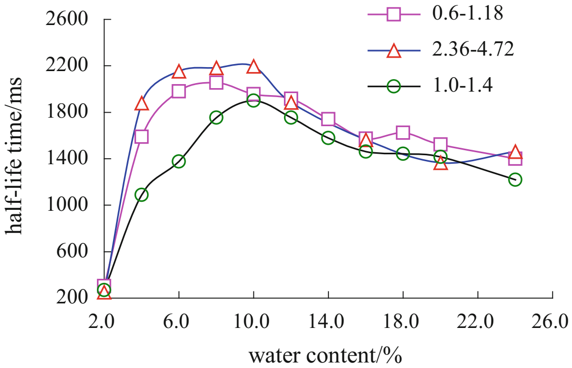

4.72 mm which has the biggest particle size and porosity. But the half-life time of the group of particle size 1.0–1.4 mm is smaller than the one of the group of particle size of 0.6–1.18 mm. Half-life time is not sensitive to size of particle because of the effect of compacting condition. By and large, the bigger the size of particle the more obvious the phenomenon will be. The test result conforms to the theoretical results.

Half-life time started two phase change with the increase of water content. Half-life time increases quickly at the beginning and then get slowly with the increase of water content when the water content changes from 2 to 10%. When water content is above 10% half-life time decreases slowly with the increase of water content and finally tends to be stable.

Some rules of the difference of the half-life time could be gained by comprehensive analysis the Fig. 6. When the water content is small (w < 6%) the half-life time of big current is larger than the small one. so the difference of the half-life time presents a slight positive value. When the water content becomes bigger (6% < w < 10%) the positive value of the difference of the half-life time reach the maximum. So the difference of the half-life time increases with the increase of water content when the water contest is less than 10% which lay the groundwork for detecting water by induced polarization.

As shown in Fig. 7 the half-life time increases when the increase within a range. Half-life time does not change with current in linear phase induced polarization, but it will appear induced polarization nonlinear phenomenon and increases with the increase of current when the current exceeds a certain value (3 mA);

Fig. 6 Half-life time test result of three kinds of sand

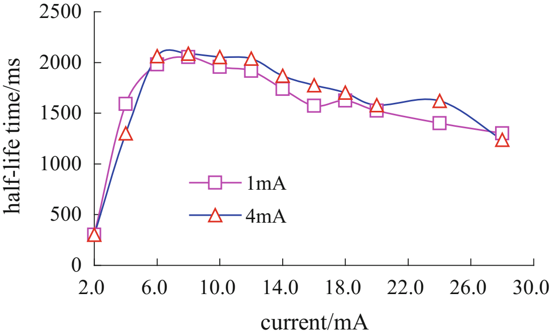

(a) Half-life time test result of w<6%.

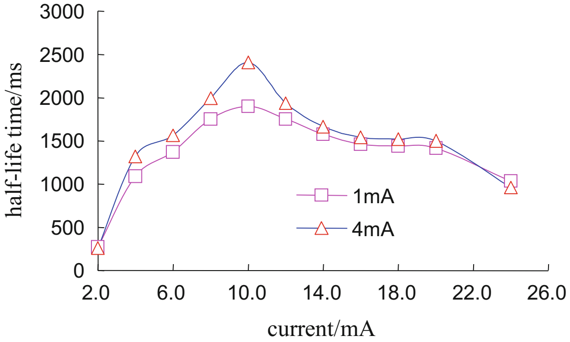

(b) Half-life time test result of 6%<w<10%.

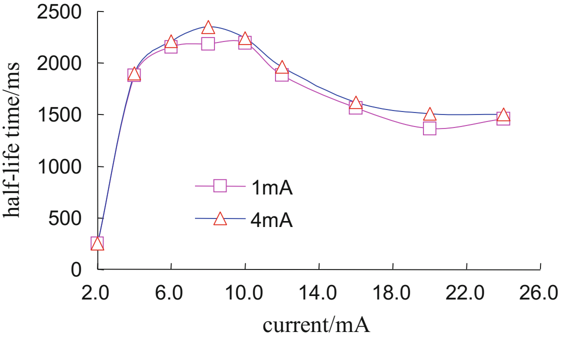

(c) Half-life time test result of w>10%.

Fig. 7 Relationship between the half-life time and current

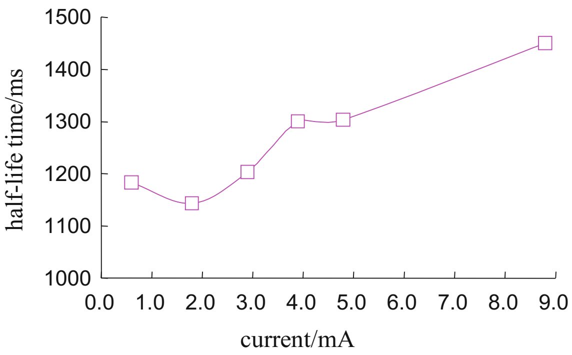

5 Conclusion

From laboratory test and analysis of the micro mechanism. Following conclusions can be drawn.

- Half-life time does not change with current in linear phase induced polarization, but it will appear induced polarization nonlinear phenomenon and increases with the increase of current when the current exceeds a certain value (3 mA);
- Half-life time is not sensitive to size of particle, but the bigger the size of particle the more obvious the phenomenon will be on the whole;
- Half-life time started two phase change with the increase of water content. Half-life time increases quickly at the beginning and then get slowly with the increase of water content when the water content changes from 2 to 10%. When water content is above 10% half-life time decreases slowly with the increase of water content and finally tends to be stable.
- When the water content is small ($w < 6\%$) the half-life time of big current is larger than the small one. so the difference of the half-life time presents a slight positive value. When the water content becomes large ($6\% < w < 10\%$) the positive value of the difference of the half-life time reach the maximum. So the difference of the half-life time increases with the increase of water content when the water content is less than 10%.

References

1. K. Titov, A. Kemna, A. Tarasov, and H. Vereecken, "Induced polarization of unsaturated sands determined through time domain measurements." Vadose Zone Journal, 3, 1160–1168, 2004.
2. Andreas Hördt, Roland Blaschek, Andreas Kemna, and Norbert Zisser, "Hydraulic conductivity estimation from induced polarization data at the field scale- the Krauthausen case history," Journal of Applied Geophysics, 62, 33–46, 2007.

3. A. Ghorbani, Ph. Cosenza, A. Revil, et al. "Non-invasive monitoring of water content and textural changes in clay-rocks using spectral induced polarization: A laboratory investigation," Applied Clay Science, 43, 493–502, 2009.
4. J. M. Li et al. "The basic theoretical research of Induced Polarization Method in the Water source Exploration," Beijing, Geological Publishing House, 1994.
5. Q. Wang, J. T. Guan, et al., "The microscopic mechanisms of induced polarization relaxation time spectra in shaly sandstone," Coal Geology & Exploration, 38(3), 61–65, March 2010.
6. M. K. Xie, "Detection of groundwater by two time-difference method," Computing Techniques for Geophysical and Geochemical Exploration, 9(4), 331–337, April 1987.
7. H. Wang, R. K. Xu, et al. "Soil Acidification of Alfisols as Influenced by Tea Cultivation in Eastern China," PEDOSPHERE, 20(6):799–806, June 2010.
8. L. K. Fu, R. G. Liu, "Experimental study on the nonlinear excitation effect in time domain," Journal of Guilin College of Metallurgy and Geology, 10(2):159–172, February 1990.
9. J. T. Guan, H. Yu, et al., "Mathematical simulation on induced polarization of reservoir rock in time domain," Chinese Journal of Computational Physics, 29(3), 354–360, 2012.
10. J. T. Guan, Q. Wang, et al., "Study on the mechanisms of electrochemical logging response in shaly sandstone on capillary model," Chinese Journal of Geophysics, 53(1), 214–223, January 2010.

The Trust Region Method for Time-Domain Full Waveform Inversion

Suping Peng, Peng Lin, Wenfeng Du and Yongxu Lu

Abstract Full waveform inversion is an effective inversion method to obtain high resolution and precision seismic imaging. The problem of full waveform inversion aims to solve the optimization problem of the misfit between the synthetic and recorded data. There are a lot of conventional local optimization methods, such as the methods depending on gradient and Hessian matrix, to solve the ill-posed nonlinear problem. Gradient and Hessian matrix information plays an important role in inversion algorithms. However, these methods always lead to local minimum so that the result of inversion could not be accepted. To confront the problem, we propose a new approach called the trust region method, to solve the unconstrained optimization problem. Strong convergence properties are the key for trust region method, and the new step is limited to the neighbourhood of the current step. The gradient and Hessian matrix information has an effect on inversion algorithms. To test the capability of this method, we apply it to the model of salt domes and synthetic Marmousi from the time-domain acoustic full waveform inversion point of view for reconstructing velocity model. Inversion results show that the model inverted by our method fits the true model well and the precision is high. Hence, the trust region method is a promising method for the problem of full waveform inversion.

Keywords Full · Waveform inversion · Depth domain modeling · Trust region method · Acoustic wave equation

1 Introduction

With the development of oil and petroleum prospect, the challenge that geologists and geophysicists are confronting is tremendous. Full waveform inversion (FWI) is a new inversion method, which considers the whole waveform to reconstruct the

---

S. Peng · P. Lin (✉) · W. Du · Y. Lu
China State Key Laboratory of Coal Resources and Safe Mining,
China University of Mining and Technology, Beijing, China

Q. Di et al. (eds.), *Technology and Application of Environmental and Engineering Geophysics*, Springer Geophysics,
DOI 10.1007/978-981-10-3244-8_6

subsurface parameters. Due to the potential of obtaining the high resolution and precision models, FWI has become a research focus of many scholars in the world. FWI is a least-square optimization problem, whose objective function is the misfit between the synthetic and the recorded seismic data. To solve the non-linear and ill-posed problem of FWI, the gradient-based and Newton's methods are the conventional nonlinear optimization methods.

Lailly [1], Tarantola [2, 3] introduced the full waveform inversion in time-domain for the first time and the algorithm applied the steepest-descent gradient method to solve the nonlinear optimization problem, but the convergence rate of this method was low for the large-scale problems. Pratt [4, 5] applied FWI theory to invert subsurface parameters in frequency-domain, which make it possible for practical seismic data. However, the obvious shortcoming is local convergence for FWI in time and frequency domain. Shin [6–8] presented FWI theory in Laplace-domain, but the inversion resolution is a little bad because of only utilizing phase and zero frequency information. As for algorithms in FWI, in order to improve the inversion efficiency, Brossier et al. [9] applied the limited-memory BFGS quasi-Newton method to reconstruct velocity structure based on the elastic wave equation, which made better use of the Hessian matrix information. L-BFGS method has been widely used to FWI problem since then. Bae et al. [10] inverted P-wave, S-wave velocity and density for acoustic and elastic FWI problem by Gaussian-Newton method. Malinowski et al. [11] applied L-BFGS method to reconstruct subsurface parameters in 2D visco-acoustic media. Métivier et al. [12, 13] presented a feasible implementation of the truncated Newton (TN) method to the FWI problem, using a second-order adjoint-state approach to calculate Hessian matrix. TN method increases the inversion robustness, though its computation cost is more expensive than conventional methods.

However, a serious disadvantage of conventional methods is that the gradient-based methods only use the gradient information so that the convergence rate is generally quite low. In addition, the Newton's methods consider the Hessian matrix information into the updated direction iteratively, which could improve the inversion precision. However, from the perspective of computation cost, Hessian matrix is more expensive and requires large memory. It is worth to mention that these conventional methods may suffer from a wrong result due to the presence of local minima. Due to the strong convergence properties, the trust region method has been applied to the geophysical inversion problem. Tian and Chen [14] has proved that the convergence rate was better than Quasi-Newton method in the inversion of source and velocity structures. Li and Wang [15] combined the trust region method to seismic migration inversion, all of which illustrated this method was effective for ill-posed nonlinear inversion problem.

In this paper, we propose the trust region method [16] for the full waveform inversion problem, overcoming the drawbacks of conventional methods. This method has strong global convergence properties theoretically, which can produce a better result for full waveform inversion.

2 Theory and Methods

2.1 Mathematical Model

FWI is an ill-posed and unconstrained optimization problem. The objective function is usually formulated as a least-squares unconstrained optimization problem. The velocity reconstruction is aimed at minimizing the L2-norm formation of objective function [2], the unconstrained optimization problem

$$\min E(\mathbf{m}) = \frac{1}{2}\left\|\mathbf{d}_{\mathrm{syn}} - \mathbf{d}_{cal}\right\|_2^2. \tag{1}$$

The mathematical optimization algorithms aim to balance the misfit $\boldsymbol{E}$ between the synthetic $\mathbf{d}_{syn}$ and recorded data $\mathbf{d}_{cal}$. $\|\cdot\|_2$ denotes a distance of the Euclidean norm and $\mathbf{m}$ represents velocity model. Generally the conventional line search methods approximate the solution iteratively by a search direction and step along the direction based on the initial assumed model. The model can be updated as

$$\mathbf{m}_{k+1} = \mathbf{m}_k + \alpha_k \mathbf{d}_k \tag{2}$$

where k denotes the current number of iterations, α is the step length obtained by line search methods and $\mathbf{d}$ is the updated direction of model.

2.2 Algorithm

The trust region method has better convergence properties for nonlinear unconstrained problems than line search methods [17, 18]. The updated step length is forced in the neighbourhood of current solution, that is, the distance between new and current point is limited within a constant called trust region to prevent the trial step become large. Compared with the conventional line search algorithms, our proposed method determines the trial step directly according to the current point, rather than to determine the search direction firstly, then the step length.

In trust region method, we convert the original problem to the trust region subproblem in order to get updated increment. The subproblem is generated from the Taylor expansion for the objective function and ignores the higher order terms. The solution is forced within the trust region. The subproblem is defined as

$$\begin{aligned} &\min \quad \phi(\omega_k) = \mathbf{g}^T\omega_k + \frac{1}{2}\omega_k^T\mathbf{H}_k\omega_k \\ &s.t. \quad \|\omega_k\|_2 \le \Delta_k \end{aligned} \tag{3}$$

where $\mathbf{g}$ and $\mathbf{H}$ are the gradient and Hessian matrix, $\|\cdot\|_2$ is the L-2 norm of Euclidean space, and Δ_k denotes the trust region radius. Plessix [19] showed that the calculation of gradient made use of wavefield variation caused by perturbations on model parameter called adjoint-state method. This means that the seismic data residual was backpropagated by conjugate forward operator to calculate the gradient value of objective function with respect to model parameter. Otherwise, the Hessian matrix can be updated by the popular BFGS method [20]

$$\mathbf{H}_{k+1} = \mathbf{H}_{\mathrm{k}} + \frac{\mathbf{y}_k \mathbf{y}_k^T}{\mathbf{s}_k^T \mathbf{y}_k} - \frac{\mathbf{H}_k \mathbf{s}_k \mathbf{s}_k^T \mathbf{H}_k}{\mathbf{s}_k^T \mathbf{H}_k \mathbf{s}_k}, \tag{4}$$

where $\mathbf{s}_{\mathrm{k}}$ and $\mathbf{y}_{\mathrm{k}}$ are the change amount of model parameter value and gradient value. The identity matrix is usually considered as the initial Hessian matrix H_0.

The solution ω_k of trust region subproblem is the key problem, and the computation cost of Eq. (3) is expensive. There are a lot of methods to solve the subproblem, such as the dogleg, double dogleg techniques and the truncated CG method [21], etc. In this paper, the truncated CG method is applied to obtain the trial step. The parameter R_k determines whether the solution of subproblem accepts and how to update the trust region radius, defined as

$$R_k = \frac{A_k}{P_k} = \frac{E(\mathbf{m}_k) - E(\mathbf{m}_k + \omega_k)}{\Phi_k(0) - \Phi_k(\omega_k)} \tag{5}$$

where A_k is the actual reduction of Eq. (1), and P_k denotes the predicted reduction of Eq. (3). Generally speaking, if $R_k > 0$ the solution will be accepted, otherwise, the new step ω_k is rejected. The trust region radius and model parameter can be updated as

$$\Delta_{k+1} = \begin{cases} \min(r_2\Delta_k, \Delta_{\max}), & R_k > \eta_2 \\ \Delta_k, & \eta_1 \le R_k \le \eta_2 \\ r_1\Delta_k, & R_k < \eta_1 \end{cases}, \tag{6}$$

$$\mathbf{m}_{k+1} = \begin{cases} \mathbf{m}_k + \omega_k, & \text{if } R_k \ge \eta_1 \\ \mathbf{m}_k, & \text{otherwise} \end{cases} \tag{7}$$

where $0 < r_1 < r_2 < 1$, $0 \le \eta_1 < \eta_2 < 1$, all of which are constants. For clarity, the flow chart is outlined for application of trust region method in Fig. 1.

Now the trust region algorithm is carried out as the following steps:

Algorithm 1 Trust region algorithm for unconstrained optimization problem

STEP 1 Give initial model $\mathbf{m_0}$, relative parameters, $0 < \mathrm{r1} < \mathrm{r2} < 1$, $0 \le \eta 1 < \eta 2 < 1$, the number of maximum iteration $\mathrm{K}_{\max}$, the initial radius Δ_0 and maximum radius $\Delta_{\max}$; Compute the gradient $\mathbf{g}_0$ and initial Hessian matrix $\mathbf{H}_0$; Set the index k := 0.
STEP 2 If $\mathrm{k} > \mathrm{K}_{\max}$ or $\Delta_{\mathrm{k}} < 0.001$ is satisfied then STOP; Else, do next step.
STEP 3 Solve the subproblem Eq. (3) to get trial step length ω_k.

Fig. 1 Flow chart for the trust region method

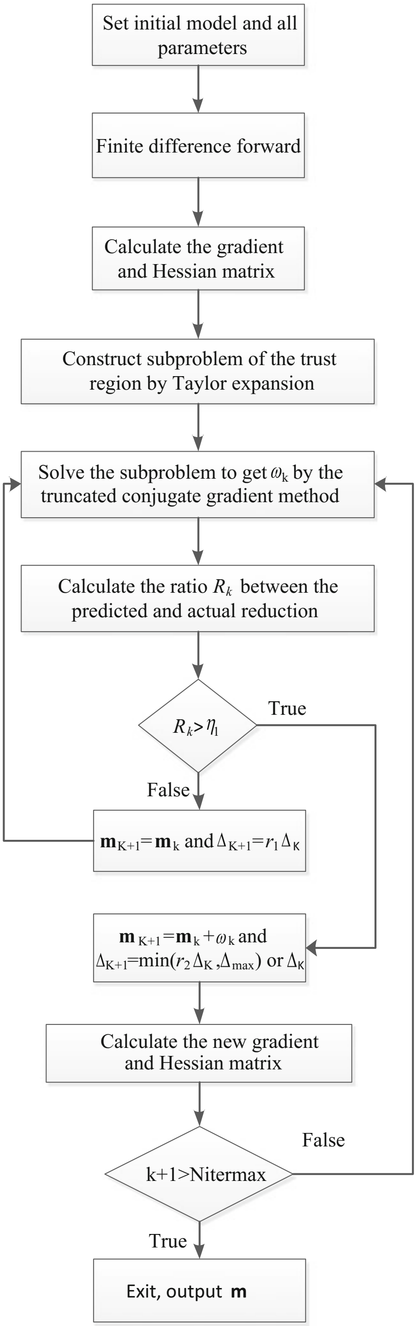

STEP 4 Compute the radio Rk Eq. (5), and if Rk > 0, evaluate the model parameter Eq. (6) and the trust region radius Eq. (7).
STEP 5 Evaluate the gradient $\mathbf{g}_k$ and hessian matrix $\mathbf{H}_k$;
STEP 6 k := k + 1; GOTO STEP 2.

2.3 Numerical Results

To verify the capability of our proposed method, we apply this method to the depth domain model of salt domes and Marmousi model. The inversion is performed in time-domain acoustic wave equation. The first model we choose is salt domes shown in Fig. 2a.

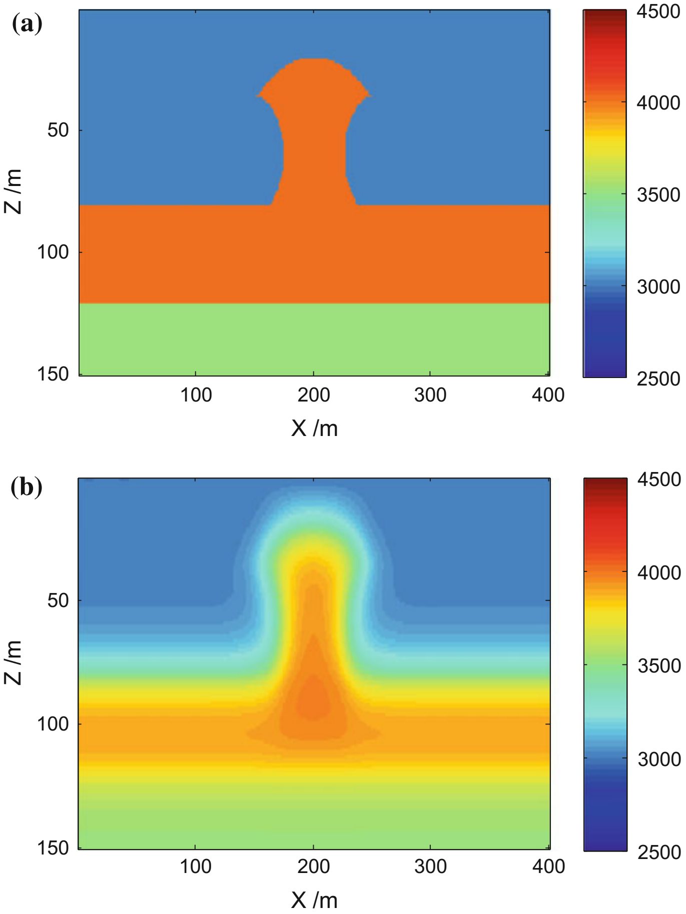

Fig. 2 Salt domes. **a** True model; **b** Initial model obtained from smooth2 function and 20 points in depth, 20 points in crossline direction smoothed by SU

The true model consists of 400 × 150 grids, and the intervals is 10 m × 10 m. There are 19 shots at intervals of 200 m, and 400 receivers are distributed near the surface every 10 m. The source estimation is Ricker with the dominant frequency 8 Hz. The initial model is generated by smoothing the true model shown in Fig. 2b.

In order to save the computational cost, we cut out a part of Marmousi as the second model shown in Fig. 3a. The horizontal extent 7200 m, and the depth is 2400 m in the model which contains 600 × 200 grids at intervals of 12 m × 12 m. The acquisition system consists of 19 sources at intervals of 300 m and 599 receivers every 12 m along the horizontal surface. We adopt Ricker wavelet to estimate the source, with the dominant frequency 10 Hz. The synthetic data are generated by applying the finite difference approach. The true model is smoothed to be used as starting model shown in Fig. 3b. Inversion results are shown in Fig. 4a, b. It is worth

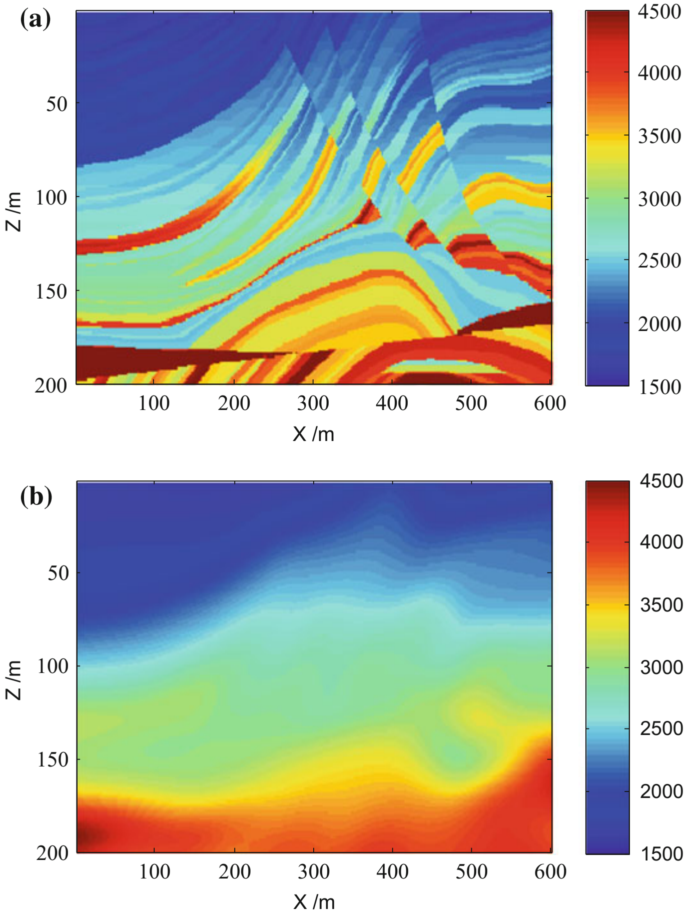

Fig. 3 Marmousi. **a** True model; **b** Initial model obtained from smooth2 function and 10 points in depth, 20 points in crossline direction smoothed by SU

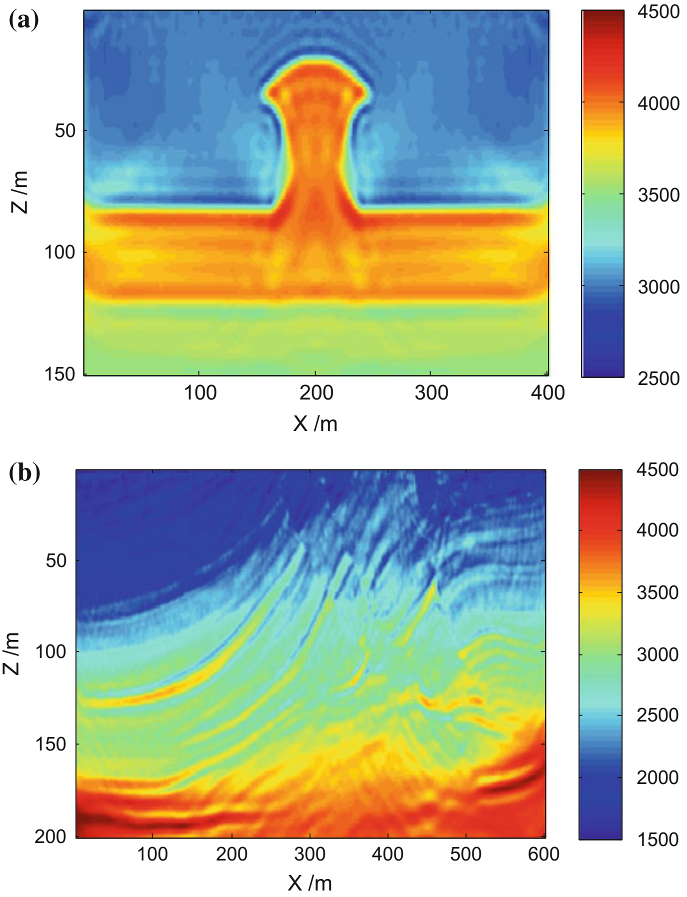

Fig. 4 Inversion results. **a** A velocity model of salt domes constructed with the trust region method; **b** A velocity model of Marmousi constructed with the trust region method

to mention that the initial radius is 100, and the forced maximum radius is 200, which have a distinct effect on inversion results. To further illustrate the effectiveness of results quantitatively, we display the velocity profiles from the salt domes and Marmousi respectively shown in Fig. 5.

From Figs. 2 and 3, it is obviously that the initial model is far different from the truth in detail. Figure 4 shows the inversions result with the trust region method by the model of salt domes and Marmousi. It is clear that FWI with the trust region method converges fast towards the true model. The structure of salt domes and Marmousi is characterized clearly by the inversion with the trust region method. The inversion result could be improved greatly by our new method, especially for the shallow area. In addition, it can be found that the reconstructed velocity model is quite close to the true model, and the new method improves the inversion

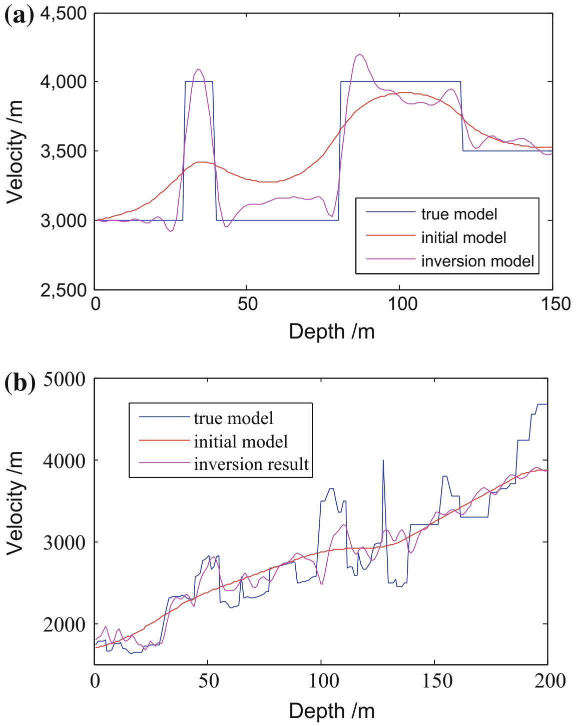

Fig. 5 The velocity profiles. **a** The velocity curves of salt domes at distance of 2370 m; **b** The velocity curves of Marmousi model at distance of 2800 m

precision and solutions greatly. The velocity curves in Fig. 5 show that the inversion results converges to the true model perfectly at both the shallow area of salt domes and Marmousi. For the salt domes, the velocity curve fits better in both the shallow and deeper area. But as for Marmousi model, the convergence for the deeper area becomes poorer than the shallow subsurface.

3 Conclusion

In the above of this paper, we have demonstrated the trust region method could succeed to solve the problem of full waveform inversion, which is typically ill-posed problems in seismic imaging. The trust region method is a robust optimization method with the global convergence different from the conventional methods. The conventional line search methods fail to have perfect convergence when the problem is large-scale and the starting model is far from the true model, but the trust region method could break through the limitation of local convergence of gradient method in theory, and improve the inversion accuracy greatly and produce better results, especially for the shallow structure. The trust region method is a promising method for full waveform inversion.

We have to note that the initial trust region radius should be chosen properly. In this paper, we conduct several attempts to have a choice although this way is not optimal. In addition, the inversion resolution deserves our further research for the deeper area. Furthermore, this method can be applied to elastic wave equation with anisotropic media and even real seismic data.

Acknowledgments This work is supported by National Key Research and Development Program (Grant No. 2016YFC0501102), National Science and Technology Major Project (Grant No. 2016ZX05066-001), Coal United Project of National Natural Science Foundation (Grant No. U1261203), Shanxi Natural Science Funds Project (Grant No. 2013012001).

References

1. Lailly P. The seismic inverse problem as a sequence of before stack migrations[C]. Philadelphia: SIAM, 1983: 206–220.
2. Tarantola A. Inversion of seismic reflection data in the acoustic approximation[J]. Geophysics, 1984, 49(8): 1259–1266.
3. Tarantola A. A strategy for nonlinear elastic inversion of seismic reflection data[J]. Geophysics, 1986, 51(10): 1893–1903.
4. Pratt R. G., Shin C., HICKS G. J. Gauss-Newton and full Newton methods in frequency-space seismic waveform inversion[J]. Geophysical Journal International, 1998, 133(2): 341–362.
5. Pratt R. G. Seismic waveform inversion in the frequency domain, Part1: Theory and verification in a physical scale model[J]. Geophysics, 1999, 64(3): 888–901.
6. Shin C., Ho C. Y. Waveform inversion in the Laplace domain[J]. Geophysical Journal International, 2008, 173(3): 922–931.
7. Shin C., Ho C. Y. Waveform inversion in the Laplace-Fourier domain[J]. Geophysical Journal International, 2009, 177(3): 1067–1079.
8. Shin C. Laplace-domain full-waveform inversion of seismic data lacking low-frequency information[J]. Geophysics, 2012, 77(5): 199–206.
9. Brossoer R., Operto S., Virieux J. Seismic imaging of complex onshore structures by 2D elastic frequency-domain full-waveform inversion[J]. Geophysics, 2009, 74(6): 105–118.
10. Bae H. S., Pyun S., Chung W., et al. Frequency-domain acoustic-elastic coupled waveform inversion using the Gauss-Newton conjugate gradient method[J]. Geophysical Prospecting, 2012, 60(3): 413–432.
11. Malinowski M., Operto S., Ribodetti A. High-resolution seismic attenuation imaging from wide-aperture onshore data by visco-acoustic frequency-domain full-waveform inversion[J]. Geophysical Journal International, 2011, 186(3): 1179–1204.
12. Métivier L., Brossier R., Virieux J., et al. Full waveform inversion and the truncated Newton method[J]. SIAM Journal On Scientific Computing, 2013, 35(2): 401–437.
13. Métivier L., Bretaudeau F., Brossier R., et al. Full waveform inversion and the truncated newton method: quantitative imaging of complex subsurface structures. Geophysical Prospecting, 2014, 62(6): 1353–1375.
14. Tian Y., Chen X. Simultaneous Inversion of hypocenters and velocity structure using the Quasi-Newton method and trust region method. Chinese Journal of Geophysics, 2006, 49(3), 740–750.
15. Li Z., Wang Y. A subspace trust-region method for seismic migration inversion[J]. Optimization Methods and Software, 2014, 29(2): 286–296.

16. Powell M. J. D. A new algorithm for unconstrained optimization In: Rosen B., Manfasarian K. and Ritter K., (eds), Nonlinear programming. Academic Press, New York, 1970, 31–66.
17. Yuan Y. Numerical methods for nonlinear programming[C], Shanghai Science and Technology Publication, 1993.
18. Wang Y., Yuan Y. Convergence and regularity of trust region methods for nonlinear ill-posed inverse problems[J]. Inverse Problems, 2005, 21(3): 821–838.
19. Plessix R. E. A review of the adjoint-state method for computing the gradient of a functional with geophysical applications[J]. Geophysical Journal International, 2006, 167(2): 495–503.
20. Nocedal J. Updating quasi-Newton matrices with limited storage. Math. Comput., 1980, 35 (151): 773–782.
21. Yuan Y. On the truncated conjugate gradient method[J]. Mathematical Programming, 2000, 87(3): 561–573.

Research on the Channel Wave Field Characters of Goaf in Coal Mine and Its Application

Feng Lei, Wei Wang, Songying Li, Xiaoshuai Yao, Jiwen Teng and Xing Gao

Abstract Goaf badly affects coal mine production safety; therefore, accurate geophysical exploration method to ascertain the goaf is urgently needed. Channel wave seismic technology is suitable for coal mine goaf detection because it has many advantages, such as long transmission distance, high resolution. Because coal seam thickness affects the wave propagation, firstly, we carry out numerical simulation under the condition of coal seam thickness variation in the goaf. Secondly, we analyze the channel wave field characteristics of the goaf. Thirdly, we pick up the dispersion curve of transmitted channel wave. Lastly, we discuss the effects goaf makes on channel wave and imaging condition under the variation of the coal thickness. The results show that, the Airy-phase velocity of channel wave decreased as thickness of coal seam increases, and the dispersion strengthens as Wave propagation distance becomes longer. Firstly, seismic reflection survey is carried out in the target area: 15,030 working face of Xin'an coal mine. Through the analysis of dispersion, spectrum, direct wave's velocity and travel time of the shot-gather records, we recognize the reflected waves from the goaf. The goaf boundary is imaged by the Kirchhoff migration method. Combining the other results of geophysical exploration with the known geological data we geologically explain the imaged results.

Keywords Goaf · Channel wave · Dispersion · Migration

F. Lei
Collaborative Innovation Center of Coalbed Methane and Shale Gas for Central Plains
Economic Region, Henan Polytechnic University, Jiaozuo 454000, Henan Province, China

W. Wang (✉) · X. Gao
The State Key Laboratory of Resources and Environmental Information System,
Institute of Geographic Sciences and Natural Resources Research,
Chinese Academy of Science, Beijing 100101, China
e-mail: wang_wei@lreis.ac.cn

S. Li · X. Yao
HenanYima Coal Group Co., LTD, Yima 472300, China

J. Teng
Institute of Geology and Geophysics, CAS, Beijing 100029, China

Q. Di et al. (eds.), *Technology and Application of Environmental and Engineering Geophysics*, Springer Geophysics,
DOI 10.1007/978-981-10-3244-8_7

1 Introduction

Goaf is a typical kind of geological disasters, and its detection and control in the world also belongs to the problem difficult to solve [1]. China is one of the countries having the most coal producing and largest area of goaf in the world. Especially before integrating coal resources, production activities of many small coal mines are not standardized and the design data is always not incomplete or missing, so it is hard to determine the goaf's location and boundary, which brings great security risk to the mine production and engineering construction [2, 3]. When goaf is filled with water, the exploitation of the follow-up work often causes flooding accident, which leads huge casualties and economic losses [4]. Therefore, the precise detection of goaf has no time to delay [5].

At present, geophysical methods to detecting goaf are classified into surface and subsurface techniques. Surface detection method mainly includes: high density resistivity method, electromagnetic method, 3D seismic, Rayleigh wave method, vertical seismic profile (VSP), the inter pore radio wave perspective, radioactive method (such as measuring radon method) and gravity method (such as micro-gravity). Underground detection method includes: pit radio wave penetration method, mine direct current method, down-hole instant electromagnetic grooving method, seismic wave method [6–10] and so on. These geophysical methods try to detect the differences of physical properties between the coal and the goaf to obtain the distribution of anomalous body. Because of the seismic wave's long propagation distance in the coal seam and the huge differences of the elastic parameters and the dispersion characteristics between the anomalous body and the coal, the seismic wave method can detect target body farther and the result of it has a higher resolution. Goaf's boundary's physical properties are quite different with coal seam and rock elastic wave, so it is more likely to produce reflected wave, but generally does not have the condition of transmission. So the channel wave reflection detection method for detecting goaf has more advantages and huge application value [11–19].

"The research on coal mine accidents and characteristics of seismic wave field—the relationship between coal seam thickness variation and the detection of fault and goaf" focuses on the detection and identification of goaf and fault. Small coal mines and goafs are widely distributed in Henan Yima mining area, and ascertaining the location of goaf can effectively reduce the flooding accidents. Due to the large change of Yima coal seam thickness, to analyze the goaf of channel wave signal response characteristics, we design the mining goaf models under the condition of coal seam thickness variation, and numerical simulations are carried out in this paper, mainly to study the characteristics of the wave spectrum and dispersion under the condition of the coal thickness subtle changes. In the target area of Yima Henan coal mine Xin'an coal mine 15,030 working face, we detected 15,050 working face by wave reflection method to explained the coal seam change and goaf boundary.

2 Theory and Method

2.1 Theory

The wave reflection detection method layout the shot points and receiving points in the same roadway of coal seam to receiving the reflection wave signal of anomalous bodies. The channel wave signal with dispersion formed in the process of seismic wave spreading along the coal seam to the distance and when it encountered anomalies (such as goaf), in other word, the wave impedance interface, produces the reflection wave signal. By identifying and analyzing the reflection wave signal, and carrying out migration imaging processing, we will be able to directly detect the distribution of anomalous body in the coal seam (Fig. 1).

The ahead of the channel wave detection is regarded as the underground half infinite space Z in land seismic prospecting, and the roadway, in which sources and receivers are located, is regarded as the free surface. According to the Huygens principle, every point of vibrating in a wave propagation space can be regarded as a secondary original source, so the wave propagation space is made up by scattering points. The Kirchhoff integral migration method based on the wave equation integral solution, makes use of Kirchhoff diffraction integral formulas to converge diffraction energy from the same point and distribute it in different seismic traces, and to map into the corresponding physics diffraction point. In Fig. 2, the observation plane S1 receives the diffracted wave field generated from point diffraction source S. Here, coordinate origin locates at R (0, 0, 0). The following is Kirchhoff migration derived from the wave equation [20].

$$P(x,y,z;t) = \frac{1}{4\pi}\int\limits_{\omega}\int\limits_{s_1}\left(\frac{1}{r}\frac{\partial P}{\partial z} + \frac{\cos\,\theta}{r^2}P + i\frac{w}{v}\frac{\cos\,\theta}{r}P\right)\exp\left(-i\omega\left(t-\frac{r}{v}\right)\right)ds_1 d\omega \quad (1)$$

The first term of integral formulas is controlled by the vertical gradient of wave field; and the second is the near-field source term; these two terms are ignored in the

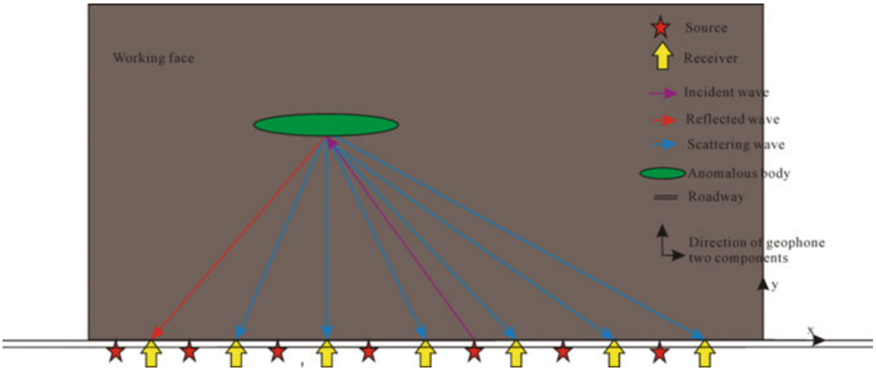

Fig. 1 Schematic diagram of channel wave reflection survey principle

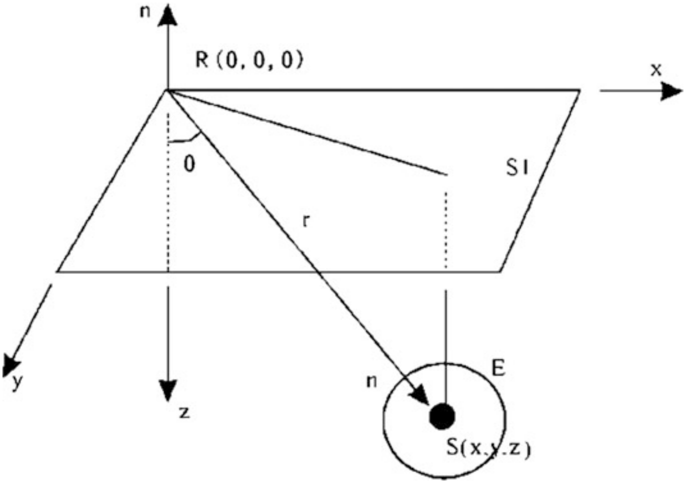

Fig. 2 Point diffraction geometric sketch map from the wave equation based on kirchhoff integral solutions

seismic migration. Taking into account the time-variations and the dispersion of channel, the channel wave migration formula is discretized into the following form:

$$I(x,y) = \left| \sum_{n=1}^{N} \frac{\cos\,\theta}{rU} P_n(t_n) \exp(i\omega_c(1-\frac{U}{c})t_n \right|^2 \tag{2}$$

where ω_c is the center frequency of channel wave, U is the group velocity and c is the phase velocity; $t_n = (r_{n1} + r_{n2})/U$ is the travel time of $n = s_m \times r_k$-th recorded trace; $P_n(t_n)$ is the amplitude of n-th recorded trace at the time of t_n; $I(x, y)$ is the sum of the amplitudes in the migration surface.

3 Method

3.1 Goaf Channel Wave Forward Simulation

According to the variation of coal seam thickness, a two dimensional model is designed to carry out the forward modeling on the condition of goaf and non-goaf. The size of the model x and model z is 300 m * 50 m; thickness of coal seam decreases from 10 m (left) to 5 m (right) linearly; the length of goaf boundary is from 135 to 165 m. The bottom of the coal bed is horizontal. The grid's size is 0.2 m * 0.2 m; and Ricker wave frequency is 300 Hz. The shot points are located at the left-most and the right-most of the coal seam, and the receiver point is located

Table 1 Physical parameters of two-dimensional model

	Vp (m/s)	Vs (m/s)	Den (kg/m^3)	Lithology
Bottom	3200	1700	2450	Mudstone
Upper	3200	1700	2450	Mudstone
Coal	2100	1050	1450	Coal seam
Goaf	1500	0	1000	Water-filled

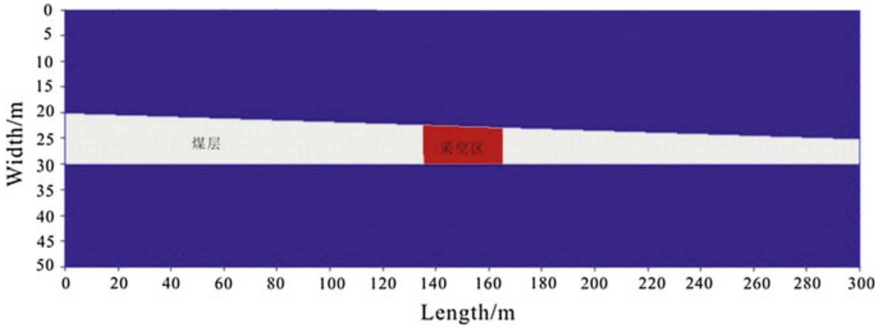

Fig. 3 Goaf model under the condition of 2d coal seam thickness variation, the receiving point at z = 25 m, shot point at the end of the receiving line, goaf is at 135–165 m in the direction of x

in coal seam. Sample interval is about 0.02 ms and the time length of each record is 300 ms. The physical parameters of rock, coal seam and goaf are as Table 1 (Fig. 3).

The shot point is located on the left side, no goaf and with goaf shot gathers is showed in Fig. 4. We can clearly identify the rock and coal seam, the P wave, the S wave and the reflection wave. The channel wave formed by the propagation of the seismic wave in coal seam can be clearly identified too. In the near source region channel wave has not formed, but with mutual interference of the direct wave and reflection in the coal seam the power of channel wave strengthened. In thin coal

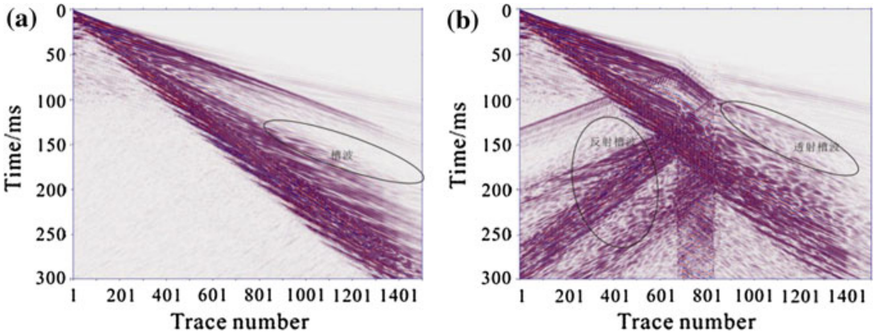

Fig. 4 2d simulation shot gathers, no goaf (**a**) and with goaf (**b**)

seam, channel wave is more obvious, because the propagation path and absorption of multiple wave in coal seam is reduced. When there is a goaf filled with water in the mining area, 3 sets of reflecting groove wave are formed when the direct channel wave propagate to the boundary of goaf and the left side of the tunnel.

3.2 Research on Characteristics of Goaf Spectrum

Figure 5 shows the result of spectrum analysis of data. Seismic source dominant frequency energy moves to low frequency with the distance increased in non-goaf area because the high frequency decreases faster (Black dotted line in Fig. 5). But because frequency dispersion characteristic gradually enhanced as the thickness of the coal seam decreases, interference signal energy decreases and moves to high frequency (red dotted line in Fig. 5). When the goaf is filled with water, the changes of reflection spectrum are not obvious, which indicates that reflection cannot change the frequency. Meanwhile main frequency band gets wider and the interference strengthens. The energy of high frequency component in the transmission area is strengthened, and the frequency band becomes wider.

We extract the dispersion curves without goaf showed in Fig. 6, which shows that channel airy phase velocity decreases gradually (760–1000 m/s) and airy phase moves to high frequency as the thickness of coal seam increases. But frequency

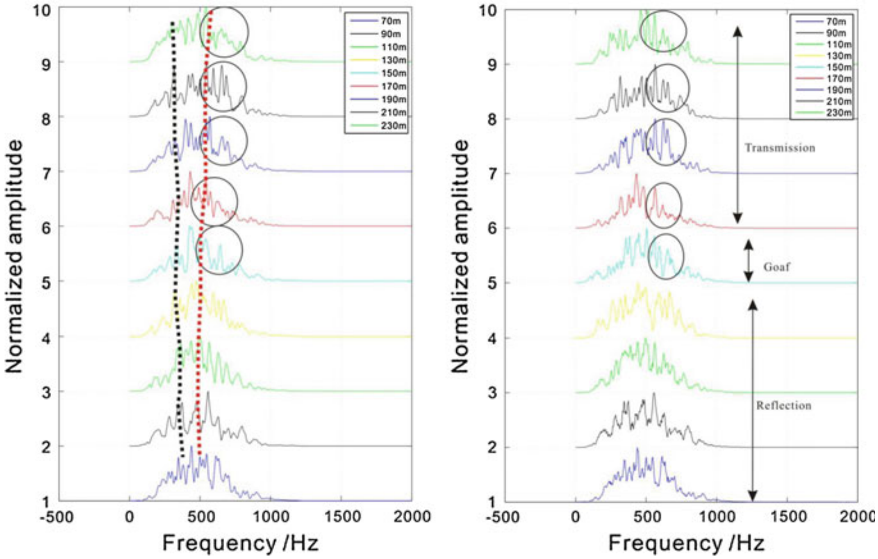

Fig. 5 2d model spectrum without goaf (*left*) and with goaf (*right*), the spectrum curve from the *bottom* to the *top* are the signals from the receiving points which coordinates are 70, 90, 110, 130, 150, 190, 210, 230 m

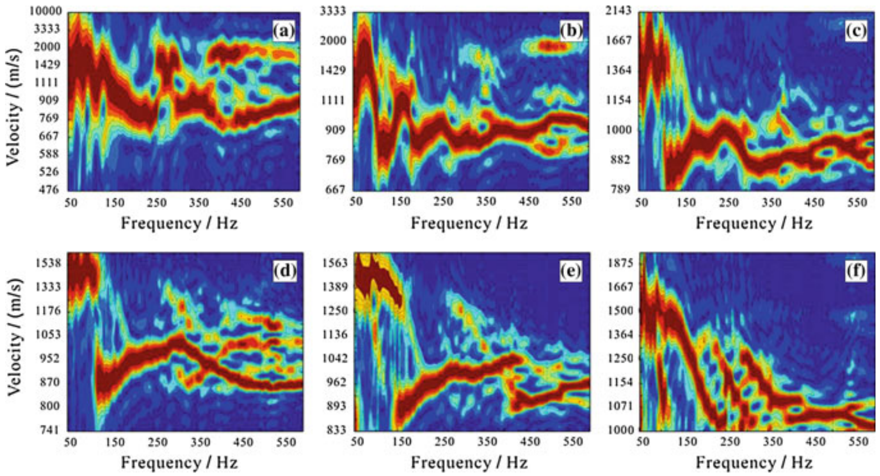

Fig. 6 Dispersion curves without goaf, **a** x = 50 m, h = 9.2 m, **b** x = 100 m, h = 8.3 m, **c** x = 150 m, h = 7.5 m, **d** x = 200 m, h = 6.7 m, **e** x = 250 m, h = 5.8 m, **f** x = 300 m, h = 5 m

dispersion curve in layered medium model shows airy phase velocity is unchanged, which is different from the model above. The model is of more practical significance, after the multiple reflection's propagation of the seismic wave in the upper and lower base plate, the path decreases and airy phase velocity increases.

Compared with frequency dispersion curves of goaf filled with water (in Fig. 7), channel reflection wave's (in Fig. 7a) energy is weaker than direct wave's. Because the propagation path of the wave is the distance between the source and the receiving point, apparent velocity of the reflection is lower than the direct wave, but after considering the propagation path, the velocity of reflection wave and direct wave is equal, which is confirmed by the linear relationship between reflection

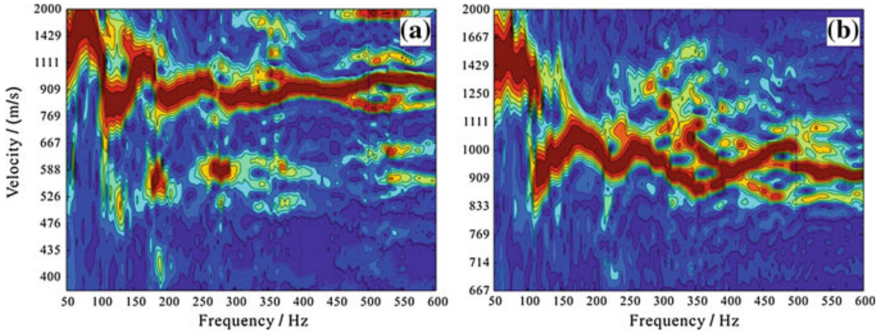

Fig. 7 Dispersion curves of goaf filled with the water, **a** x = 100 m, contains the reflection frequency dispersion curve; **b** x = 200 m, the transmission frequency dispersion curve

wave and direct wave in shot records. The continuity of transmission channel frequency wave dispersion curve in coal seam with goaf (in Fig. 7b) is better than transmission channel frequency wave dispersion curve in coal seam without goaf (in Fig. 6d), the shape of which is more complex, showing that characteristics of the Rayleigh wave dispersion.

4 Examples

The in-seam seismic reflection method exploration working area is located in the 15,030 working face of Yima, Henan province. 19 Shots spaced at 20 m intervals and 15 receivers spaced at 20 m intervals; minimum offset distance is 10 m; depth is 2 m. The observation system is showed by Fig. 8, The single shot blasting charge is 100 g; sampling time interval 0.25 ms; the sampling time is 1024 ms.

The original shot gathers are shown in Fig. 9. Firstly we record first arrival time of P, S wave of every trace and get the distance between any two traces to get all the velocity of direct wave (In EXCEL ascending any gun of each offset horizontally and vertically, then getting the distance and first arrival between any two traces, the velocity is the distance divided by the first arrival time). Secondly by analyzing the velocity, we find that the seismic wave speed is divided into three sections: $V_{middle} > V_{right} > V_{left}$, P wave's velocity of rock is 4–4.4 km/s and S wave's velocity of rock is 2.4–2.6 km/s. The average of velocity ratio was 1.75 and the average of Poisson ratio is 0.256. The direct wave is not formed in near offset, so there is a channel wave blind area. According to the channel wave formation principle, this channel wave blind area is similar with the refraction blind area.

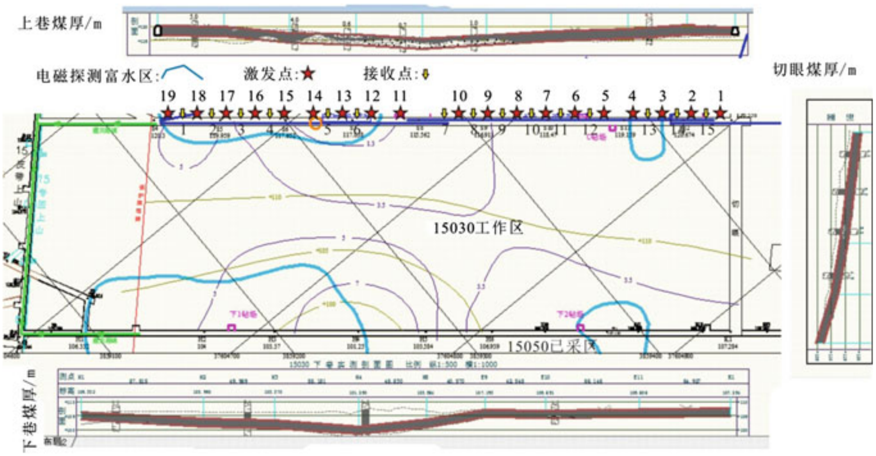

Fig. 8 Schematic diagram of reflection method on 15,030 working face

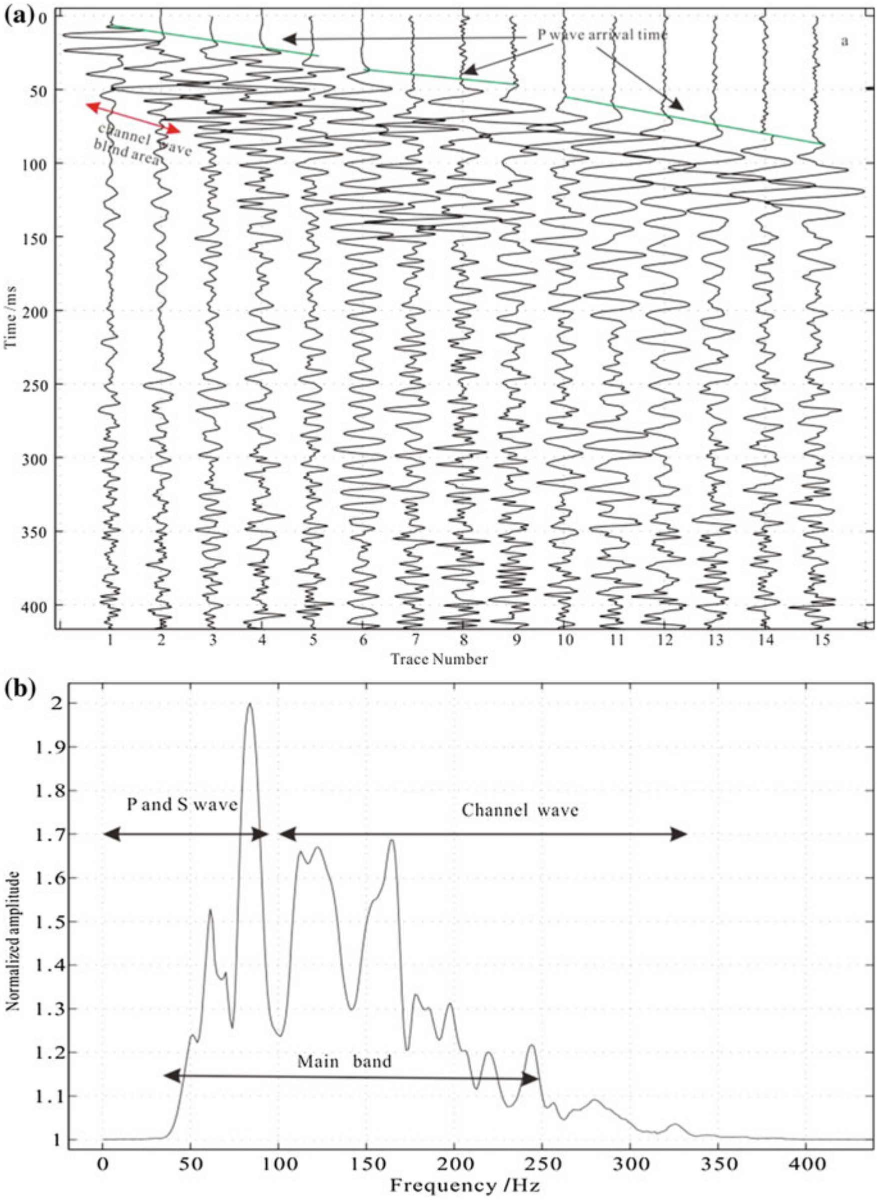

Fig. 9 Shot19 traces record (**a**) and frequency (**b**)

In addition, when faults or other anomalies nearly parallel to observation line, the traveltime of direct and reflected wave is in the same one envelope range, so it becomes difficult to distinguish between direct and reflected wave, which exists interference detection blind area. In the CMP traces gather dynamic correction stack seismic imaging results, there is a “fault” in-phase axis closed to observation roadway. And we can make a reliable explain to the “fault” by the data received when the difference of time curves of the reflection wave and direct wave is largest. This kind of blind treatment will be detailed in another instance in Huainan coal mine. The shot records obtained in the area within the main band of 30–250 Hz, the channel wave signal frequency is above 100 Hz (in Fig. 9b).

In Fig. 10, the velocity of P waves of rock is 4300 m/s, S waves of rock is 2400 m/s, P waves of coal is 2100 m/s, S waves of coal is 1200 m/s, and the distance from measuring line to goaf is 145 m. The direct wave and reflection wave time distance curve are obtained by the 19th observation system. We can recognize the seismic phase of converted S waves and reflected S waves comparing with the original records (in Fig. 9). At the same time, it is found that there is a cross section between the reflection waves and the direct waves, and the amplitude is enhanced obviously.

Extracted the X component frequency dispersion curve (the coordinates of receiving point x are 110, 190, 250, 370 m) (in Fig. 11) of 5th, 7th, 10th, 15th receiving point in 19th point (x coordinates of the point is 0 m). From the dispersion curves the change of direct channel wave airy phase velocity can be seen: Vc > Vb > Va > Vd, and it is consistent with the velocity distribution of rock. This is associated with the variation in thickness of coal seam, and velocity and thickness have an inverse relationship. In the far offset distance frequency dispersion curves, the reflection groove wave energy was strengthened and the apparent velocity is lower than the direct waves’ velocity.

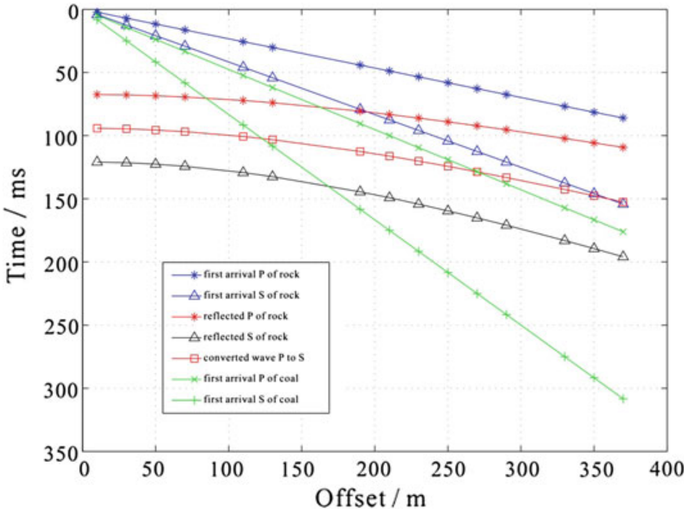

Fig. 10 Shot19 theoretical time curves

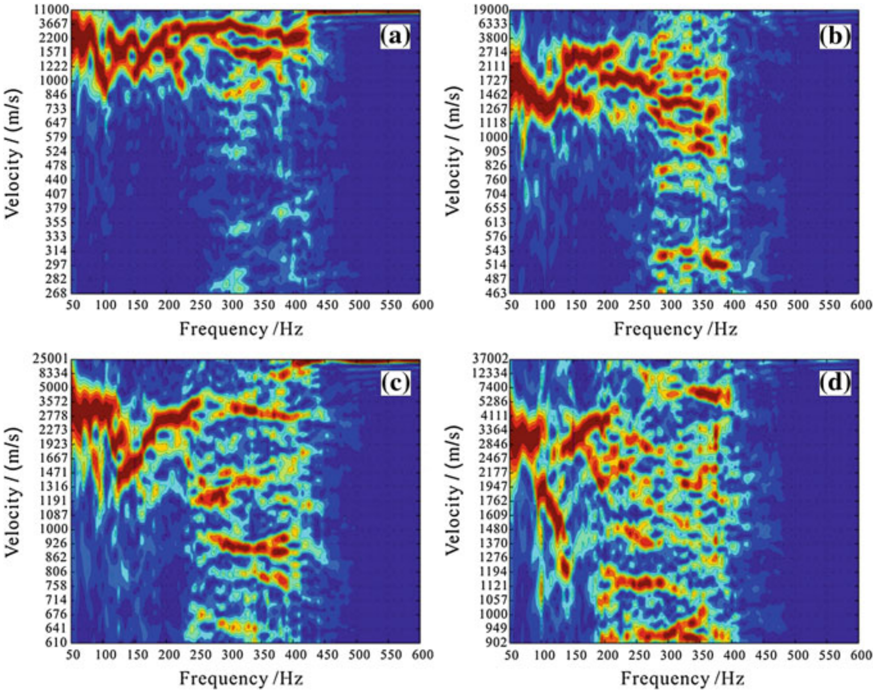

Fig. 11 Dispersion curves, Shot point X = 0 m, **a** receiver X = 110 m, **b** B = receive 190 m, **c** B = receive 250 m, **d** B = receive 370 m

Figure 12 shows Yima of Xin'an minefield 15,030 coal working face thinning zone (parting) and goaf boundary based on Kirchhoff integral migration method. According to the TEM results and roadways revealed, the imaging results can be divided into five areas: water-rich anomaly area, subsidence area, roof collapse area, coal seam stability area and coal seam thinning zone. Transient electromagnetic results show that water-rich anomaly area just is the low amplitude area, divided into three parts. Coal seam thinning zone is middle amplitude area, which is consist with the roadway reveled. Data shows, the goaf is 150 m away from dip aside and there is also one anomalous area parallel to roadway. The reflection interface is irregular and is divided into two parts: the roof sunken area (left side) and the roof un-sunken area (right side) combined with reduced data of thin strip. In the imaging area the low amplitude zone is the stable zone of coal seam.

The change rules of the wave energy, phase and frequency information reflect lithological changes of strata, which can improve the accuracy of interpretation. In subsequent research combining with attribute analysis making quantitative interpretation to tectonics and lithology provides detailed and reliable geophysical basis for coal mine mining plan, estimated reserves, hazard evaluation, and mine water management.

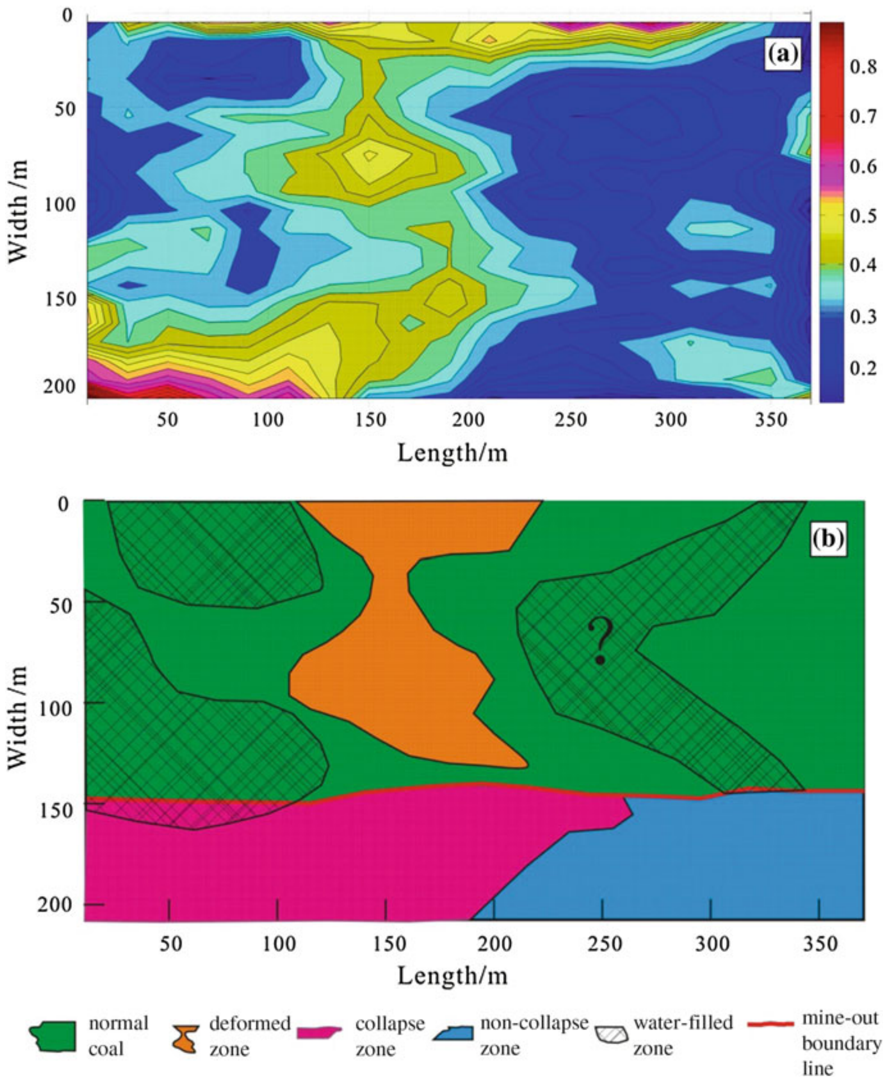

Fig. 12 Migration results (**a**), interpretation results (**b**)

5 Conclusions

In the research we conduct numerical simulation and analyze the characteristics of channel wave field, spectrum and dispersion in coal seam thickness variation conditions, and the major conclusions and contributions. So based on this study some conclusions can be made as follows.

- Airy phase velocity and airy phase frequency decreases gradually as the thickness of coal seam increases. But the seismic wave frequency width increases as the thickness of coal seam increases.
- When the goaf is filled with water, reflection channel wave energy is weaker than the direct wave, apparent velocity of reflection wave is lower than the direct channel wave velocity; transmission channel wave dispersion curve is continuous and the shape is more complex.
- With the increase of seismic wave propagation distance the effect of direct wave on dispersive wave decrease and the dispersion characteristic of channel enhance in the same coal seam condition.
- When using the reflection exploration method, blind channel wave exists in the near source region and there is an interference detection blind zone near the line range.
- The effective combination of the direct wave information and time curve can improve the reliability of identifying reflection wave seismic phase.

Acknowledgments The research was supported by the National Natural Science Foundation of China (Grant No. 41130419, 41240027, 41374061, 41204048)

References

1. Shuangan Yang, Shunian Ning, 2004, Research on Seismic Surveying Goafing of the Old Mine: Coal geology of China, 16, 44–47.
2. Lihui Wang, Dongming Pan, and Xingyan Zhang, 2008 Three Techniques for Detecting Underground Mined-out Areas: Geophysical and Geochemical Exploration, 32, 291–294.
3. Chengping Wu and Xiangyun Hu, 2007, Geophysical Methods on Survey of Mined-out Area: Contributions to Geology and Mineral Resources Research, 22, 19–23.
4. Suoliang Chang, Shuting Zhang, Guishan Li, 2002, Application of Multi-channel Transient Rayleigh Wave Method on Survey of Goaf in Coal Mine: Coal Geology of China, 14, 70–74.
5. Shuliu Yang, 2009, Application of Comprehensive Geophysical Prospecting to Dabaoshan Mining Cavities: Chinese Journal of Engineering Geophysics, 6, 203–207.
6. Zhaoliang Zhu, 1994, The application of geophysical prospecting in coal mine. Beijing: Coal Industry Press.
7. Jianyuan Cheng, Hongxing Sun, Qingbiao Zhao, 2008, The detection technology of excavated region in coal mine and case study: Journal of China Coal Society, 33, 252–255.
8. Juanjuan Li, Dongming Pan, Mingshun Hu, 2009, Application of Geophysical Methods in Detecting Coal Mined-out Areas: Chinese Journal of Engineering Geophysics, 6, 728–732.
9. Changhui Liu, Shucai Liu, Sai Yan, 2011, Application of Integrated Geophysical Exploration Techniques to Detecting Shallow Coal Gob: Chinese Journal of Engineering Geophysics, 8, 51–54.
10. Laifu Wen, Haiqiang Hao, Zhiyuan Liu, 2014, Application of Comprehensive Geophysical Prospecting Method in the Detection of Coal Mine-out Areas in Lingshi, Shanxi: Chinese Journal of Engineering Geophysics, 11, 112–117.
11. Qibin Wu, Linpei Gui, 1998, Some Advances in Exploration Geophysics Abroad-1996: Geophysical and Geochemical Exploration, 22, 10–15.

12. Min Qi. Baolin Zhang, Guanghe Liang, 2006, High-resolution prediction of space distribution characteristics of complicated underground cavities—Preliminary application of high-density electrical technique in an area of Yangquan, Shanxi: Progress in Geophysics, 21, 256–262.
13. Haisheng Liu, 2006, The Appliance Research of High-Density Resistivity Method of Detecting Colliery Underground Gob. Master Dissertation of Taiyuan University of Technology.
14. Jinfang Xue, Zhi Cai, 2007, The Application of High Definition Electricity Method in Coal Mine Empty Area: Journal of Anyang Normal University, 2, 137–139.
15. Ruofei Cui, Hui Wang, 1994, Depth Interpretation of Coal Beds Using Synthetic Seismic Parameter: Coal geology and prospecting, 22, 51–55.
16. Yuping Gao, Zhiyi Yan, Yingwei Liu, 2008, Detection of coal mine goaf by high density resistivity method: Mining Safety & Environmental Protection, 35, 61–63.
17. Department of geophysical exploration, Chinese Mining Institute, 1981, Geophysical prospecting in China. Beijing: Coal Industry Press, 138–312.
18. Shuangan Yang, Shunian Ning, 2004, Research on Seismic Surveying Goafing of the Old Mine: Coal geology of China, 16, 44–47.
19. Zhigang Zong, 2006, Application of seismic exploration method in the exploration of coal mine goaf. China University of Geosciences (Beijing) Master Dissertation.
20. Wei Wang, Xing Gao, Songying Li, Yong Le, Jiwen Teng, Yuying Li, 2014, Fault Detection in Coal Seam by the Channel Wave Method: Scientific Journal of Earth Science, 4, 27–37.

The Study of Well Logging Sedimentary Microfacies in Tengge’er Formation Baiyinchagan Depression

Xinhu Li, Qiuling Wang and Wenhui Ma

Abstract Through analyzing the corresponding relationship between the log characteristics parameters and sedimentary microfacies, the electrofacies mode of Tengge’er Formation Baiyinchagan Depression is established based on the regional sedimentary background, the rock characteristics and its electrical response characteristics and the extraction of logs curve amplitude and the characteristic’s parameters which can reflect sedimentary microfacies. The results show that the southern ramp of Tengge’er Formation in the Baiyinchagan Depression takes the braided delta facie as the major style, and it can be further divided into 7 sedimentary microfacies, including upperwater distributary channel, flood plain, underwater distributary channel, interdistributary bay, mouth bar, frontal sheet sand and frontal wedge-shaped sand. The divisions of sedimentary system and sedimentary facies are perfected through analyzing the logging microfacies, sedimentary and sequence stratigraphy characteristics of single well, which can provide an effective basis for the further exploration of oil and gas in this area.

Keywords Well logging · Sedimentary microfacies · Rock-electricity response · Electrofacies mode

1 Introduction

Baiyinchagan depression is Mesozoic sedimentary basin developed on the hercynian fold of upper palaeozoic basement and dustpan-like depression whose north side is faulted and south side overlapped controlled by boundary normal fault. On

---

X. Li (✉) · Q. Wang · W. Ma
Collage of Geology and Environment, Xi’an University of Science and Technology,
Shaanxi Xi’an 710054, China
e-mail: 147569652@qq.com

Q. Wang
e-mail: 147569652@qq.com

W. Ma
e-mail: 147569652@qq.com

Q. Di et al. (eds.), *Technology and Application of Environmental and Engineering Geophysics*, Springer Geophysics,
DOI 10.1007/978-981-10-3244-8_8

the basis of sedimentary background, sedimentary characteristics and actual development, the depression is divided into the southern gentle slope belt and the northern steep slope zone, the southern gentle slope belt is the key area for exploration and which reveals Tengge'er group of the BaYanHua group of under Mesozoic cretaceous system (K1bt) is the main oil-bearing strata. From the point of view of the existing research [1–4], Tengge'er group reservoir sand body distribution and combination rule of the southern ramp zone are mainly controlled by sedimentary microfacies, but the current research on sedimentary characteristics and sedimentary microfacies can't meet the needs of production, so the study of sedimentary microfacies through lithology and logging sedimentology becomes more popular.

Through the analysis of the rock composition, parent rock of Tengge'er group provenance is given priority to metamorphic rock, Tengge'er group rocks are mainly quartz, feldspar, mica sheet, and all kinds of debris, the rock compositional maturity of the depression are generally lower. Since Tengge'er group reservoir belongs to middle-low porosity, middle-low permeability reservoirs, lithology is dense, acoustic time (Δt) curve whose change is small is less sensitive to lithology. Resistivity (RT) curve is affected by various factors such as lithology, physical property, fluid properties and so on, it is easy to make the multi solution when the lithology analysis is processed, but spontaneous potential (SP) and natural gamma ray (GR) logging curve can make a good response to the size of rock and shale content, so this article make the electrofacies study mainly through GR and SP log curve and meanwhile referring to the curve characteristics of RT and Δt curve, in order to distinguish different lithology and sedimentary microfacies.

2 Rock-Electricity Response

The main focus of the study is to develop a regional sedementart facies model based on well log features of the study area:

- Coarse grained glutenite and gravelly sandstone show the lower Δt value, SP curve shows the higher negative anomaly, GR is less than 100 API and Rt value is generally low; gravel bearing sandstones show the lower Δt value, SP presents negative values, GR value is smaller and Rt value is medium.
- Medium grained gritstone has the lower Δt value, SP shows obvious negative anomaly, GR and Rt present low value; packsand presents the lower Δt value, SP shows negative anomaly, and GR and Rt show low value.
- Fine grained siltstone has increscent Δt value, SP shows negative anomaly, GR and Rt show low value.

- Dark mudstone shows the higher GR value, the bigger Δt value and the smaller Rt value, SP shows base line; the basic characteristics of red mudstone are similar to dark mudstone's, RT value of red mudstone is larger than dark mudstone's; Rt value of Shale is significantly greater than dark mudstone's, Δt value and GR value decrease.
- Some special lithologies such as dolomite has the large density and Δt value, GR and Rt are relatively small and SP shows not obvious anomaly.

3 Well Logging Facies Model

3.1 The Sedimentary Facies Types

According to the study analysis of the southern gentle slope belt regional geology, Tengge'er group of the southern gentle slope belt of Baiyinchagan depression presents the characteristics of the braided river delta sedimentary. On the basis of previous data, combining with this research, the braided river delta of the southern gentle slope belt of Baiyinchagan depression can be further divided into 3 subfacies and 7 microfacies. Specific conditions are shown in Table 1.

3.2 The Establishment of the Electrofacies Mode

Analysis of 50 well logs of the southern gentle slope belt showed the sedimentary facies in the studied area, GR curve characteristics as the supplement, therefore, according to the characteristics of GR and SP log curve, the electrofacies model in the study area are established.

Table 1 The Braided River delta facies classification table

The sedimentary facies	The sedimentary subfacies	The sedimentary microfacies
The braided river delta	The braided river delta plain	Water distributary channel and flood plain
	The braided river delta front	Underwater distributary channel, interchannel underwater (distributary bay), river mouth bars,front sheetsand, frontal sand wedge
	Before the braided river delta	

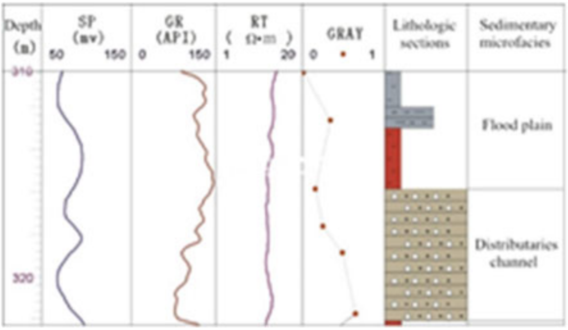

Fig. 1 Water distributary channel and flood plain microfacies (Well Da 6)

- Upperwater distributary channel
  The bottom of distributary channel is given priority to aubergine gravel-bearing sandstone (Fig. 1), the Erosional surface is developed at the bottom. Upper is aubergine unidirectional inclined beddings or parallel beddings medium-coarse sandstone, on the well logging curve, distributary channel shows the combination of high amplitude box-like and finger-like, the dentation box SP curve, the flat bell RT curve and gradual decrease of its optimal eigenvalue [5] from bottom to top, in turn, reduced.
- Flood plain
  Flood plain is mainly aubergine mudstone intercalated with silty mudstone and plant carbon bits are visible (Fig. 1).
- Underwater distributary channel
  Underwater distributary channel deposits with comparatively thin grain size, good sorting and subprime arris state-subprime cone, and overall show the superposition of multiple whole rhythm with the characteristic of becoming thin upward. The single sand body thickness is 0.5–2 m, the logging curve often shows abrupt contact of the top and the bottom, the bigger feature classification function show scour contact of the top and bottom, RT and GR have the characteristics of low amplitude and low value and SP presents box-like or bell-like. Lithology of lakeshore with partly coarse grain and gravel-bearing mainly are glutenite supported by grain, conglomeratic sandstone or fine sandstone and show the positive rhythm features, single thickness is more than 5 m and SP presents box-like (Fig. 2a).
  Lithology of shallow lake with partly fine grain and middle-fine sandstone-based mainly are siltstone and fine sandstone and single layer thickness is 2–5 m (Fig. 2b).
- Interdistributary bay
  Interdistributary bay located in the delta front underwater distributary channel sand body and linking the open lake is the wedge-shape argillaceous sedimentary bodies whose tip points to land. The very fine lithology mainly are mudstone, silty mudstone and argillaceous siltstone. SP and GR display low amplitude slightly dentate or smooth curve, and the thickness is variable (Fig. 2).

Fig. 2 Underwater distributaries channel and interdistributary bay microfacies

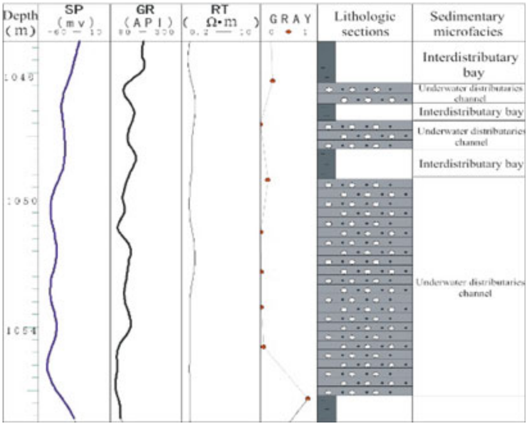

(a) Well Da 30

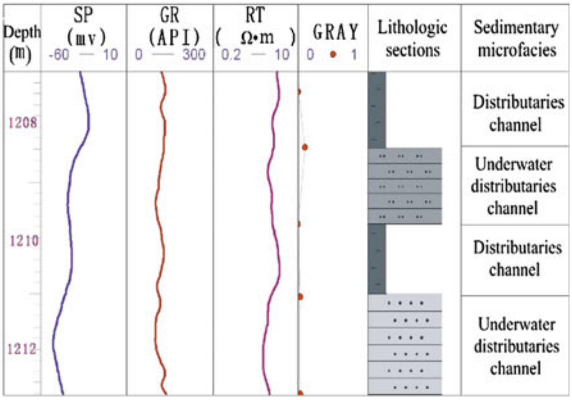

(b) Well Da 31

- Mouth bar
  The lithology of side sheet characterised by fine sandstone orderly are silt-fine sandstone, middle-coarse sandstone and conglomerate from bottom to top, which constitutes the reverse cycle with fine bottom and coarse top. The physical property becomes good from bottom to top and single layer thickness is more than 2 m, SP presents the funnel-shaped, GR shows funnel-shaped with sawtooth and RT presents low value (Fig. 3).
- Frontal sheet sand
  The lithology of front sheet sand is gray fine sandstone and siltstone has the bedding, biological remains relatively are rich. Sand body is thickening toward the shore, thinning to the direction of the lake and shows thin layers in vertical, and presents skirt hem shape or belt along terminal sandbank or the edge of the riverway. SP shows unequal amplitude dentation, finger-like and pectination, single layer thickness is 1–2 m and overall shows funnel-shaped (Fig. 4).

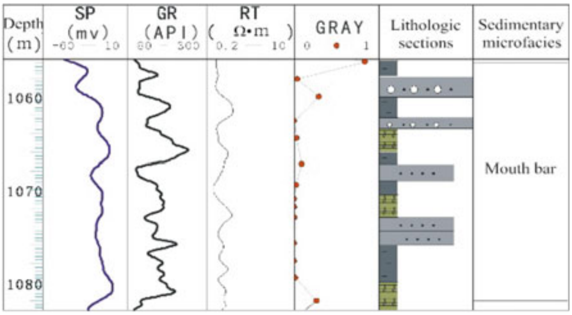

Fig. 3 Mouth bar microfacies

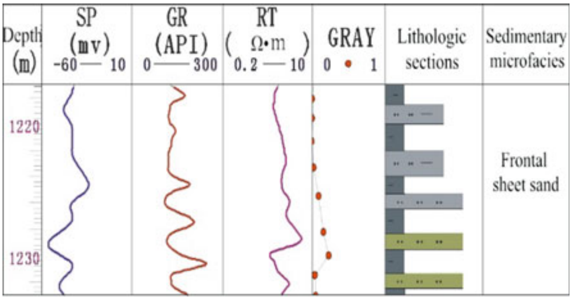

Fig. 4 Frontal sheet sand microfacies

- Frontal wedge-shaped sand

  The southern gentle slope belt of Baiyinchagan depression occasionally develops a coarser granularity front sheet sand microfacies, because of its particularity is named frontal sand wedge and generally distributes on the forefront of underwater distributary channel, whose lithology is thin layer conglomeratic sandstone and the thickness of single layer is 1–2 m. The thickness of sandstone accounts for 15–30% of strata thickness, GR shows the combination of small irregular bell-shaped, finger-shaped and funnel-shaped, SP presents negative anomaly and amplitude difference is 5–20 mv (Fig. 5).

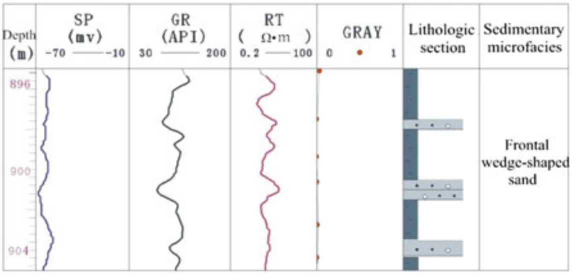

Fig. 5 Wedge-shaped sand microfacies (Well Da 2)

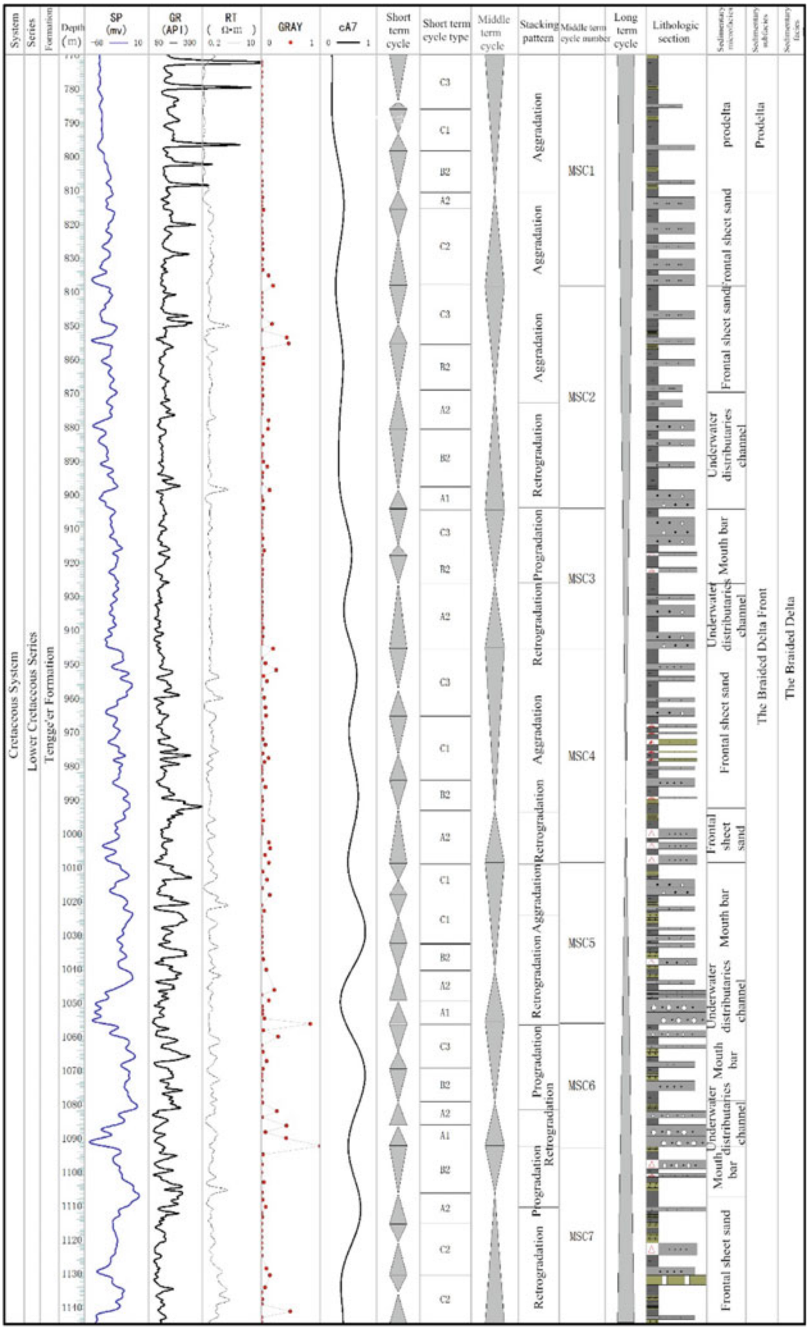

Fig. 6 The analysis diagram of single well logging sequence stratigraphy (Well Da 30)

4 The Analysis of Single Well Logging Sedimentary Microfacies

The representative Well Da 30 is selected in the southern gentle slope belt and its constitution, characteristics and vertical evolution of sedimentary facies are dissected (Fig. 6). The Tengge'er formation sedimentary type of Well Da 30 mainly is braided river delta front.

From logging characteristics, the bottom of Well Da 30 is given priority to combination of retrogradation and progradation and overall presents the retrogradation type, the upper is given priority to combination of retrogradation and aggradation and overall presents the characteristics of aggradation. The analysis of variation characteristics of accommodation space (A)/sediment supply (S) [6, 7] show that the bottom mainly displays the change trend of low accommodation-high accommodation-low accommodation space, the corresponding middle-term cycles are formed, and sediment supply relatively is strong, sand body, underwater distributary channel and mouth bar microfacies are developed and the sediment granularity are relatively coarse. The upper mainly presents the high accommodation space sediment, accommodation space increases, but the sediment supply relatively decreases, the granularity become thin, sand body is not gradually developed, muddy intercalation or muddy layer become thick and single sand layer thickness becomes thin. Tengge'er formation overall presents the coarse-to-fine characteristics and sedimentary microfacies change from the combination of underwater distributary channel and mouth bar to the front sheet sand and predelta. From this point of oil-bearing, mouth bar and front sheet sand could be better reservoir.

5 Conclusion

Based on the research of petrological characteristics and rock-electricity response relationship, the electrofacies mode eventually are established and the sedimentary microfacies in the study area are divided. We get the following conclusions:

- The study area is mainly characterized by the braided river delta deposits that could be further divided into three subfacies including the plain, the front and the front braided river.
- According to research of rock electricity relationship and well logging facies model, the sedimentary microfacies of the study area are further divided into 7 sedimentary microfacies including upperwater distributary channel, flood plain, underwater distributaries channel, interdistributary bay, mouth bars, front sheet sand and frontal wedge-shaped sand.

- The bottom of Well Da 30 is given priority to logging curve combination of retrogradation and progradation, and the whole presents the retrogradational type; the upper is given priority to combination of retrogradation and aggradation and presents aggradational type overall.
- Generally, Tengge'er group presents characteristics from coarse to fine, and sedimentary microfacies change from the combination of underwater distributary channel and mouth bar to the front sheet sand and predelta.

References

1. Xu, S. T., Ma, W. M., Wang, D. R., et al, 2004, Sequence strata of lower cretaceous in Baiyinchagan Depression, Erlian Basin: Acta Sedimentologica Sinica, 22, 644–650.
2. Zhang, F. S., Fan, T. L., Wang, S. L., et al, 2003, The sequence stratigraphic framework and the filling style of Baiyinchagan Depression: Acta Geoscientia Sinica, 24, 137–142.
3. Zhang, F. S., Wang, S. L., Sun, Y. P., et al, 2003, Framework of sequence stratigraphy and filling style of Baiyinchagan Depression: Petroleum Exploration and Development, 30, 32–33.
4. Wu, M. R., Jiang, Z. X., Qiu, L. W, et al, 2001, Sequence stratigraphy and hydrocarbon pattern of cretaceous in the south slope area of Baiyinchagan Depression: Journal of the University of Petroleum, (edition of natural science), 25, 1–5.
5. Li, X. H., 2006, The identify of sequence surface using the best eigenvalue from geophysical logging curve: Journal of Hunan University of Science and Technology (Natural Science Edition), 21, 26–30.
6. Cross, T. A., Lessenger, M. A., 1996, Sediment Volume Partitioning: Rationale for Stratigraphic Model Evaluation and High-Resolution Stratigraphic Correlation: Accepted for publication in Norwegian Petroleums-Forening Conference Volume, July: 1–24.
7. Deng, H. W., 2002, High-Resolution Sequence Stratigraphy—Principle and Application. Beijing: Geological Press.

Improvement on AVO Equations in VTI Media

Xiaoting Li, Hongwei Wang, Suping Peng, Wenfeng Du and Yingchuan Sun

Abstract In weakly anisotropic VTI media, it is assumed that the ray directions of phase and group velocities are consistent, and P wave excites the horizontal interface, we take into account the equations between the anisotropic angle and the isotropic angle with the same horizontal slowness, and re-deduce AVO equations for VTI media again. The new equation shows that it has no effect on AVO equation for P wave, but improves AVO equation for SV wave.

Keywords VTI media · AVO equation · SV wave

1 Introduction

A study of AVO (Amplitude Variation With Offset) equations is very important for a good understanding of the phenomena of wave propagation. Aki and Richards deduced AVO equations for isotropic media at an earlier year [1], however underground media are anisotropy rather than isotropy. Daley and others saw this as VTI media and deduced accurate Zoeppritz equations in VTI media [2]. Thomsen firstly proposed to use anisotropic parameters to describe media's anisotropy, and soon gave approximate AVO equations in VTI media. He assumed that the phase angle and the group angle are the same in weakly anisotropic media when he deduced the equations [3]. Ruger used Christoffel equations and polarization approximation, simplified equations, got different types of seismic waves polarization precise expression, and finally got AVO equations [4]. This paper is based on Thomsen assume, takes into account the equations between the anisotropic angle and the isotropic angle with the same horizontal slowness, re-deduces AVO

X. Li (✉) · H. Wang · S. Peng · W. Du
State Key Laboratory of Coal Resources and Safe Mining, China University of Mining and Technology, Beijing, China
e-mail: lxt_cumtb@126.com

Y. Sun
Mining Institute, Liaoning Technical University, Liaoning, China

Q. Di et al. (eds.), *Technology and Application of Environmental and Engineering Geophysics*, Springer Geophysics,
DOI 10.1007/978-981-10-3244-8_9

equations for VTI media again. The new equation shows that it has no effect on AVO equation for P wave, but improves AVO equation for SV wave.

2 Theory and Method

2.1 Approximate Polarization Equations in VTI Media

There are three kinds of seismic waves in weakly anisotropic media, including P wave, SV wave, SH wave. The phase velocity equations are defined as (1) [4].

$$\begin{aligned} V_P &= \alpha(1+\delta\sin^2\theta\cos^2\theta+\varepsilon\sin^4\theta) \\ V_{SV} &= \beta[1+(\frac{\alpha}{\beta})^2(\varepsilon-\delta)\sin^2\theta\cos^2\theta] \\ V_{SH} &= \beta(1+\gamma\sin^2\theta) \end{aligned} \tag{1}$$

Here, α, β are P wave and S wave velocity in vertical direction of seismic wave propagation, θ is the angle between wave propagation direction and vertical direction in VTI media, δ, ε, γ are Thomsen parameters. According to the equations between phase velocity and group velocity, we get the vector equations of group velocity [5].

$$\begin{aligned} V_{gx} &= (v\sin\theta+\cos\theta\frac{\partial v}{\partial\theta})\cos\varphi-\frac{\sin\varphi}{\sin\theta}\frac{\partial v}{\partial\varphi} \\ V_{gy} &= (v\sin\theta+\cos\theta\frac{\partial v}{\partial\theta})\sin\varphi-\frac{\cos\varphi}{\sin\theta}\frac{\partial v}{\partial\varphi} \\ V_{gz} &= (v\cos\theta-\sin\theta\frac{\partial v}{\partial\theta}) \end{aligned} \tag{2}$$

Here, V_{gx}, V_{gy}, V_{gz} are group velocity components, v is any phase velocity in (1). Assuming that the phase angle and the group angle are same, we use (1) in (2). After normalizing, we obtain P-wave polarization approximation equations [6], defined as

$$P_x = (1+\Delta l)\sin\theta, P_z = (1+\Delta m)\cos\theta \tag{3}$$

where

$$\begin{aligned} \Delta l &= (\delta-2\sin^2\theta(\delta-\varepsilon))\cos^2\theta \\ \Delta m &= -(\delta-2\sin^2\theta(\delta-\varepsilon))\sin^2\theta \end{aligned} \tag{4}$$

SV wave and SH wave equations, defined as:

$$SV_x = (1 + \Delta m)\cos\theta, SV_z = -(1 + \Delta l)\sin\theta \tag{5}$$

$$SH_y = 1. \tag{6}$$

2.2 AVO Equations in VTI Media

We assume that P-wave excites the horizontal interface from isotropic media to weakly anisotropic VTI media. It will refer to following parameters during AVO equation's linearization.

$$\frac{\Delta\alpha}{\bar{\alpha}}, \frac{\Delta\beta}{\bar{\beta}}, \frac{\Delta\rho}{\bar{\rho}}, \delta, \varepsilon, \gamma \tag{7}$$

We just consider the effect of anisotropic parameters, regardless of the matrix parameters. So $\frac{\Delta\alpha}{\bar{\alpha}}, \frac{\Delta\beta}{\bar{\beta}}, \frac{\Delta\rho}{\bar{\rho}}$ all equal zero.

During deducing VTI approximate equations, Ruger regards the angel used in $(M^u)^{-1}$ as isotropic angle, and the angel used in b as isotropic angle, which may exist deviation. According to the classic angle difference equation $\Delta\theta = \tan\theta\frac{\Delta v}{v}$ given by Aki and Richards and the same horizontal slowness, we get the relation between anisotropic angel θ_{ani} and isotropic angel θ_{iso}, defined as

$$\begin{aligned} \sin\theta_{ani} &= \sin\theta_{iso}(1 + \frac{\Delta v}{v}) \\ \cos\theta_{ani} &= \cos\theta_{iso}(1 - \frac{\Delta v}{v}\tan^2\theta_{iso}) \end{aligned} \tag{8}$$

Take P wave polarization for example, Eq. (3) update to (9) using (8) by changing P-wave polarization in equation.

$$\begin{aligned} P_x &= (1 + \Delta l)(1 + \frac{\Delta V_P}{V_{P0}})\sin\theta_P \\ P_z &= (1 + \Delta m)(1 - \frac{\Delta V_P}{V_{P0}}\tan^2\theta_P)\cos\theta_P \\ \frac{\Delta V_P}{\alpha} &= \varepsilon\sin^4\theta_P + \delta\sin^2\theta_P\cos^2\theta_P \end{aligned} \tag{9}$$

Here, θ_P is P-wave angel in isotropic media. The linear expression that anisotropic parameters affect the reflection and transmission coefficients is

$$\Delta R = -(M^u)^{-1}\Delta M R^u \tag{10}$$

Here, $\Delta R = (\Delta R_{pp}, \Delta T_{pp}, \Delta R_{psv}, \Delta T_{psv})^T$, ΔM is the perturbation in Zoeppritz equations caused by anisotropic parameters [4] $R^u = (0, 1, 0, 0)^T$. $(M^u)^{-1}$ is defined as (11). While simplify (10), we just keep anisotropic parameter's linear term, and get the final reflection and transmission coefficients simplified equations.

$$(M^{\mu})^{-1} = \begin{pmatrix} (\frac{\beta}{\alpha})^2 \sin\theta_p & \dfrac{1 - 2(\frac{\beta\sin\theta_p}{\alpha})^2}{2\cos\theta_p} & \dfrac{\sin\theta_p}{2\alpha\rho\cos\theta_p} & \dfrac{-1}{2\alpha\rho} \\ \dfrac{(1 - 2\sin^2\theta_s)}{2\cos\theta_s} & -\sin\theta_s & \dfrac{1}{2\beta\rho} & \dfrac{\sin\theta_s}{2\beta\rho\cos\theta_s} \\ -(\frac{\beta}{\alpha})^2 \sin\theta_p & \dfrac{1 - 2(\frac{\beta\sin\theta_p}{\alpha})^2}{2\cos\theta_p} & \dfrac{\sin\theta_p}{2\alpha\rho\cos\theta_p} & \dfrac{1}{2\alpha\rho} \\ \dfrac{(2\sin^2\theta_s - 1)}{2\cos\theta_s} & -\sin\theta_s & \dfrac{1}{2\beta\rho} & \dfrac{-\sin\theta_s}{2\beta\rho\cos\theta_s} \end{pmatrix} \tag{11}$$

The equations simplified of P-wave reflection and transmission coefficients is defined as (12). The equations simplified of S-wave reflection and transmission coefficients is defined as (13)

$$\begin{aligned} \Delta R_{pp} &= \frac{1}{2}\delta\sin^2\theta_P + \frac{1}{2}\varepsilon\sin^2\theta_P\tan^2\theta_P \\ \Delta T_{pp} &= \frac{1}{2}\delta\sin^2\theta_P + \frac{1}{2}\varepsilon\sin^2\theta_P\tan^2\theta_P - (\delta - \varepsilon)\sin^4\theta_P \end{aligned} \tag{12}$$

$$\begin{aligned} \Delta R_{psv} &= \frac{1}{2}(\frac{1}{\cos\theta_s} - \frac{\beta\cos\theta_P}{\alpha})\delta\sin\theta_P + \frac{\beta}{\alpha}(\delta - \varepsilon)\cos\theta_P\sin^3\theta_P - \frac{(\delta - \varepsilon)}{\cos\theta_s}\sin^3\theta_P \\ &\quad - \frac{1}{2}\frac{\beta\delta\cos\theta_P\sin^5\theta_P}{\alpha} - \frac{\beta^2\delta\sin^5\theta_P}{\alpha^2\cos\theta_s} \\ \Delta T_{psv} &= -\frac{1}{2}(\frac{1}{\cos\theta_s} + \frac{\beta\cos\theta_P}{\alpha})\delta\sin\theta_P + \frac{\beta}{\alpha}(\delta - \varepsilon)\cos\theta_P\sin^3\theta_P + \frac{(\delta - \varepsilon)}{\cos\theta_s}\sin^3\theta_P \\ &\quad - \frac{1}{2}\frac{\beta\delta\cos\theta_P\sin^5\theta_P}{\alpha} + \frac{\beta^2\delta\sin^5\theta_P}{\alpha^2\cos\theta_s} \end{aligned} \tag{13}$$

Here, θ_s is S-wave angel in isotropic media.

In case, both sides are weakly anisotropic VTI media. Upside's Thomsen parameters are $\delta_1, \varepsilon_1, \gamma_1$, while downside are $\delta_2, \varepsilon_2, \gamma_2$. We just need to replace the parameters in (12) and (13) as (14).

$$\delta = \delta_2 - \delta_1, \varepsilon = \varepsilon_2 - \varepsilon_1, \gamma = \gamma_2 - \gamma_1 \tag{14}$$

Equation (12) conforms to the AVO equations of classic P-wave reflection and transmission coefficient. Equation (13)'s coefficient is changed beginning from $\sin^3\theta_P$.

3 Examples

For comparing of AVO approximation equations in VTI media, we give both sides' background parameters. P-wave velocity is 2200 m/s, S-wave velocity is 1100 m/s, density is 1.4 g/cm^3, downside VTI media's δ, ε are three different value, that is (0.189, 0.204), (0.110, −0.035), (0.065, 0.059). In the figures, (a) is ΔR_{PSV} coefficient comparison, (b) is ΔT_{PSV} coefficient comparison.

By comparing the Figs. 1, 2 and 3 we can see new reflection and transmission for SV wave which is based on our equation are more close to the exact value.

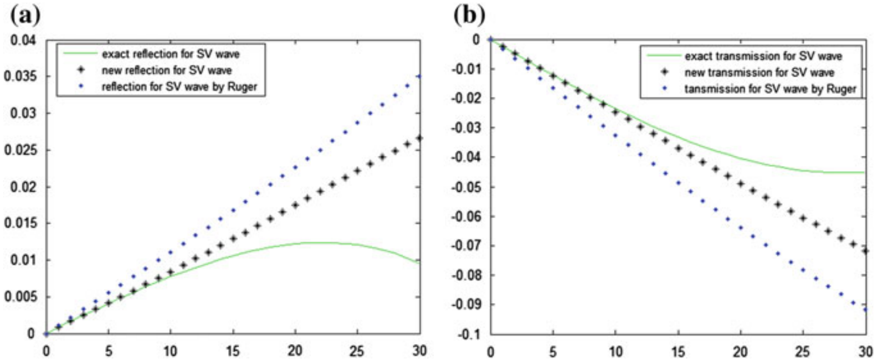

Fig. 1 δ, ε are respectively 0.189 and 0.204

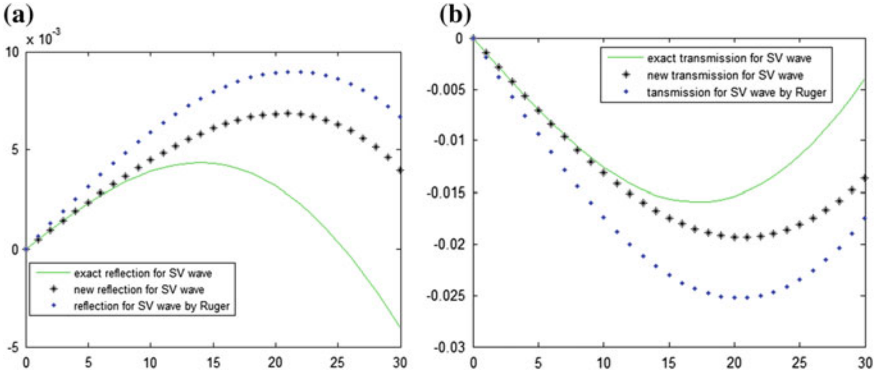

Fig. 2 δ, ε are respectively 0.110 and −0.035

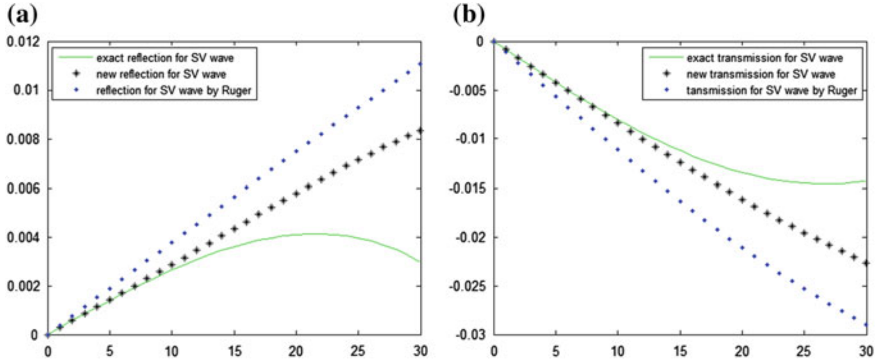

Fig. 3 δ, ε are respectively 0.065 and 0.059

4 Conclusions

In this paper, we take into account the relation between anisotropic angle and isotropic angle during seismic wave propagation, and improve the accuracy of converted-wave equation. The improvement on AVO equation in VTI media which is based on Thomsen assumption with with the same horizontal slowness, shows that it has no effect on AVO equation for P wave, but improves AVO equation for SV wave.

Acknowledgments This research is financially supported by National Natural Science Funds Coal Joint Project (U1261203), National Key Scientific Instrument and Equipment Development Program (2012YQ030126), Shanxi Natural Science Funds Project (2013012001).

References

1. Aki, K., and P. G. Richards, “Quantitative Seismology: Theory and Methods”, M. W. H. Freeman & Co. San Francisco, 1980.
2. Daley, P.F. and F. Hron, “Reflection and transmission coefficients for transversely isotropic media”, Bulletin of the seismological society of America, 67, 3, pp. 661–675, 1977.
3. Thomsen, L., “Weak elastic anisotropy: Geophysics”, 51, 10, pp. 1954–1966, 1986.
4. Ruger, A., “Reflection coefficients and azimuthal AVO Analysis in anisotropic media: SEG geophysical monograph series number 10”, Soc. Expl. Geophys, 2001.
5. G.C. Wu, K. Liang, Y.P. Qi, “Phase velocity and group velocity in 3D TTI media”, PROGRESS IN GEOPHYSICS, 24, 6, pp. 2097–2105, 2009.
6. Thomsen, L., “Weak Anisotropic Reflections, invited for inclusion in Offset Dependent Reflectivity”, SEG Special Publication, Castagna and Backus, eds., Tulsa, 1992.

Determination of the Conversion Point for P-SV Wave of Horizontal Interface Under Rugged Surface

Liang Sun, Suping Peng, Dengke He and Chao Sun

Abstract P-SV wave requires accurate conversion point to get common conversion point collection. However, there is no method to get exact conversion point under rugged surface. This paper established an iterative equation to get the exact conversion point under the rugged surface, and proved effectiveness and accuracy of the iterative equation.

Keywords Converted wave · Conversion point · Rugged surface · Iterative equation

1 Introduction

The determination of the conversion point for P-SV wave directly affects velocity analysis, common conversion point gather extraction, P-SV wave stacking and P-SV wave pre-stack migration in P-SV wave seismic data processing. Although many scholars [1–4] have given many methods to calculate the coordinate of the P-SV wave conversion point. However these methods are based on the condition of horizontal surface. However, with land exploration of our country to western and southern parts where the surface dramatic ups and downs and the high-speed strata expose [5], caused that P-SV wave seismic data processing cannot accurately obtain conversion points, which has become the restriction factor of conversion wave processing technology development. In this paper, according to the Snell's law, the quartic equation of conversion point coordinate is established, and the iterative equation is derived to get the accurate conversion point.

L. Sun (✉) · S. Peng · D. He · C. Sun
State Key Laboratory of Coal Resources and Safe Mining,
China University of Mining and Technology, Beijing, China
e-mail: yksunliang@163.com

Q. Di et al. (eds.), *Technology and Application of Environmental and Engineering Geophysics*, Springer Geophysics,
DOI 10.1007/978-981-10-3244-8_10

2 Method

Definition the horizontal distance between shot point and receiving point is $x = RM_2 + SM_1$, the horizontal distance between shot point and conversion point is $x_p = SM_1$, the shot point is $S(x_1, z_1)$, the receiver-point is $R(x_2, z_2)$, the distance between shot point and reflecting interface is $SH = h$. As shown in Fig. 1, that is the ray path of P-SV wave. According to the law of Snell, we can get the following relations.

$$G \sin \alpha = \sin \beta \tag{1}$$

$$G = v_s / v_p$$

The S-wave velocity and P-wave velocity are respectively represented by v_s and v_p in the formula.

Definition the converted point is C (x_3, z_3), in addition $x_3 = x_p$ and $z_3 = h + z_1$. According to relationship in Fig. 1, the following equations can be got.

$$\sin \alpha = \frac{x_p}{\sqrt{x_p^2 + (z_3 - z_1)^2}}$$

$$\sin \beta = \frac{x_s}{\sqrt{x_s^2 + (z_3 - z_2)^2}}$$

Equation (2) is obtained after putting the above equation into the Eq. (1).

$$\frac{G x_p}{\sqrt{x_p^2 + (z_3 - z_1)^2}} = \frac{x_s}{\sqrt{x_s^2 + (z_3 - z_2)^2}} \tag{2}$$

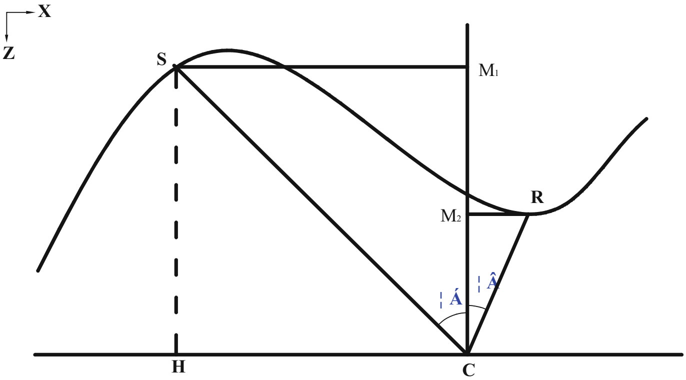

Fig. 1 Ray path of P-SV wave

On both sides of the Eq. (2) for the square and finishing, the Eq. (3) that is related to x_p can be got.

$$a_4x_p^4 + a_3x_p^3 + a_2x_p^2 + a_1x_p + a_0 = 0 \tag{3}$$

Among them,

$$a_4 = (1 - G^2),\ a_3 = -2x(1 - G^2),\ a_2 = x^2 + (z_3 - z_1)^2 - G^2x^2 - G^2(z_3 - z_2)^2$$
$$a_1 = -2x(z_3 - z_1)^2 a_0 = x^2(z_3 - z_1)^2$$

Solving Eq. (3) can get x_p. But the Eq. (3) is one of quartic equations, and the solution of the equation has three kinds of conditions; (1) two pairs of conjugate complex roots; (2) a pair of conjugate complex roots and pair of real root; (3) four real roots. However we know that the conversion point will be a real root. It is still difficult to select the true root from those roots. In practice, it can be obtained by an iterative equation, and its iterative method can effectively obtain the exact location of conversion point.

$$x_p = \frac{x\sqrt{(z_3 - z_1)^2 + (1 - G^2)x_p^2}}{\sqrt{(z_3 - z_1)^2 + (1 - G^2)x_p^2} + G(z_3 - z_2)} \tag{4}$$

Equation (4) is the iterative equation that used to get coordinate of conversion point, which is useful under the condition of horizontal interface and rugged surface, and the initial value of iteration can select $x_p = x/(1 + G)$.

Based on the above derivation, a lot of data calculation is carried out. The calculation results show that using the iteration equation to solve conversion point coordinate rapidly and efficiently.

Tables 1 and 2 show the results under different parameters of two groups where x is the distance from shot point to geophone point, G is the velocity ratios of v_s and v_p, h is the distance from shot point to reflection interface and Δh is the difference between shot point and receiver-point.

Table 1 x_p Iterative solution and exact solution ($G = 0.4$, $h = 400$ m, $x = 200$ *m*, $\Delta h = 20$ *m*)

Iteration number	Iterative solution	Exact solution	Error
1	144.8961	147.0470	2.1509
5	146.8975	147.0470	0.1495
10	147.0416	147.0470	0.0054
15	147.0468	147.0470	0.0002
20	147.0470	147.0470	0

Table 2 x_p Iterative solution and exact solution ($G = 0.4$, $h = 400$ m, $x = 200$ m, $\Delta h = -20$ m)

Iteration number	Iterative solution	Exact solution	Error
1	142.9000	142.9453	0.0453
5	142.9421	142.9453	0.0032
10	142.9452	142.9453	0.0001
15	142.9453	142.9453	0
20	142.9453	142.9453	0

3 Conclusions

This paper deduced the quartic equation of horizontal interface under rugged surface condition and derived its iterative equation to compute conversion point. A large number of calculation result show that the iterative algorithm can get the high-precision solution with no higher than 40 iterations. According to the accurate conversion point position, we can accurately extract common conversion point gathers, and realize the P-SV wave NMO and stacking accurately.

Acknowledgment The authors thank these following projects for financial supporting this research, including the Coal United Project of National Natural Science Foundation (U1261203) and China Geological Survey Project (1212011220798).

References

1. Tessmer G., Behle A., “Common reflection point data-stacking technique for converted waves,” Geophysical Prospecting, vol. 36, pp. 671–6882, October 1988.
2. Taylor G G., “The point of P-S mode-converted reflection: An exact determination,” Geophysics, vol. 54, pp. 1060–1063, August 1989.
3. Yuan C. F., Peng S. P., et al., “An exact solution of the coordinate equation of the conversion point for P-SV converted waves at a horizontal reflector,” Chinese Journal of Geophysics, vol. 48, pp 1179–1184, September 2002.
4. Zhang H. Y., “Determination of conversion points in slant interface, “ Oil Geophysical Prospecting, vol. 28, pp. 752–760, December 1993.
5. Zhang H., “3D prestack time migration including surface topography,” Chinese Journal of Geophysics, vol. 55. pp. 1336–1343, April 2012.

The Study of Anti-noise Immunity for Electromagnetic Method Based on m Pseudo-random Sequence

Xianxiang Wang and Juzhi Deng

Abstract Electromagnetic methods play an important role in the exploration of metal ore mineral, oil and gas resources. It is very difficult to obtain a high signal to noise ratio with increasingly electromagnetic noise using conventional anti-noise method. In recent years, the pseudo random sequence attracts a lot of attention because of its anti-noise performance. This paper describes two common methods used to extract the impulse response from the pseudo-random sequence response studies have shown that the two methods are available to get high-precision impulse response without noise.The extraction accuracy of the results using the two methods were compared with date contained in the noise, that shows that the results of method 2 is better than 1, then analyzing the reasons for this situation. Finally, the study is made to improve the ability of the anti-pseudo-random sequence of methods, including to improve the order of the pseudo-random sequence, using a different encoding, change the number of cycles in order to achieve the purpose of noise suppression.

Keywords Electromagnetic method · m pseudo-random sequence · Style · Anti-noise immunity

---

X. Wang (✉) · J. Deng
School of Nuclear Engineering and Geophysics, East China Institute of Technology, Nanchang, China
e-mail: Wangxianxiang09@163.com

J. Deng
e-mail: jzdeng@ecit.cn

Q. Di et al. (eds.), *Technology and Application of Environmental and Engineering Geophysics*, Springer Geophysics,
DOI 10.1007/978-981-10-3244-8_11

1 Introduction

Electromagnetic method has become an important exploration method for deep exploration depth, high resolution, convenience and low cost. In last few decades, it is increasingly used in the exploration of metal ores, hydrocarbon reservoirs, geothermal and groundwater [1–3].

Electromagnetic fields increasingly decay with the offset increasing, and the electric field intensity is on the level of millivolt per kilometer, even only nanovolt per kilometer. On the other hand, electromagnetic interference signal, including all kinds of electrical interference, mechanical interference, and random noise and so on, is getting stronger in urban areas. The traditional methods are mainly through increasing the transmitter power, notch filtering, stack and other methods to suppress the effects of noise in strong noise zone, it is very difficult to obtain high SNR electromagnetic signals with conventional methods. In this paper, we provide a new method to suppress strong noise, in which the pseudo-random binary sequence current is emitted as the source.

This paper will discuss anti-interference utilizing PRBS. We can get the electromagnetic signal in time or frequency domain from PRBS response. The conversion is also an important process of eliminating noise the conversion to the frequency or the time domain. In order to understand the principle of anti-interference for PRBS, we firstly introduce the methods that how get the impulse response from the PRBS response.

So we firstly discusses the two main methods getting impulse responses from the PRBS response, and compare two methods accuracy without considering noise. Then impulse responses results, from the PRBS response with noise, are compared, and the results are analyzed. Finally, the method PRBS response with noise is better.

2 Theory and Method

The PRBS responses need to be converted to the impulse response or frequency domain for two reasons. Firstly, it cannot directly show ground structure, bringing a lot of inconvenience to explainers. On the other hand, although it is feasible in theory to use the PRBS responses for inversion directly, but it will bring the noise to the inversion process. So we usually get the time domain or frequency domain date from the PRBS responses.

The process of converting the PRBS responses to the impulse response or frequency domain is also the important processes of eliminating interfering signals. Therefore, this section will first introduce two popular methods, obtaining the impulse response. In the first method, the dates of the transmitter and receiver are converted to frequency domain. We can get the normalized electromagnetic response by a series of processing. The dates are converted to time domain to get the impulse response. In the second method, the impulse responses are mainly obtained by solving Wiener-Hopf equation.

To test the results of extracting the impulse response in both methods, the uniform half-space model is described as an example. The analysis shows that the two methods are very good to obtain the impulse response from the PRBS responses without considering the noise.

Through the analysis, pseudo-random sequence order n, the encoding method, and the number of cycles can affect the precision of the impulse response when the pseudo-random sequence responses are with noise. Besides the pseudo-random order, the influence of other parameters is very complex. It is the problem to be solved, that how to select the appropriate parameters in order to improve the accuracy. Through a large number of experiments, we can get the conclusions:

- For description convenience, the number of cycles, when the accuracy of the impulse responses are best, is called the best cycles number. The initial phase of the interference signal is independent of the best cycles number.
- The ability, for anti-noise immunity, of the different encoding methods is different.
- The pseudo-random sequence cycle is not a multiple of the interference signal, but the interference signal can be a multiple of the pseudo-random sequence.
- For the noise of f_0, the length N, the code width Δt, the cycles number n should meet the following conditions:

$$n * N * \Delta t * f_0 = m \tag{1}$$

In which, m is an integer.

To compare the accuracy of extracting the impulse response for two methods, the noise of 50 Hz is joined in the pseudo-random sequence of response:

$$10^{-8} \cos(2\pi * 50t) \tag{2}$$

In which, t is the time. Fig. 1b is the signal of 50 Hz, Fig. 1c is the pseudo-random sequence response with 50 Hz noise. The results of method 1 and 2 are shown in Fig. 1d. By analysis of this figure, we can get the conclusion: the results of method 1 are different with the analytical solution, and are completely unavailable; the impulse response, obtained using the method 2, is still consistent with analytical solution. Through the above analysis, the anti-noise capability of method 2 is much better than method 1.

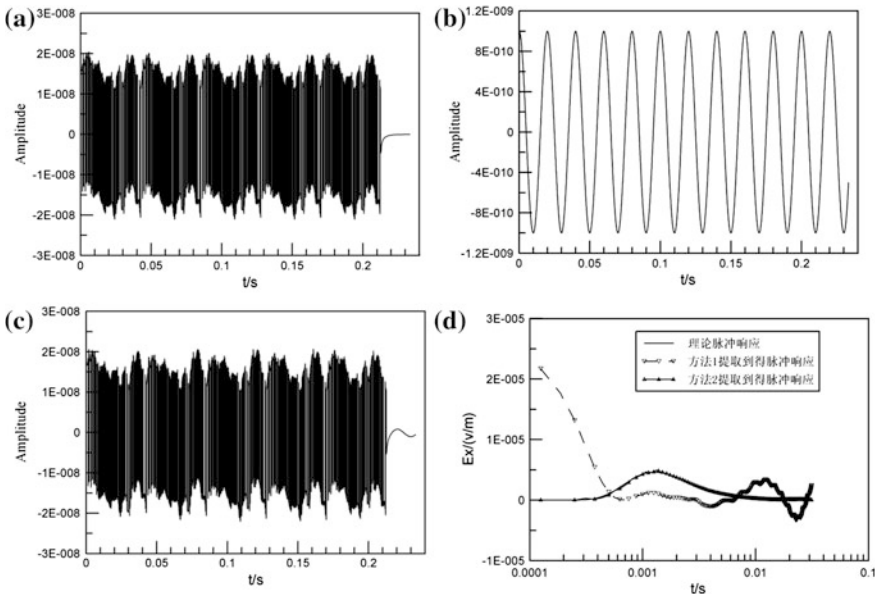

Fig. 1 Simulation of pseudo-random sequence response with 50 Hz noise and results comparison of two methods, **a** pseudo-random sequence response, **b** the 50 Hz noise, **c** pseudo-random sequence response with 50 Hz noise, **d** results comparison of two methods

3 Example

To test the validity of the above conclusion, we use a uniform half-space model as an example. The field excited by pseudo-random sequence is calculated through forwarding, added 25 Hz interference signal following expression:

$$2 * 10^{-7} \cos(2\pi * 25t + \frac{\pi}{4}) \tag{3}$$

The field excited by pseudo-random sequence, the field excited by pseudo-random sequence with the interference signal are shown in Fig. 2a, b respectively. By analyzing the above two figures, we know that data SNR is about −10 dB. Figure 3 correlation function of pseudo-random sequence current and pseudo-random sequence response b correlation function of pseudo-random sequence current and noise are shown in Fig. 3a, b, the above conditions are met in law summarized above, we can see the data within the subject area of interest less noise. Earth's impulse response data obtained, the error are shown in Fig. 2c, d. The maximum error rate is no more than 8%, with a higher.

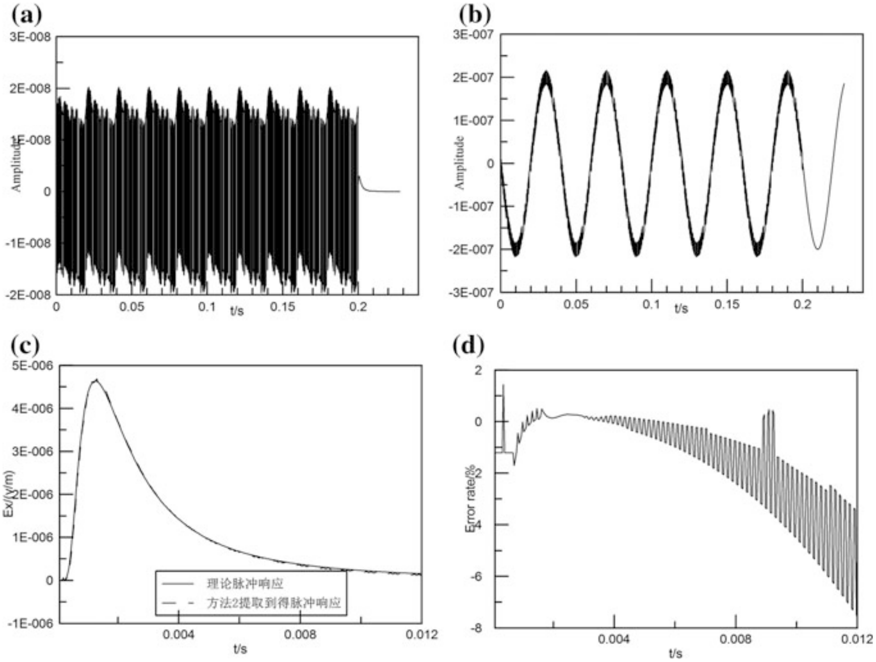

Fig. 2 Simulation of pseudo-random sequence response with 50 Hz noise and results comparison of two methods, **a** pseudo-random sequence response, **b** pseudo-random sequence response with 50 Hz noise, **c** results comparison with the analytical solutions, **d** error rate

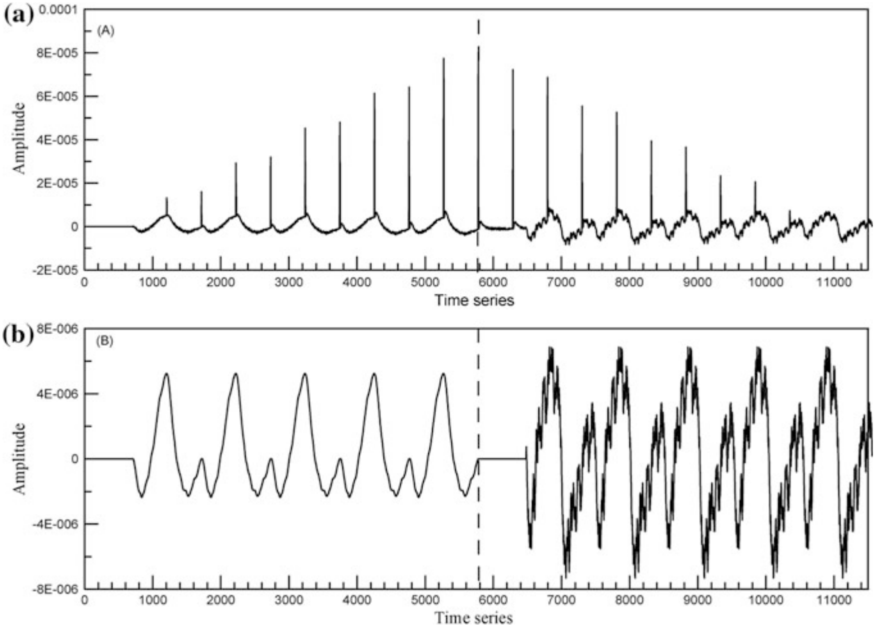

Fig. 3 Correlation function, **a** correlation function of pseudo-random sequence current and pseudo-random sequence response, **b** correlation function of pseudo-random sequence current and noise

4 Conclusion

This paper describes main methods to extract the impulse response from PRBS responses, which is closely related with the anti-noise immunity ability. In the first method, the dates of the transmitter and receiver are converted to frequency domain. We can get the normalized electromagnetic response by a series of processing. The dates are converted to time domain to get the impulse response. In the second method, the impulse responses are mainly obtained by solving Wiener-Hopf equation. We can get good impulse response through the both ways without noise.

Taking into account the noise, the results of method 2 are better than method 1. A method of extracting the first pulse signal earth is lower than the accuracy of the second method.

The reason is that the noise is strengthen in the process of the PRBS responses converted to frequency domain, because the power spectrum density is low outside the bandwidth range. The reason, that the results of method 2 are better, is that the cross-correlation can suppress the noise.

Finally, the studies, to improve the results, have shown that the noise can be suppressed by increasing the order of the pseudo-random sequence, changing the encoding method and the number of cycles and other means. Further studies showed that we can greatly reduce the effects of noise when the multiplication for the number of cycles, the length of a pseudo-random sequence, width and cycle symbol is an integer.

References

1. Di Q Y, K F Shi et al. 2002. CSAMT Research Survey for Preventing Water Flooding in Mining. Chinese J. Geophysics (in Chinese), 45(5): 744–748.
2. Di Q Y, G J Wang et al. 2006. Geophysical exploration over long deep shield tunnel for the west route project of diverging water from Yangtze River to Yellow River. Chinese J. Geophysics (in Chinese), 49(6): 1836–1842.
3. Di Q Y, R Wang et al. 2008. CSAMT forward modeling and inversion and its application. Beijing: Science Press.

Pit-Surface Electromagnetic Receiver

Kai Chen, Haifeng Wang, Ming Deng, Hong Chen, Di Zeng and ShuangChao Ge

Abstract The purpose of a multi-parameter observation system for pit-surface is to achieve high-accuracy observations via electromagnetic signals in tunnels and on surface. The existing ground electromagnetic observation systems have high background noise with low field applicability. The existing non-polarized electrode and inductive magnetic sensors are difficult to operate in tunnels. To solve the problems, an electromagnetic observation system with chopper amplifier circuits for pit-surface has been developed. According to the non-contact electrode principle in the medical field, a non-contact electrode was developed for electric field observation to solve the difficulty of connecting tunnels to ground surface. A 3-axis audio magnetic sensor was developed to solve the existing problem of poor adaptability of large inductive magnetic sensors in narrow tunnels. In the meantime, a number of good improvements for field applicability have been made for the observation system, which greatly enhanced the efficiency of field operation. A series of indoor and field tests were performed, and results confirmed the validity and advancement of the multi-parameter electromagnetic observation system for pit-surface.

Keywords Pit-surface EM receiver · Non-contact electrode · 3-axis induction coil · Non-polarized electrode

1 Introduction

Currently, the widely used electromagnetic method for solid mineral resource exploration still comes with problems of shallow probing, low accuracy, low resolution, and poor anti-interference ability. Therefore, a new technology with strong anti-interference ability, deep probing, and high resolution power for mineral exploration is desperately needed [1]. Through increasing transmitting power in the field source and using existing tunnels, mines, and boreholes to perform

---

K. Chen (✉) · H. Wang · M. Deng · H. Chen · D. Zeng · S. Ge
Key Laboratory of Geo-detection Ministry of Education, China University of Geosciences, Beijing, Beijing, China

Q. Di et al. (eds.), *Technology and Application of Environmental and Engineering Geophysics*, Springer Geophysics,
DOI 10.1007/978-981-10-3244-8_12

three-dimensional observations on the surface and underground, the high-power pit-surface electromagnetic (EM) imaging system can obtain underground medium conductivity, polarization, and many other parameters more effectively and give a more comprehensive interpretation. As a main field device of the high-power borehole-to-surface multi-parameter EM imaging system, the pit-surface EM receiver is developed to perform EM field observations on the surface and in tunnels by carrying out EM sounding and receiving induced polarization signals.

Most of the domestic and foreign counterparts incorporate mature methods such as CSAMT, AMT, SIP, and TDIP in the ground EM observation systems. Considerable progress in distributed measurement, multi-channel, high precision clock synchronization, field applicability, and field data pretreatment has been made [2–6]. The background noise of most of the equipment in low frequency band was affected by1/*f* noise, leading to a rising low-frequency noise level, poor field working conditions, inadequate portability and applicability, and inefficient manufacturing processes. The following deficiencies exist especially when EM observation is used in tunnels: (1) the poor ground connection condition in tunnels and the inapplicability of existing non-polarized electrodes; (2) the narrow working space in tunnels and limited operation due to the large size of inductive magnetic sensors; (3) when GPS navigation cannot be used in tunnels, the requirement for crystal oscillator clock synchronization is higher. In light of the above shortcomings, further study on multi-parameter observation systems for pit-surface is required.

2 Hardware Principle

2.1 Function Diagram

The function diagram of an observation system is shown in Fig. 1. This includes ground surface devices, tunnel devices, emission auxiliary, and indoor test

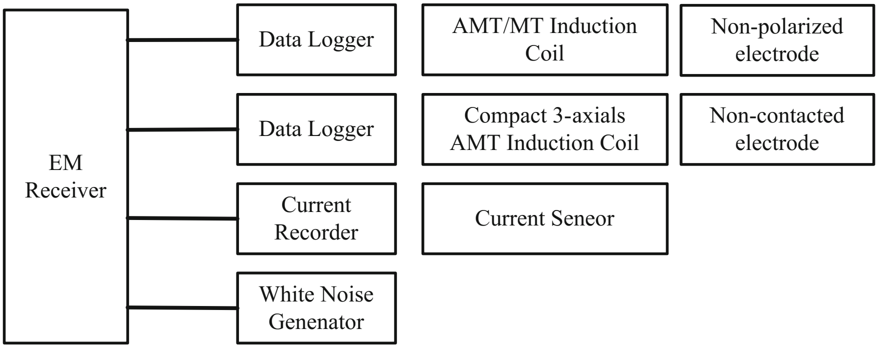

Fig. 1 Observation system structure diagram

equipment. The ground surface devices mainly include a data logger, a magnetic sensor, and a non-polarized electrode. The tunnel devices include a data logger that's consistent with the surface data logger, a small 3-axis audio magnetic sensor, and non-contact electrodes. The emission auxiliary mainly includes a current recorder used to collect the full waveform of the current. The indoor test equipment is a white noise signal generator.

2.2 Non-polarized Electrodes

Non-polarized electrodes mainly solve the deficiency of poor range stability of existing non-polarized electrodes. Some improvements in formulation and manufacturing processes have been made, which mainly are reflected in mud formulation (pH value, Cl^- concentration), small channel design, waterproof seal design, and lead and copper welding processes. The long-period non-polarized electrode is composed of a PVC outer shell, copper cable, wire, mud, cork, and O-rings. Mud is composed of kaolinite, $PbCl_2$, NaCl, and HCl. At the lower end of the electrode, a small channel is placed to stabilize the range.

The main technical indicators of the non-polarized electrode are:

- Initial range: $<\pm 1$ mV;
- Internal Resistance: $<500\ \Omega$ (one pair);
- Weight: ≈ 700 g;
- Size: about 300 mm long and 52 mm in diameter.

2.3 Non-contacted Electrodes

When collecting electric field data in tunnels, the condition of ground connection is very poor. The function of existing non-polarized electrodes cannot be fully carried out. We incorporated the principles of non-contact electrode used for bioelectricity observation in medical devices [7], [8] into tunnel operation, and conducted principle optimization, hardware manufacture, indoor tests, and field comparison tests.

2.4 Small 3-Axials Audio Magnetic Sensor

In tunnel operations, existing large audio magnetic sensors are difficult to fit into small tunnels. When the 3-axis coils are combined into a 30 cm square cube, the 3-axis coils have a good orthogonal degree. When it is placed in tunnels with a smaller body, it guarantees better noise performance. The main technical indicators in small 3-axis audio magnetic sensors are:

- Bandwidth: 0.1–10 kHz;
- Volume: 30 × 30 × 30 cm;
- Weight: 21 kg;
- Noise: 0.5 pT/rt (Hz) @1 Hz;
- Power: 300 mW.

2.5 AMT/MT Magnetic Sensor

We customized the broadband magnetic field sensor, and performed a comparison test on the functionality of the sensor. The test results showed that the performance of a customized broadband magnetic field sensor reached the same level as similar foreign products.

2.6 Data Logger

The data logger, a three-channel magnetic and electric sensor, collects high-precision data simulating voltage signal outputs and provides high-precision timestamps of the original time sequence. The hardware mainly has a built-in acquisition circuit, built-in lithium battery, chassis, and connector components. See Fig. 2 for the hardware diagram. The peripheral interface includes a BNC socket for the GPS antenna, a RJ45 base with an IP65 waterproof rating, three-channel magnetic field bases, three-channel electric field bases, bright LED indicator lights, soft switch buttons, external lead-acid battery input and a built-in lithium battery charging port.

All connectors are installed at the top of the aluminum chassis with an IP66 waterproof rating. The built-in acquisition circuit and lithium battery are installed inside the casing. The capacity of the lithium battery is 11.1 V 20A h. The acquisition

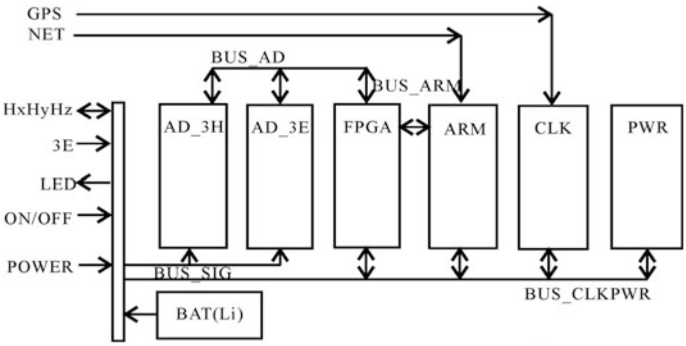

Fig. 2 Data recorder circuit diagram

circuit consists of a front-end interface board, a magnetic field board, an electric field board, an FPGA clock logic board, an ARM control board, a clock board, and a power board, for a total of seven parts.

2.7 *Current Recorder*

The current recorder is similar to the aforementioned data recorder on the whole. The difference is that the data are collected using a single-current channel. The original 3H, 3E input ends were changed to a BNC plug in the matching current sensor, and the electric field board and track plate were replaced with a single-current channel. The working principle of the AD_CUR board in the current recorder is similar to the electric channel plate in the data logger with bandwidth of DC—10 kHz, measuring range of ±1 V and a fixed sampling rate of 24 kHz.

3 Innovative Design

3.1 *Full-Time Collection*

This data collection is different from the existing method which is done by different time frames. It is also not stored in the real-time downsampling, but is collected at a continuous high sampling rate (f_s = 24 kHz). The advantages are acquisition of all-band data and improved data integrity. The disadvantage is the requirement of storage space for a large amount of data, which creates higher requirements for subsequent data processing.

3.2 *Low Noise*

The existing channel has clear $1/f$ noise, which directly affects the signal-to-noise ratio of the original data. In this study, the chopper amplifier is designed to achieve low noise in whole band and to eliminate $1/f$ noise. The test result is shown in Fig. 3. In comparison, the low frequency noise is lower than that of MTU5A.

3.3 *The Applicability to Tunnel Operation*

In tunnel operations, the size of existing magnetic sensor is hard to meet the requirement for tunnel operation due to the limited working space. When the three

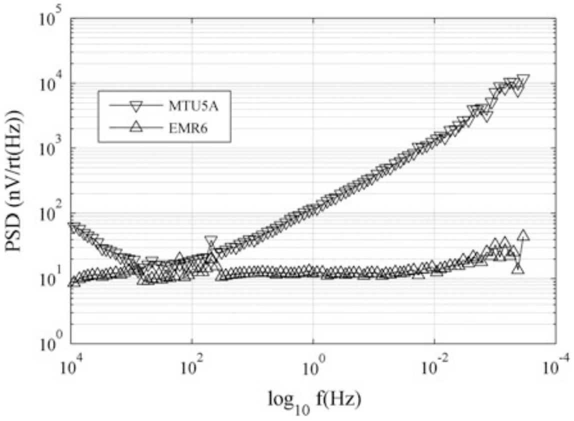

Fig. 3 The results of data logger noise test

magnetic sensors are grouped into a small cube box, the size is smaller and operation becomes more easy and efficient. In hard rock tunnels, it's hard to establish a connection with the ground surface. To solve this problem, a non-contacted mechanism was used to avoid damaging the surface of the hard rock tunnel and achieve electric field observation.

3.4 Accessibility

Considering the complex and changeable operational environment, improving system integration helps the pit-surface observation systems to cope with the poor environment. A low power consumption design helps integrate the built-in battery, making the external lead-acid battery in field operation unneeded. The GPS antenna in the field operation is considered to be a consumable part. The built-in GPS antenna eliminates the need for frequent unplugging to reduce field equipment failure rate. There is no need to pull out memory card for real-time network data downloading, and raw data and field calculation results can be examined in real time.

4 Field Tests

4.1 Non-polarized Electrodes

Eighteen new electrodes was examined. They were immersed in NaCl solution and connected to the input ends of a multimeter. One of them was used as the reference

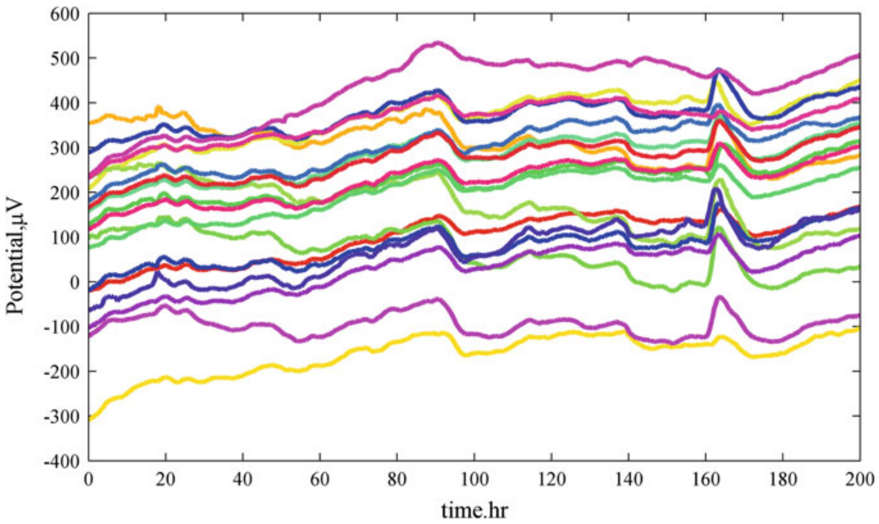

Fig. 4 Range of change for 17 Electrodes

electrode, and the range change of the other was measured. With a sampling interval of one minute, the observation was lated for about ten days. Figure 4 shows the change ranges of 17 electrodes relative to the reference electrode. The result shows that the relative range is about ±200 uV and the range change in ten days is less than 100 uV. The improved electrode has been successfully used in the long period MT field observation.

4.2 Integrated Test

To assess the overall performance of the multi-parameter observation system for pit-surface, we tested carefully all of the indicators in lab for many times and carried out several field data acquisition.

The analysis focused on the technical indicators of the stability and reliability of the observation system, the field applicability, noise level, time synchronization accuracy, etc. Figure 5 shows MT sounding curves under the natural source condition. The impedance tensor in band of 10 kHz-3000 s was obtained. This has preliminarily proved the efficiency of the observation system in ground surface condition.

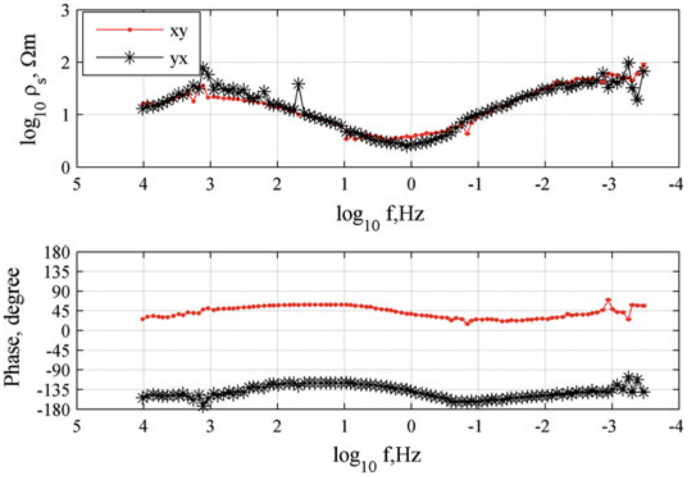

Fig. 5 MT sounding curve under natural source

5 Conclusion

In order to receive a high-accuracy observation via EM signals in tunnels and on the ground surface, the existing observation equipment was upgraded in light of the existing deficiency in background noise level and field applicability. We mainly innovatively designed the electric and magnetic sensors for tunnel environments. The indoor and field tests preliminarily confirmed the efficiency of the observation system.

Acknowledgments This research is sponsored by National 127 special project (GZH201100307), National Natural Science Foundation of China (61531001), and 863 Program (2012AA09A201, 2014AA06A603)

References

1. Teng Jiwen. Strengthen the second depth space and explore metallic minerals resource. Quickly develop geophysical exploring technology. Develop and industrialize equipments. Progress in Geophysics, vol. 25, pp. 729–748, 2010 [in Chinese].
2. GDP32II instruction manual [OL]. http://www.zonge.com/grgdp322.htm.
3. Di Qingyun. Gansu Jinchang Jinchuan nickel mine. Comparison test between SEP system and foreign instruments. Chinese Journal of Geophysics, vol. 58, pp. 3845–3854, 2015 [in Chinese].
4. Zhang Wenxiu, Lin Jun, Liu Lichao, et al. The design and implementation of distributed electromagnetic detection broadband data collection system. Journal of Jilin University (Engineering Science Edition), vol. 6, pp. 1426–1431, 2010.

5. Lin Pinrong, Guo Peng, Shi Fusheng, et al. Study in depth on technology of multi function electromagnetic detection. Journal of Geophysics, vol. 31, pp. 149–154, 2010.
6. Jiang Qiyun. Research on the key technology of wide field electromagnetic sounder. Central South University, 2010 [in Chinese].
7. Shima H., Sakashita S., Kobayashi T. Developments of non-contact data acquisition techniques in electrical and electromagnetic explorations. Journal of Applied Geophysics. vol. 35, pp. 167–173, 1996.
8. Aleksandrowicz and S. Leonhardt, “Wireless and non-contact ecg measurement system—the “Aachen smart chair”,” Acta Polytechnica, vol. 47, pp. 149–154, 2007.

Three-Dimensional Resistivity and Induced Polarization Data Inversion with Image Focusing

Yixin Ye, Zhiyong Zhang, Zelin Li and Yong Zhao

Abstract A maximum smoothness stabilizing functional constraint is normally used to stabilize the three-dimensional (3D) direct current (DC) resistivity and induce polarization (IP) data inversions process. These kinds of algorithms can converge stably, but the obtained solution is a smooth image, which in many practical situations does not describe the examined object properly. In this paper, we present a regularized inversion with image focusing of 3D DC resistivity and IP data. In the inversion approach, the minimum support functional constraint is incorporated into the objective functional, then the damped Gauss-Newton method is used to find the optimization of the objective function, and the preconditioned conjugate gradient algorithm is used to calculate the model updates. The model tests show that the proposed inversion approach owns good reliability and stability. The comparisons show that the program helps to generate more focused and resolved images of blocky geoelectrical structures and with better convergence than the traditional smoothing inversion approach.

Keywords Inversion · Image focusing · Resistivity · Induced polarization · Three-dimensional

1 Introduction

Over the last two decades, many inversion approaches of DC and IP data have been discussed in the geophysical literature. However, most of conventional inversion schemes are based on a standard smoothness constraint, which produces fuzzy images that only poorly reflect the reality of the subsurface structures with sharp resistivity contrast. To overcome this insufficiency, several approaches have been

---

Y. Ye (✉) · Z. Zhang · Z. Li
Fundamental Science on Radioactive Geology and Exploration Technology Laboratory,
East China University of Technology, Nanchang, China

Y. Zhao
Institute of Geological and Mineral Resources Survey of Qinghai Province, Xining, China

Q. Di et al. (eds.), *Technology and Application of Environmental and Engineering Geophysics*, Springer Geophysics,
DOI 10.1007/978-981-10-3244-8_13

described to produce images with sharp boundaries. Portniaguine and Zhdanov [1] describe an gravity inversion approach, in which minimum gradient support (MGS) function is used to minimize the volume of an anomalous body and very compact structures and homogeneous bodies and layers are obtained by this stabilizer. The stabilizer has also been used to the inversion of 3D magnetic data [2] and 3D gravity gradient tensor data [3]. DeGroot-Hedlin and Constable [4] develope an linearized inversion algorithm for 2D magnetotelluric data that only solve for both a fixed number of subsurface resistivities and for the boundary locations between adjacent units. Yoshioka and Zhdanov [5] use both a smoothing and focusing regularized inversion approach to generate more reliable images of the subsurface structures. Blaschek et al. [6] present a new sensitivity-controlled focusing regularization scheme for the spectral IP data inversion by using the minimum gradient support function. Chen et al. [7] present a focusing inversion of 3D full tensor gravity gradient data using the minimum support functional [8] and conjugate gradient method.

In this paper, we present a regularized inversion approach of 3D DC resistivity and IP data. In the inversion algorithm, the damped Gauss-Newton method as well as the preconditioned conjugate gradient algorithm are used to calculate the model updates.

2 Theory of Inversion

We use the Tikhonov approach to solve the ill-posed inverse problem. The formulation of the objective function of this approach can be described as [9]

$$P^{\alpha}(\mathbf{m}) = \|\mathbf{W}_d(\mathbf{d}(\mathbf{m}) - \mathbf{d}_{obs})\|^2 + \alpha s(\mathbf{m}) \tag{1}$$

where $\mathbf{d}_{obs}$ is a vector containing the observed data, $\mathbf{d}(\mathbf{m})$ is a vector containing calculated data for a given model, $\mathbf{W}_d$ is the weighting matrix of data, $s(\mathbf{m})$ is the stabilizing functional, α is a regularization parameter that balances the weight of data misfit and model roughness during the minimization.

In our implementation, $\mathbf{W}_d$ has a simple, standard form. The term $\mathbf{W}_d$ is a diagonal matrix that contains the entries of absolute observed data error:

$$\mathbf{W}_d = diag\left(\frac{1}{|\mathbf{d}_{obs}|S(\mathbf{d}_{obs}) + \varepsilon}\right) \tag{2}$$

where $S(\mathbf{d}_{obs})$ means the standard deviation of the observed data, and ε is a weighting term that keeps the inversion from placing too much weight on very low amplitude data.

$s(\mathbf{m})$ computes differently for different stabilizer, in the case of the minimum support functional, it can be written as

$$S(\mathbf{m}) = \left\|\mathbf{W}_\beta(\mathbf{m})(\mathbf{m} - \mathbf{m}_{ref})\right\|^2 \tag{3}$$

where $\mathbf{W}_\beta(\mathbf{m}) = diag\left(\frac{1}{((\mathbf{m}-\mathbf{m}_{ref})^2+\beta^2)^{1/2}}\right)$, is the minimum support functional, a variable matrix which depends on $\mathbf{m}$, β is a small number. More detailed illustrations about the stabilizing functional can be found in Portniaguine and Zhdanov [2].

After the above objective function is given, the damped Gauss-Newton method is used to find the optimization of the objective function, and the preconditioned conjugate gradient algorithm is used to calculate model updates.

3 Synthetic Model Test

The synthetic model is a half space with a single square block embedded. The half space has a resistivity of 200 Ω m and a chargeability of 1%. The single square block has a resistivity of 10 Ω m and a chargeability of 10%, with the top 2 m

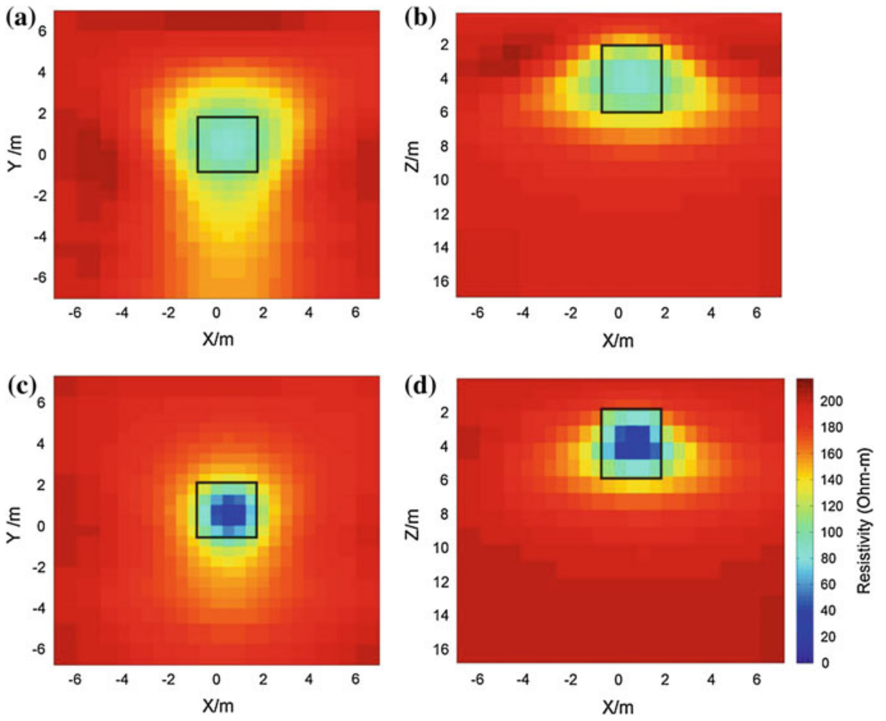

Fig. 1 Resistivity recovered from smoothing inversion and focusing inversion respectively. **a** A *x*-*y* slice of the smoothing inversion result taken at z = 4 m. **b** A *x*-z slice of the smoothing inversion result taken at y = 0 m. **c** A *x*-*y* slice of the focusing inversion result taken at z = 4 m depth. **d** A *x*-z slice of the focusing inversion result taken at y = 0 m

below the Earth's surface. The model domain is subdivided into 40 × 40 × 20 elements. The computations were performed on a personal computer with double-cored 3.2G Hz CPU and 3.35G RAM.

The initial model is set to the half space. The best-fitting model achieved by this inversion is attained after ten iterations. It takes only 13.5 min. Comparison of the solution (Figs. 1c, d and 2c, d) with the original block shape shown superimposed on the model, indicates that both the unit resistivity (chargeability) and boundary locations have been well imaged. For comparisons, we inverted these data using the traditional smoothing inversion algorithm [10], which solves for the smooth possible model. The solution to this inversion is also attained after ten iterations (Figs. 1a, b and 2a, b). The resistivity and chargeability are less well recovered. Also, it is not clear where one would choose to place the boundary location of the block structure. The comparisons show that the focusing inversion approach helps to generate more focused and resolved images of blocky geoelectrical structures than traditional smoothing inversion approach. The normalized misfits (Fig. 3) show that it has good reliability and stability, withbetter convergence.

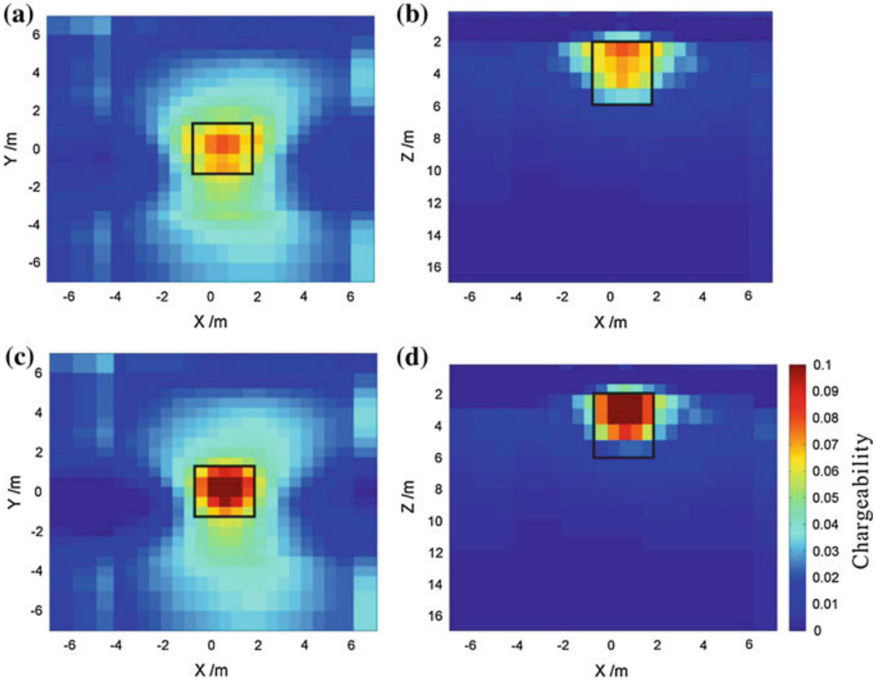

Fig. 2 Chargeability recovered from smoothing inversion and focusing inversion respectively. **a** A *x*-*y* slice of the smoothing inversion result taken at z = 4 m. **b** A *x*-z slice of the smoothing inversion result taken at y = 0 m. **c** A *x*-*y* slice of the focusing inversion result taken at z = 4 m depth. **d** A *x*-z slice of the focusing inversion result taken at y = 0 m

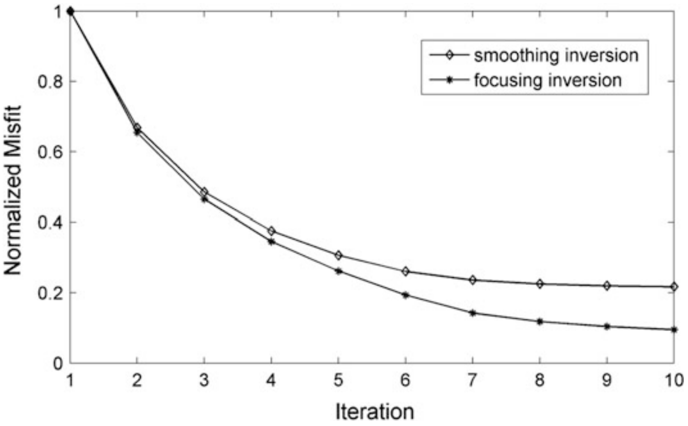

Fig. 3 The normalized misfit curves with iteration numbers for smoothing inversion and focusing inversion respectively

4 Conclusions

This paper presented a focusing inversion approach to the 3D DC resistivity and induced polarization inversion problem. The minimum support functional incorporated in this approach helps to generate more focused and resolved images of blocky geoelectrical structures than traditional inversion approach. The inexact Gauss-Newton solver and conjugate gradient method implemented here make the algorithm computation efficiently. The validations show that it has good reliability and stability, and better convergence. More powerful properties of the focusing inversion approach should be tested in geometrically complex cases.

Acknowledgments This work was supported by the National Natural Science Foundation of China (No. 41204055, 41304054, 41304055, 41104074) and the Natural Science Foundation of Jiangxi province (20161BAB211027).

References

1. O. Portniaguine, and M. S. Zhdanov, Focusing geophysical inversion images, Geophysics, 64, pp. 874–887, 1999.
2. O. Portniaguine, and M. S. Zhdanov, 3D magnetic inversion with data compression and image focusing, Geophysics, 67(5), pp. 1532–1541, 2002.
3. M. S. Zhdanov, R. Ellis, and S. Mukherjee, Three-dimensional regularized focusing inversion of gravity gradient tensor data, Geophysics, 69, pp. 925–937, 2004.
4. C. DeGroot-Hedlin, and S. Constable, Inversion of magnetotelluric data for 2D structure with sharp resistivity contrasts, Geophysics, 69, pp. 78–86, 2004.

5. K. Yoshioka, and M. S. Zhdanov, Three-dimensional nonlinear regularized inversion of the induced polarization data based on the Cole-Cole model, Physics of the Earth and Planetary Interiors, 150, pp. 29–43, 2005.
6. R. Blaschek, A. Hördt, and A. Kemna, A new sensitivity-controlled focusing regularization scheme for the inversion of induced polarization data based on the minimum gradient support, Geophysics, 73(2), pp. F45–F54, 2008.
7. Y. Chen, T. Li, C. Fan, B. Xu, Y. Sun, The 3D focusing inversion of full tensor gravity gradient data based on conjugate gradient, Progress in geophysics (in Chinese), 29(3), pp. 1133–1142, 2014.
8. M. S. Zhdanov, Geophysical inverse theory and regularization problems, Elsevier Science, 2002.
9. A. N. Tikhonov, and V. Y. Arsenin, Solution of ill-posed problems, V. H. Winston and Sons, 1977.
10. A. Pidlisecky, E. Haber, and R. Knight, RESINVM3D: A 3D resistivity inversion package, Geophysics, 72(2), pp. H1–H10, 2007.

A Study of the Southern Segment of the Greater Khingan Range Mineralization Belt, China, Based on the 3D Parallel Inversion of Potential Data

Wuyang Li, Jian Zhang, Daeung Yoon and Wei Lin

Abstract In this paper, a geophysical interpretation of the southern segment of the Greater Khingan Range mineralization belt is firstly introduced. The conventional analytic methods (e.g. continuation) are implemented to illustrate the source of the regional anomalies. Also, we use a new massively parallel inversion code to provide a high-resolution 3D imaging of density and magnetic susceptibility of the whole studying area. The deposit-scale 3D susceptibility inversion models of Dajing and Huanggang are compared and discussed as typical mineral deposits model. The result offers an intuitive overview of geophysical properties and shows a high agreement with the geology settings.

Keywords 3D inversion · Potential field · Parallel computing · CUDA · The greater Khingan range

1 Introduction

The southern segment of the Greater Khingan Range is the biggest polymetallic metallogenic belt of north-east China. The mineralization is associated with the Mesozoic magmatism and Permian strata in this area. The Permian strata is incomplete in outcrop, and the Jurassic-Cretaceous volcanic-plutonic rocks are widespread. The Paleozoic EW-stretching Paleo-Asian Ocean tectonic domain is

---

W. Li (✉) · J. Zhang
College of Earth Science Key Laboratory of Computational Geodynamics,
University of Chinese Academy of Sciences, Beijing, P.R. China
e-mail: wuyang.li@outlook.com

D. Yoon · W. Lin
Department of Geology and Geophysics, University of Utah,
Salt Lake City, USA

Q. Di et al. (eds.), *Technology and Application of Environmental and Engineering Geophysics*, Springer Geophysics,
DOI 10.1007/978-981-10-3244-8_14

overprinted by the NE and NNE-stretching Circum-Pacific tectonic domain [1], which dominates the direction of mineralization.

For geophysical prospecting, although an airborne total magnetic intensity (TMI) data in the southern segment of the Greater Khingan Range was acquired by the China Aero-Geophysical Survey & Remote Sensing Center (AGRS) in the 1980s, it is currently still hard to implement the inversion for a study area of nearly 92 × 80 km because of the limitation of computer memory and CPU time. Recently, there has been several publications about parallel gravity or magnetic modeling and inversion reported [2–6]. However, all the truly massively inversion methods reported are designed for high performance computing (HPC) clusters, which is not flexible and easily available to solve this problem.

We introduce a new parallel 3D inversion code to solve the massively inversion on PCs or Laptops. This program is designed to utilize modeling and inversion for gravity or magnetic or tensor components. The Re-weighted Regularized Conjugate Gradient Method was used to minimizing the parameter functional. Conventional parallel computing skills for clusters were discussed [7], and new strategies for personal computer were also introduced in our optimization. We use the CUDA extension to parallelize our massive inversion on GPU, leading a ~100 times basic speedup as compared to CPU code in the same test laptop (Fig. 1). Moving sensitive domain approach [8, 9] was successfully added in our structure for further speedup. We demonstrate that personal computer would be able to conduct a massively fast parallel inversion for even billion cells as clusters did. The method has been successful tested on synthetic model and real data set.

With the new method, we implement the geophysical interpretation of the southern Greater Khingan Range using not only conventional analytic approaches, but also the inversion method for whole area, typical geological profile and deposits.

Fig. 1 Comparison of computing time between unparallel and parallel code of 10,000 data point l

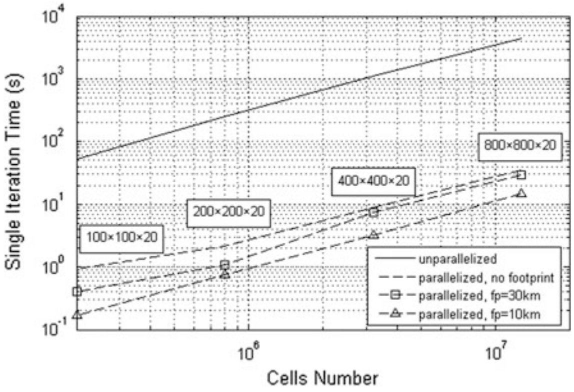

2 Methodology

2.1 Forward Modelling

We choose the single point Gaussian integration with pulse basis function to calculate the response of the modeling domain, which is widely used in potential field inversion [11–13]. The 3D geology model is discretized into a grid of Mcell rectangular cells with constant density or susceptibility, and dx, dy, dz is the length of single prism in the x, y, and z direction respectively. In the magnetic part, we assume that susceptibility is isotropic, and the self-demagnetization is neglected.

The potential field can be expressed as:

$$\mathbf{F}(\mathbf{r}) = C\sum_{m=1}^{Mcell} \beta_k k(\mathbf{r}-\mathbf{r}')\frac{1}{|\mathbf{r}-\mathbf{r}'|^3}\Delta v \tag{1}$$

where r = (x, y, z) is the center point of a prism, r′ = (x′, y′, z′) denotes the point of observation, Δv is the volume of the prism, C is the gravitational constant (G) or the absolute value of the inducing magnetic field (H0), β denotes the density (ρ) anomaly or susceptibility (χ), and k(r − r′) denotes the kernel function of the potential field.

For gravity components, the kernel function is as follows:

$$\left(k_{gx},\ k_{gy}, k_{gz}\right) = \left(x_m - x',\ y_m - y',\ z_m - z'\right) \tag{2}$$

The kernels of gravity tensor are expressed as follow:

$$\begin{pmatrix} k_{gxx},\ k_{gxy}, k_{gxz} \\ k_{gyx},\ k_{gyy}, k_{gyz} \\ k_{gzx},\ k_{gzy}, k_{gzz} \end{pmatrix} = \begin{pmatrix} \frac{3(x_m - x')^2}{|\mathbf{r}-\mathbf{r}'|^2} - 1, \frac{3(x_m - x')(y_m - y')}{|\mathbf{r}-\mathbf{r}'|^2}, \frac{3(x_m - x')(z_m - z')}{|\mathbf{r}-\mathbf{r}'|^2} \\ \frac{3(y_m - y')(x_m - x')}{|\mathbf{r}-\mathbf{r}'|^2}, \frac{3(y_m - y')^2}{|\mathbf{r}-\mathbf{r}'|^2} - 1, \frac{3(y_m - y')(z_m - z')}{|\mathbf{r}-\mathbf{r}'|^2} \\ \frac{3(x_m - x')(z_m - z')}{|\mathbf{r}-\mathbf{r}'|^2}, \frac{3(z_m - z')(y_m - y')}{|\mathbf{r}-\mathbf{r}'|^2}, \frac{3(z_m - z')^2}{|\mathbf{r}-\mathbf{r}'|^2} - 1 \end{pmatrix} \tag{3}$$

For the magnetic field vector and total magnetic intensity (TMI), the kernels are as follow:

$$\begin{pmatrix} k_{H_{total}} \\ k_{H_{TMI}} \end{pmatrix} = \begin{pmatrix} \frac{3(\mathbf{l}\cdot(\mathbf{r}-\mathbf{r}'))(\mathbf{r}-\mathbf{r}')}{|\mathbf{r}-\mathbf{r}'|^2} - \mathbf{l} \\ \frac{3(\mathbf{l}\cdot(\mathbf{r}-\mathbf{r}'))^2}{|\mathbf{r}-\mathbf{r}'|^2} - 1 \end{pmatrix} \tag{4}$$

So for the magnetic components:

$$\begin{pmatrix} k_{Hx} \\ k_{H\mathrm{y}} \\ k_{H\mathrm{z}} \end{pmatrix} = \begin{pmatrix} \dfrac{3(\mathbf{l}\cdot(\mathbf{r}-\mathbf{r}'))(x_m - x')}{|\mathbf{r}-\mathbf{r}'|^2} - l_x \\ \dfrac{3(\mathbf{l}\cdot(\mathbf{r}-\mathbf{r}'))(y_m - y')}{|\mathbf{r}-\mathbf{r}'|^2} - l_y \\ \dfrac{3(\mathbf{l}\cdot(\mathbf{r}-\mathbf{r}'))(z_m - z')}{|\mathbf{r}-\mathbf{r}'|^2} - l_z \end{pmatrix} \tag{5}$$

where l = (cos(I)cos(D-A), cos(I)sin(D-A), sin(I)), the inclination (I), declination (D) and azimuth (A) of the inducing magnetic field can be obtained from the International Geomagnetic Reference Field model (IGRF).

2.2 Parallel Inversion

We implement the Re-weighted Regularized Conjugate Gradient (RRCG) method in our parallel inversion. Regularization guarantees the result of ill-posed inversion problem plausible. Weighting function is chosen by the integrated sensitivity method.

The iteration algorithm of the RRCG method can be summarized in parallel numerical form as follow:

$$\mathbf{r}_n = \mathbf{i}_{par1}[N_{data}] - \mathbf{d} \tag{6}$$

$$\mathbf{l}_n^{\alpha} = \mathbf{j}_{par1}[M_{cell}] + \alpha_n(\mathbf{W}_m\mathbf{W}_e)^2(\mathbf{m}_n - \mathbf{m}_{ap\mathrm{r}}) \tag{7}$$

$$\beta_n^{\alpha_n} = \frac{||\mathbf{l}_n^{\alpha_n}||^2}{||\mathbf{l}_{n-1}^{\alpha_{n-1}}||^2}, \tilde{\mathbf{l}}_n^{\alpha_n} = \mathbf{l}_n^{\alpha_n} + \beta_n^{\alpha_n}\tilde{\mathbf{l}}_{n-1}^{\alpha_{n-1}}, \tilde{\mathbf{l}}_0^{\alpha_0} = \mathbf{l}_0^{\alpha_0} \tag{8}$$

$$k_n^{\alpha_n} = \frac{(\tilde{\mathbf{l}}_n^{\alpha_n}, \mathbf{l}_n^{\alpha_n})}{||\mathbf{i}_{par2}[N_{data}] + \alpha\mathbf{W}_m\mathbf{W}_e\tilde{\mathbf{l}}_n^{\alpha_n}||^2}, \mathbf{m}_{n+1} = \mathbf{m}_n - k_n^{\alpha_n}\tilde{\mathbf{l}}_n^{\alpha_n} \tag{9}$$

where n is the iteration number, rn is the residual vector, ln is the gradient direction, l̃n is the conjugate gradient direction, kn is the step length, and ipar1, ipar2 and jpar1 denote the output vector of the GPU parallel computing, d is the data vector, m is the model vector, α is the regularization parameter, Wd is the matrix of data weight, Wm is the matrix of the model weight, and We is the variable reweighting matrix.

The method of choosing weighting functions was discussed in many lectures [10–12], which is not included in this paper.

3 Examples

Our gravity and topography data is acquired from the website of Scripps institution of Oceanography, University of California, San Diego (UCSD), which has been gridded to $1' \times 1'$. The magnetic data is derived from an airborne survey by the AGRS, which has been gridded to 500×500 m. We implement the inversion using the same configuration in a midrange laptop as described in the previous section. All the results are acquired from the same laptop with a 2.5 GHz i7-4710HQ processor (4 cores), 16 GB of RAM, and discrete NVDIA GeForce GTX 860 M graphics processor based on Maxwell architecture (4 GB video memory and 640 CUDA cores).

Figure 2 shows the 3D inversion structure of density and susceptibility. There is mainly a strip-shaped NE-trending high anomaly in both density and susceptibility distribution, which indicates the Circum-Pacific tectonic domain. The high susceptibility and density anomalies in the south section are caused by the wedge-shaped and lens-shaped iron polymetallic ore in Huanggang deposit. The high susceptibility anomalies in the northeast part are caused by granodiorite and magnetic minerals in Longtoushan deposit. In the Shijiangshan district, there is a low-amplitude high anomaly in the middle of the susceptibility distribution, which is caused by the magnetic Mesozoic strata. In general, our inversion result shows a good agreement with geological settings.

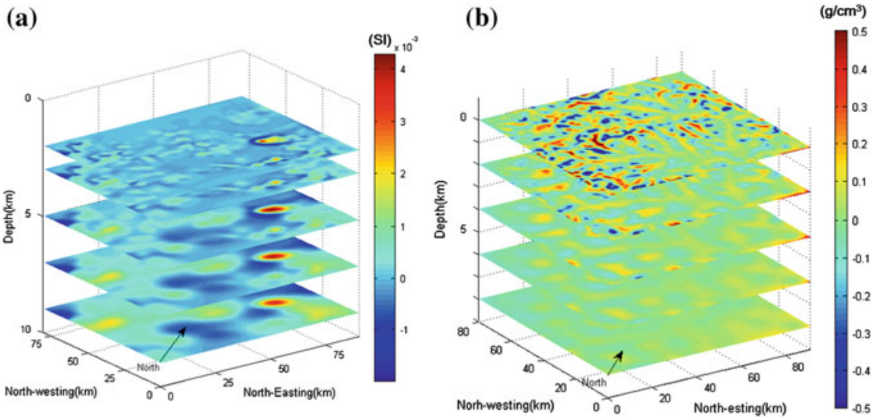

Fig. 2 The 3D Sliced view of **a** susceptibility model and **b** density model of inversion result

4 Conclusions

We utilized a parallel inversion of 91.8 million cells inversion in a 92 × 80 km region, which took several hours. The 3D geophysical model, typical profile and deposit is interpreted respectively.

Optimizations were applied to insure traditional parallel computing skills that commonly used in clusters effective, meanwhile, our new strategies solved the shared memory and computation limits of GPU in PCs. The new method enables us to get an overview of geophysical properties (density and magnetic susceptibility) without using clusters or taking too much computing time.

Acknowledgment Li thanks the China Scholarship Council (CSC) for supporting the joint Ph.D. Training Program and the Consortium for Electromagnetic Modeling and Inversion (CEMI), University of Utah.

References

1. LIU, J., YE, J., LI, Y., CHEN, X. and ZHANG, R., 2001. A Preliminary Study on Exhalative Mineralization in Permian Basins, the Southern Segment of the Da Hinggan Mountains, China–Case Studies of the Huanggang and Dajing Deposits–. Resource Geology, 51(4), pp. 345–358.
2. Chen, Z., Meng, X., Guo, L. and Liu, G., 2012. GICUDA: A parallel program for 3D correlation imaging of large scale gravity and gravity gradiometry data on graphics processing units with CUDA. Computers & Geosciences, 46, pp. 119–128.
3. Lin, W., Zhang, J. and Li, J. 3D inversion of gravity anomaly with GPU in the Mesozoic residual basins of Nansha Thitu Island and reefs area [J] (in Chinese). JOURNAL OF TROPICAL OCEANOGRAPHY, 2013, 32(4): 36–42.
4. Čuma, M., Wilson, G.A. and Zhdanov, M.S., 2012. Large-scale 3D inversion of potential field data. Geophysical Prospecting, 60(6), pp. 1186–1199.
5. Čuma, M. and Zhdanov, M.S., 2014. Massively parallel regularized 3D inversion of potential fields on CPUs and GPUs. Computers & Geosciences, 62, pp. 80–87.
6. Gross, L., Altinay, C. and Shaw, S., 2015. Inversion of potential field data using the finite element method on parallel computers. Computers & Geosciences, 84, pp. 61–71.
7. Akimova, E.N., Belousov, D.V. and Misilov, V.E.E., 2013. Algorithms for solving inverse geophysical problems on parallel computing systems. Numerical Analysis and Applications, 6 (2), pp. 98–110.
8. Cox, L.H., Wilson, G.A. and Zhdanov, M.S., 2010. 3D inversion of airborne electromagnetic data using a moving footprint. Exploration Geophysics, 41(4), pp. 250–259.
9. Zhdanov, M.S., Smith, R.B., Gribenko, A., Cuma, M. and Green, M., 2011. Three-dimensional inversion of large-scale EarthScope magnetotelluric data based on the integral equation method: Geoelectrical imaging of the Yellowstone conductive mantle plume. Geophysical Research Letters, 38(8).
10. Li, Y. and Oldenburg, D.W., 1996. 3-D inversion of magnetic data. Geophysics, 61(2), pp. 394–408.
11. Li, Y. and Oldenburg, D.W., 1998. 3-D inversion of gravity data. Geophysics, 63(1), pp. 109–119.
12. Zhdanov, M.S., Ellis, R. and Mukherjee, S., 2004. Three-dimensional regularized focusing inversion of gravity gradient tensor component data. Geophysics, 69(4), pp. 925–937.
13. Boulanger, O. and Chouteau, M., 2001. Constraints in 3D gravity inversion. Geophysical Prospecting, 49(2), pp. 265–280.

A Fast Topographic Correction Method for TEM Data

Guoqiang Xue, Weiying Chen, Jiangwei Cui and Shu Yan

Abstract Topography affects electromagnetic data and leads to wrong interpretation of shallow resistivity layers. In this paper, we propose a new method for correcting topographic error in electromagnetic data. In order to achieve this, we used a small DC configuration to obtain the surface resistivity, and then used the surface resistivity to construct a new topographic correction formula. Both synthetic and field TEM and CSAMT data were processed using this method. The results show that our method is a fast, effective and practical tool for correcting topographic effects in electromagnetic data.

Keywords Topographic correction · TEM · CSAMT

1 Introduction

Data obtained when electromagnetic method is used in a mountainous area includes topographic anomaly and useful anomaly. The presence of the topographic anomaly interferes with data interpretation [1–3]. The ratio correction method has been found to be a classic correction method for topographic effect. In previous years, topographic effects were corrected with physical simulation methods where sink, soil groove, conducting paper were used to obtain pure topographic effect. However, with the development of computer technology, 2D and 3D forward modeling has become the main methods of obtaining pure topographic anomaly. 2D and 3D forward and inversion of pure topographic effects have strong simulating capability, which requires a large memory capacity and high speed computers [3]. Thus, from a practical stand point, with development of numerical forward modeling and inversion, it is meaningful to eliminate topographic effects using

---

G. Xue (✉) · W. Chen · J. Cui
Institute of Geology and Geophysics, Chinese Academy of Sciences, Beijing, China

S. Yan
School of Computer Science and Telecommunication Engineering, Jiangsu University, Zhenjiang, China

Q. Di et al. (eds.), *Technology and Application of Environmental and Engineering Geophysics*, Springer Geophysics,
DOI 10.1007/978-981-10-3244-8_15

different methods and techniques so as to have diversity in electromagnetic data interpretation. In this paper, we used numerical simulation to replace actual standard resistivity with the resistivity of homogeneous half-space. Since it is known that topographic effects reduces with lower frequency, frequency point change rate and time trace can be used as correction coefficient to realize topographic correction based on actual data and this is known as the ratio correction method. The new ratio correction method involves less work, it is also fast and easy to implement. The results obtained from correction example indicates that the new ratio correction formula is effective.

2 Analysis of Topographic Effect

As shown in Fig. 1, the intensity of electric field is proportional to the current density;

$$\boldsymbol{J} = \sigma \boldsymbol{E} \tag{1a}$$

Voltage of electric field is proportion to electric field intensity;

$$V = \int_{l} \boldsymbol{E} \cdot \mathrm{d}\boldsymbol{l} \tag{1b}$$

Thus, the amplitude of voltage is opposite to the change in topography.

When Transient vortex field is induced by low-resistivity body, the observed voltage, that is, EMF (Electromotive Force) will increase when resistivity increases. The vortex field is relatively small and EMF will decrease when resistivity decreases. Resistivity represents EMF with opposite size, that is change in resistivity and topography are in-phase, resistivity increases in higher region while it decreases in lower region, which is a different characteristic when compared with frequency-domain survey and direct-current prospecting. However, they are the same in nature because they all observe the change in voltage amplitude that results from divergence effect and influx effect of current line. The main purpose of the

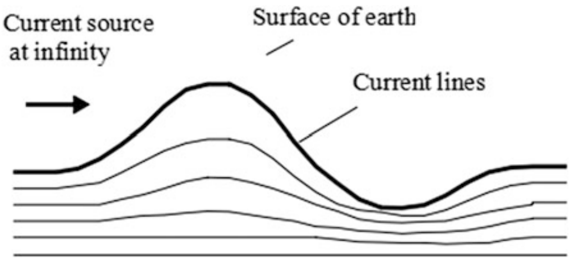

Fig. 1 The gathering and diverging effect of topography to current

Fig. 2 The topographic influence on central loop TEM data (600 m × 600 m)

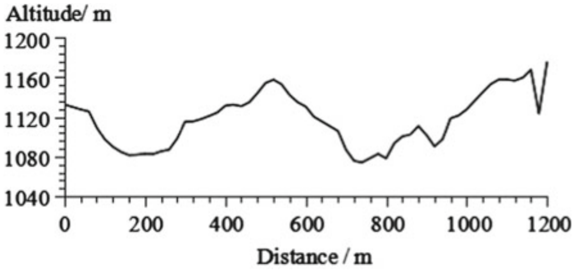

(a) Topography

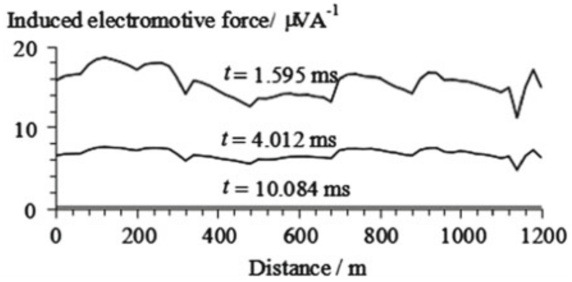

(b) Measured EMF curves

topographic effect analysis is to define a criterion to judge to which extent EM data is affected by the undulating terrain.

Figure 2a shows the topographical profile graph of L14 using central loop TEM in Huangling coal mine, Shan Xi province. While Fig. 2b shows the measured EMF curves at early, middle and late stages. Topographic undulation, electric field change and EMF along survey the line indicates that: since the EMF curve bulges concavely and it sinks in convexly, EMF will change acutely in regions where topography changes acutely. With decrease in frequency or exiting from early stage to late stage, topographic effect becomes weak. Thus, in mountainous electromagnetic exploration, receiver layout point should be in the flat region. However, total effect of undulating terrain always exists, making correction very necessary.

3 Ratio Correction Method

Classic ratio correction formulas have the same forms in time domain. And apparent resistivity is used as the correction constant.

$$\rho_{\text{correctd}}(i) = \frac{\rho_{\text{measured}}(i)}{\frac{\rho^{\text{pure}}_{\text{topography}}(i)}{\rho_1}} \tag{2}$$

In this formula, $\rho_{\text{correctd}}(i)$ and $\rho_{\text{measured}}(i)$ are all corrected and measured apparent resistivity (it is obtained by converting the measured data). $\rho^{\text{pure}}_{\text{topography}}(i)/\rho_1$ is pure topography anomaly, that is, the response of isotropic earth whose resistivity is ρ_1, where i denotes polar moment or frequency point. Formula (2) indicates that if the resistivity increases n times with topographic effect, we can calculate it using numerical simulation:

$$n = \frac{\rho^{\text{pure}}_{\text{topography}}(i)}{\rho_1}$$

Resistivity can be returned to its normal value when the measured value is divided by n. Conversely, if the apparent resistivity decreases n times:

$$\frac{1}{n} = \frac{\rho^{\text{pure}}_{\text{topography}}(i)}{\rho_1}$$

Similarly, resistivity can be returned to its normal value when the measured value is multiplied by n.

In order to avoid having to do large work on 2D and 3D numerical forward modeling for ratio correction and geodetic work results without topographic correction, a new ratio correction formula that uses measured data itself is proposed according to classic formula (2) correction theorem.

$$\rho_{\text{correctd}}(i) = \frac{\rho_{\text{measured}}(i)}{\frac{\rho_{\text{measured}}(1)}{\rho_{\text{standard}}}} C(i) \tag{3}$$

In this formula, frequency point 1 changes from high frequency to low frequency. And the differences between formula (3) and classic ratio correction formula (2) are given below:

① Using measured laboratory value from small polar distance direct current survey method to obtain the standard resistivity ρ_{standard} of shallow layer instead of homogenous half-space resistivity ρ_1 in formula (2). If the resistivity is homogenous on the surface of the measured region, the highest frequency in high frequency asymptote can be considered as the standard resistivity of each point.

The aim of the small polar observation is to avoid topographic effects and to provide criterion for correction. Appropriate polar distance can be chosen to conduct observation, when polar distance decreases to a level small to the extent that change in resistivity can be ignored, then topographic effects can be ignored.

② A $\rho_{\text{measured}}(1)$ affected by topography at highest frequency resistivity point is used to replace the pure topography resistivity in numerical forward modeling.

③ Topographic effects reduces and later vanishes with increase in frequency. Assuming that this process is linear, the slope of topographic change effects between frequency points can be calculated by linear interpolation, $C(i)$ can be used as coefficient instead of using $i-1$ pure topography resistivity which is needed for numerical forward modeling.

$$C(i)=\frac{\rho_{\text{measured}}(1)/\rho_{\text{standard}}(i)-1}{f(N)-f(1)}[f(i)-f(1)]+1 \tag{4}$$

In this formula, $f(j)$ is frequency and its values range between $1\sim N$ from high frequency to low frequency.

For TEM, coefficient $C(i)$ is:

$$C(i)=\frac{\rho_{\text{measured}}(1)/\rho_{\text{standard}}(i)-1}{t(N)-t(1)}[t(i)-t(1)]+1 \tag{5}$$

In which, $t(i)$ is time channel and its number ranges between $1\sim N$ from early stage to late stage.

The accuracy of coefficient $C(i)$ can be enhanced by increasing the frequency point or time channel.

The Correlation between the field from oscillating dipole and the field from a charge in acceleration motion and uniform motion has been established. As mentioned above, a dipole is a pair of equivalent charges with opposite polarities in periodic motion. When the antenna element is electrified by an alternating current, its charge will be accelerated and produce elemental electric current that induces electromagnetic field in the surrounding space. Therefore, if the antenna element is electrified with step current, there should also be some correlation between the field from transient dipole and the field from a moving charge.

In classic electromagnetic theory, transient field is obtained by performing frequency-time transform on the harmonious field. Hence, in this section we have provided the derivation of transient electric dipole field in details.

4 Field Example for Correction of TEM Measured Data

The land surface at Huangling coal mine in Shan Xi province is loess erosion landform, and the underlying layer is gentle and stable. The size of central loop in this example was 600 m × 600 m, receiver area was 100 m^2, while the observation time-period was 30 ms with 20 channels. Figure 3a is the topographical profile graph along the line. For a clear expression, actual TEM apparent resistivity profile graph (Fig. 3b) used time channels $t = 0.318\,\text{ms}$, $t = 0.504\,\text{ms}$, $t = 1.005\,\text{ms}$,

$t = 15.985$ ms and so on. Table 1 lists resistivities of each measured point using direct resistivity method with small polar-distance, which was used as standard resistivity in formula (3). Notice that TEM apparent resistivity is in-phase with topography (Fig. 3a), meaning the apparent resistivity decreases when topography

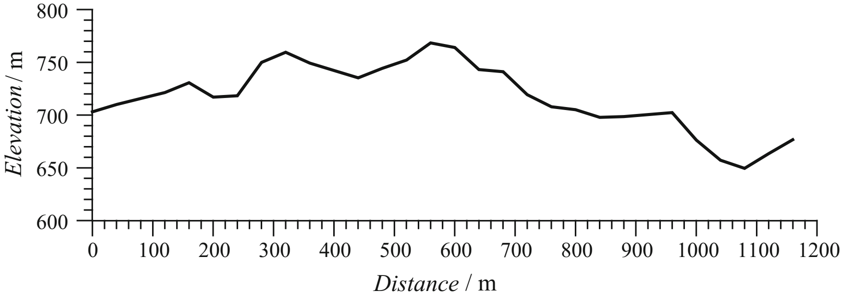

(a) Topography profile

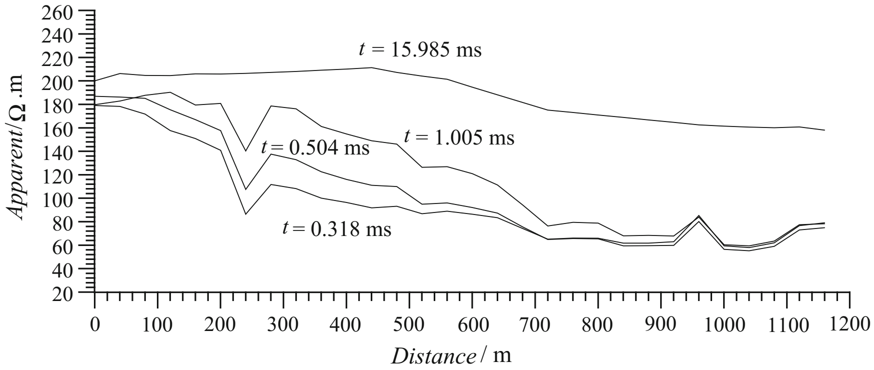

(b) Apparent resistivity curves before correction

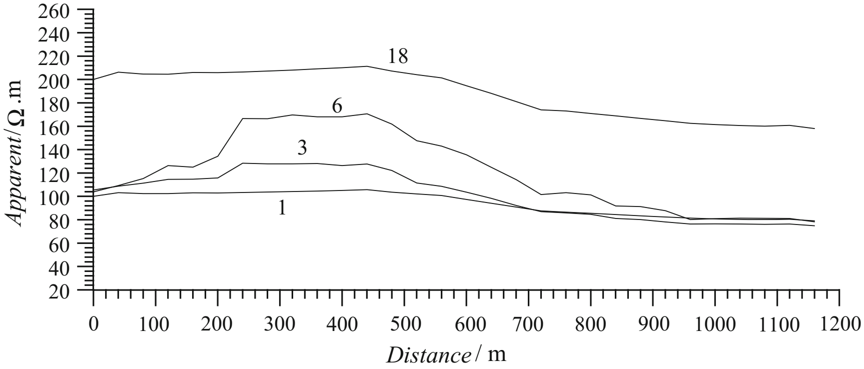

(c) Apparent resistivity curves after correction

Fig. 3 Topographic correction of field data

Table 1 Resistivity measurements using DC configuration

Measurement point/m	Resistivity/Ω m	Measurement point/m	Resistivity/Ω m
0	100.00	600	97.250
40	103.10	640	94.000
80	102.26	680	90.750
120	102.25	720	87.500
160	102.95	760	86.500
200	102.89	800	85.400
240	103.20	840	84.400
280	103.60	880	83.350
320	104.00	920	82.300
360	104.50	960	81.242
400	105.00	1000	80.700
440	105.62	1040	80.250
480	103.55	1080	80.000
520	102.00	1120	80.325
560	100.64	1160	79.000
560	100.64	1160	79.000

descends, it increases when topography ascends, and it changes acutely when topography changes acutely (as seen at distance 240 m and at distance 960 m in Fig. 3b). Based on acknowledged TEM response characteristics, we know that topographical effect disappears at time $t = 15.985\,\text{ms}$, so using times $t(1) = 0.318\,\text{ms}$, $t(N) = 15.985\,\text{ms}$ from the measured data and Table 1, serving as the standard resistivity of surface resistivity, we substituted it into formulas (3) and (5). And we obtained the corrected TEM apparent resistivity profile (Fig. 3c). Figure 3 indicates that besides pure topography response, measured TEM apparent resistivity also adds to changes in geological structures.

5 Conclusion

We have proposed in his paper, a new fast correction formula for correcting topographical effects on electromagnetic data. In the process of applying this correction method, measurement of topography altitude is unnecessary except at measurement points. This new method is similar to classic correction method where only topographical effects are corrected but the response of geological structure is retained.

References

1. Haber E, Oldenburg D W, Shekhtman R. 2007. Inversion of time domain three-dimensional electromagnetic data. Geophysical Journal International, 171(2): 550–564.
2. Hördt A, Müller M. 2000. Understanding LOTEM data from mountainous terrain. Geophysics, 65(4): 1113–1123.
3. Leppin M. 1992. Electromagnetic modeling of 3-D sources over 2-D inhomogeneities in the time domain. Geophysics, 57(8): 994–1003.

Distinguishing Multi-layer Mined-Out Area Through TEM

Shu Yan, Guoqiang Xue and Weizhong Qiu

Abstract Loop TEM has over the years played important role in detecting single water-filled goaf. In order to exploit deep coal beds, the investigation of multi-layer aquifer became an important new task for coalfield hydro-geophysical prospecting using TEM. Because it has become necessary to modify the traditional interpretation technology. In this paper, based on the numerical calculation of typical horizontal layered earth model, the feasibility of probing multi-layer aquifers was analyzed. Secondly, while fitting inversion to TEM sounding curves, the number of layers was supposed to be equal to the number of time channel. Multi-layer aquifers were detected using central loop TEM in Shanxi Province. The exploration result has been validated by borehole drilling. This study shows that it is feasible to detect multi-layer aquifers with central loop TEM technique.

Keywords TEM · Multi-layer · Mined-out area

1 Numerical Simulation and Characteristic Analysis of Multi-layer Mined-Out Area Response

1.1 The Model Design of Multi-layer Mined-Out Area

The coal strata and deeper mined-out area constitute a geoelectric model where the layers with high resistivity are interbedded with the layers with low resistivity. Table 1 contains the list of average parameters for the classic geoelectric model

---

S. Yan (✉)
Jiangsu University, Zhenjiang, China

G. Xue
Institute of Geology and Geophysics, CAS, Beijing, China

W. Qiu
115 Coal Geological Exploration Institute, Datong, China

Q. Di et al. (eds.), *Technology and Application of Environmental and Engineering Geophysics*, Springer Geophysics,
DOI 10.1007/978-981-10-3244-8_16

Table 1 Classic geoelectric model of the measured coal strata (model 0)

Sequence	Lithology	Resistivity (Ω m)	Thickness (h/m)	Depth (d/m)
1	Loess	30	30	30
2	Sandstone	80	45	75
3	Coal 1	300	5	80
4	Sandstone	120	45	125
5	Coal 2	300	3	128
6	Sandstone	120	45	173
7	Coal 3	300	3	176
8	Sandstone	120	45	221
9	Coal 4	300	3	224
10	Sandstone	120	45	269
11	Coal 5	300	3	272
12	Sandstone	120	45	317
13	Coal 6	300	3	320
14	Sandstone	120		

Table 2 Geoelectric model for mined-out area 1 (model 1)

Sequence	Lithology	Resistivity (Ω m)	Thickness (h/m)	Depth (d/m)
1	Loess	30	30	30
2	Sandstone	80	45	75
3	Mine-out 1	5	5	80
4	Sandstone	120	45	125

(the model 0) that is a type of North China coalfield. The Norh China Coalfield is composed of 13 electric layers in total including loess, sandstone and coal. Also, there are 6 coal seams marked as coal seam 1, coal seam 2…, and coal seam 6 respectively.

In order to conveniently compare the detectability of multi-layer mined-out area, the whole model shown in Table 1 is divided into 7 geoelectric models based on the coal seams contribution. In the 7 models, all coal seams in Table 1 are assumed as seeper mined-out areas and the resistivity changes from 300 to 5 Ω m. Furthermore, Table 2 and 3 contains the geoelectric model parameters of mined-out

Table 3 Geoelectric model for mined-out area 2 (model 2)

Sequence	Lithology	Resistivity (Ω m)	Thickness(h/m)	Depth (d/m)
1	Loess	30	30	30
2	Sandstone	80	45	75
3	Mine-out 1	5	5	80
4	Sandstone	120	45	125
5	Mine-out 2	5	3	128
6	Sandstone	120	45	173

area 1 and mined-out area 2 (model 1 and model 2) respectively. And model 3 to model 6 were formed using Table 2.

1.2 Model Calculation and Analysis of Multi-layer Mined-Out Area

1D forward calculation was done for the 7 geoelectric models containing different mined-out numbers respectively (Fig. 1). However, the induction electromotive force (emf) curves were uplifted with increase in low resistivity of thin layer. And in the actual exploration, it is possible to detect, if the difference between the curves is greater than the difference between the receiver sensitivity and measured data [1–3].

In order to distinguish between the curves, the flowing error formation was used to calculate the error.

$$d_i = \frac{2|emf_{ki} - emf_{li}|}{(emf_{ki} + emf_{li})} \times 100\% \tag{1}$$

The subscripts of emf_{ki} and emf_{li} represent the i-th time channel and k, l represents k, and represents l layer seeper.

The formation (1) is used to calculate the difference between various curves and the result is presented in Table 4. The difference between various curves decreases gradually with increasing low resistivity water containing. The two final curves has error values of up to 6.52% between curve 5–6.

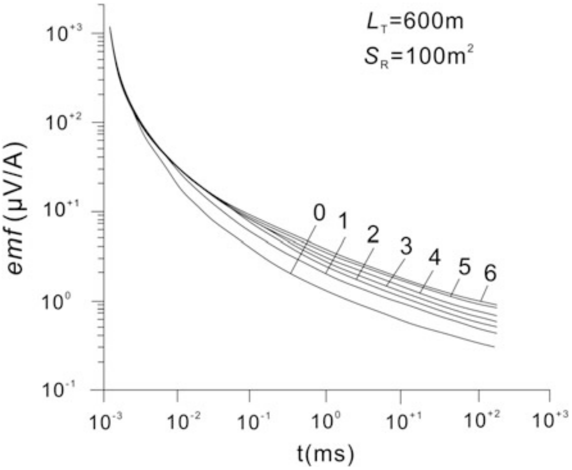

Fig. 1 The forward curve of multi-layer coal mined-out area 0: 0 coal mined-out area curve; 1:1 coal mined-out area curve; 2:2 coal mined-out area curve; 3:3 coal mined-out area curve; 4:4 coal mined-out area curve; 5:5 coal mined-out area curve; 6:6 coal mined-out area curve

Table 4 Forward curve difference table of multi-layer coal mined-out area seeper model

Time ms	Curve 1–2 $d_{1-2\%}$	Curve 2–3 $d_{2-3\%}$	Curve 3–4 $d_{3-4\%}$	Curve 4–5 $d_{4-5\%}$	Curve 5–6 $d_{5-6\%}$
0.05	0.03	0.00	0.00	0.00	0.00
0.07	0.25	0.00	0.00	0.00	0.00
0.10	1.14	0.04	0.00	0.00	0.00
0.14	2.91	0.30	0.01	0.00	0.00
0.19	4.79	1.03	0.10	0.00	0.00
0.25	5.75	2.16	0.42	0.04	0.00
0.32	5.45	3.25	1.01	0.19	0.02
0.4	4.11	3.82	1.74	0.51	0.09
0.49	2.10	3.70	2.37	0.96	0.27
0.59	0.26	2.96	2.67	1.43	0.57
0.70	2.70	1.76	2.59	1.82	0.88
0.82	5.13	0.30	2.13	1.96	1.21
0.95	7.41	1.26	1.38	1.87	1.43
1.09	9.47	2.85	0.40	1.59	1.50
1.24	11.3	4.38	0.62	1.10	1.44
1.40	12.9	5.87	1.68	0.44	1.22
1.57	14.3	7.23	2.72	0.32	0.86
1.75	15.5	8.42	3.81	1.03	0.37
1.94	16.5	9.55	4.85	1.76	0.11
2.14	17.2	10.5	5.78	2.55	0.66
2.35	17.9	11.2	6.60	3.33	1.24
2.57	18.5	11.9	7.30	4.12	1.82
2.80	18.9	12.7	8.10	4.67	2.41
3.04	19.1	13.2	8.75	5.42	3.03
3.29	19.1	13.8	9.47	5.87	3.42
3.55	19.7	13.9	9.96	6.57	3.96
3.82	19.0	14.5	10.31	6.93	4.47
4.10	19.3	14.4	10.8	7.26	5.08
4.39	19.0	14.5	11.4	7.68	5.46
4.69	18.9	15.0	11.4	8.45	5.72
5.00	19.5	15.4	11.2	8.49	6.52

2 The Detection Experiment

The mined-out areas mainly contribute to 2#, 8#, 11# coal seams at the Shanxi mine area and each layer may contain water. For this experiment, the Terra TEM which was made in Australia was used. It has an Emission current value of 7.6 A and an equivalent receiver coil area of 100 m^2. The vertical component of the magnetic field was observed in the 200 m × 200 m area with a center loop transmitter.

2.1 Qualitative Analysis of the Measured Curves

Figure 2 shows the measured curve of L185 at one minefiled. The emf is divided into 3 clusters along each line of: 940–1240 points, 1260–1540 points and 1560–1860 points. The emf lifts gradually along lines in each curve, which shows that resistivity is steep (adjacent cluster) and progressively (inner cluster) decreases. If resistivity decreases segmentally it implies that the layer number of mined-out seeper areas increases. And can be speculated that each step changes a layer and that the seeper of each horizon also increases. That is,

$$n = m \tag{2}$$

2.2 Fitted Inversion of Measured Curve

The setting number used for reversion fitting was less in the past and meticulous degree of the generated resistivity-depth profile was not enough. In fact, the number of layers can be equal to time channels used for the inversion with generalized inverse matrix of fitted curves in order to get more precise information [4–7].

Figure 3a shows the comparison between the measured curve and the fitted curve and Fig. 3b is L185 resistivity-depth profile generated by inversion. The fitted difference is 10.6%. It is speculated that: 940–1240 is 2# mined-out water on L185 line, 1260–1540 is 2#, 8# mined-out water and 1560–1860 is 2#, 8#, 11# mined-out water respectively. Finally, the borehole data obtained at point 1780 proved that there are three layers of water.

Fig. 2 The measured curve of L185 at one mine field

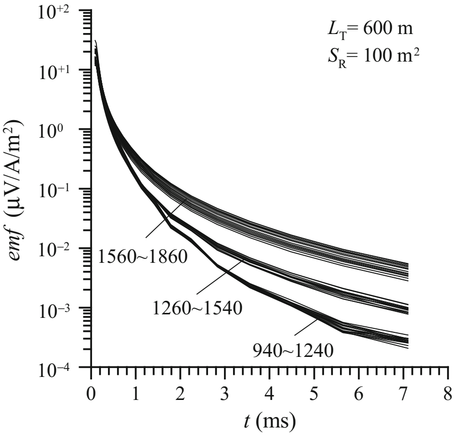

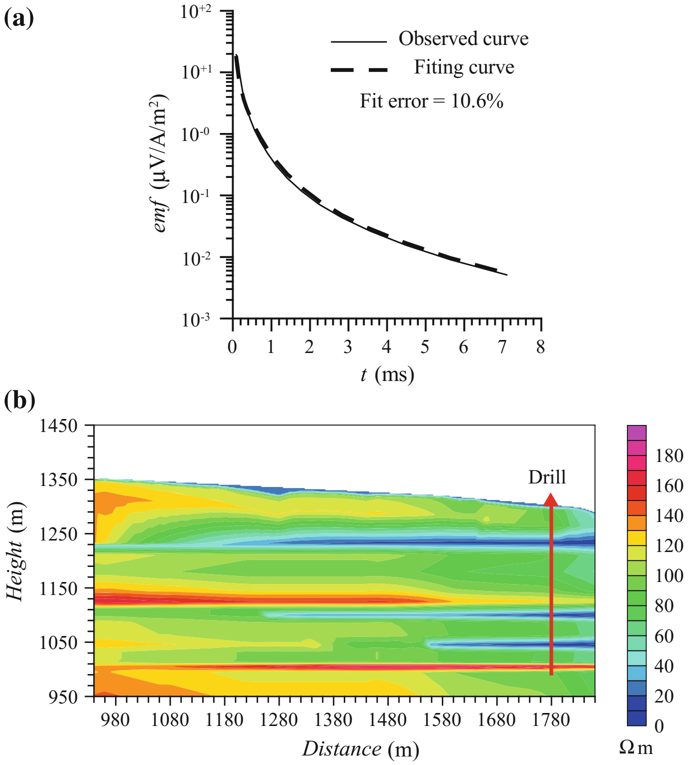

Fig. 3 The fitted inversion resistivity-depth profile of L185 line at one mine area of Shanxi

3 Conclusions

The multi-layer water-filled goaf can be distinguished when the electromagnetic response outliers are greater than receiver and noise sensitivities. In the fitted inversion curves, the resistivity-depth profile is formed when the number of layers equals to time channel, which improves the inversion longitudinal resolution. Also, in the investigation of multi-layer aquifers, the anomaly of lower strata is weak because it is shielded by the upper low resistivity layer. However, with the improvement of production, noise interference in the mining area will be more challenging. Hence, another important area of concern will be the improvement of signal to noise ratio and extraction of weak signal.

References

1. Chen, M. S., and Yan, S., 1995, Problems on application of frequency soundings, Beijing: Geological Publishing House, 36–37.
2. Nabighian, M. N., 1992, Electromagnetic methods in applied geophysics, Volume 1, Theory. Society of Exploration Geophysics.
3. Kaufman, A. A., and Keller, G. V., 1983, Frequency and transient soundings, New York: Elsevier Science Publishing Company Inc., 545–551.
4. Li, X, 2002, Theory and application of transient electromagnetic method. Xi'an: Shaanxi science and Technology Press, 29–35.
5. Macnae, J., and Mutton, A., 1996, Can sulphides be discriminated from conductive states? A case history at Dugald River. Exploration Geophysics, 27(2/3), 119–130.
6. Shi, X. X., Yan, S., and Chen, M. S., 2005, Study on screening of conductive bed in transient electromagnetic prospecting, Journal of China Coal Society, 30(2), 160–163.
7. Smith, R., 2013, Using combinations of spatial gradients to improve the detectability of buried conductors below or within conductive material, Geophysics, 78(1), E19–E31.

Bias in Transient Electromagnetic Method Due to Non-rectangular Loop

Nannan Zhou, Guoqiang Xue, Dongyang Hou, Huasen Zhong, Hai Li, Jiangwei Cui and Kang Chen

Abstract Rectangular loop is one of the most popular transient electromagnetic (TEM) devices, which is widely used in engineering, hydro-geological and ore deposit exploration. However, in theory, circular loop is used to approximately simulate the rectangular loop. Traditionally, this gives rise to a series of problems. Meanwhile, in practice, the rectangular loop is not easy to layout on field especially in complex terrains or mountainous areas. Therefore, we have modified the rectangular loop. The geometry of the loop may now be arbitrarily named, modified-rectangular loop. However, some bias will be caused if standard rectangular-loop parameters are used to invert the field data from modified rectangular loop. And this bias lowers the detection precision of the modified rectangular loop. Therefore, the bias caused by the approximation of circular and modified rectangular loop is analyzed in this paper. Firstly, the response distribution and bias between circular loop and rectangular loop are compared using induced voltage and primary field. Then, the forward method of vertical magnetic field from modified rectangular loop based on coordinate transformation is given. The bias between rectangular loop and modified rectangular loop are then analyzed using vertical magnetic field. From theoretical modeling that there is an indication that changing the loop geometry will result in some error and lower the detection precision.

Keywords Circular loop · Rectangular loop · Modified rectangular loop · Bias · TEM

N. Zhou (✉) · G. Xue · D. Hou · H. Zhong · H. Li · J. Cui · K. Chen
Key Laboratory of Mineral Resources, Institute of Geology and Geophysics,
CAS, Beijing, China

Q. Di et al. (eds.), *Technology and Application of Environmental and Engineering Geophysics*, Springer Geophysics,
DOI 10.1007/978-981-10-3244-8_17

1 Introduction

Rectangular-loop TEM has been widely used in shallow engineering investigation, hydro-geological survey and ore prospecting. In earlier times, the response of circular loop is used to simulate that of rectangular loop for the dual Bessel integral expression of circular-loop response because rectangular loop response is not easy to obtain. For central point, there is a subtle difference between circular loop and rectangular loop with equal magnetic moment [1]. However, for the non-central points, some computational error is caused by using circular loop to simulate rectangular loop. Thus, it is not reasonable to simulate the response of rectangular loop using that of circular loop.

In recent years, the vertical magnetic field of rectangular loop is calculated using linear integration of electric dipole or surface integration of magnetic dipole [2, 3]. We present in this paper the forward modeling method of induced voltage and primary field for circular loop and rectangular loop. We also present the analysis of relative difference r between the response of circular loop and rectangular loop from the aspects of response distribution and difference variation with time.

For the modified rectangular loop, the vertical magnetic field was calculated in transformed coordinate system. The bias between modified rectangular loop and rectangular loop was analyzed, and verified by the apparent-resistivity-depth section of the theoretical model.

2 Bias of Primary Field Due to Circular Approximation of Rectangular Loop

Rectangular-loop size was set as 177.25 × 177.25 m while the radius of the circular loop was 100 m carrying a current of 10A. The distribution of the fields on surface is shown in Fig. 1. Figure 1a shows the distribution of primary field

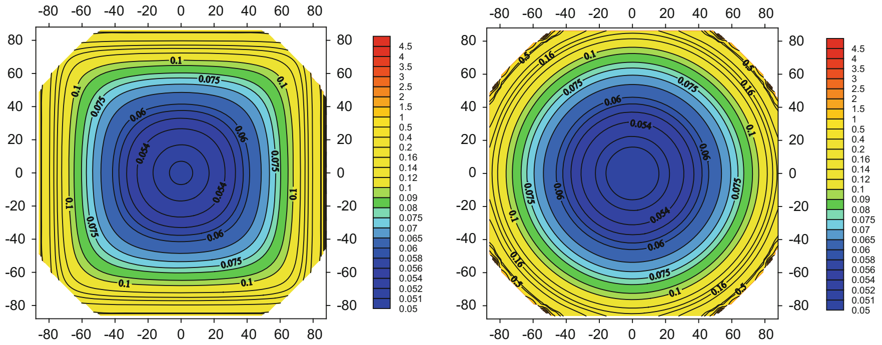

(a) rectangular loop (b) circular loop

Fig. 1 Distribution of primary fields for circular and rectangular loop

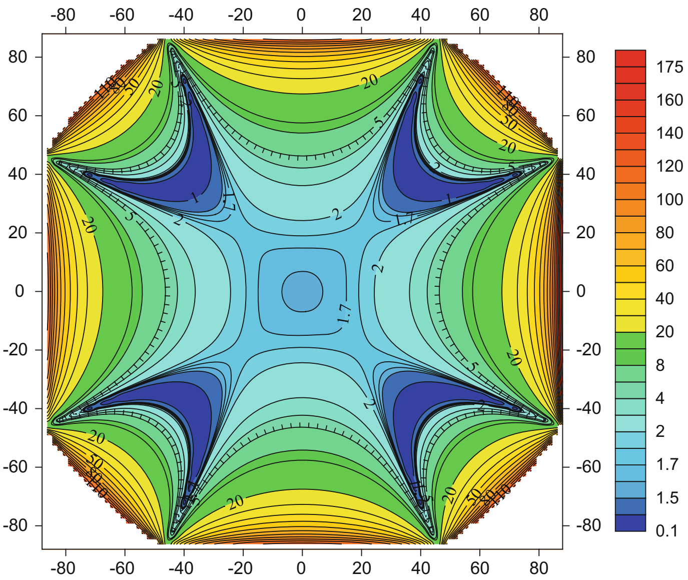

Fig. 2 Distribution of relative difference between circular loop and rectangular loop

generated by the rectangular loop. The response value increases from center to side significantly, and the field is axially symmetric in the loop. Figure 1b displays the distribution of primary field generated by circular loop. Unlike the field distribution of rectangular loop, the field of circular loop is centrally symmetrical.

In order to better understand the difference between these two sources, we calculate the relative difference using formula (1).

$$Err = 2\left|\frac{V_{Cir} - V_{\mathrm{Rec}}}{V_{Cir} + V_{\mathrm{Rec}}}\right| \times 100\% \tag{1}$$

The distribution difference is shown in Fig. 2. As seen in Fig. 2, there is relative small value, which is smaller than 5% around center point. The distribution difference increases from center to side. However, the minimum value is not existent in the center point. Therefore, there is no universal rule to analyze the difference between circular loop and rectangular loop.

3 Bias of Induced Voltage Due to Circular Approximation of Rectangular Loop

3.1 Distribution at Different Times

The distribution of induced voltage at 1e-6s is shown in Fig. 3. Although, only the overlapped parts of the two loops are given.

As shown in Fig. 3a, b, the distribution of induced voltage around the center of rectangular loop is circular at 1e-6s. The shape of isolines changes to rectangular when the receiver point is far away from the center. But for the circular loop, the isoline shape is circular for large and small-offset points in loop at 1e-6s. Similar distribution occurs at 1e-5s (Fig. 3c, d). The distribution of induced voltage for the two loops at 1e-4s is the same, i.e. the two sources have equal field at late time.

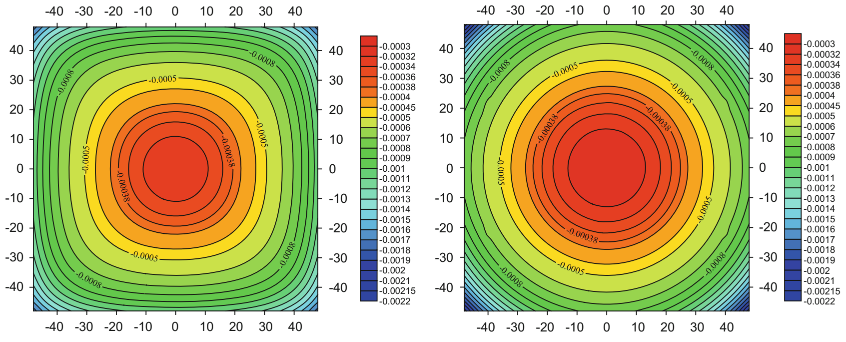

(a) response of rectangular loop at 1e-6s

(b) response of circular loop at 1e-5s

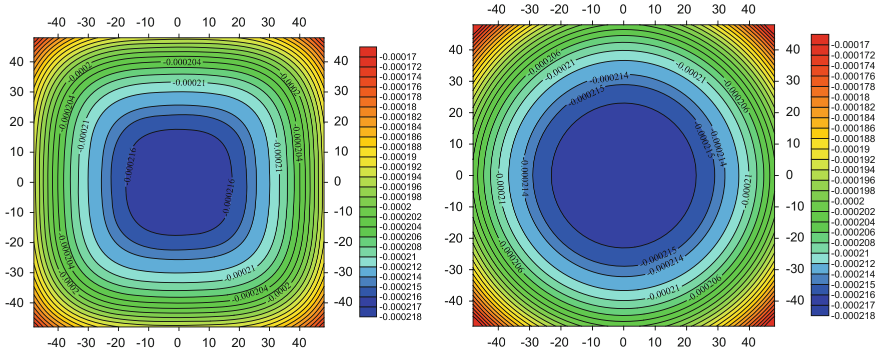

(c) response of rectangular loop at 1e-5s

(d) response of circular loop at 1e-5s

Fig. 3 Distribution of relative differences between circular loop and rectangular loop

3.2 Relative Error Distribution

To be able to better comprehend the relative differences, x the relative difference between the two sources were calculated using formula (1). As shown in Fig. 4, the minimum difference value does not exist at the center of the loop. Thus, the approximate simulation of the rectangular loop using circular loop is not reasonable at early time. Especially, since the maximum difference occurs at 1e-4s which is the center of the loop.

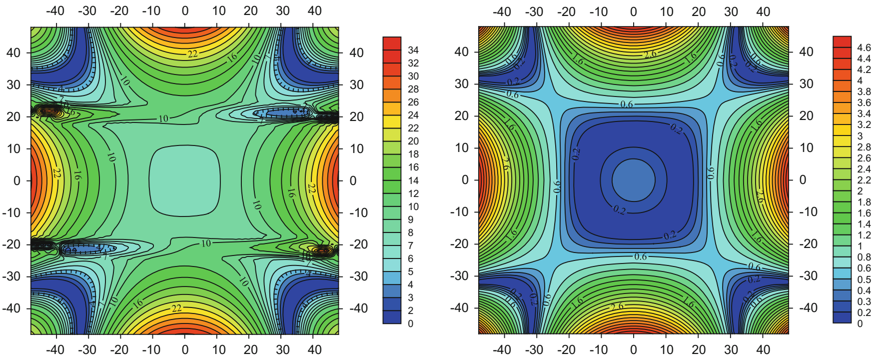

(a) 1e-6s (b) 1e-5s

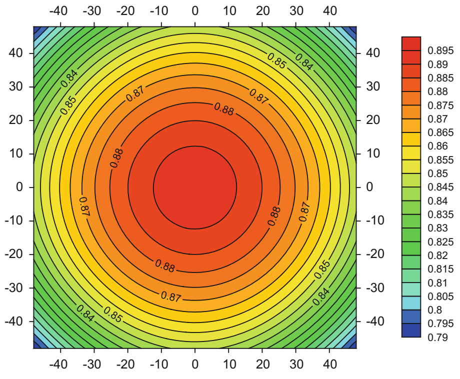

(c) 1e-4s

Fig. 4 Distribution of relative difference at different times

4 Bias in Time-Domain Due to Modified-Rectangular Loop

According to the rectangular loop forward modeling method of, the modified rectangular loop response can also be calculated using electric dipole superimposing method. Each side of the loop will be an individual coordinate system. So, the coordinate system transformation will be used.

Figure 5 shows the sketch map of modified rectangular, convex and indent loops. The perimeter of the modified rectangular loop is the same with that of

Fig. 5 Sketch map of modified rectangular loop

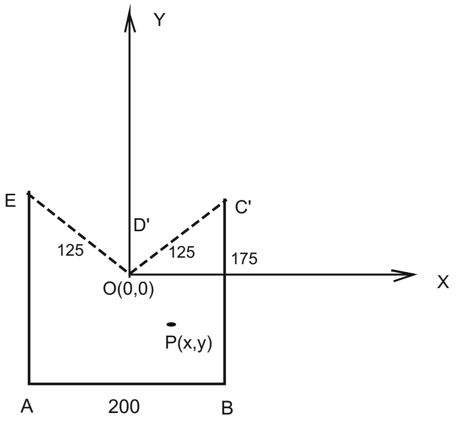

(a) indent loop

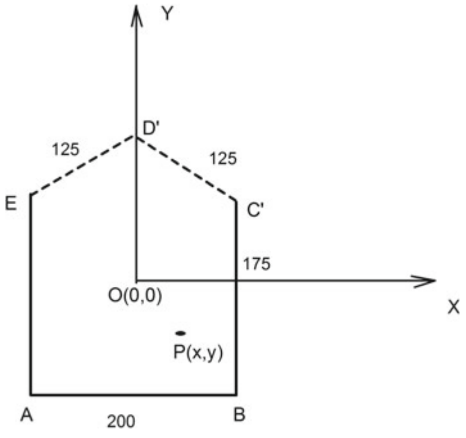

(b) convex loop

Fig. 6 Decay curves and relative difference between indent and rectangular loops at point (0, −10)

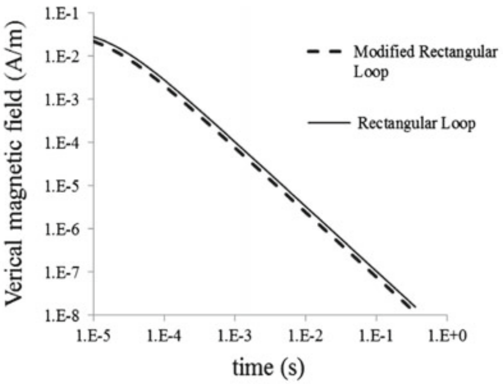

(a) decay curves

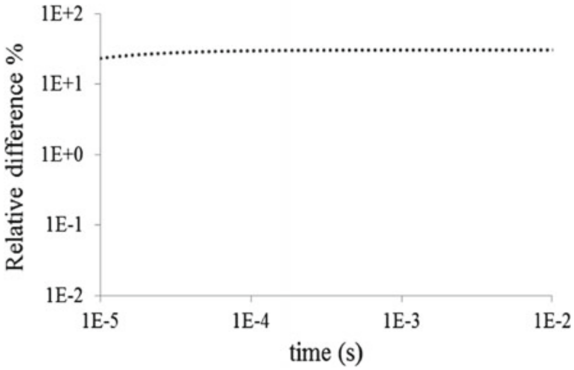

(b) relative difference

rectangular loop (200 × 200 m). The decay curves and difference between the rectangular loop and indent rectangular loop at point (0, −10) are shown in Fig. 6. The relative difference is calculated using formula (1). And as shown in Fig. 6, the decay curves are detached (Fig. 6a) and the difference is far larger than 10% (Fig. 6b).

5 Comparison of Theoretical Models

According to the monotonicity between magnetic field and time, the method of bisection can be used to calculate the all-time apparent resistivity. Let the geo-electric parameters to be:

Fig. 7 Apparent resistivity-section of rectangular loop using circular-loop approximation

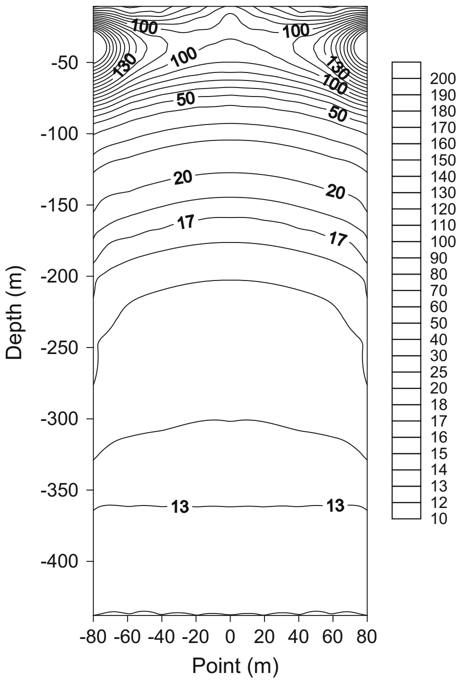

$$\sigma_1 = 0.01S/m, \sigma_2 = 0.1S/m, \boldsymbol{h}_1 = \mathbf{100}\boldsymbol{m}\,.$$

As shown in Fig. 7, apparent resistivity increases in the shallow layer and decreases with depth, that does not conform to a real model.

The obtained apparent resistivity-depth section is shown in Fig. 8. As shown in Fig. 8, apparent resistivity decreases with depth. However, the isoline is not horizontal. There is a trap in the shallow layer near point (0,−10), which does not fit the real model.

Hither the circular simulation of rectangular loop, or the rectangular approximation of modified rectangular loop will bring about some error, which will lower the detection precision.

Fig. 8 Apparent resistivity-section of modified rectangular loop using rectangular-loop approximation

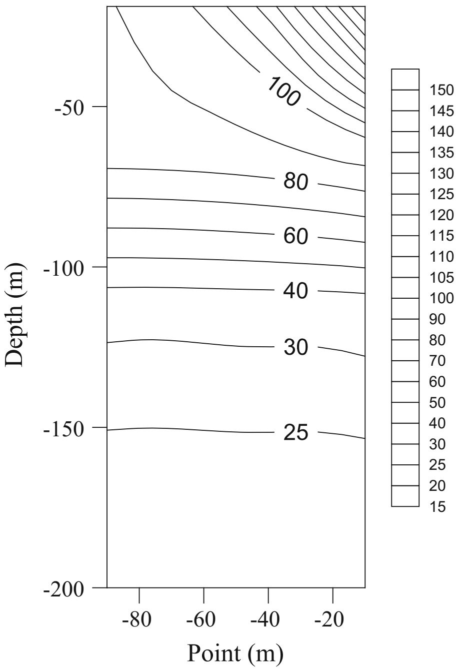

6 Conclusion

The bias caused by change of loop geometry in TEM is discussed from the theory and practice perspective. Theoretically, approximate simulation of rectangular loop using circular loop will affect the shallow-layer response. And in practice, the geometry of rectangular loop is always changed by terrain or geomorphology hence, modified rectangular loop should be adopted. However, some errors will arise due to the change of loop geometry, which may weaken the detection accuracy. Therefore, the geometry of the loop in TEM should be considered in theory and practice.

References

1. Nabighian, M. N., 1988, Electromagnetic methods in applied geophysics, Volume 1: Society of Exploration Geophysicists, Tusla, 203–252.
2. Xue, G. Q., Bai, C. Y., Yan, S., et al., 2012, Deep sounding TEM investigation method based on a modified fixed central-loop system. Journal of Applied Geophysics, 76, 23–32.
3. Spies, B.R., 1989, Depth of investigation in electromagnetic sounding method. Geophysics, 54, 872–888.

The Shielding Effect of Low Resistivity Layer in TEM

Dongyang Hou, Guoqiang Xue, Nannan Zhou and Shu Yan

Abstract Transient electromagnetic method can penetrate high-resistivity shielding layer and delineate underlying strata or structure. However, the shielding effects of low-resistivity layer on transient electromagnetic exploration are often ignored, especially for low-resistive overburden. It is of great importance to ensure exploration depth and improve detection precision by researching the relationship between low-resistive layer and electromagnetic field. In this paper, the propagation process of the subsurface and surface TEM field responses were simulated using finite-difference time-domain method (FDTD). And the characteristic response of low-resistivity overburden was studied using numerical modeling. The observation time with low-resistivity layer was estimated using observation time formula. It was shown that a low-resistivity layer will not only reduce the propagation speed of the field, but also weaken the response of low-resistivity target.

Keywords Low resistive layer · Shielding effect · TEM

1 Introduction

Transient electromagnetic method (TEM) has both the ability to penetrate highly-resistive shielding layers and good detection capability to delineate structures of underlying strata with highly-resistive shielding layer. But, the effects of low-resistive layer, particularly covered layer on transient electromagnetic exploration are often ignored [1–3]. Coincidentally, most of the earth's surface is covered by the low-resistive quaternary sediments with thickness range of about 100 m to 400–600 m in some areas in the North-China coal field area in China. The recent main detection targets in coalfield hydrologic geophysical exploration with

D. Hou (✉) · G. Xue · N. Zhou
Institute of Geology and Geophysics, Chinese Academy of Sciences, Beijing, China

S. Yan
School of Computer Science and Telecommunication Engineering, Jiangsu University, Zhenjiang, China

Q. Di et al. (eds.), *Technology and Application of Environmental and Engineering Geophysics*, Springer Geophysics,
DOI 10.1007/978-981-10-3244-8_18

increasing depth are collapsing column of deep Ordovician limestone and water bearing faults. The assertion of the exploration penetration depth of TEM method to about 800–1200 m is very crucial. Therefore, studies on the interactions between low resistive layer and electromagnetic field is of great significance to ensure its exploration depth and improve its detection precision [4–6].

In this paper, we used the finite-difference time-domain method (FDTD) to simulate the subsurface and surface propagation process of TEM field. The propagation process and response characteristics of low-resistive layer were compared. In addition, the shielding effect of low-resistive inter-bed layer was analyzed. Finally, the observation time with low-resistive layer was estimated.

2 The Shielding Effect of Low Resistive Overburden in TEM

In order to study the propagation process and effect of low resistive layer on time-varying field, we adopted finite-difference time-domain method (FDTD) in our simulation. Under the quasi static approximation:

$$\nabla \times \boldsymbol{E}(\boldsymbol{r}, t) = -\mu \frac{\partial \boldsymbol{H}(\boldsymbol{r}, t)}{\partial t} \tag{1}$$

$$\nabla \times \boldsymbol{H}(\boldsymbol{r}, t) = \boldsymbol{J}(\boldsymbol{r}, t) \tag{2}$$

$$\nabla \cdot \boldsymbol{E}(\boldsymbol{r}, t) = 0 \tag{3}$$

$$\nabla \cdot \boldsymbol{H}(\boldsymbol{r}, t) = 0 \tag{4}$$

In this formula, H represents magnetic field, and E represents its corresponding electric field.

The diffusion equation of quasi static electric field can be derived from the passive Maxwell equation:

$$\nabla^2 E(r, t) - \mu\sigma(r) \frac{\partial E(r, t)}{\partial t} = 0 \tag{5}$$

With the given boundary conditions, finite difference computation was carried out.

Figure 1 shows the simulation results of subsurface and surface electric field propagation process. The resistivity of earth is 100 Ω m. The length and width of low- resistive target with resistivity of 10 Ω m are 200 and 45 m respectively. The thickness of low-resistivity covered layer is 50 m. As shown in Fig. 1a and c, there is no low-resistive overburden. At the first arrival of the field at the target, the electromotive force (emf) recorded on the surface does not contain any information

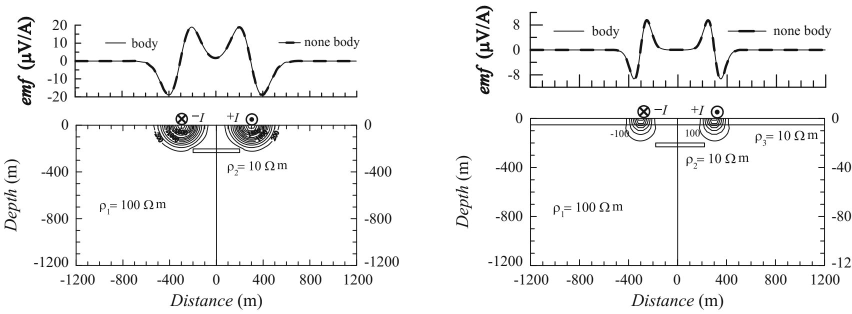

(a) t= 0.055 ms

(b) t= 0.15 ms

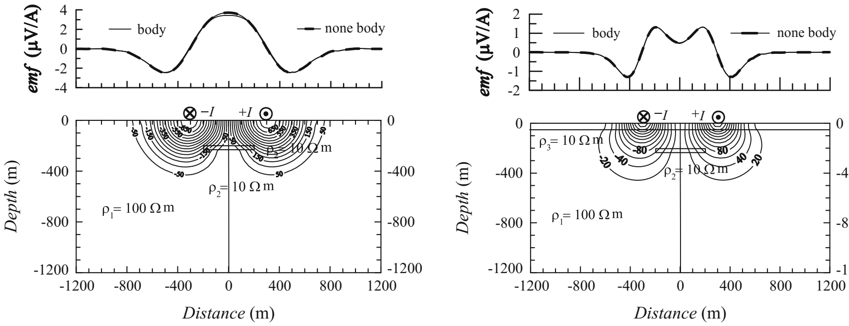

(c) t = 0.22 ms

(d) t = 0.60 ms

Fig. 1 Propagation process of the subsurface electric field (*bottom*) and emf on the surface (*top*) of TEM

on the low-resistive target. However, as time increases, the emf curves observed are representative of the homogeneous earth and low-resistive target respectively. If the difference between the two curves is larger than receiver sensitivity and noise level, then the anomalous body can be delineated.

As shown in Fig. 1b and d, the low resistive overburden reduces the speed of the field and it needs more time to spread to the same depth. Also, it will weaken the anomaly response of low-resistive target.

3 Shielding Effect of Low-Resistive Thin Layer in TEM

For the situation where low-resistive thin layer is existed, we designed a three-layer geo-electric model and then simulate the loop source response. Its parameters are as follows (Fig. 2): the thickness of first layer is 300 m with resistivity of 500 Ω m, the thickness of second layer is 100 m with resistivities as 50, 100, 200, 300 Ω m, and the resistivity of third layer is 500 Ω m. The loop size is 100 m × 100 m with transmitter current of 10A.

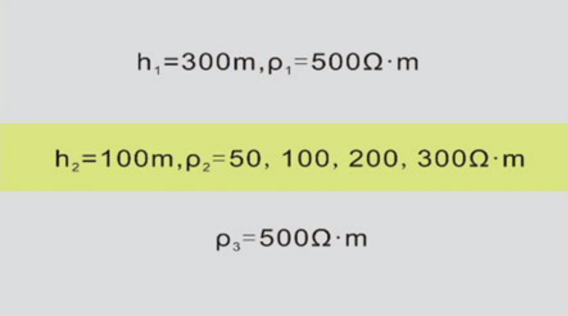

Fig. 2 Three-layer geo-electric model

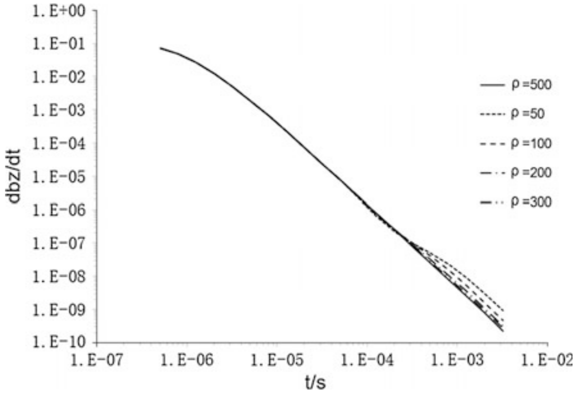

Fig. 3 db/dt changes over time with different low resistive layers

As shown in Fig. 3, we can see that this model generates a larger response, which is not the best for detecting subsurface low-resistive targets. In a situation like this, what happens is that the low-resistive layer shields the real response of the target and then introduces multiple solutions to the geophysical interpretation.

4 Time Observation of Low Resistive Layer

It is well known, that the high frequency step pulse attenuates and the beginning of the pulse becomes flat after a distance of propagation in the conductive earth. According to the phase velocity formula for a good conductor, given as:

$$v_p = (2\omega\rho/\mu_0)^{1/2} \tag{6}$$

The group velocity which is gradually dominated by low frequency components is slowed down due to earth dispersion. So it takes a twofold propagation time for

Table 1 Resistivity measured using DC configuration

$d(m)$	ρ_1 Ω m			
	50	100	150	200
50	0.13	0.06	0.04	0.03
100	0.50	0.25	0.17	0.13
300	0.84	0.59	0.50	0.46
500	1.84	1.59	1.51	1.46
800	4.60	4.35	4.27	4.23

the field to reach the target layer and to carry the geological information back to the surface. Hence, the time estimation formula is given as:

$$t = d^2 \frac{2\mu_0}{\rho} \tag{7}$$

For a layered media, comprehensive resistivity in the direction perpendicular to the bedding can be obtained using:

$$\rho_n = \frac{h_1\rho_1 + h_2\rho_2 + \cdots + h_n\rho_n}{h_1 + h_2 + \cdots + h_n} \tag{8}$$

In the formula above, h_n is the thickness of the nth layer, ρ_n is the resistivity of the nth layer, and n is the corresponding layer.

Based on formulas (7) and (8), the variation law of observation time was calculated and is shown in Table 1.

Among them, the thickness of low resistive layer is 100 m, d is the detection depth and ρ_1 Ω m is the resistivity of the low-resistive layer. The resistivity of second layer is 300 Ω m.

As shown in Table 1, when the thickness of low resistive layer is definite, the observation time at the same depth decreases gradually as its resistivity increases, which further illustrates the influence of the low-resistive medium on the propagation velocity and the observation time. The higher the resistivity, the faster the propagation velocity.

5 Conclusion

Through the analysis of the two-dimension simulation, we established that the existence of conductive covered layer can lower the speed of electromagnetic field, which will take more time to spread to the same depth. We also found that the existence of conductive covered layer will weaken the anomaly response of a subsurface low-resistive target. And that even the existence of low resistive thin layer generates large anomalous response, which covers the real response of the subsurface target. This introduces multiple solutions to the geophysical interpretation, and which is not favorable for the improvement of exploration accuracy.

References

1. Chen M S, Chen L S, Wang T S, Bai G X. 1983. The interpretation of magnetotelluric and electrical soundings data by modified generalized inverse matrix. Chinese Journal of Geophysics, 26(4): 390–400.
2. Chen M S, Yan S. 1995. Problems on application of frequency soundings. Beijing: Geological Publishing House, 36–37.
3. Hohmann G W, Raiche A P. 1992. Chapter 8 Ten inversion of controlled source electromagnetic data. In Nabighian M N, Eds., Electromagnetic methods in applied geophysics Volume 1, Theory. Society of Exploration Geophysics.
4. Jiang B Y. 1998. Applied near zone magnetic source transient electromagnetic exploration. Beijing: Geological Publishing House, 13.
5. Li X, Xue G, Song J. 2005. Application of the adaptive shrinkage genetic algorithm in the feasible region to TEM conductive thin layer inversion. *Applied Geophysics*, 2(4): 204–211.
6. Xue G Q, Deng X. 2007. Capacity of Transient Electro-Magnetic (TEM) method for detecting thin layer. Oil Geophysical Prospecting, 42(6):709–713.

Research Progress in High Power Multi-functional Borehole-Ground Electromagnetic Transmitter for Metal Exploration

Meng Wang, Sheng Jin, Ming Deng, Bo Wang, Zheng Xiang and Ziheng Zhao

Abstract Enhancement of transmitting power is an effective way to improve the depth of electrical prospecting. The objective of this method is to provide adequate offset observation in order to minimize source field effect and to reach a deeper depth of exploration. In addition, placement of electrically excited field source underground close to the exploration object and underground is a new prospecting technology in metal exploration. This method is implemented using existing pit, mine or borehole with the purpose of obtaining stronger and improved information on both the exploration depth and the definition of the anomalous body. Therefore, we have developed a transmitter that can be used as the excitation device for artificial electromagnetic source. It uses a type of large power inverse rectangular wave that works in an automatic sweep manner, the frequency of the transmitter signal range between 10 and 0.01 Hz, the maximum transmitter power is 48 KW, the maximum transmitter current is 60 A, it can realize the on-time planned power supply transmitting with the GPS clock and real time clock (RTC), and also record the information of several auxiliary status. We have been able to certify through experiments that the performance of the device is reliable and stable. And that the device can satisfy the demand for electromagnetic prospecting of metal mining, prospecting for deep and concealed ore bodies and the exploration of sustainable resources for solving resource mining crisis.

Keywords High power · Multi-functional · Borehole-ground electromagnetic transmitter · Metal exploration

1 Introduction

China is presently in the period of quick economic growth, which has led to a yearly increase in the demand for mineral resources [1, 2]. Therefore, the development of new geophysical technologies under the present condition has become an

---

M. Wang (✉) · S. Jin · M. Deng · B. Wang · Z. Xiang · Z. Zhao
China University of Geosciences, Beijing, China

Q. Di et al. (eds.), *Technology and Application of Environmental and Engineering Geophysics*, Springer Geophysics,
DOI 10.1007/978-981-10-3244-8_19

effective way to turn the disadvantaged situation around. Hence, the research on the new technology for borehole-ground electrical prospecting is very timely. These developments would be of great practical significance in saving the resource mining crisis situation and solving the imbalance of mine source supply and demand in China [3]. During metal mine prospecting, the key factors that influences the improvement of electrical prospecting performance are: distinguishing between the ore and non-ore anomaly and the reduction of non-uniqueness in interpretation. In order to solve these issues, it is necessary to obtain more information for comprehensive analysis. This can be done through with the application of the excitement polarization parameter, resistivity parameters and the utilization of precise devices for borehole-borehole observation, borehole-ground observation and ground-borehole observation [4]. However, thankfully the 863 deep mine resource prospecting technology project in the area of resource environment technology, has been able to record the following achievements under its 25 year plan: development of high power borehole-ground electromagnetic imaging system, development of large power borehole electromagnetic multi-parameter imaging technology and devices, development of high and new mine resource exploration technologies that have independent intellectual property, and strong resisting interference capability, with large exploration depth and high definition. All these achievements were based on deep resources experiments and researches.

Actually, high power borehole-ground electromagnetic transmitter is one of the critical components of electrical prospecting, and many domestic and international instrument manufacturers, research institutes and academies have been carrying out vast researches on this topic for a long time. The following technological issues are involved in the research for a transmitting system: (1) The design of high power current supply system and plan for the generator and transformer rectifier unit; (2) high power electromagnetic pulse inversion as well as the technology (the high power input DC current would be inverted into AC rectangular electromagnetic signal and then the load current is supplied into the ground via transmission electrode; (3) the design of buffer circuit for high voltage sharp pulse with the purpose of ensuring the stability and reliability performance of the instruments; (4) the design of low voltage software and hardware for the main control unit in transmitter. This requires hardware circuit with superior performance, reliable and intelligent software control program. In addition, it is also necessary to carry out auxiliary information measurement with the purpose of completing the monitoring status in the course of the electromagnetic transmission; (5) development of synthetic multi-frequency signal and transmission technology, which provides rectangular signal with several frequency components of same amplitude, which enhances the performance efficiency; (6) design of accurate transmission and receiving synchronization technology, which realizes the automatic and high precision time synchronization in electromagnetic measurement network based on high precision crystal oscillator and time synchronization technology in the GPS module [5].

Our independently developed high power borehole-ground electromagnetic imaging device system has now entered the integral stage of testing. The system has undergone the integral device function test at Sunitezuoqi in Neimenggu. The test results suggest that the device can be used to obtain better apparent resistivity and exciting parameters even in an area with serious 50 Hz electromagnetic interference. Therefore, correctness and stability of system have been approved. And this can serve as the foundation for further instrument comparison test and integral device prospecting.

2 The Design of Transmitting System

It is required in the contract that the project should deliver one set of high power multi-functional, borehole-ground electromagnetic transmitting system. The technological index for the system are as follows:

- Suitable for the transmission of several wave signals for the frequency sounding and induced polarization method;
- Wave shape of signal transmitted: multi-wave shape transmission based on inverted rectangular signal (including time-domain induced polarization power supply mode);
- Maximum power: 48 KW; Maximum transmitting current: 60 A; Operation frequency range: 10–0.01 Hz (IP:100–0.01 Hz);
- Synchronization method: GPS + constant temperature crystal (GPS precision: UTC ± 0.1 μs, crystal precision: 20 μs/h);
- Full load continuous operation hour should not be less than 8 h.

The transmitting system consists of high power generator, adjustable transformer rectifier unit, high power electromagnetic transmitter and the transmitting electrode. The technical schematic diagram is shown in Fig. 1. We utilized a 380 V/50 Hz

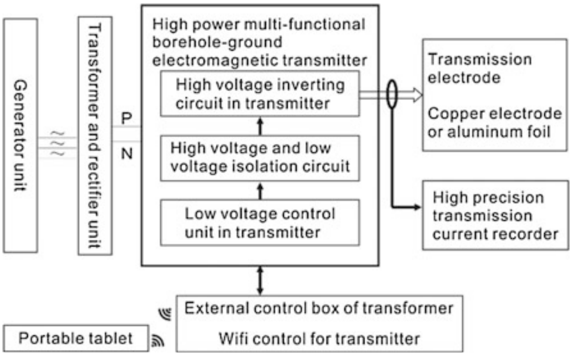

Fig. 1 Schematic diagram for high power electromagnetic transmitting system

three phase AC diesel generator to supply the power, the output power was 80 KVA, and the efficient power was up to 64 KW which satisfied the power supply demand of 48 KW for the system. We adjusted the high power transformer (the effective power output of the transformer rectifier unit was 60 KW) for the suitable voltage value (0–1000 V) based on the ground condition in the work area, the current was delivered to the transmitter. Now, inside the transmitter, the DC power was inverted into multiple-mode rectangular pulse with single frequency or multiple frequencies, and then the electromagnetic signal was transmitted to the medium at the work area awaiting measurement via electrode wire and current electrode. Special external control box was used in the transmitter for the purpose of realizing the wireless control, while a portable tablet was used for the core of control. The control pattern is flexible, the interface is friendly and distinct.

The critical issue in the transmission project is the research of control circuit for the high power transmitter. the plan shown in Fig. 2 was designed and implemented as follows; designed, the STM32 single chip computer and programmable logic CPLD (Complex Programmable Logic Device) chip EPM570 were adopted as the main control core in the control module, aided with WiFi communication module, calibration crystal oscillator, real time clock PCF8563 and direct digital frequency synthesize module AD9850 to complete the generation of induced polarization and multiple frequency driving signal. The hardware circuits designed are as shown in Figs. 3 and 4. The driving signal once generated is delivered to the transmitting module in the ear part. The transmitting module consists of IGBT (Insulated Gate Bipolar Transistor) driver and IGBT Bridge. Thus, the transmitting module can generate high power inverted rectangular signal.

The transmitter control software shown in Fig. 5, first initializes the transmitter, and then establishes the IP connection. Thereafter, the RTC time service is clicked, this is followed by a period to of waiting for the success time service signal and GPS signal from the lower computer, after this a new shift report is established in

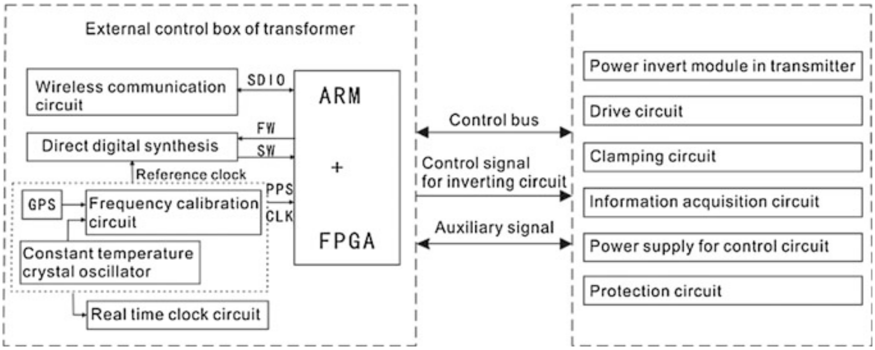

Fig. 2 The schematic diagram for the electromagnetic transmitter control system

Fig. 3 Circuit of external control box in the transmitter

Fig. 4 Physical objects in the transmitter driver and auxiliary monitoring circuit

excel format with the GPS information. The software imitates the current transmission according to GPS time and display the operation parameters of current and power after the procedure above is completed. The control interface for the host computer in the control box is shown in Fig. 6. Also, single or several signals can be transmitted as needed, in addition to selecting the frequency; the transmission mode is also selected (which can be classified into two modes, namely single transmission and cycle transmission). Finally, the time to transmit several frequency is used to set up the transmission time and then the host computer operation is saved in the log using another thread.

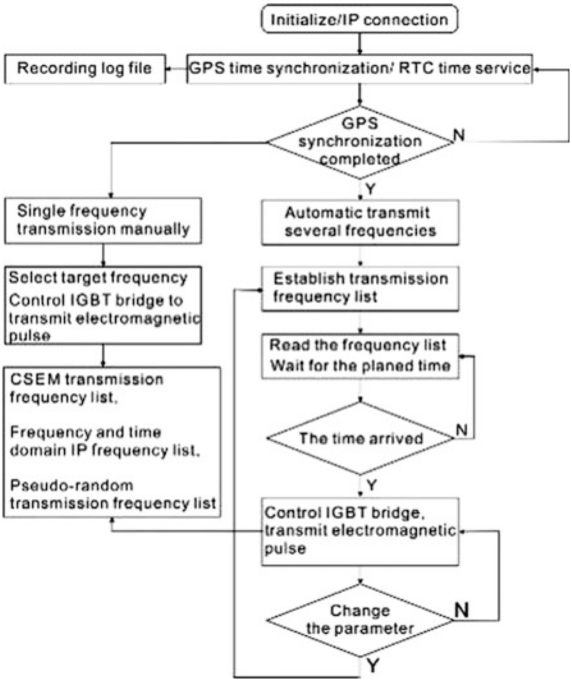

Fig. 5 Diagram of the transmitter software control process

IP：192.168.11.254　端口：8080

```
$D:3,0,0,37,EE
$D:3,0,0,36,EE
$D:3,0,0,37,EE
$D:3,0,0,36,EE
```

Get：4337

频率(Hz)：9600

暂时没有数据，
请先读取文件

设置时间
1 月 27 日
00 : 00 : 00

最高电压(V):0000 最高电流(A):00.0 最高温度1(℃):00 最高温度2(℃):00
最低电压(V):0000 最低电流(A):00.0 最低温度1(℃):00 最低温度2(℃):00

Fig. 6 Diagram of control software in the transmitter host computer

3 Test for Transmitting System

A number of outdoor tests have been carried out within China University of Geosciences (Beijing) campus since the high power multi-functional, borehole-ground electromagnetic transmitting system and the high definition current data recorder were developed in July, 2015. The transmitter functionality has been time tested. The purpose of the experiments was to test the functionality of the transmitter features. We used portable tablet to test the control operation of the transmitter and transformer rectifier source. Figure 7 shows the scene of the campus transmitting system test. Figure 8 is the picture of the result obtained during the outdoor experiment for the transmitting system. The frequency of transmitter satisfies the requirements for various methods such as CSAMT, TP, SIP, TDIP; and the GPS synchronization, time synchronization and on-time transmission as well as other functions show normal performance. Additionally, the continuous power current can go up to 80 A which satisfies the maximum transmitting current under the sink condition and the ground resistance condition of 5 O; The maximum power voltage can go up to 1000 V which also satisfies the maximum transmitting voltage requirement when the outdoor ground resistance is 100 O. However, because the maximum transmitting power is 48 KW, the test for transmission power has not yet been completed.

Figure 9 is the scene of the wild experiment carried out in Sunizuoteqi, Neimenggu in early to mid-October, 2015. The experiment focused on transmitter functionality test, which included tests of the acquisition function for apparent resistivity and induced polarization parameters. The transmitting power used was 16.69 KW while the transmitting current used was 19.9 A (under wild ground condition), the amplitude frequency of supplied current is as shown in Fig. 10. The Following results were observed from the experiment: The error in GPS clock during the wild test was no more than 0.02 μs and the clock drift was also no more

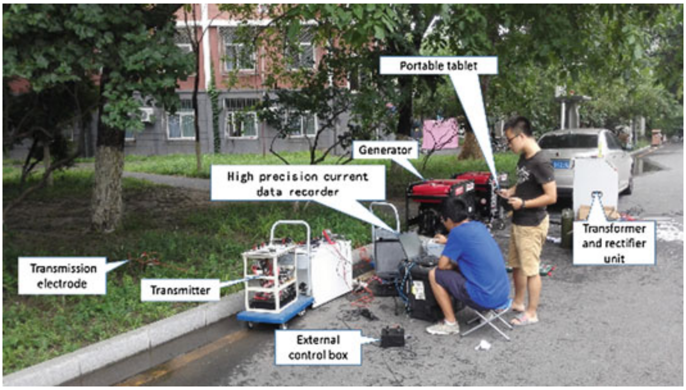

Fig. 7 Outdoor experiment for high power electromagnetic transmitter

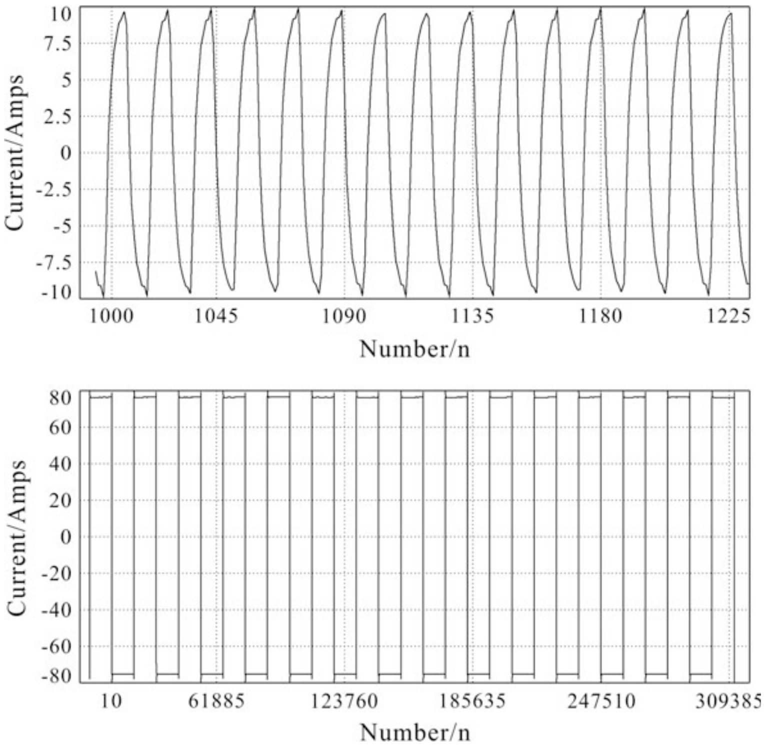

Fig. 8 Data obtained from the data playback software in the transmitting current collector (high frequency 9600 Hz is above, 0.9375 Hz)

Fig. 9 Wild experiment for high power electromagnetic transmitting system

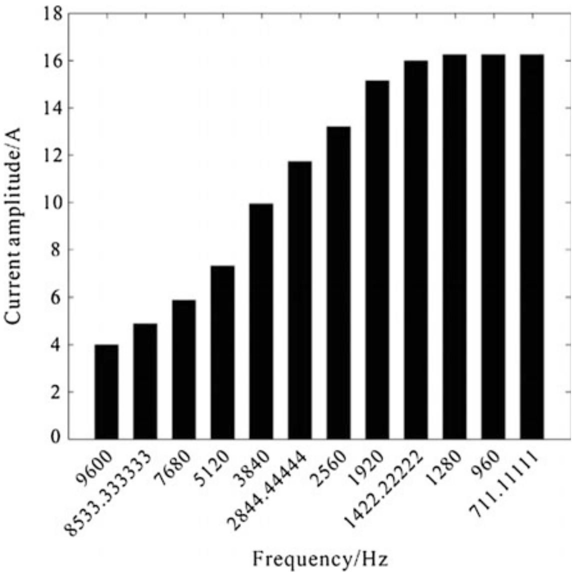

Fig. 10 Schematic diagram for current

than 36 μs/h. A new remote control pattern which separates the control function and drive function was utilized in the transmitter. This made it more convenient to realize multi-function and wild operations with this control pattern.

4 Conclusions

A set of high power multi-functional, borehole-ground electromagnetic transmitting system has been developed based on the existing national and international research findings. Taking the development of devices of same category as reference, our system has turned into a critical component in the high power borehole-ground electromagnetic imaging system for the large depth, high definition metal exploration technology in China. Although the fundamental functions of the transmitter have been realized, both the transmitting current and the transmitting voltage have satisfied the designed requirement, it is still necessary to carry out further tests including outdoor experiments and wild land experiments for continuous long time power supply under full load. Conversely, other indexes also need gradual improvements and optimization in future experiments.

Acknowledgment I would like to acknowledge the national 863 project plan on high power borehole-ground electromagnetic imaging system (2014AA06A603), the support fund from the National Science Foundation (41504138) and other organizations. I also, appreciate my tutor Professor Deng Ming for his helpful comments on the literature and our work team for their assistance.

References

1. Z. Z. Ma, “The thought of Chinese guarantee of mineral resources,” Land and Resources Information, vol. 3, pp. 2–7, 2009.
2. H. Zeng, X. Q. Hu, H. Zhang, “Problems in Exploitation and Utilization of Mineral Resources in China and Counter measures,” Scientific and Technological Management of Land and Resources, vol. 2, pp. 72–75, 2007.
3. Z. Y. Jia, F. M. Jin, “The Application of Surface 2 Borehole Electrical Method in Reservoir Evaluation,” Chinese Journal of Engineering Geophysics, vol. 5, no. 3, pp. 326–331, 2008.
4. Z. G. Wang, Z. X. He, Y. Liu, “Research of Three-Dimentional modelling and anomalous rule on borehole-ground DC method,” Chinese Journal of Engineering Geophysics, vol. 3, no. 2, pp. 87–92, 2006.
5. S. W. Kim, S. Y. Kim, “Analysis of cross-borehole pulse radar signatures measured at various tunnel angles,” EXPLORATION GEOPHYSICS, vol. 41, no. 1, pp. 96–101, 2010.

Research on Investigation Characteristic of Multicomponent Induction Logging in Mineral Logging

Jian Wang, Hao Chen and Xiuming Wang

Abstract We introduce the multicomponent induction logging method to model mineral deposit of limited distribution in order to realize fine evaluation of the solid mineral deposit. In this study, the azimuthal and radial detection characteristics of the components were studied using numerical simulation. The results show that XZ- and ZX-components have the farthest depth of investigation and also exhibits azimuthal sensitivity, which could be used to determine the relative position between an ore body and borehole.

Keywords Multicomponent induction logging · Solid mineral deposit

1 Introduction

The deep-seated deposits, especially "Second space", has become the main investigation targets for the geophysicists due to the increasing shortage of mineral resources [1]. Thus, logging methods is now more important because of the decrease in resolution and accuracy of the surface methods and the increase in the cost and risk for drilling and sampling [2]. Presently, mineral deposit logging methods are not developed early, and severe circumstance introduces large difficulties to instrument design, such as small borehole scale, high pressure and temperature. It is generally thought that oil logging instruments have the characteristics of finite depth of investigation and resolution. However, recent research developments has changed this assumption. For example, remote detection technology can reach tens of meters to hundreds of meters using electromagnetic waves and acoustic waves, while the depth of investigation of cross-borehole electromagnetic method can get as far as thousands of meters [3]. As a result, it would be a good idea to apply the modified instrument in mineral deposit exploration [4].

Multicomponent induction logging method was proposed originally to identify the anisotropy of thin Sand-shale layers. It consists of three orthonormal receiver

---

J. Wang (✉) · H. Chen · X. Wang
State Key Laboratory of Acoustics, Chinese Academy of Sciences, Beijing 100190, China

Q. Di et al. (eds.), *Technology and Application of Environmental and Engineering Geophysics*, Springer Geophysics,
DOI 10.1007/978-981-10-3244-8_20

coils and three orthonormal transmitter coils, the measured components are XX, YY, XY, YX, XZ, YZ, ZX, ZY and ZZ [5]. We can identify many parameters by analysing and processing the responses, such as faults, ruptures of formation, boundaries, azimuths and strikes of mineral deposit. Thus, the method has particular future advantage in evaluation of solid mineral deposit. However, it is more difficult to obtain the ore body geometry information from the nine components than to evaluate resistivity only [6]. Especially for deposits with a lot of variety, complex distributions and different shapes. Deposits such as this needs a sum of numerical simulations, full understanding of the detection characteristics of different couplings and discovery of an effective evaluation method to describe relative positions of the ore body and well. In this study, we used the vector finite element method to simulate the responses of multicomponent induction instrument for a 3-D ore body model. We also discuss the azimuthal and radial detection characteristics of the components.

2 Theory and Method

The vector finite element method is widely used to solve Maxwell equations in complex media [7]. Considering the complex structure and boundary of the deposit model, we adopted unstructured grids for the mesh. Taking advantage of the UMFPACK software based on LU decomposition to solve the linear system of equations, we obtained multipoint numerical results for each of the meshes. The Ore body model is showed in Fig. 1. There is one sphere of ore body at each side of

Fig. 1 Model of ore body

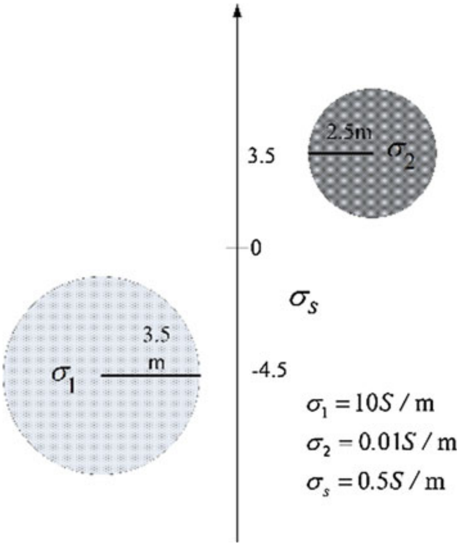

borehole at different depths. The radiuses of the sphere ore bodies are 2.5 and 3.5 m respectively, and conductivities are 0.01 and 10 S/m. Conductivities of formation and mud are 0.5 and 1 S/m respectively. The distance between boundary of ore body and axis of borehole is 0.8 m. The instrument works at a frequency of 26 kHz, and its main coil and auxiliary spacing are 1.82 and 1.37 m respectively.

3 Numeric Results

Figure 2 depicts the computed responses of multicomponent induction instrument in ore body model of different radial depths, with the azimuths of sphere ore bodies fixed at 0° and 180°. The amplitudes response of seven components largely decay with increase in radial distance. Of all the components, ZZ-component is the most sensitive to resistance when the borehole does not pass through the ore body. It presents resistive anomaly as more conductive ore body close to instrument which results in the evaluation failure of the conductive properties using ZZ-component. YY-component on the other hand is more sensitive to conductive ore body. YY-component presents less conductive anomaly as more resistive ore body close to instrument. Compared to YY-component, XX-component largely decays and presents negative anomaly beside more conductive ore body and less positive anomaly beside more resistive ore body only when ore body and instrument is closer (Fig. 3).

For XZ- and ZX-components, they both present large anomalies as the instrument passing by more conductive ore body and less anomaly as the instrument passing by more resistive ore body. Furthermore, XZ- and ZX-component exhibit higher amplitude responses than the other components. Thus, XZ- and ZX-component have the farthest measurement depth of investigation. In Fig. 3, the black lines denote the center locations of sphere ore bodies. It is generally thought that XZ+ZX components are more sensitive to the anisotropy of the media and less sensitive to formation boundary in oil reservoirs. However, XZ-ZX components are largely affected by the formation boundary which is shown in the form of peaks on the curves relative to the formation boundary [8]. It must be pointed out that peak values of XZ-ZX components do not match the centers or boundaries of ore bodies. Similarly, peak values of XX-, YY-, ZZ-, XZ- and ZX-components do not match the depths of ore body either. The zero points of the curves could match the depths of ore bodies exactly in spite of weak responses of XZ+ZX components.

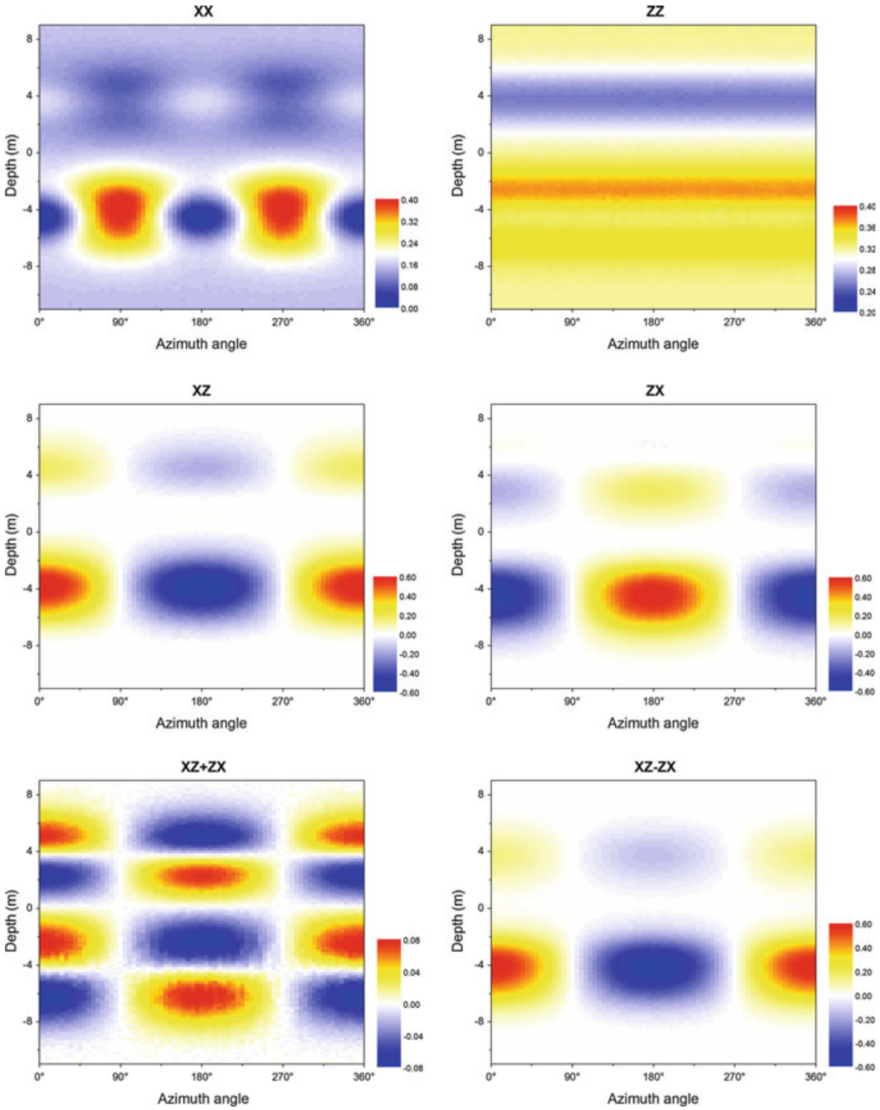

Fig. 2 Computed responses of multicomponent induction logging as functions of azimuth angles

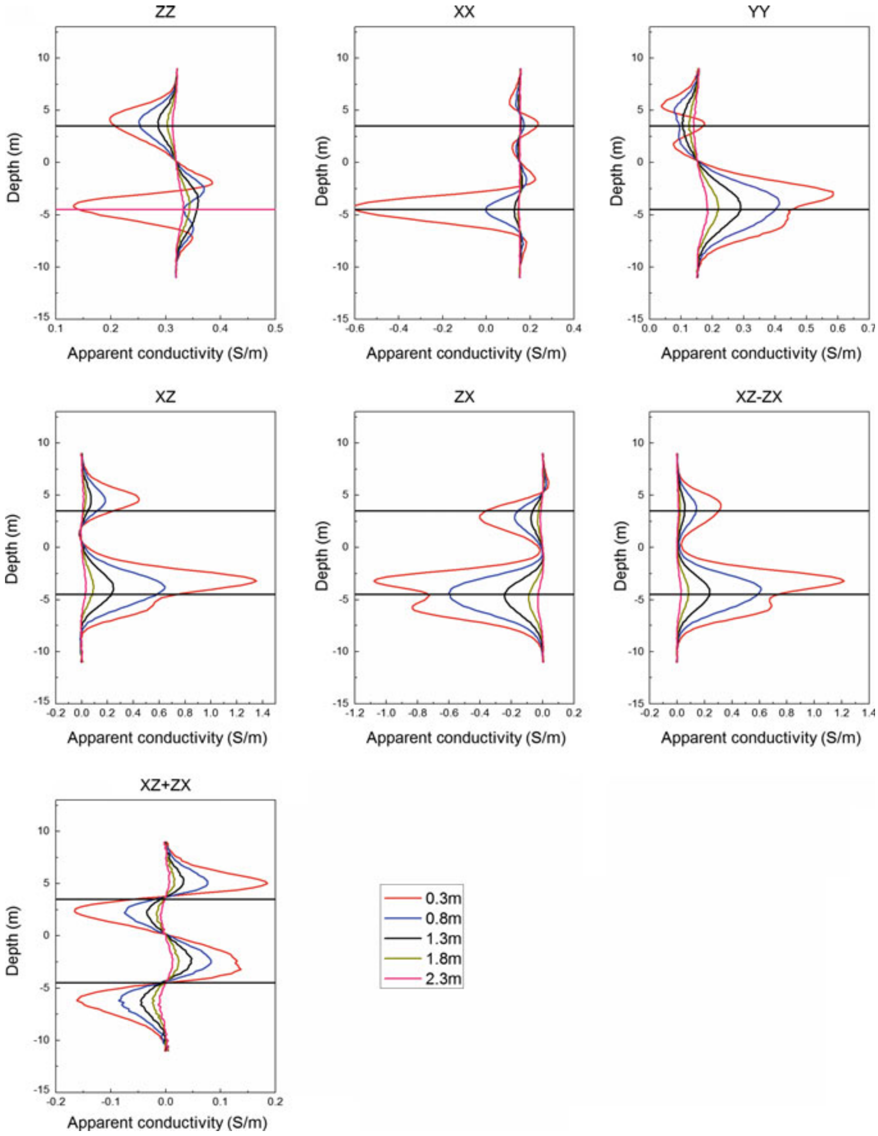

Fig. 3 Computed responses of multicomponent induction logging as functions of radial depths

4 Conclusions

In this study, multicomponent induction logging method was introduced to sphere ore body model in limited distribution. Our results show that ZZ-, XX-, YY-components exhibit shallow depths of investigation. And that XZ- and

ZX- components, both have much deeper depths of investigation also their signal response symbols are relative to the ore body azimuth which can be used to determine the relative position between ore body and well. This research can provide theoretical foundation for the application of multicomponent induction logging instrument in solid deposit exploration.

References

1. J.W. Teng, L.Q. Yang, J.Q. Yao, H.C. Liu, C. Liu, L.G. Han, X.M. Zhang, “Deep discover ore exploration and exploitation for metal mineral resources and its deep dynamical process of formation”, Progress in Geophysics (in Chinese), vol. 22, 2007, pp. 317–334.
2. P. Zhou, S.L. Chen, L.L. Zhu, “Review of a number of subsurface geophysical prospecting methods used for metallic deposits”, Geological Bulletin of China, vol. 28(2/3), 2009, pp. 224–231.
3. X.M. Tang and Z.T. Wei, “Single-well acoustic reflection imaging using far-field radiation characteristics of a borehole dipole source”, Chinese Journal Geophysics, vol. 55, 2012, pp. 2798–2807.
4. R.W. Baltosser and H.W Lawrence, “Application of well logging techniques in metallic mineral mining”, Geophysics, vol. 35, 1970, pp. 143–152.
5. D. Kennedy, E. Peksen, and M. Zhdanov, “Foundations of tensor induction well-logging”, Petrophysics, vol. 42, 2001, pp. 588–610.
6. M. Rabinovich, L. Tabarovsky, B. Corley, J. van der Hors, M. Epov, “Processing multicomponent induction data for formation dips and anisotropy”, Petrophysics, vol. 47, 2006, pp. 506–526.
7. J.M Jin, The finite element method in electromagnetic, New York: Wiley. 2002.
8. S. Davydycheva, “Separation of azimuthal effects for new-generation resistivity logging tools —Part I”, Geophysics, vol. 75, 2010, pp. E31–E40.

The Extraction of TEM Response from Pseudo Random Binary Sequence Source EM Data

Hai Li, Guoqiang Xue, Pan Zhao, Huasen Zhong and Nannan Zhou

Abstract This paper presents a method for converting the full waveform electromagnetic response excited by the pseudo-random binary sequences (PRBS) into subsurface resistivity cross section, based on the recovery of the transient electromagnetic diffusion field. The impulse response of the earth is extracted from the full waveform data efficiently using the Wiener-Hopf equation. Then, the backward accumulation is used to obtain the step off response from the extracted earth impulse response. An OCCAM inversion routine, which incorporates the band limitation of the derived transient, is adopted to produce the geoelectric models. Finally, the method was applied to the experimental field data set, and the consistency between the recovered models and the geological condition verifies the validity of this method.

Keywords TEM response · Pseudo random · Binary sequence · Source EM data

1 Introduction

Over the few past decades, transient electromagnetic method (TEM) has been widely applied to the hydrogeophysical investigation [1], mineral [4, 6] and hydrocarbon exploration [5]. However, with the rapid development of engineering construction capability, the precision attained during TEM prospecting is yet to meet the increasingly stringent demands of engineering geology. Therefore, the development of a new technique to increase the accuracy of TEM sounding is of utmost importance.

The TEM method records and utilizes the transient field generated during the transmitters off-time period. At present, the commonly used source signals for the

---

H. Li (✉) · G. Xue · P. Zhao · H. Zhong · N. Zhou
Key Laboratory of Mineral Resources, Institute of Geology and Geophysics,
Chinese Academy of Sciences, Beijing, China

H. Li · P. Zhao · H. Zhong
University of Chinese Academy of Sciences, Beijing, China

Q. Di et al. (eds.), *Technology and Application of Environmental and Engineering Geophysics*, Springer Geophysics,
DOI 10.1007/978-981-10-3244-8_21

TEM method are bipolar triangular, square or trapezoidal waveforms. These waveforms permit direct measurement of earth step response. Nevertheless, the amplitude spectra of these waveforms demonstrate that the energy of the response will concentrate on the low-frequency range, typically lower than tens of Hz. The frequency contents of the response higher than this frequency range attenuate rapidly and are usually submerged into large noise levels, consequently reducing the resolution of the target.

The frequency content of the source waveform strongly affects the resolution of TEM method. Recently, the pseudo-random binary sequence (PRBS) was adopted as the source waveform for the broadband EM systems. The PRBS signal has the advantage that the frequency components within the bandwidth share almost the equal amplitude and can be designed by properly setting the parameter of the PRBS signal. Besides, the frequency range and its density are controllable by properly setting the stage and the bit duration of the PRBS signal. Hence, the resolution of the target at a depth related to this frequency band can be increased. However, different from the conventional waveform signal used for TEM surveys, the full waveform data excited by PRBS is recorded. These responses can neither be inverted nor interpreted directly; hence, an extraction process is needed required in other to further determine the electrical resistivity contrast between the target and their hosting environment. Duncan et al. [2] derived the expression for impulse response at different frequency range and combined them into a wide band frequency domain response. Ziolkowski et al. (2007) carefully integrated the impulse response which was deconvolved from the full waveform PRBS signal and obtained the mathematical expression for earth step response [7]. Nevertheless, the process involves the integration of the airwave in the impulse response, which strongly influences the precision and stability of the integrated results. Therefore, the use of alternative techniques to interpret these full waveform data is required.

In this paper, a novel method which extracts the transient electromagnetic response from the full waveform response was demonstrated. Based on the characteristics of the PRBS signals, an inversion scheme that incorporates the band limitation of the response was used to convert the extracted TEM data into resistivity profile. Finally, an experimental field data was presented and geoelectric models were obtained using the above-described method.

2 Method

Grounded bipole source configuration TEM method was considered in this paper. The source signal, which is also measured and recorded, is injected between two source electrodes. The inline or broadside time varying voltage response is recorded simultaneously using a pair of receiver electrodes. Assuming that the earth is a linear time-invariant system, the measured voltage response can be express as the convolution

$$v(x_r, x_s, t) = \Delta x_s \Delta x_r i(x_r, t) * g(x_r, x_s, t) * r(t) + n(x_r, t) \tag{1}$$

where $v(x_r, x_s, t)$ is the measured voltage response, $i(x_r, t)$ represents the source current, Δx_s and Δx_r are the source and receiver electrodes spacing, x_r and x_r donate the position of the source and receive respectively, $n(x_r, t)$ represents the uncorrelated noise, $g(x_r, x_s, t)$ is the earth impulse response which carries the geoelectric information about the subsurface material, $r(t)$ is the system response related to the equipment. The principles and advantages of the system response removal, which will be made in the subsequent deconvolution process, have already been studied.

The source waveform transmitted into the earth is the PRBS signal. The PRBS signal appears random but can be predictable by the designer. It can be described by two freely adjustable parameters; the bit duration, $-T$ (or the source switching frequency) and the stage, M. The sequence is repeated after $2^M - 1$ clock pulse. Figure 1 shows the amplitude spectra of 9-stage and 12-stage PRBS sequences with a bit rate of 512 samples per second. As shown in the figure, the nulls in the spectra occur at $f = n/T$, and from 0 to $1/T$ Hz, the spectra has almost the same amplitude from 0 to $1/T$ with a spacing of $1/(2^M - 1)T$ Hz. The frequency band and its density within it are designable by setting the stage and bit duration of the PRBS source signal so that the resolution of the target at a depth related to this frequency band can be increased.

As the first step to data processing, the earth impulse response is recovered from the full waveform voltage response and the recorded source current using deconvolution. Given that the PRBS signal of length N has an ideal autocorrelation function which is given by

$$R_{ss} = \begin{cases} 1 & for \quad i = 1 \\ -\frac{1}{N} & for \quad 1 \le i \le N - 1 \end{cases} \tag{2}$$

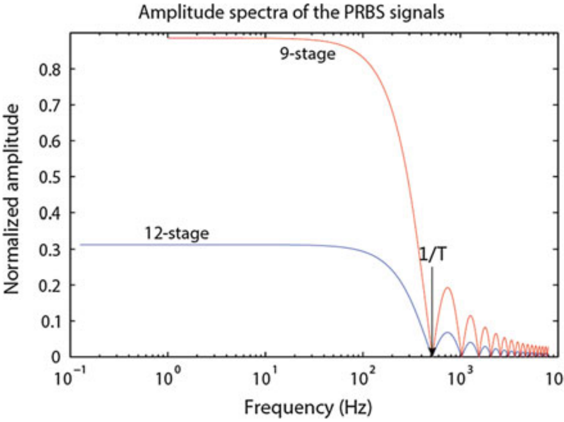

Fig. 1 The amplitude spectra for 9 stage (*red*) and 12 stage (*blue*) PRBS signals

The deconvolution process used in extracting the earth impulse response $g(t)$ from Eq. (1) is defined by the famous Wiener-Hopf equation

$$R_{vs}(\tau) = \int_0^{T_s} g(t)\mathrm{R}_{ss}(\tau - t)dt \tag{3}$$

where R_{vs} is the cross-correlation of the received voltage and the source current. It is crucial that the uncorrelated noises are eliminated in this process. Equation (3) can be written in matrix form as

$$\begin{bmatrix} R_{ss}(0) & R_{ss}(1) & \dots & R_{ss}(N) \\ R_{ss}(1) & R_{ss}(0) & \dots & R_{ss}(N-1) \\ \vdots & \vdots & \dots & \vdots \\ R_{ss}(N) & R_{ss}(N-1) & \dots & R_{ss}(0) \end{bmatrix} \begin{bmatrix} g(0) \\ g(1) \\ \vdots \\ g(N) \end{bmatrix} = \begin{bmatrix} R_{vs}(0) \\ R_{vs}(1) \\ \vdots \\ R_{vs}(N) \end{bmatrix} \tag{4}$$

The coefficient matrix in Eq. (4) is the Toeplitz matrix so that Eq. (4) can be solved efficiently using the Levinson recursion.

After the deconvolution process, the required band limited impulse response is obtained by using a low-pass filter to screen out the unwanted frequency range. It is very difficult to get the step response through direct integration of the filtered impulse response because of the appearance of the airwave at the early time. Considering that the time domain and frequency domain response are related by the Fourier transform and that the symmetry arguments simplify these transforms to use either a sine or cosine multiplication, the time domain responses can be calculated using the cosine multiplication,

$$f^{step-on}(t) = F(0) + \frac{2}{\pi}\int_0^{\infty} \mathrm{Im}(\frac{F(\omega)}{\omega})\cos(\omega t)\mathrm{d}\omega \tag{5}$$

$$f^{step-off}(t) = -\frac{2}{\pi}\int_0^{\infty} \mathrm{Im}(\frac{F(\omega)}{\omega})\cos(\omega t)\mathrm{d}\omega \tag{6}$$

In which $F(\omega)$ is the frequency domain response, $F(0)$ is the resistive limit, $f^{step-on}(t)$ and $f^{step-off}(t)$ are the step on response and step off response respectively. It is illustrated in Eqs. (5) and (6) that the sum of step on and step off response are equal to the resistivity limit, which is the asymptotic value at the late time for the step response. Therefore, if we backward accumulate the band-limit impulse response from the late time, we can obtain the band-limit step off response.

$$f^{step-off}(t_m) = \int_{t_m}^{t_{\max}} g(t)\mathrm{d}t = \sum_{i=m}^{M} \left[\frac{g(t_{i+1}) + g(t_i)}{2} (t_{i+1} - t_i) \right] \tag{7}$$

where $t_{\max}$ is the starting point of accumulation. Figure 2 shows the comparison between the integrated results and the analytic solution for a homogeneous half space. The responses represent the inline electrical field obtained from using a horizontal dipole source at an offset of 1000 m offset and normalized by the source dipole moment. Based on the calculations, we found out that if the starting time of the integration is two orders of magnitude larger than the peak time of the impulse response, the relative error will be less than 1.0%. In addition, by using the inverse integral Eq. (7), we can avoid the integration of the airwave at an early time and get the stabilized step off response.

After recovering the band-limit step off response, the popular OCCAM algorithm is used to invert these data. OCCAM's inversion uses the discrepancy principle to search for the solution that minimizes the model roughness subject to the constraint.

$$\|\mathbf{Wd} - \mathbf{WF}[\mathbf{m}]\|^2 \le \delta \tag{8}$$

where **d** represents the data vector, **m** represents the model vector, **F** is the forward operator, $\mathbf{W} = diag(\sigma_1^{-1}, \sigma_2^{-1}, \ldots, \sigma_N^{-1})$ is the data weighting matrix. Then the unconstrained functional is gives as;

$$U = \|\delta\mathbf{m}\|^2 + \mu^{-1}\left\{\|\mathbf{Wd} - \mathbf{WF}[\mathbf{m}]\|^2 - X_*^2\right\}, \tag{9}$$

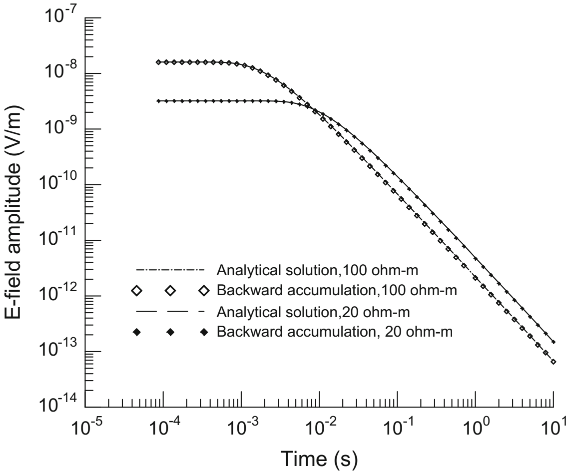

Fig. 2 The backward accumulation of impulse response for a homogeneous half space

where ∂ denotes the roughness operator for the model, and X_*^2 is the target misfit. The Lagrange multiplier μ serves to balance the trade-off between the data fit, the model roughness and model preference. The band limitation will distort the derived step off transients because of the damping of the high-frequency content. Thus, the frequency band is incorporated into the inversion process to acquire more accurate results. Finally, the inversion routine of band-limit response has been validated on the synthetic data.

3 Examples

In this section, the previously stated methods were tested on the experimental field data. A 12th order PRBS signal with a bit rate of 512 samples per second was transmitted into the earth via grounded wire source. The source current and the inline electric field were measured simultaneously. The bit rate was chosen so that the penetration depth corresponding to the frequency range of the source signal will cover the required depth interval.

In this experiment, 250 s full waveform responses were collected at each source-receiver position. In order to reveal the form of the recorded signal, Fig. 3a shows a small part of the normalized voltage and the recorded source current. It was inferred from the figure that the recorded response is totally different from the conventional TEM transient. The deconvolution techniques based on Eq. (1) was then applied to the recorded source current and the voltage response.

Figure 3b shows the extracted step off response from the voltage response and the source current in Fig. 3a. The 250 s full waveform response was compressed into an impulse response whose time interval can be projected by setting the length of the correlation function Eq. (4). The frequency band of the step response was limited according to the bit rate of the source signal. Effersø et al. [3] demonstrated that the distortion due to the cut-off frequency can lead to incorrect inversion results

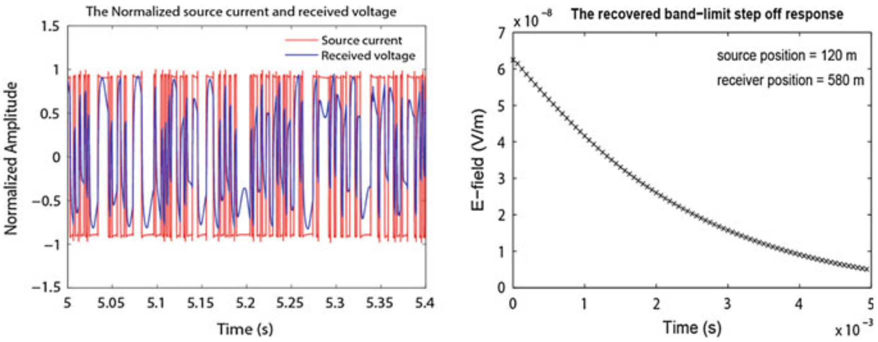

Fig. 3 The (*left*) recorded response and source waveform, and the (*right*) extracted band-limit step off response at 120 m source position and 580 m receiver position

if the low-pass filters are not included in the inversion scheme. Hence, the band limitation was incorporated into the inversion of these field data.

The 1D OCCAM's inversion are performed to trace the subsurface geology from these band-limit responses. Figure 4 shows the inversion results at 120 m source position and 540 and 700 m receiver position.

The consistency of the inversion results is good when we compare the model parameter of the adjacent sites in Fig. 4. The conductive feature at a depth of around 200 m consistently showed up both of the inverted models. This is a good indication that these conductor layers are actually resolved. Further on, the inversion results are also confirmed by the dual frequency induced polarization sounding results [5].

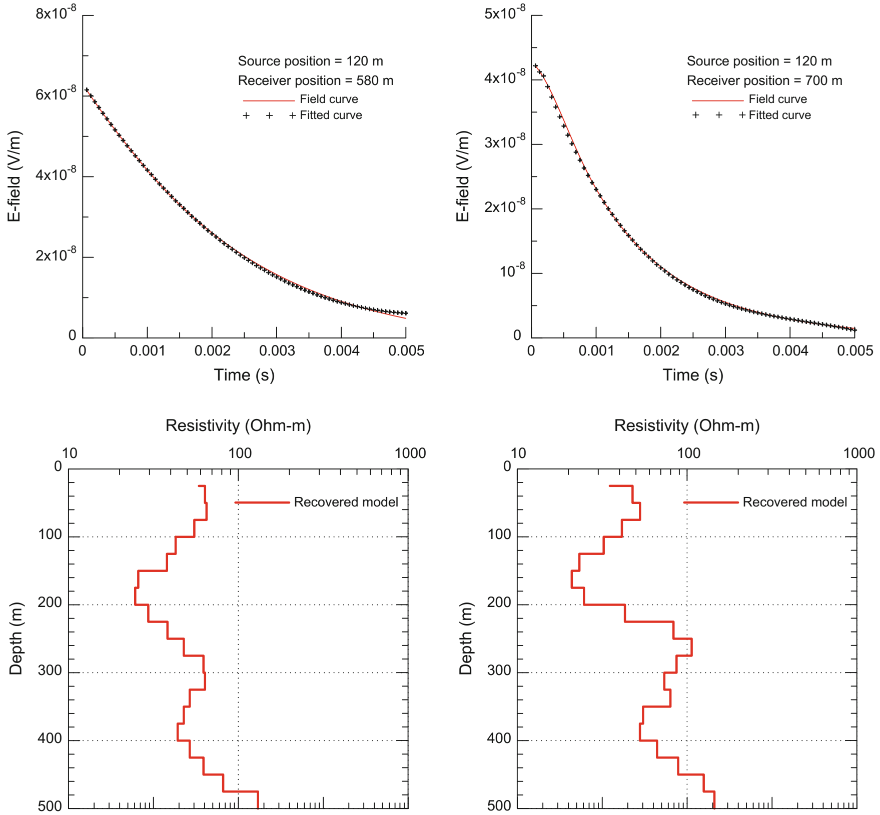

Fig. 4 The inversion result of recovered band limited response

4 Conclusion

This paper demonstrates the interpretation of EM data excited by a PRBS source. Based on the properties of the spectra amplitude of PRBS waveforms, this method was expected to give a better resolution of the subsurface resistivity distribution than the conventional TEM techniques by properly design the PRBS source waveform.

Although only the grounded bipole configuration was considered in this paper, the method can be extended to other configurations by introducing the corresponding forward operator to calculate the forward response and the jacobian during the inversion process. Nevertheless, the late time characteristics should be carefully considered to guarantee the correctness and stability of the backward accumulation.

Acknowledgments This research was supported by R&D of Key Instruments and Technologies for Deep Resources Prospecting (the National R&D Projects for Key Scientific Instruments), Grant No. ZDYZ2012-1-05-04.

References

1. Danielsen, J.E., Auken, E., Jørgensen, F., Søndergaard, V., Sørensen, K.I., 2003. The application of the transient electromagnetic method in hydrogeophysical surveys. Journal of Applied Geophysics 53, 181–198.
2. Duncan, P., Hwang, A., Edwards, R., Bailey, R., Garland, G., 1980. The development and applications of a wide band electromagnetic sounding system using a pseudo-noise source. Geophysics 45, 1276–1296.
3. Effersø, F., Auken, E., Sørensen, K.I., 1999. Inversion of band-limited TEM responses. Geophysical Prospecting 47, 551–564.
4. Smith, R., 2014. Electromagnetic Induction Methods in Mining Geophysics from 2008 to 2012. Surveys in Geophysics 35, 123–156.
5. Wang, W.-d., Li, Z.-h., Gu, G.y., Ban, Y.h., Liu, Y.w., 2014. Application of dual frequency induced polarization in Caosiyao molybdenum deposit area, Inner Mongolia, Mineral Exploration, pp. 789–795.
6. Wright, D., Ziolkowski, A., Hobbs, B., 2002. Hydrocarbon detection and monitoring with a multicomponent transient electromagnetic (MTEM) survey. The Leading Edge 21, 852–864.
7. Ziolkowski, A., Hobbs, B.A., Wright, D., 2007. Multitransient electromagnetic demonstration survey in France. Geophysics 72, F197–F209.

Application of Ant Tracking Technique in Fault Interpretation of YC Coal Mine

Dongyang Liu, Suzhen Shi, Wenfeng Du and Tailang Zhao

Abstract In coalfield seismic exploration study, the general interpretation is based on the observation and identification of the characteristics of seismic section. The space distribution of the fracture system can be well demonstrated by an advanced automatic tracking method, the ant tracking technique. Due to the limitations on the manual interpretation technique, it can only identify the fault and fracture that are evident. The automatic interpretation results obtained from the ant tracking technology, when compared with manual interpretation result, was more clearer, intuitive and accurate. It was considered that the technique has good application value in the interpretation of coalfield structures.

Keywords Ant tracking · Fault interpretation · Coalfield

1 Introduction

In the interpretation of coalfield structure, accurate fault system interpretation is a key part in seismic data interpretation, the accuracy and precision of the results are very important for the safety production of coal mine [1]. But the fault interpretation methods at the present stage are mostly dependent on the artificial interpretation, with strong subjective. At the same time, due to the fault structures in coal strata complexity, the fault that is less than 5 m is often either unclear or not

---

D. Liu (✉) · S. Shi · W. Du · T. Zhao
State Key Laboratory of Coal Resources and Safe Mining,
China University of Mining and Technology, Beijing, China
e-mail: 18910219317@163.com

Q. Di et al. (eds.), *Technology and Application of Environmental and Engineering Geophysics*, Springer Geophysics,
DOI 10.1007/978-981-10-3244-8_22

displayed on the seismic section; hence, causing great trouble to the interpretation of fault system [2]. Ant tracking technology can solve this problem effectively. It can improve the interpretation accuracy by enhancing the detection of small faults which the artificial technique failed to mark out on the seismic section, and reducing the interpretation time and subjectivity. In this paper, the ant algorithm of Petrel software was studied, and combined with the variance and curvature attributes to YC coal mine for structural interpretation and the interpretation results were compared with the artificial interpretation results.

2 Theory and Method

Ant colony algorithm was proposed by Dorigo et al. [3], the formation of the mechanism for the algorithm came from the choice of the path that ants use to find food. It is a technique to find the optimal path in space. In seismic interpretation, the ant tracking technology which is based on ant colony algorithm involves the spreading out of large number of electronic ants in the seismic data, and the ant which meets the conditions of the present fault traces will "release" a signal and call on the ants in other areas to track the fault until the completion of the tracking and recognition of the fault.

The basic steps for ant tracking includes: (1) The original seismic data should be constructed smoothly in other to reduce the noise and enhance the continuity of seismic reflection interface, (2) In order to enhance the discontinuity of seismic data in space, variance attributes or curvature attributes were generated by using the smoothed data for edge detection, and (3) The discontinuity (such as curvature, variance etc.) was used as an input for the ant tracking, by setting appropriate parameters and determining the corresponding ant volume.

3 Field Example

3.1 Data Preprocessing

We cannot extract seismic attribute directly after the loading of seismic data due to the presence of interference and noise, as well as the formation factor. Therefore, we need to analyze and process the original data, using median filtering algorithm to smoothen the original seismic data. This enhances the continuity of reflection axis, highlighting the information on breakpoint. After the preprocessing step has been carried out, the noise and formation impacts will either be weakened or

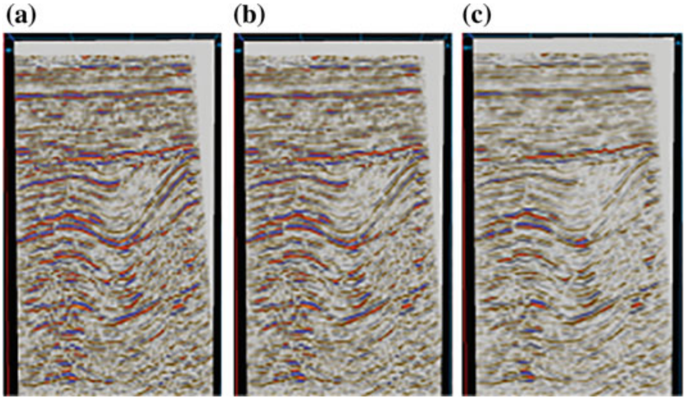

Fig. 1 The treatment effect of different smoothing coefficient map. **a** Smoothing coefficient is 1. **b** Smoothing coefficient is 1.5. **c** Smoothing coefficient is 2

eliminated, and high signal-to-noise ratio data will be provided for attribute extraction. At the same time, different smoothing factors will have different effects on the degree of smoothing of the data, so we need to select the appropriate smoothing.

The greater the smoothing factor,the higher the degree of smoothing of the original data and the ability to eliminate noise. But excessive smoothing coefficient will also filter out the useful information in the stratum (Fig. 1). So, the suitable smoothing coefficient used was 1.5.

3.2 Ant Tracking Parameter Selection

The key to the ant tracking technology is to select the appropriate parameters for the extraction of ant attribute. The tracking parameter setting does not only affects the ant attribute extraction and fault information, but it also has a great influence on the later extraction credibility. In this paper we analyzed the example of the YC coal fault interpretation, by comparing and analyzing the results of tracking gradually in other to determine the best tracking parameters. At the same time, it was more detailed and intuitive to understand the process of ant tracking.

The parameters for ant tracking are mainly divided into six aspects. Initial Ant Boundary, Ant Track Deviation, Ant Step Size, Illegal Steps, Legal Steps, Stop Criteria.

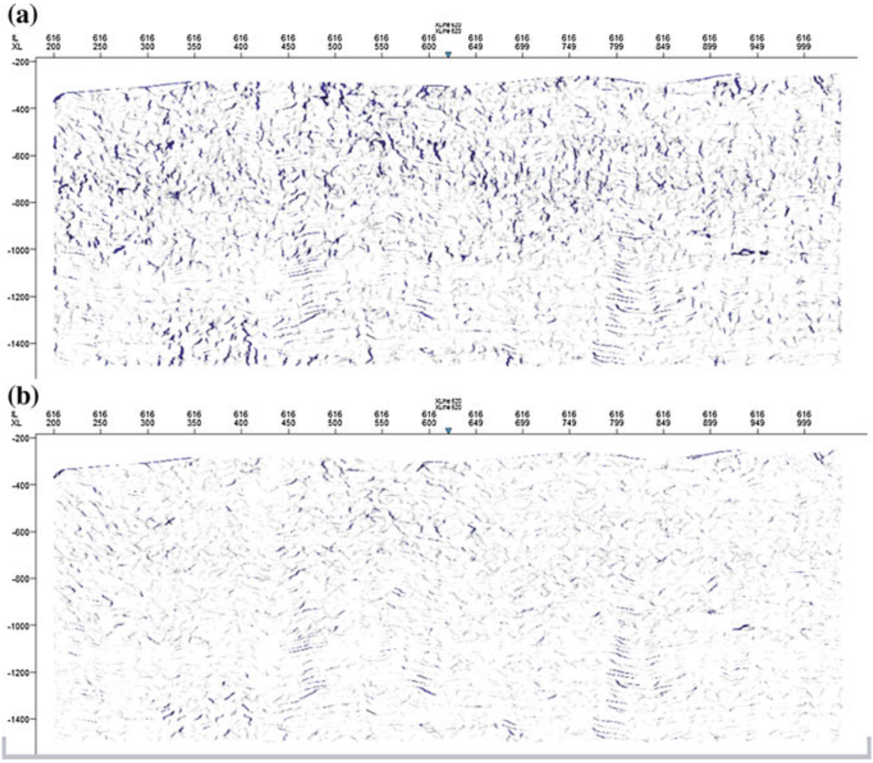

Fig. 2 Different value for initial ant boundary. **a** The value is 5. **b** The value is 10

Initial Ant Boundary: This value refers to the number of ants spread. This controls the distribution of ants density, but also determines the ant tracking time. The higher the value, the higher the ant distribution density in units of data and the shorter the tracking time; although, it will be fuzzy for small structures (Fig. 2). The initial ant boundary value is usual set between 4 and 7.

Stop Criteria is the parameter used to terminate the ant search. It screens the number of illegal steps in the total number of ants that passed by. The greater the value, the stronger the capability of ants. From Fig. 3, we observed clearly that Fig. 3b expressed the fault information more than Fig. 3a with lower Stop Criteria value. Through analysis, we observed that the Stop Criteria is related to the continuity of the fault tracking. The greater the value of Stop Criteria, the higher the continuity of the fault tracking system.

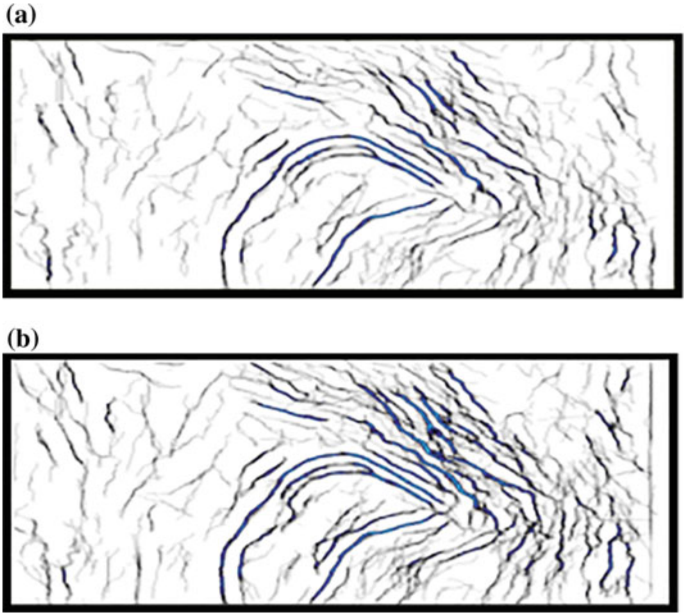

Fig. 3 Comparison of different stop criteria. **a** The value of stop criteria is 5%. **b** The value of stop criteria is 10%

Through the analysis of the ant tracking parameters, we automatically tracked the fault system within the acquired seismic data over the YC coal mine. For 3D seismic data, using an appropriate seismic attribute technology to highlight transverse discontinuity between Stratum was the key to the fine structural interpretation of the fault system. For example, variance attributes can identify the fault, fracture and some other geological anomalous bodies very well. In this paper, we extracted the variance and curvature attributes in other to enhance the recognition of the fault system, and then used the ant tracking technology to obtain the ant attribute cube. Finally, we select a better ants attributes for better explanation.

Through the repeated experiments, we finally set the following parameters for the ant tracking process; For the ant attribute of variance, Initial Ant Boundary was 5, Ant Track Deviation was 2, Ant Step Size was 3, Illegal Steps was 2, Legal Steps was 2, Stop Criteria was 10%. For the ant attribute of curvature, Initial Ant Boundary was 5, Ant Track Deviation was 2, Ant Step Size was 3, Illegal Steps was 1, Legal Steps was 1, Stop Criteria was 4%.

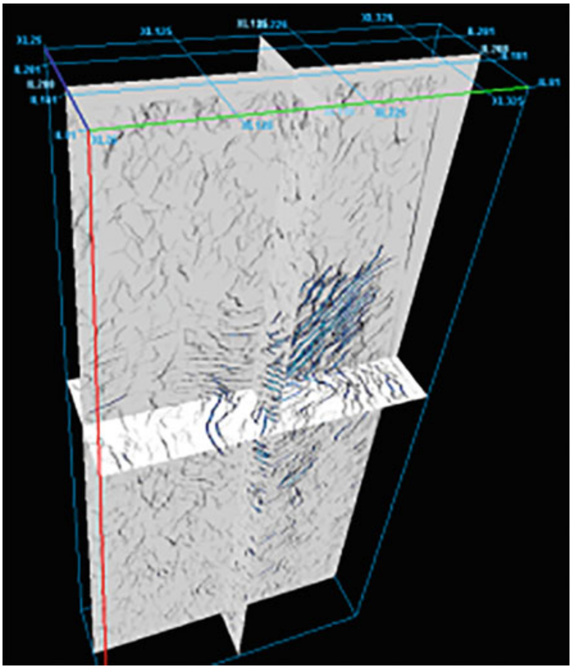

Fig. 4 The ant attributes of variance

3.3 Comparison Between the Ant Attribute of Variance and Curvature

Using ant tracking technology to obtain the ant attribute cube, we observed some traces on the seismic data. This means that we got the ant attribute cube which showed the fracture system. We can see that there are many fine lines in the ant attributes of variance, these lines show the distribution of fracture system in space (Fig. 4). Figure 5 shows the comparison of the ant tracking slice, amplitude slice and variance attribute slice. The fault display on the amplitude depth slice was very vague. Mapping of the fault distribution was very difficult and almost impossible. For the variance depth slice, the information was very messy. It had low resolution and high noise interference. Also, mapping of the fault distribution system was very difficult. However, not only was the big fault and fracture very obvious on the ant attribute slice, the minor fault was also seen clearly. This shows that the interpretation of ant tracking results can shed more light on the crustal fault and fracture

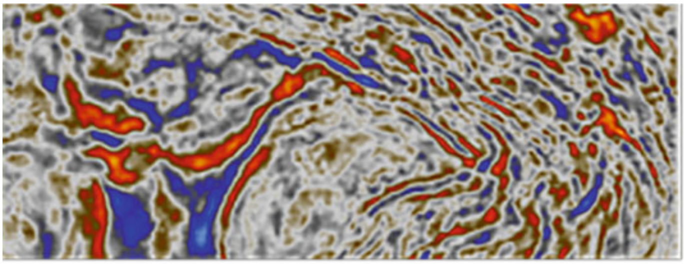

(a) Amplitude slice

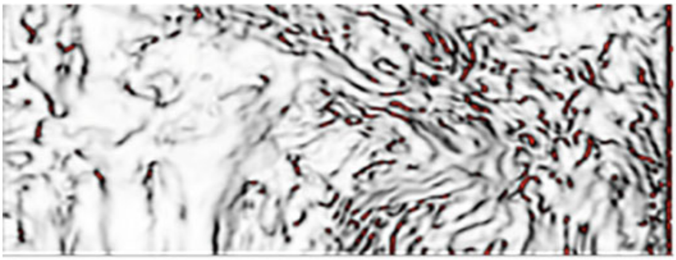

(b) Variance attribute slice

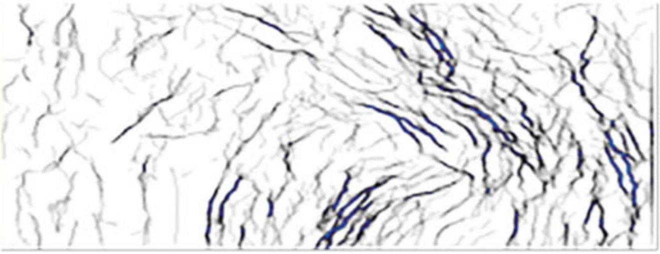

(c) Ant tracking slice

Fig. 5 Ant tracking results compared with the original seismic slice

system and give a more intuitive and accurate image of the subsurface structural geology.

In the two slice map (Fig. 6), The darker lines represent the fault traces, the depth of the color represents the degree of confidence. It can be seen from Fig. 6 that the ant attribute of variance can be used to identify the major and minor faults very clearly. Considering these factors, we used the ant attribute of curvature to track the faults automatically.

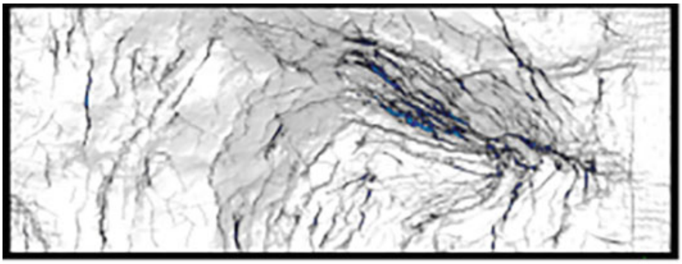

(a) The ant attribute of curvature slice map

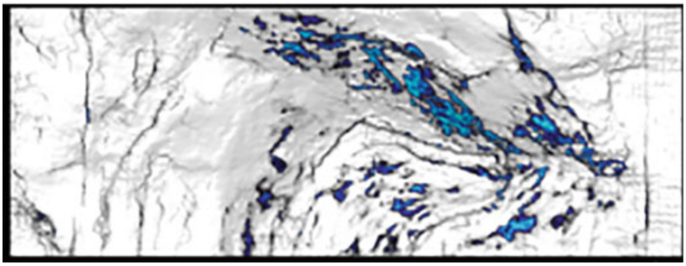

(b) The ant attribute of variance slice map

Fig. 6 Slice comparison

3.4 Ant Tracking and Manual Interpretation

It can be seen from Fig. 7 that the fault prediction in curvature—ant tracking section is highly visible and it can be used to characterize the distribution of fracture system qualitatively. In this picture, gray lines represent the fault interpretation system obtained by using the ant automatic tracking technique, the colored lines represent manual interpretation faults. For the large faults, the interpretation of the results obtained from the two methods were almost the same. However, the ant tracking technique was better in the mapping of minor faults and fractures and some other small-scale targets. The main reason for this phenomenon is that, it is difficult to explain the fractures in seismic data for manual interpretation. For manual interpretation, only fractures which had appreciable distance between its two sides were observed. Through analysis and supplementary explanation, we obtained the final distribution of the crustal fault system from the seismic exploration study (Fig. 7). The number of detectable faults increased by eight, in comparison to the manual interpretation. The average offset was 5 m and the strike was major in the NE direction.

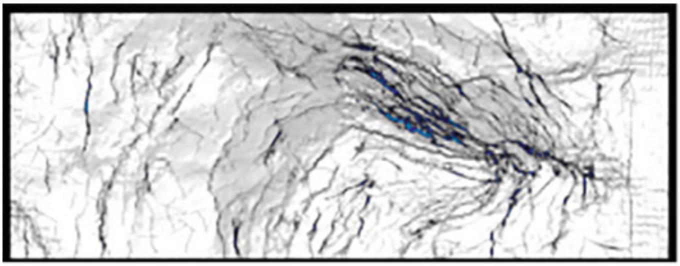

(a) Ant tracking

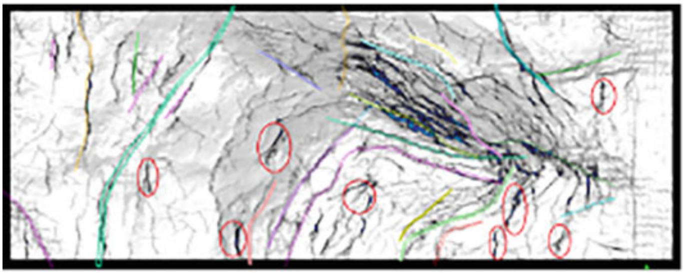

(b) Manual interpretation

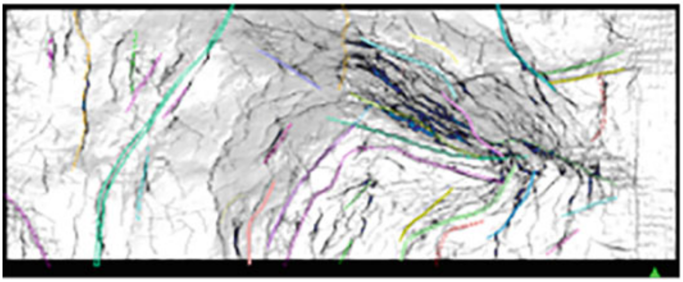

(c) The final explanation of the fault

Fig. 7 Ant tracking and manual interpretation

4 Conclusion

(1) The ant attribute was very effective in the mapping of faults and fracture systems, it shows the 3D embodiment of fault and fracture system.

(2) By comparing the results obtained from both techniques, we observed that the ant tracking technology had higher interpretation accuracy. It was able to detect not only the large faults, but also the minor fault. This is an advantage that is difficult for the manual interpretation to achieve.

(3) The use of ant tracking technology can help interpreters understand the coal-field structure better and make more accurate recommendation.

References

1. Du, W. F., Peng, S. P., 2008, Seismic horizon curvature for predicting small fault in coalfield: Chinese Journal Of Rock Mechanics And Engineering(in Chinese), 27, 2901–2906.
2. Li, X.R., Meng, X.D., 2004, Using seismic attribute technology research karst fractured zones: North China Earthquake Sciences(in Chinese), 22(4):20–21.
3. Dorigo M, Maniezzo V, Colomi A. Positive Feedback as a Search Strategy[R]. Milan Politecnico di Milano, 1991:91–106.

Earthquake Detection with Seismic Exploration Method

Guanghe Liang

Abstract Seismic exploration technology has been widely used in petroleum exploration and engineering fields, but it has received little attention for the study of structural changes and detection after earthquake. In this paper, at first we analyzed the data obtained in 2008 from trenches, coring, well logging and geophysical exploration after/during the Wenchuan Ms8.0 earthquake. The results show that the Wenchuan earthquake was formed by cryptoexplosion process which was gradually triggered from the southwest to the northeast. The energy of cryptoexplosion includes two aspects, one of which is underground supercritical fluid phase explosion, and the second is discharge lightning of underground negative charge accumulation. From seismic section, we identified the characteristics of underground changes caused by cryptoexplosion. Lastly, seismic exploration carried out in the Japan South Sea was further compared and it also has underground cryptoexplosion characteristics. This means that genetic mechanism of earthquake is not mainly caused by structural movement but mainly by underground explosion. These results show that seismic exploration is very effective in identifying the underground explosion characteristics caused by earthquake.

Keywords Earthquake detection · Cryptoexplosion · Genetic mechanism · Seismic exploration

1 Introduction

Seismic exploration technology has been successfully applied in the field of petroleum exploration and engineering geology. But there are only few studies that are related to the detection and characterization of structural changes after earthquake.

G. Liang (✉)
Key Laboratory of Mineral Resources Research, Chinese Academy of Sciences,
Beijing 100029, China
e-mail: lgh@mail.iggcas.ac.cn

G. Liang
Institute of Geology and Geophysics, Chinese Academy of Sciences, Beijing 100029, China

Q. Di et al. (eds.), *Technology and Application of Environmental and Engineering Geophysics*, Springer Geophysics,
DOI 10.1007/978-981-10-3244-8_23

This arises as a result of the dispute over the genetic mechanism of earthquakes. There are several hypotheses for the genetic mechanism of earthquakes, which includes the famous elastic rebound hypothesis [1] and magma impact hypothesis proposed by Matsuzawa [2], and phase transition hypothesis proposed by American scholars Bridgman [3]. Many Chinese scholars have also put forward several other hypotheses, Yue [4] presented a natural gas explosion hypothesis Yang et al. [5] proposed the origin model of sandwich structure Du [6], Du et al. [7] proposed underground fluid cryptoexplosion hypothesis. Jiang [8], etcetera also put forward underground Lightning hypothesis [9]. These hypotheses were found to be supported by some evidence, but not without adverse proof questioning their accuracy. This shows that they still need to be improved on.

At present, it is generally believed that the genetic mechanism for the earthquake is the fault movement.

Wenchuan Ms8.0 Earthquake on May 12, 2008 along the Longmenshan fault belt in the Yingxiu Beichuan fault and Guanxian Anxian fault produced strong surface deformation. The deformation was mainly thrust and squeeze faults accompanied by dextral strike slip [10]. After the earthquake, Chinese government set up a special project to study the genesis of the earthquake, and drilled 5 holes along the Longmen Shan fault zone (Fig. 1) [11]. They found the new graphitization phenomenon and pseudotachylyte that were not been paid attention to in the past within the earthquake rupture zone. They also trenched for near surface study and implemented seismic exploration study to detect underground structural changes. The conclusion of these works indicated that the earthquake was a kind of hidden explosion process.

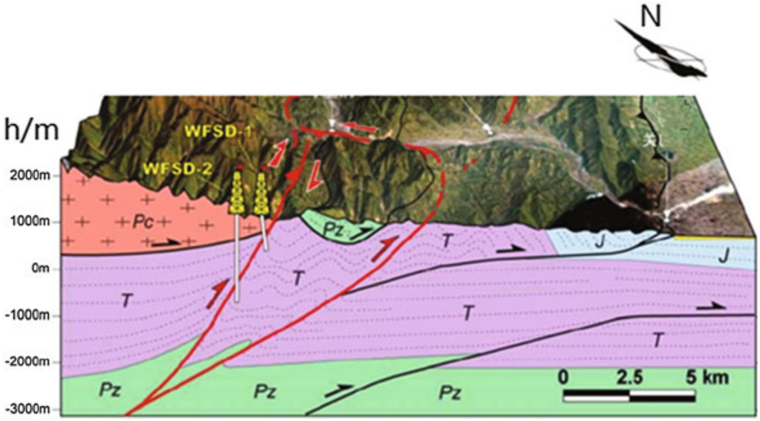

Fig. 1 The scientific drilling holes distribution of Wenchuan earthquake (modified from Wang [11])

There have been several major earthquakes in the history of the Japan South Sea trough, which is the most earthquake prone area. The seismic exploration study and drilling activities carried out in this area also indicated that hidden explosion processes occur in these range.

2 Underground Explosion Process of Earthquake

2.1 Shallow Evidence in Wenchan Earthquake

A geological sketch of trenches on the near surface part of the Mianzhu area in Wenchuan earthquake shows that there was an underground spray blast with the earthquake [12]. The clay sandstone spray penetrated into the red clay (Fig. 2).

Immediately after this earthquake, geologists found at least three burning explosion craters in Chenjiaba. Along the central fault F2, they found some similar phenomenon which includes circular pit and burning sticks with scattered porous dark brown rock on the surface of landslide (Fig. 3). This illustrates the close relationship between explosion and geological disasters within the earthquake region.

Zeng Mingguo's study [13] showed that before Wenchuan earthquake, great amount of energy had accumulated in the deep crustal region of Wenchuan area. The energy was mainly from outbreak of dephasing process of supercritical water fluid (SCW) at the critical moment of fault movement. At least, up to tens of millions tons TNT of equivalent energy may be released. The SCW is a

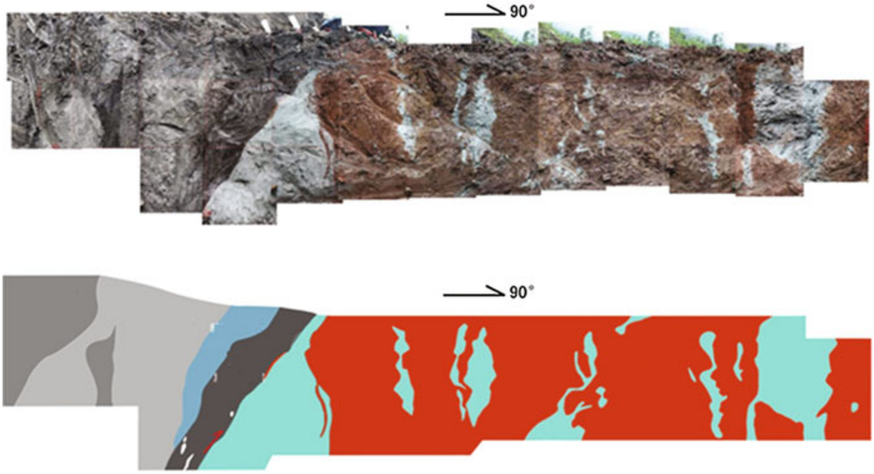

Fig. 2 Trench N sketch of Jiulong in Mianzhu

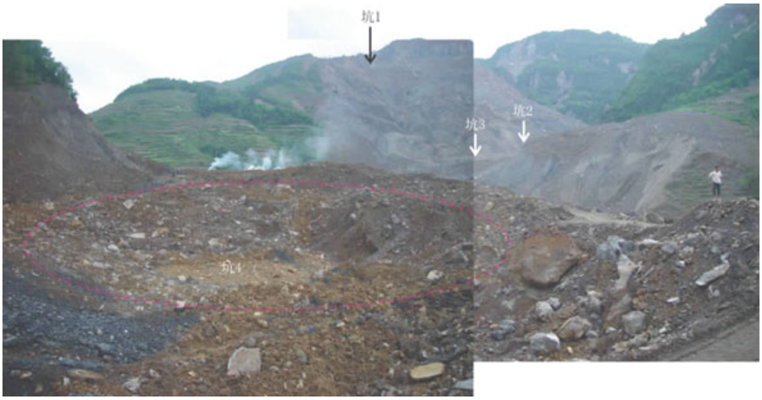

Fig. 3 Huge amounts of loose materials and circular pits over the Donghekou landslide

multicomponent of H_2O–CO_2–CH_4 in deep crust, whenever there is fault movement, it diphases and its volume expands several hundred times.

Study also show that in the earthquake fracture zone of Guanxian, complex rock body occurred due to strong graphitization phenomena accompanied with new pseudotachylyte formation [11]. But the newly generated fracture angle cuts across the old fracture zone. More exploration data shows that the new graphite strip was more than one and intensive on Wenchuan earthquake section. At the depth of the Wenchuan fault zone, the change in the fluid during the aftershock was observed. This shows the sudden increase in CH_4 [15]. More studies have shown that what causes of Wenchuan earthquake has close relation to the abnormally high pressured natural gas explosion in deep Longmenshan fault zone [16].

In addition, it was found that there was an obvious abnormal electromagnetic pulse during the period of this earthquake, which shows that there was not only the hidden explosion of the super critical fluid, but also the underground lightning explosion which causes strong graphitization and pseudotachylyte formation.

2.2 Deep Character of Wenchuan Earthquake

X ray spectrum analysis of mineral from the core of WFSD-1 hole showed that the pseudotachylyte glass within the fault zone had similar or near similar mineral composition with the fault gouge and breccia [12]. This suggests that they probably originated from deep booster injection, which causes at least part of the material to move to shallow crust.

The main slip fault of WFSD-1 hole is located at 589.2 m, its angle cuts across the old fracture [14]. How did it overcome the fault gouge in the old fracture zone? The main slip fault of WFSD-1 hole extends to WFSD-2 hole at a depth of 1449 m, corresponding to the fault zone FZ1449, but there was no fresh fault mud in the

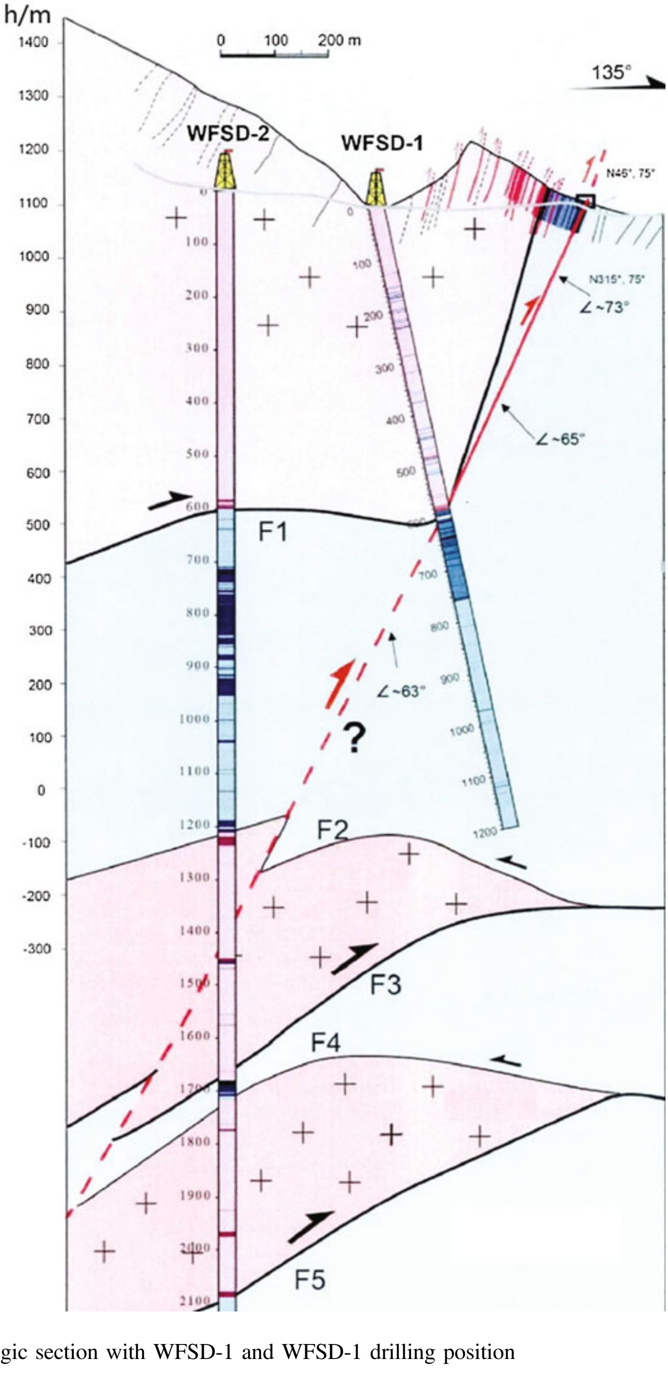

Fig. 4 Geologic section with WFSD-1 and WFSD-1 drilling position

borehole (Fig. 4), and no abnormal features in well logging [15]. A large number of liquefied cryptoexplosive breccia was found in these 2 drilling cores.

These evidences indicate that it is hard to explain the abnormal phenomena of these structures by the traditional genesis mechanism of structural earthquake, but it can be reasonably explained by the mechanism of cryptoexplosion.

3 Seismic Exploration Detection After Wenchuan Earthquake

There is characterized by abnormal low seismic velocity at depth of about 30 km on the deep seismic exploration profile across Wenchuan earthquake area. In magnetotelluric sounding profiles, it is shown as a low resistivity layer. These indicate the existence of deep crustal flow.

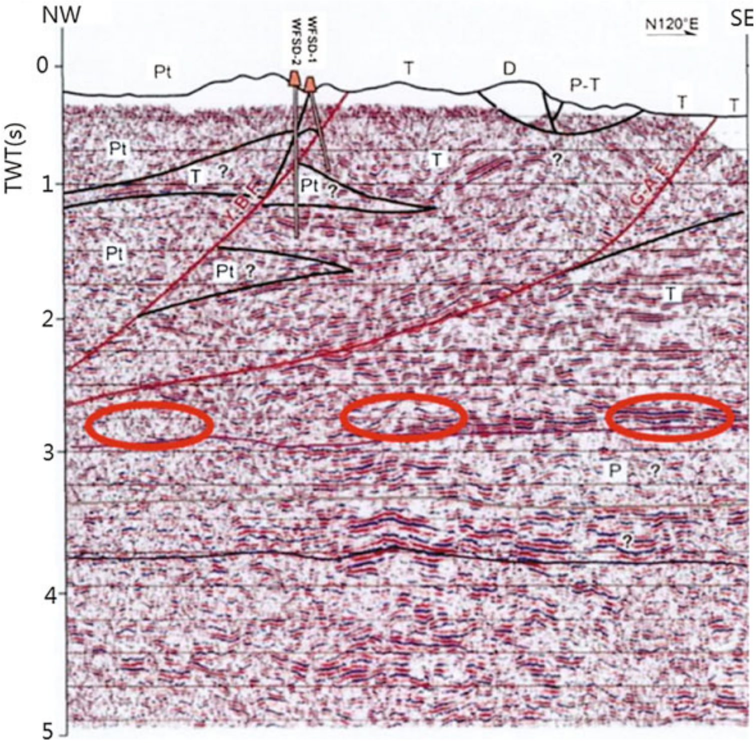

Fig. 5 Geological profile and seismic interpretation profile of Hongkou-Line15 [15]

After Wenchuan earthquake high resolution seismic exploration has been implemented, the geological profile and seismic interpretation profile of Hongkou-Line15 (the red ellipse circle is the newly added) is displayed in Fig. 5. WFSD-1 and WFSD-2 were located across this profile. Red ellipse circles represent different points of the same seismic reflection layer. The red ellipse at the right hand side of the section shows that the seismic reflection wave was regular, which means that there was rarely any fluid alteration, the formation is still intact. But in the middle ellipse region, the seismic reflection wave began to appear distorted with weak reflections, indicating that there exist a portion of the crust with fluid alteration and disturbance within the Wenchuan region. The left red ellipse presents the characteristics of clutter and weak seismic reflection, indicating that the region may have undergone a strong alteration or melting. The depth of this area is about 8–15 km.

High precision seismic exploration results show that the formation of abnormality and distortion are caused by the presence of high temperature and high pressure fluid within the deep crustal region. This shows that there was a hidden

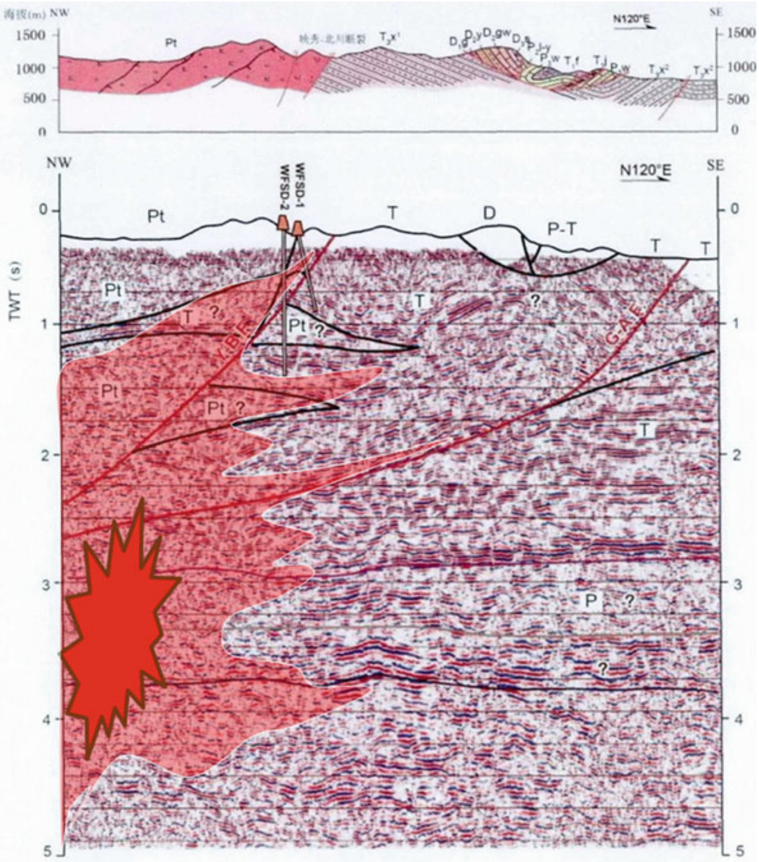

Fig. 6 Schematic diagram of cryptoexplosion interpretation from Fig. 5

explosion within the subsurface. Figure 6 shows a schematic diagram of the mechanism of cryptoexplosion. So, it is easy to explain the phenomenon that brought about the structure of WFSD-1 and WFSD-2, which was difficult to explain by the structure earthquake.

4 Seismic Exploration Detection for Earthquake in Japan South Sea

The Japan South Sea trough is one of the most earthquakes prone region in the world. There occurred 12 big earthquakes with magnitude of over 7.5 in 1300 years, more than half of the earthquakes were over the magnitude of 8, which includes Tonankai 8.2 magnitude earthquake in 1944 and Nankaido 8.3 magnitude earthquake in 1946.

The seismic exploration line is shown in Fig. 7 with red line.

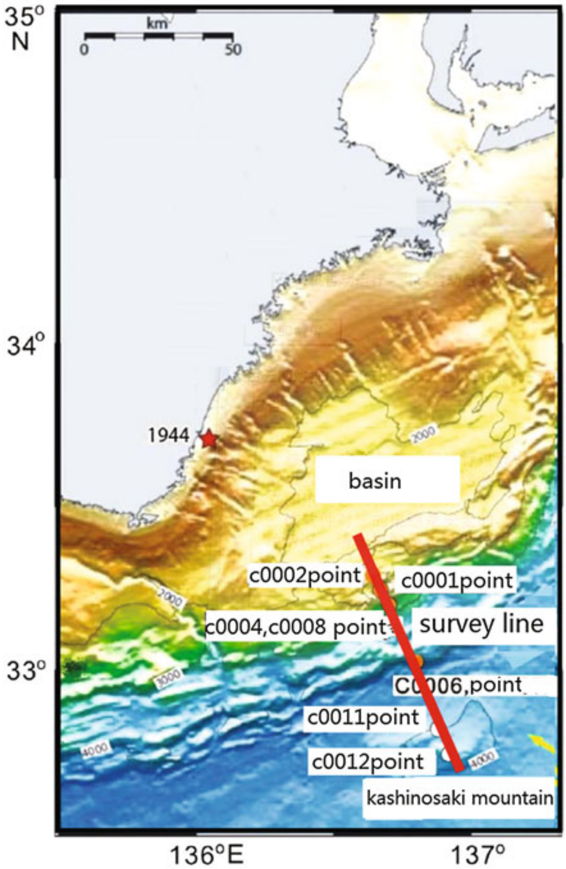

Fig. 7 The location of seismic exploration line in Japan South Sea

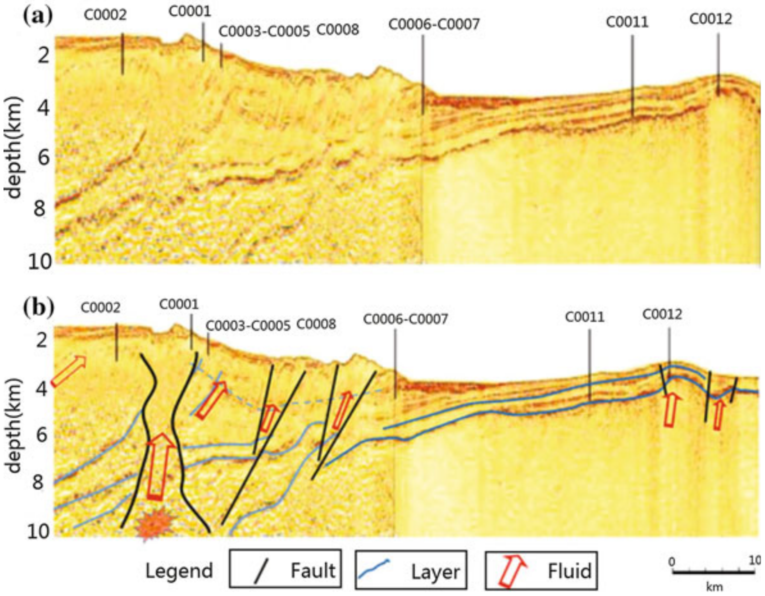

Fig. 8 **a** Seismic exploration profile. **b** The interpretation of the seismic exploration

The seismic exploration results in Fig. 8 clearly shows the existence of underground cryptoexplosion with crustal fluid flow. These may be caused by multiple earthquakes.

5 Conclusion

Large earthquake is caused by hidden underground explosion process with multiple focal points. The crushed structure and the underground lithological changes caused by earthquake can be detected by high resolution seismic exploration. The traditional seismic exploration technique can be competent enough for the detection of high incidence area of earthquakes. The formation mechanism for natural earthquake is characterized by underground explosion caused by instantaneous diphase of super critical fluid with fault movement. At the same time, the underground super critical fluid is a kind of charged fluid. It can also cause explosion with charge leakage during the earthquake process, which results in abnormal transient electromagnetic anomaly and earthquake light.

References

1. Reid, HF. The Mechanics of the earthquake, The California earthquake of April 18, 1906, Report of the State investigation commission. Vol. 2, Carnegie Institution of Washington, 1910. Washington, D.C.
2. Takeo Matsuzawa. Seismic theory and its application. Beijing: The Seismological Press: 1980. 1–135 (in Chinese with English abstract).
3. Song CQ, Qiu WL, Zhang ZC. Geological Principle. Beijing: Higher Education Press: 2005. 1–273 (in Chinese with English abstract).
4. Yue ZQ. Cause and mechanism of highly compressed and dense methane gas mass for Wenchuan earthquake and associated rock-avalanches and surface co-seismic rupture. Earth Science Frontier, 2013. 20(6):015–020 (in Chinese with English abstract).
5. Yang WR, Zeng ZX, Li DW, et al. Three-level tectonic model for intraplate earthquake, Earth Science Frontier. 2009. 16(1):206–217 (in Chinese with English abstract).
6. Du JG. Advances in deep fluid and Seismogenic media of the Earth. Earthquake monitoring, 1999. (3): 92–96 (in Chinese with English abstract).
7. Du JG, Li Ying, Wang CY, Liu Lei. High Pressure Geoscience. Beijing: Geological Publishing House: 2010, 1–288 (in Chinese with English abstract).
8. Jiang JF. New hypothesis about earthquake-and interesting revelation of disaster reduction. Beijing: The Seismological Press: 1994, 8.2 (in Chinese with English abstract).
9. Zhang BY. A hypothesis about the cause of the electromagnetism of earthquake. Earthquake Research in Plateau, 2005. 17(2):1–21 (in Chinese with English abstract).
10. Fu BH, Wang P, Kong P, Zheng GD, Wang Gang, Shi PL. Preliminary study of coseismic fault gouge occurred in the slip zone of the Wenchuan Ms8.0 earthquake and its tectonic implications. Actal, petrologica Sinica, 2008. 24(10):2237–2243 (in Chinese with English abstract).
11. Wang Huan. The structure Characteristics of the Wenchuan Earthquake Fault Zone and Its Relationship with Seismic Activity [D], Beijing: China University of Geoscience, 2011. 1–82 (in Chinese with English abstract).
12. Yang Guang. Fault rocks characteristics of the Anxian-Guanxian Fault, Longmen shan-Primary cores and surfaces study for the third well of the Wenchuan earthquake Fault Zone Scientific Drilling (WFSD-3) [D]. Chengdu University of Technology, 2012. (in Chinese with English abstract).
13. Zeng MG. Supercritical Water Fluid Explosion Genesis of Earthquake. Sichuan Geology, 2009. 29(3):371–377 (in Chinese with English abstract).
14. Li HB, Xu ZQ et al. The Principle Slip Zone of the 2008 Wenchuan earthquake: a thrust fault oblique cutting the Yingxiu-Beichuan fault zone. Geology in China, 2013. 40(1):121–139 (in Chinese with English abstract).
15. Wang Huan. Discussion on the fault weakening mechanism with characteristics of Pseudotachylites in the wenchuan earthquake. Qingdao: 7th National Symposium on Structure Geology & Geodynamics: 2014. 446.
16. Yue ZQ. The Source of Energy Power Directly Causing the May 12 Wunchuan Earthquake: Huge Extremely Pressurized Natural Gases Trapped in Deep Longmenshan Faults. News Journal of China Society of Rock Mechanics and Engineering, 2009. (2):45–50 (in Chinese with English abstract).

Lamellate Layer Convergence Algorithm Based on the Magnetotelluric Equivalence Principle

Rongjiang Tang, Xuben Wang, Lu Gan and Juntao Zhang

Abstract The non-uniqueness problem of inversion is a large obstacle in improving geophysical interpretation resolution. At present, the main factors which affect the non-uniqueness of the solutions of magnetotelluric sounding are equivalence and volume effect. For example, true parameters of low resistance lamellate layer are difficult to determine by inversion because of the 's' equivalence, and we usually get the biased thickness and resistivity that meets equivalence condition, which is clearly not consistent with the actual situation. In order to make the inversion results correspond to the actual situation better, the new assistant algorithm based on the Marquardt inversion and equivalence principle was designed in this paper, and we used 'S' and 'H' equivalence principle flexibly to make the thickness and resistivity converge to a result that is more close to the actual situation. This method provides a convenient means of combining magnetotelluric sounding data with logging and seismology data to make associated interpretation or inversion, so that thickness and resistivity of target can be determined effectively.

Keywords Equivalence · Lamellate layer · Magnetotelluric

1 Introduction

Multiplicity of solutions for geophysical inversion can be explained by the general solution of differential equation, or a set of solutions. But there is only one real geo-electric section which corresponds to a special solution of differential equation. In other words, geophysical inversion usually have several inverse solutions that

---

R. Tang (✉) · X. Wang · L. Gan · J. Zhang
Geophysical College of Chengdu University of Technology,
Chengdu 610059, China

X. Wang
Key Laboratory of Earth Exploration and Information Techniques
of the Ministry of Education, Chengdu University of Technology,
Chengdu 610059, China

Q. Di et al. (eds.), *Technology and Application of Environmental and Engineering Geophysics*, Springer Geophysics,
DOI 10.1007/978-981-10-3244-8_24

can fit the observed data. At present, the geophysical inversion technique can neither determine the general solution for inversion nor can it accurately present the special solution required, but only presents a special solution from many special solutions. This is the tricky non-uniqueness problem of inversion.

The effective way to obtain the true information about the model 'given' by the observed data is to use the constrained inversion method, joined with effective a priori information, to narrow the scope of the non-uniqueness of solution and to make the solution more approximate to undetermined geophysical model. The lamellate layer identification problem of magnetotelluric is a typical non-uniqueness problem. If a lamellate layer of real geophysical model parameter is, and the observation data is d, then which meet the equivalence are all solutions fitting the observed data. And any solution fitting the observed data is meaningful, because it is presented as if it contains the same information as the actual geophysical model. In order to determine the lamellate layer effectively, adding a priori condition to constrain the inversion process is a good idea, but this will increase the cost of exploration and result in the decrease of exploration efficiency. And even if the a priori conditions are added, the imperfection of the conditions and the different choice of weighting coefficient will give rise to different optimal solutions, so the inversion problem still exist. Therefore in this paper, a lamellate layer convergence algorithm was raised based on the equivalence principle, which can further optimize the model parameters on the basis of inversion and control the inversion results effectively. This method makes the thicker inverted layer converge to the lamellate layer and reduce the initially large resistivity value.

2 Literature Review

To study equivalence; Yan zhong Luo has discussed the equivalence of the direct current sounding G type curve and its application in the quantitative interpretation [1]. Shunfu Nie and Baoheng Liu on the other hand discussed the range and the law of the H equivalence of the direct current electric sounding in detail [2]. Also, Simms and Morgan used three methods to determine the range of parameter variation, standard error, error ellipses, and forward modeling, and demonstrated that the forward modeling method can achieve the best effect [3]. Simms and Morgan compared different inversion schemes that allows all parameters to vary to get the conclusion that when several models fit a set of data equally well, then the model with fewer parameter is deemed the best, and the modified F-radio was proved to be a good statistical parameter for determining the optimum number of layers to model the data [4]. Xiuming Shan designed effective iterative algorithm to get depth and thickness of high resistance layer according to unfaithful resistivity of high resistivity thin layer [5]. Shunfang Xu used Logging-constrained Inversion to correct direct current electric sounding S equivalence in dam survey [6]. Lastly, Charles H. Stoyer analyzed the DC and EM Data for layered model using the Resolution

Matrix, and the results concurred with the equivalence principle for surface thin layer and buried layer and the method is useful for the interpretation of the equivalence of the inversion results.

3 Lamellate Layer Convergence Algorithm Theory

In Magnetotelluric method, one dimensional layered model is relatively easy. The wave impedance of each layer in the layered one-dimensional medium is derived from the bottom layer, and then we can get the wave impedance of the number m layer:

$$Z_m = Z_{0m} \frac{1 + \frac{Z_{m+1} - Z_{0m}}{Z_{m+1} + Z_{0m}} e^{-2k_m h_m}}{1 - \frac{Z_{m+1} - Z_{0m}}{Z_{m+1} + Z_{0m}} e^{-2k_m h_m}} \tag{1}$$

In Eq. (1), this is the wave characteristic impedance of the number m layer is the thickness of the m layer and is complex wave number of number m layer.

The essence of Magnetotelluric equivalence principle is that when and changes, the wave impedance remains invariant. According to Eq. (1), is a function of the thickness and resistivity of the layer, which can be written as

$$Z_m = f(h_m, \rho_m) \tag{2}$$

In order to find out the variation law of the equivalence, we designed a simple three layer model with background resistivity of 1000 to calculate the interlayer's wave impedance contour map, having the interlayer thickness as x-coordinate, and the resistivity as y-coordinate.

According to Fig. 1, when the resistivity and thickness are relatively small, the wave impedance shows a linear change, this is the S equivalence; when thickness is small and resistivity is greater than the background resistivity, impact of the larger thickness on wave impedance will no longer be distinct, this is h equivalence. Low resistance lamellate layer meet S equivalence principle, while the wave impedance of inversion results are usually outside linear range. So, this article proposes an effect technique to converge wave impedance of lamellate layer close to the linear range. When the wave impedance is close to linear changed range, we can convey in the formula below:

$$\left| \frac{f(h_m + \Delta h_m, \rho_m) - f(h_m, \rho_m)}{f(h_m, \rho_m)} - \frac{f(h_m, \rho_m + \Delta \rho_m) - f(h_m, \rho_m)}{f(h_m, \rho_m)} \right| = \varepsilon \tag{3}$$

The right (change proportion) is the same as the left and it represents the convergence step. Its value is usually between 3 and 10%. If this is too small, there will

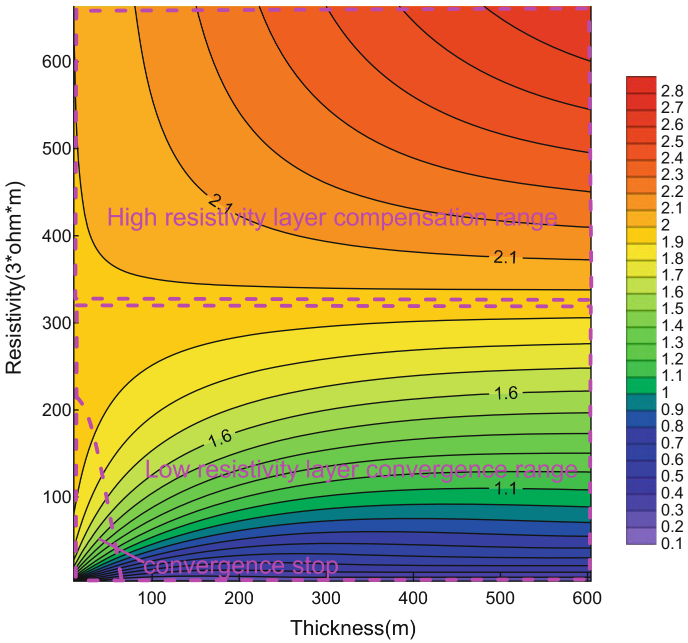

Fig. 1 Wave impedance equivalence isoline map. *Dotted box* represent high resistivity layer compensation range, low resistance layer convergence range, and convergence stop range respectively

be an increase in computation time and if too big, it can lead to lower convergence precision. shows the degree of convergence; smaller could result in higher degree of convergence.

3.1 Using S Equivalence for Low Resistance Lamellate Layer Convergence

According to Fig. 1, when the target layer's resistance is low and remain constant and corresponds to only the inverse solution of according to (1) is difficult even when is known. So, we can use an iteration method defined as;

$$\rho_m = \frac{Z_m^2}{-i\omega\mu} \times \left(\frac{1 - \frac{Z_{m+1} - Z_{0m}}{Z_{m+1} + Z_{0m}} e^{-2k_m h_m}}{1 + \frac{Z_{m+1} - Z_{0m}}{Z_{m+1} + Z_{0m}} e^{-2k_m h_m}} \right)^2 \qquad (4)$$

First, the inversion data of the number m layer's, and were worked out, then gradually reduced according to the speed of. Everytime reduces, the only corresponding is calculated using (4), we can get the final value after convergence until and meet (3). Now low resistivity lamellate layer convergence calculation is completed.

3.2 Thickness Compensation Using H Equivalence

After convergence, the thickness of the low resistive thin layer is reduced, which means the depth to the layer become shallower. We want to make the convergence layer to be at the center of the original layer. The process has two step: firstly, we added half of the changed thickness of low resistance layer to the upper high resistance layer, then calculated the new resistivity of the upper layer using the new thickness and Eq. (4). The purpose of using only half of the changed thickness is that the low resistivity layer after convergence is still in the middle of the primary low resistivity layer instead of the top.

3.3 Error Sources and Processing in Convergent Algorithm

When we used the equivalent convergence algorithm, we hoped to keep the wave impedance of the layer constant and get the resistivity and thickness of the convergent layer by iteration. This process requires that we consider only a certain frequency (we assume) of equivalent convergence, which changes the resistivity and thickness of the target layers but keeps the wave impedance of all layers constant. But when frequency changes to, the resistivity and thickness obtained by convergence when frequency is cannot guarantee that the wave impedance of convergence layer and layers above the convergence layer will remain constant when the frequency is. The change in wave impedance will inevitably lead to an error in the estimated apparent resistivity. Thus, Eq. (5) clearly describes the wave impedance of each layer's as a function of thickness, resistivity, frequency and the wave impedance. This is also a function of frequency.

$$Z_m = f(h_m, \rho_m, \omega, Z_{m+1}) \tag{5}$$

To minimize the error response, what we have to do is make the difference between wave impedance of the layer and the wave impedance after convergence as small as possible when the frequency value is arbitrary, while on the basis of guaranteeing the convergence layer's wave impedance remains constant when the frequency is. That is to say, we need to adjust the optimal frequency f1 and the degree of convergence to make the difference between the wave impedance of the layer and the wave impedance after convergence reach the minimum when the frequency value is arbitrary. At this time, the response error is also the smallest.

4 Examples on Synthetic Data

Lamellate layer convergence algorithm is based on the equivalence principle of layered model, so this theory can only be used for one dimension model. Figure 2a shows a three layer geo-electric model for/from magnetotelluric sounding curve. In the model, the resistivity of surrounding rock was 2000 and the middle thin layer's resistivity was 200, layer's thickness was 20 m. Figure 2b shows apparent resistivity response curves, Marquardt inversion and lamellate layer convergence

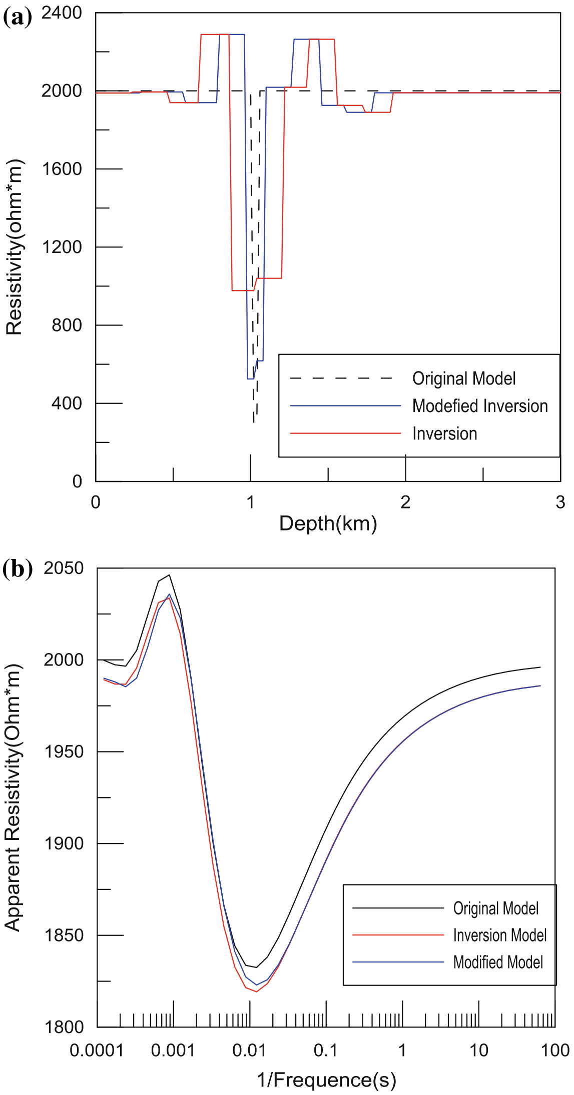

Fig. 2 **a** Damping least squares inversion and equivalence inversion contrast (one lamella). **b** Damping least squares inversion and equivalence inversion outcome fitting the observed data

outcome. Overlapping of three curves demonstrates the validity and effectiveness of convergence algorithm in this paper. In Fig. 2a, after one dimensional Marquardt inversion, we got a layer with thickness of 500 m and resistivity of 1000 (red line), whose original thickness was 20 m and resistivity was 200 (dotted line). This was far from what we expected. But after the lamellate layer convergence, we got a layer with thickness of 100 m and resistivity of 500 (blue line), which is much more closer to the actual model.

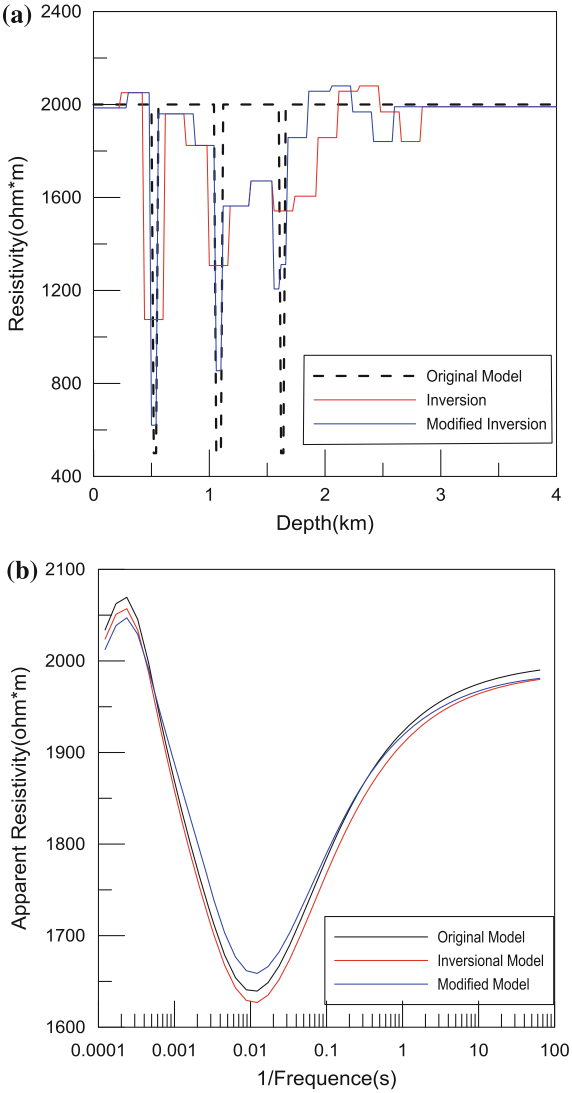

Fig. 3 **a** Damping least squares inversion and equivalence inversion contrast (three lamella). **b** Damping least squares inversion and equivalence inversion outcome fitting the observed

But in the actual production, we do not know whether it is a layer with a thickness of 500 m and a resistivity of 1000 or a layer with a thickness of 100 and a resistivity of 500. The realization of this method allows us to increase the number of inversion models and more convenient for us to select the optimal model combined with seismic data and geological data to make comprehensive interpretation and inversion evaluation. In some cases, where the target body is already know to be a lamellate layer and we only need to determine its resistivity by inversion, the convergence algorithm is particularly effective. Because when we arbitrarily determine the thickness of the thin layer or resistivity of one of them, we will easily get the other one.

Figure 3 shows a geo-electric model with 3 lamellate layers. The thickness of each thin layer was 50 m, and the resistivity was 500. The distance between the lamellate layers was 500 m and the surrounding rock's resistivity was 2000.

In Fig. 3a, Damping least square inversion results correspond well to the position of the lamellate layer, but the inverted resistivity value was very different from the real resistivity value. Both the resistivity and thickness, based on the equivalence principle and layer convergence algorithm, were more closer to the real model than the result from damped least square inversion method.

5 Conclusion

- In a relatively simple layer, the lamellate layer convergence algorithm can be used to bring the inversion results more closer to the actual geology.
- The algorithm is used for inversion interpretation software, thus form human-computer interaction in the process of mapping the lamellate layer. If the unknown formation is a lamellate layer, the method can increase the number of inversion solutions fitting the observed data, and make further evaluation of inversion results. If the formation is known to have a lamellate layer, the method can directly control the inversion solution to converge to our desired thickness of lamellate layer, at the same time obtain a more realistic lamellate layer resistivity.
- In many cases, the resistivity mutations and the gradient information can correspond to the same sounding curve, and this is another kind of equivalence in MT. If the convergence algorithm is used continuously, wrong conclusions can be drawn from the obtained result.
- The theory of this method is based on one dimensional MT equivalence principle, so if used in 2d inversion, it will have larger limitations. Hence, further study will involve 2d inversion with equivalence.

Acknowledgments This study was supported by the National Natural Science Foundation of China (grants 41274078).

References

1. Yanzhong Luo. G type curve equivalence and its application of quantitative interpretation in electric sounding curve[J], 1979, 3.
2. Shunfu Nie, Baoheng Liu. The scope of direct current sounding H equivalence[J]. 1986. 5. 57–60.
3. J E Simms and F D Morgan. Resistivity inversion parameter bounds in the presence of equivalence[C]. SEG Technical Program Expanded Abstracts 1991, 421–424.
4. J E Simms, F D Morgan. Comparison of four least-squares inversion schemes for studying equivalence in one-dimensional resistivity interpretation[C]. Geophysics, 1992, 57(10): 1282–1293.
5. XiuMing Shan, Zhenming Feng, Biao Chen. Effective iterative inversion algorithm in the electromagnetic sounding when High resistance thin layer exists [C]. The Chinese geophysical society 10th conference collected papers in 1994. P631. 81.
6. Shunfang Xu, Zhenning Li, Jinzhan Li. Electrical sounding curves S equivalence correction study in the dam survey. CT Theory and Applications[J]. 2003 12(1). 17–20.

Discussions on Resolution of Different TDEM Survey Techniques for Detecting Water-Bearing Structures

Lei Yang and R.W. Groom

Abstract It is common when using TDEM to measure only inside the transmitter loop. In groundwater and environmental applications, this is almost ubiquitous. This situation arose because inversion applications were available only for central loop readings (Anderson in Improved digital filters for evaluating Fourier and Hankel transform integrals, 1975 [1]) and geoscientists thought of such readings as soundings similar to resistivity sounding applications. But, should we consider TDEM data as analogous to reflection data and measure proximate to the source or as analogous to refraction data and measure away from the source? In mining applications, three-dimensional modeling has long been available and the use of multiple measurements inside and outside loops has been common for three decades. In this paper, we examine several misunderstandings and problems associated with in loop approaches by comparing results from different TDEM survey techniques. We utilize both synthetic and field data for our studies. Both synthetic and field data indicates that the use of in loop data is potentially dangerous, as this location is poor for sensing resistive structure. In addition, single station inversion is limited without considerable knowledge of the geology within the study area, as 1D inversion is highly non-unique. The use of multiple data in a 1D inversion helps locate the correct model subspace and it appears that out-of-loop data has fewer possible models. Fixed loop surveys can provide more accurate deep inversion results if the ground is sufficiently one-dimensional. It also provide an array for faster surveys and more area coverage.

Keywords TDEM survey techniques · Modeling · Decay curve analysis · Water-bearing structure

---

L. Yang (✉)
Department of Xin Jiang Geology Exploration, No. 203 Research Institute of CNNC, Xian Yang, People's Republic of China
e-mail: 1071927924@qq.com

R.W. Groom
Petros Eikon Incorporated, Orangeville, ON, Canada
e-mail: rgroom@petroseikon.com

Q. Di et al. (eds.), *Technology and Application of Environmental and Engineering Geophysics*, Springer Geophysics,
DOI 10.1007/978-981-10-3244-8_25

1 Introduction

A TDEM system induces current in conducting earth (Faraday's law) and this current migrates outward and downward with increase in time after the time varying current is propagated or turned off. The current moves outside the loop and downwards away from the transmitter and thus if the sensor is positioned inside the loop, it is located further away from the current concentration as time progresses. We suggested that the receivers outside the loop should be more sensitive to the deeper rocks and soils as they are closer to the concentration of migrating currents beneath the earth surface, thus providing better resolution of different layers beneath the earth. The rate of migration is determined by the resistivity of the soils and rocks. In very resistive environment, the current's concentration is not observed except in very early time and thus the more resistive the ground, the poorer is the results of the in loop inversions.

2 Current Migration Synthetic Studies

For this study, we considered zones of unconsolidated sediments, particularly to finding a saturated sandstone layer. The unconsolidated rocks were underlain by more consolidated, resistive rocks. This model is representative of our survey site. The instrumentation utilized here were fairly standard. We utilized a small loop, 100 m by 100 m; a bipolar current waveform with an approximate linear turn-off (ramp) and measurements of the time varying magnetic field in the off-time. In this study, the instrumentation utilizes coils to measure the voltage and thus dB/dt is sensed by the antenna. However, most conclusions are unaffected by measurement with a magnetometer. In our examples, we utilized a 25 Hz base frequency, as this serves to illustrate all of our points. We will utilize fairly standard time windows with no particular early window, so as not to overcomplicate the analyses with bandwidth issues. For forward modeling algorithm, standard frequency domain simulations (e.g. [2–5]) with a non-standard band limited frequency was used and then transformed into time domain [6], which is more representative of the typical instrument's system response.

We simulated the horizontal components of the electric field (Ex, Ey) at a depth of 200 m in the 6 Ωm clay zone using our standard model (Fig. 4). We displayed the total current density as a function of horizontal position at this depth for a current of 25A. Figure 1 shows current migration at 2.2 ms after the end of the ramp (0.4 ms). We observed from this figure that the areas of largest current concentration are outside the loop and thus, the total current underneath the loop and within the clay zone is small. When attempting to resolve this layer, receivers at a distance of approximately 200 m from the centre would be more useful.

In Fig. 2, the propagation was observed by displaying the amplitude of Hz measured at the earth surface as a function of space at different times. Figure 2a

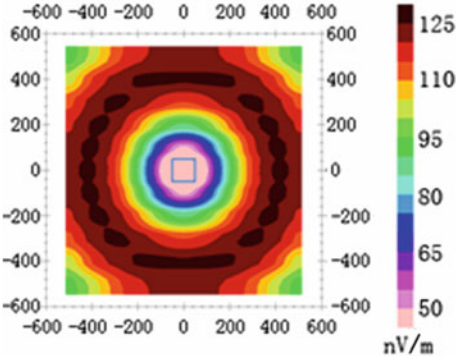

Fig. 1 Currents at mid-time at z = 200

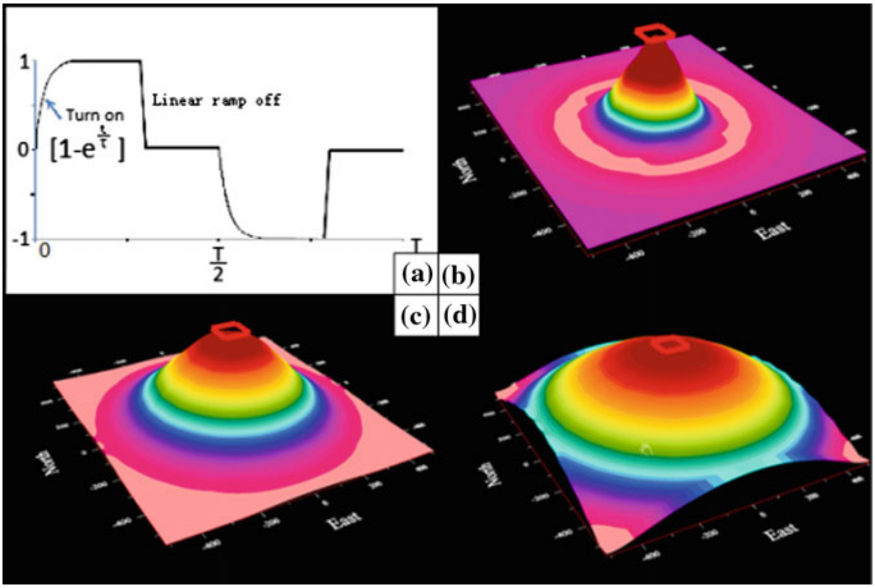

Fig. 2 Subsurface current propagation measured at the surface as change in Hz

represents the current waveform, Fig. 2b–d map the early, intermediate and late time current migration. We can observe that at early times the induced currents are concentrated near the loop but by late time, they are now distributed over a very large region.

Figure 3 displays the total horizontal current as a function of depth for the standard model below two positions, one inside the loop and the other one outside the loop. Figure 3a shows these fields at the early time, Fig. 3b shows the fields at channel 15. The red curve represents the total electric field in mV/m below a point

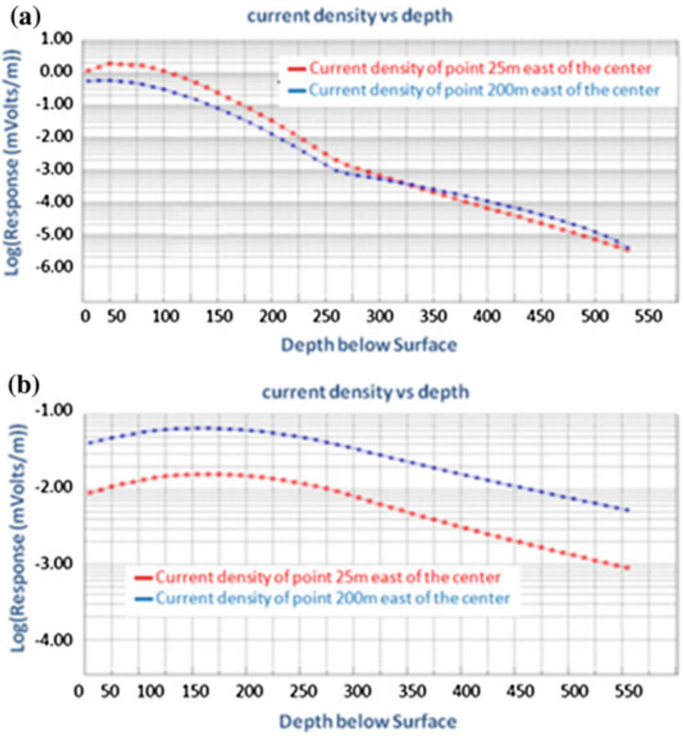

Fig. 3 Total horizontal voltage below an inside and outside station

25 m east of the centre of the loop and the blue curve the same field but below a point 200 m east of the center of the loop.

At early time, the electric fields are concentrated near the surface and closer to the centre of the loop but with increase in time (2 ms), the electric fields, and thus the currents have migrated not only downward to be concentrated within the conducting zone (between 45 and 245 m) but also outward so that the currents at 200 m are a full order of magnitude greater than those below the loop. For inversion of measurements carried out inside the loop, the enhanced current at large distance is not of great use in resolving deeper layers.

3 Simulation Result Comparison

Figure 4a shows the basic model that was utilized for this study. Figure 4b shows the response decay for a central loop coil receiver due to the model and the waveform described, and normalized to current. Figure 4c is a comparison between

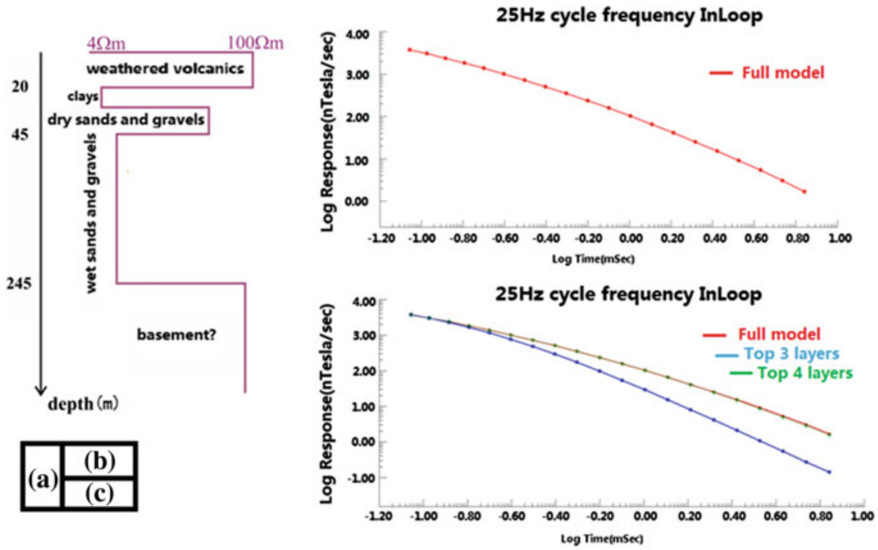

Fig. 4 Comparison of in-loop data from standard model versus similar models

the response of our full model, the response (blue) when the 3rd layer is infinite and the response (green) when the 4th layer is infinite.

With this comparison, we learnt that the simulated data with an in-loop configuration cannot clearly distinguish the characteristics of the basement, and without an excellent a prior starting model, the basement is difficult to discriminate. This model at later time, with lower base-frequency, will stretch the dynamic range even further. Even at 25 Hz base frequency, the response covers 3 decades of amplitude which is hard for most commercial equipments to reproduce such a dynamic range.

Figure 5 is a comparison of different inversion results calculated from the in-loop data. Figure 5a is a 5 layer over a half space inversion [7] with no constraints using only a half space as the starting model. The blue data line is the simulation of the inversion of model shown below the plot but utilizing only the top 3 layers for the inversion. This demonstrates that at least 3 models could have identical response. Figure 5b is a multi-layered Occam inversion [7], starting with a half space. Again, we have another model with precisely the same response but again little resolution of actual structure. Figure 5c represents an entirely different approach. We assumed that we have some knowledge of the structure but not the true thicknesses or resistivities. Thus, we utilized a starting model which has alternating resistive and conductive layers. The blue curve is the response of the starting model. It does not have the same amplitude but does have similar decay pattern as the true model. The derived inversion model is shown in green and it is quite close to the true model. There were no constraints applied other than the number of layers. This can be described as a case of sampling the starting model from the correct model subspace.

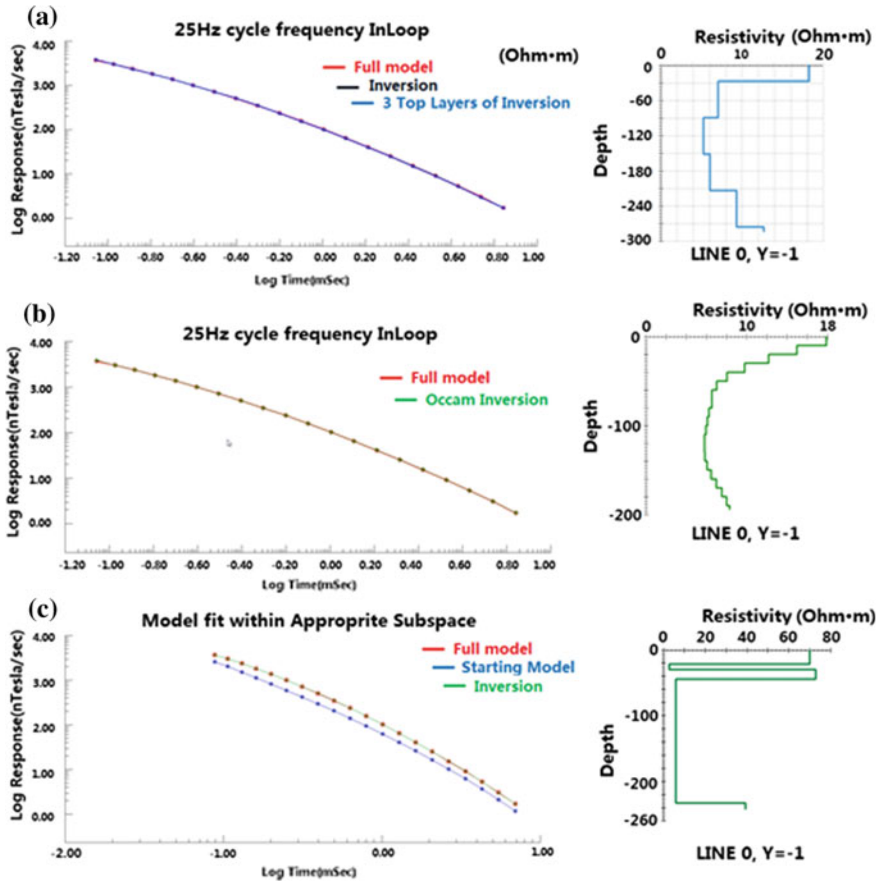

Fig. 5 Comparison of different inversion results

All curves from different inversions above can fit the original curve reasonably well, but only with a starting model which is approximately the correct structure can reproduce a result which is close to the real situation underground. From this experiment, we can see that a given position and separation has multiple possible models, particularly with data centered within the loop. Without the use of geological control to constrain the model, we cannot derive the correct model. As demonstrated, smooth over-parameterized inversions do not provide accurate estimations of resistivity or depths but only a rather unfocussed image of the ground.

For inversion problems with many suitable models, it is standard theory to use additional data to find more unique models. For TEM soundings, it has become quite common to use multiple base frequencies in order to have more data available and to have more low frequency data in an attempt to derive better depth resolution. However, if the same instrument is being used, there will be little variation in the decays except additional late time channels.

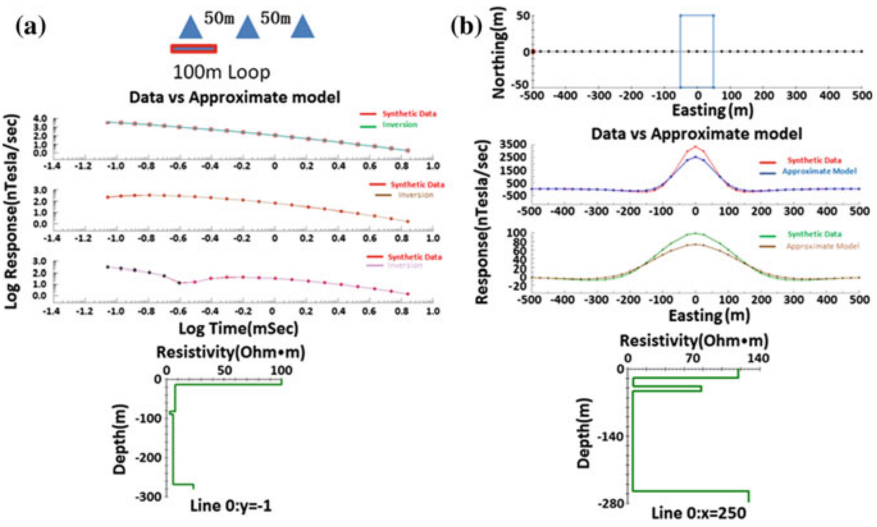

Fig. 6 Multiple data strategies

In the second simulation, we utilized a central loop measurement with an additional two measurements outside the loop. This is analogous to the step-wise moving loop technique [8] adopted in the Canadian Athabasca basin for uranium exploration. In the first example, we used no a priori information but rather a uniform half-space starting model. Figure 6 shows results utilizing multiple data points. In Fig. 6a, we drew at the top the array configuration, the loop in red and the 3 stations as blue triangles. The 3 plots below are all in Hz and represents response from the three locations. Model results for a single inversion, utilizing the data for 3 stations were plotted as well for each location.

For Fig. 6a, we used as a starting model, 4 layers plus a half-space with all layers having a resistivity of 100 and the top 4 layers, equal thickness. From the inversion result, we can see that the approximate depth of top layer is found plus the average resistivity down to basement. The depth to the top layer is quite close, a conductive zone is found but the model misses the intermediate resistor although the depth to basement is quite close. This result indicates that 3 separations reduce the number of possible subspace model types but in this case even 3 separations are not sufficient for a precise resolution.

Figure 6b exaggerates this approach by utilizing many data stations. The first step is to find an approximate model using simple forward modelling to find a model which resembles Hz and Hx at all times. Figure 6b shows the results of the approximate model at an early time channel and at a late time. The approximate model was used as the starting model and then the inversion begins from west, inverting the first station and the inversion proceeds utilizing the previous inversion as a starting model. If the ground is approximately one dimensional and slowly varying then this approach is both effective and fast [9]. This seems practical as we

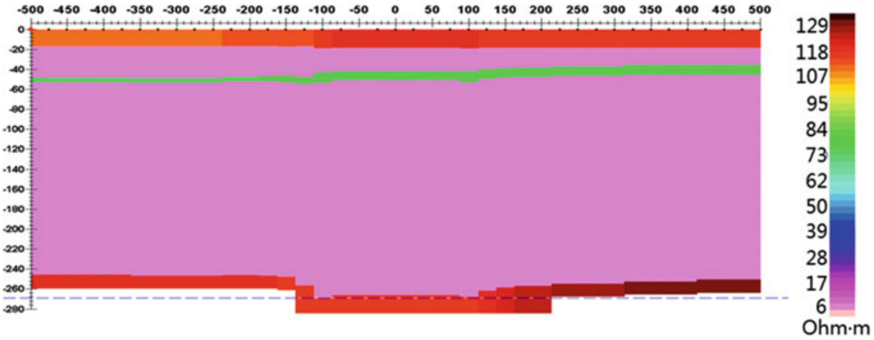

Fig. 7 Inversion results for fixed loop survey

must assume that the lateral gradients in the ground resistivity are quite slow for any 1D inversion approach. The final results are show in Fig. 7. The results are quite good implying that the non-uniqueness outside the loop is less severe than inside the loop.

4 Field Survey Examples

The synthetic studies were insightful but we must now consider practical issues regarding the theoretical work. While there have been numerous field surveys performed over the years (e.g. [8–10]), we devised a number of specific field tests which could be performed in a very favorable site. All the test surveys were carried out during May 28, 2015 and June 3, 2015. The purpose for these tests were to confirm those conclusions from our synthetic data. The survey was carried out in a very flat Gobi terrain filled with feathered volcanic gravel as the surface is flat and the stratigraphy is expected to be very flat. The geology and the survey configuration are shown in Fig. 8.

This test site is located in the mid-south of the Hami basin, located between Kazakhstan plate, Siberia plate and Tarim plate. Three tectonic units exist in this basin: North depression, Lake Ayding slope and the Nan hu rise. Our working area is located in the north of Nan hu rise.

Three survey configurations were utilized. First, 3 profiles (L181, L82, L183) were measured from a single fixed loop. As part of a separate test, a ragged loop was used with 50 m line spacing and 40 m station spacing. The base frequency utilized was 25 Hz and all three components of the time varying magnetic field were measured utilizing a Geonics Protem receiver, 3D-3 coil sensor and an EM67 transmitter. Following this survey, a 200 m × 200 m loop was laid out in the center of the 3 profiles and again with 25 Hz, 5 stations were measured on L182. Stations were located at 300 and 200 m north and south from the loop center and at the loop center. Again, all 3 components were measured.

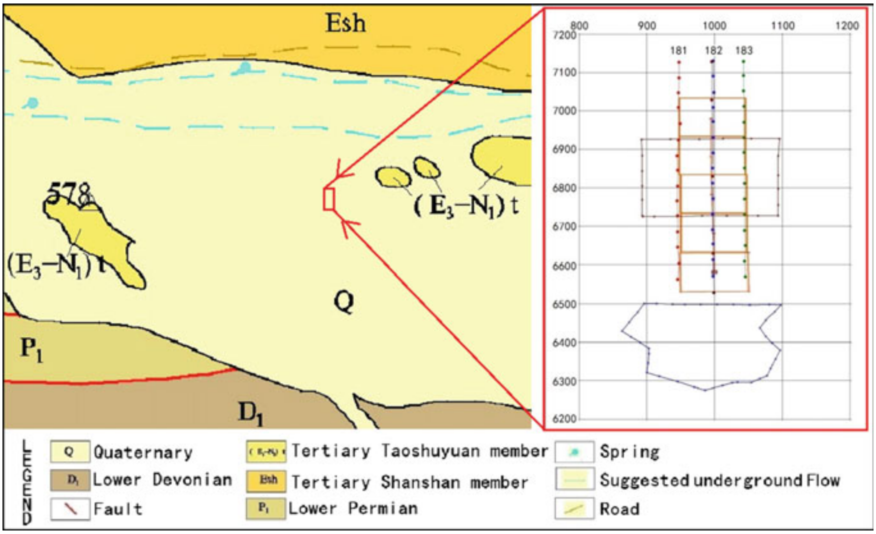

Fig. 8 Survey configuration map

Finally, a moving loop configuration was utilized along L182. A square 100 m loop was used and data were taken at the center of the loop, and 70 and 150 m north of the center of the loop. 15 stations were sampled with 3 components measured at 25 and 2.5 Hz.

First we would like to focus on fixed loop data since the fix loop data can give a quick information about a large area if the resistivity structure is approximately 1D. If the ground is not approximately 1D, then in-loop data is almost certainly of little value and thus any 1D inversion based on in loop data is likely not true representation of the subsurface structure. Figure 9 shows variation in Hz and Hx, which are representative of current propagation. Figure 9a presents the 3rd Hz channel, and Fig. 9b the 9th channel. From this, we observe that there is a weak structure striking a few degrees south of EW. From Fig. 9b the 9th Hz channel, we observed quite clearly that the currents are not migrating uniformly with Y and there is a strong three-dimensional structure to the north. Figure 9c shows the magnetic field (Hx) propagation observed at the 14th channel and it shows very clearly a shallow structure near the loop as well as the northern structure.

Observation of the fixed loop data shows that the late time data does not conform to a 1D structure in the northern portions of the survey. Thus, first we chose to invert for a 1D inversion model using the first 8 time channels of Hz with the model to fit the 12 data stations nearest to the loop. Figure 10 displays the results. Figure 10a is the Hz channel 2 inversion result and we observed that the data in this manner is quite sensitive to both the top and 2nd layer resistivity as well as the thickness of the top layer. However, we observed that the lack of 1D response in Hz measured at a few hundred meters from the loop as well as in Hy. The same situation appears in Hz measured at channel 6 (Fig. 10b). The model fits Hz data

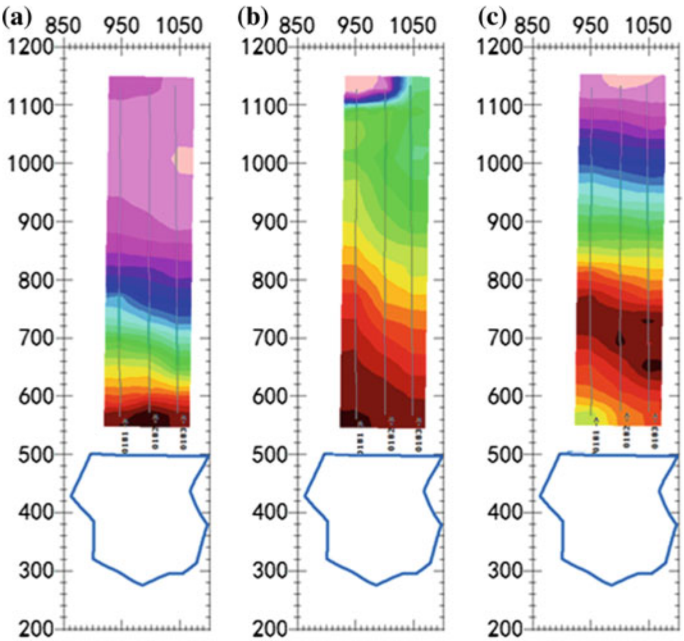

Fig. 9 *Left* to *right*, Hz channel 3, 9 and Hx channel 14

quite well but we can start to see the response from a 3D structure near the end of the line. The final model is characterized by a 142 Ω-m layer with a thickness of 68 m, 410 Ω-m with a thickness of 538 m and underneath them a very strong resistor. However, the resistor has very little effect on the synthetic data due to its depth.

The inversion results of data from Station 6630 from the 200 m loop are displayed in Fig. 11. The 3 southern stations were jointly inverted for one model. Only Hz was used in the inversion and all the time channels except the first and the last were utilized.

Initially, a 5 layer over a half-space model was used but this produced essentially a layer over a half-space result. The model is simply a 220 Ω-m layer with thickness of 525 m underlain by a resistor. The data was unable to resolve either a difference in the resistivity of the upper 500 m. However, the depth to the resistor was well resolved and the resistivity of this resistor must be over 2000 Ω-m. We could not find a 1D model that fits the 4th station from the north for both Hz and Hx, indicating that these stations were sensitive to the 3D structure in the northern part of the study area as observed in the fixed loop data.

For the 100 m moving loop data, we will first examine the 2 southern loops; Loop 1 and Loop 2. Inversion results from the two loops are shown in Fig. 12. Recall the 3 station inversion result for the 200 m loop: 220 Ω-m layer with thickness of 530 m and 8000 Ω-m resistor below it. The difference between these

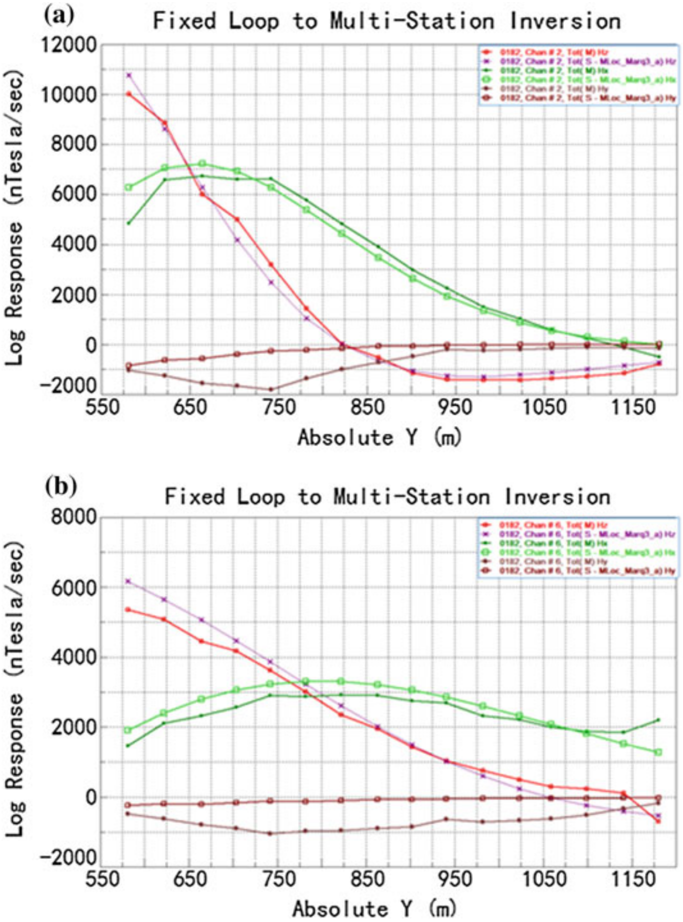

Fig. 10 Fix loop Hz data modeling result

two 100 m loops is that the top layer is divided into an upper portion somewhat more conducting than 220 and a lower section somewhat more resistive. This feature was not resolved by the 200 m loop.

Figure 12a shows a comparison of the in-loop data with the 3 station inversion from 200 m loop. The 200 m loop model was relatively close but the in-loop measurement indicated that there is a more conducting top layer than the 220 Ω-m layer and then a more conducting intermediate zone, followed by the resistive basement.

Figure 12b shows a comparison of the data at distance 70 m to the 3 station inversion result from 200 m loop. The two curves of the 200 m loop model were relatively close but the 70 m measurement indicates that 220 Ω-m is about the average resistivity. Figure 12c shows a comparison of the data at distance 150 m to

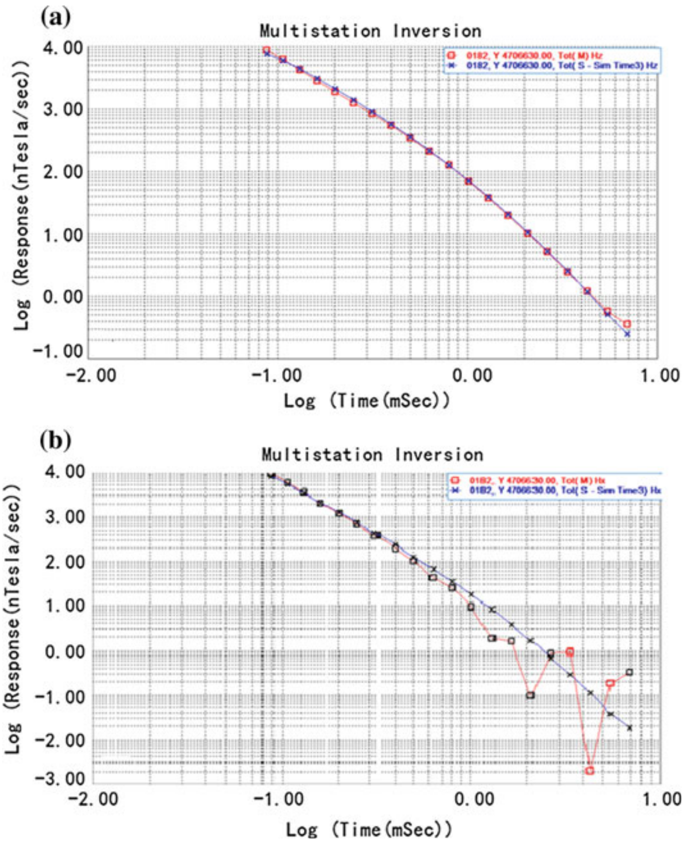

Fig. 11 Inversions results, Station 6630—200 m loop

the 3 station inversion result from 200 m loop. The 200 m loop model was also very close to the 150 m measurement but there is still the indication that the top layer of our model is divided into a top section somewhat more conductive.

We have shown that the 3 separations were consistent, but the in loop data did not recognize the division at the top layer as well as the 70 and 150 m measurements. We will continue by examining the attempts made to invert the data. We first inverted Hz at the center of the loops and found our best model to be 38 Ω-m layer with thickness of 13 m followed by 1230 Ω-m layer with thickness of 145 m and a 240 Ω-m conductive material below it. Figure 13a shows a fit of Hz to the 3-layer model with in-loop configuration. The fit relatively go down of Chap. 15. Figure 13b shows a comparison of Hz to 4 layer in-loop inversion result for the 150 m separation data. The in-loop inversion does not appear to resolve the conductivity of the 3rd layer well. Figure 13c shows a comparison of Hx to a 4 layer in-loop inversion for 150 m separation. Though affected by noises beyond Channel 7, Hx can still explain this issue.

Fig. 12 Modeling results from 3 separations of loop 2

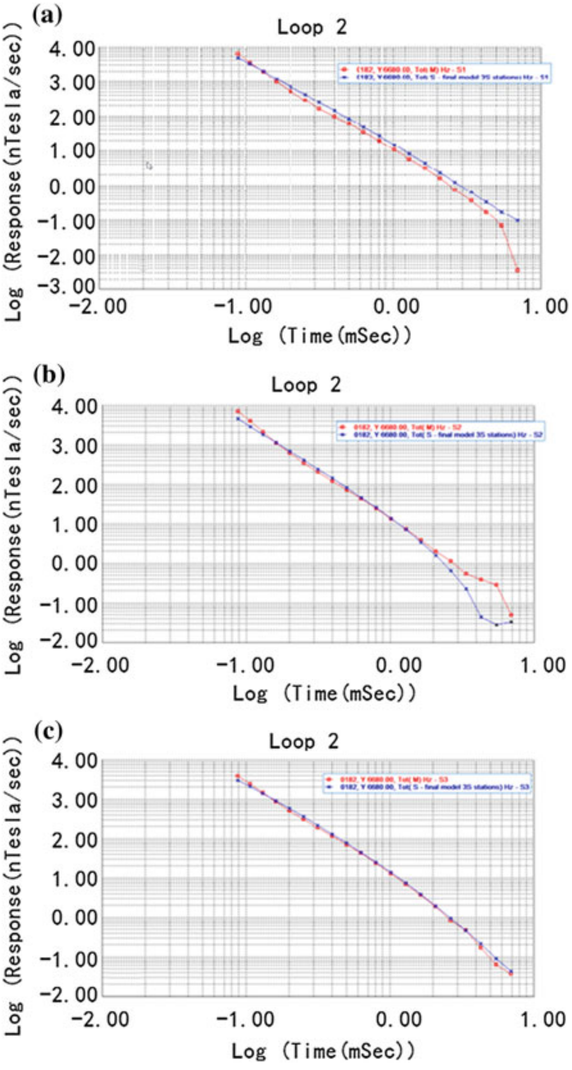

With a combination of all 3 separations, we were able to give our best fitting model for the moving loop data as 37 Ω-m layer with a thickness of 13 m, followed by 3920 Ω-m layer with a thickness of 35 m, 1300 Ω-m layer with a thickness of 162 m, 195 Ω-m layer with a thickness of 532 m, and then a resistor. The modeling result is shown in Fig. 14.

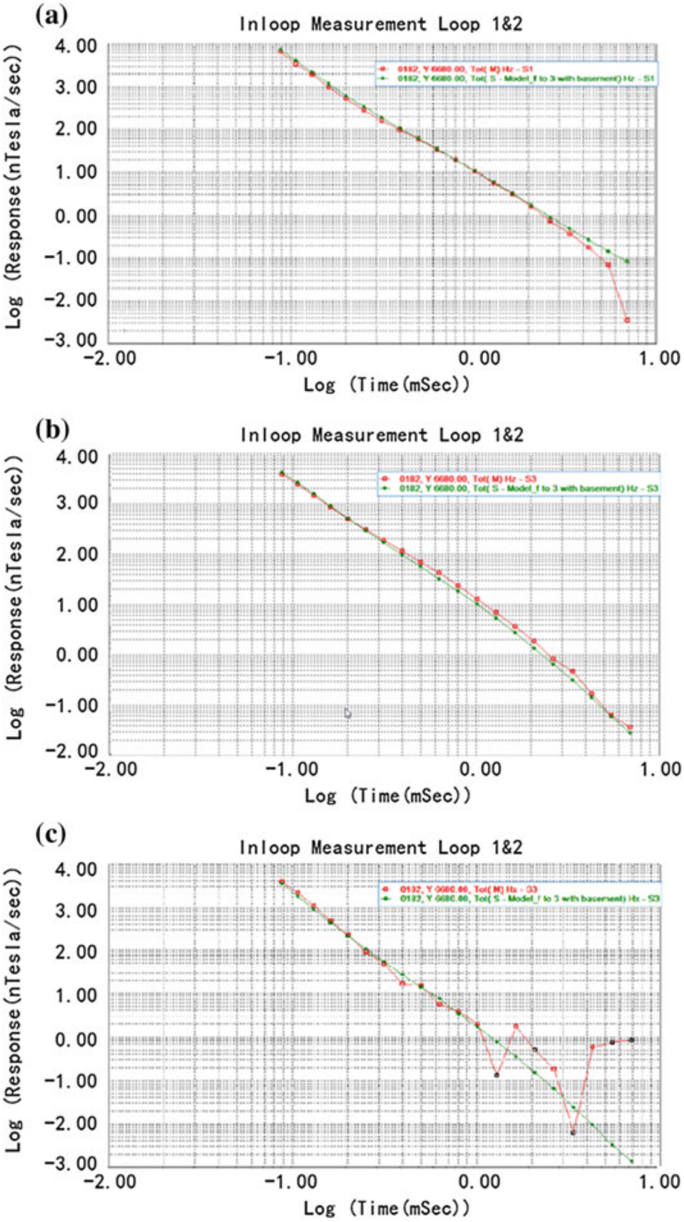

Fig. 13 Comparison between in-loop and 150 m data from loop 2

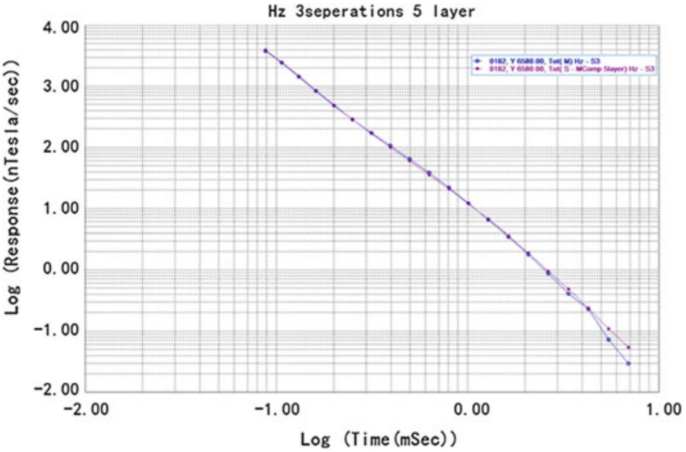

Fig. 14 A combinations of 3 separations modeling result

5 Conclusions

From this study, we discovered that the inversion of in-loop data is not good, as this location is poor for sensing the response from the subsurface material. If the ground is not approximately 1D, then in-loop data misrepresents the true resistivity structure. Measuring with a multiple separation strategy may increase the resolution and Hx can be utilized as and fewer models can fit all stations.

But this strategy still cannot provide a clear view of a large area as to whether the underground is approximately 1D. Fixed loop data gave us most of the information about the survey area: (a) The earth is mainly 1D at shallow depth because all 3 lines and all 3 components match a single model. (b) There is a strong 3D structure at the north end of the lines; all 3 components were strongly sensitive to this structure; and (c) There is a weak structure near the loop. All 3 components were sensitive to this structure but Hx was the easiest to diagnose. So, fixed loop data is reasonably reliable no matter the data quality and also in consideration of working efficiency.

References

1. Anderson, W.L., 1993, Interactive inversion of transient electromagnetic data for a central-induction loop over layered earth models V1; U.S. Geological Survey Open-File Report, 93-234-A/B
2. Anderson, W.L., 1975, Improved digital filters for evaluating Fourier and Hankel transform integrals, U.S. Dept of Commerce, National Technical Information Service Report PB-242-156

3. Anderson, W.L., 1982, Fast Hankel transforms using related and lagged convolutions: ACM Trans. On Math. Software, 8, 344–368
4. Boerner, D.E. and G.F. West, 1984, Efficient calculation of the electromagnetic fields of an extended source, Geophysics Vol. 49, p 2057–2060
5. Johansen, H.K., and Sorensen, K., 1979, Fast Hankel transforms: Geophysical Prospecting, 27, 876–901
6. Groom, R.W., 2000, FSEMTRS, an algorithm for frequency to time domain transformation, Internal Report and manual, available online, www.petroseikon.com
7. Jia, R. and Groom, R.W., 2005, On Time-Domain Transient Soundings, Symposium on the Application of Geophysics to Engineering and Environmental Problems, pg 506–512
8. Powell, B., Wood. G., and Bzdel, L., 2007, Advances in Geophysical Exploration of Uranium Deposits in the Athabasca Basin, 2007 Plenary Session: Ore Deposits and Exploration Technology, Toronto, Canada, pgs 771–789
9. Davis, L.J. and Groom, R.W., 2009, A comparison of airborne and ground electromagnetic data near the Grand Canyon, SEG Technical Program Abstracts 2009, pgs 764–768
10. Dickenson, J.E., Pool, D.R., Groom, R.W. and Davis, L.J., 2010, Inference of lithological distributions in an alluvial aquifer using airborne transient electromagnetic surveys, Geophysics V75, pgs 149–161

A Simple Apparent Resistivity Definition for Modified Central-Loop TEM System

Yunfei Lu, Guoqiang Xue, Xiu Li and Zhipeng Qi

Abstract Central-loop TEM technology can be used to survey the response of just central point. In practice, ones design modified central-loop TEM system to survey the response of several point around central location (within which the field is assumed to be uniform). However, there still exist some theoretical problems needed to be solved in obtaining TEM responses of this kind of modified system. In this paper, calculating and comparing the circle central-loop and modified circle-loop configuration of magnetic field responses at different non-center distances have been finished. The equations at non-center points are constructed using the technology of polynomial iteration. The polynomial coefficients are obtained adopting the method of least-squares iteration. Then, the improved calculation formula of the apparent resistivity at non-center points is constructed by adding an extra coefficient to the conventional formula, and this can make it better apply to TEM data collected at non-central locations of a circle-loop. Then the equivalent of circle and rectangular loop has been discussed; at last, the result due to circle loop has been introduced into square loop system and develop a new method to calculate the electromagnetic field response and apparent resistivity at non-central. An improved expression of apparent resistivity at non-center points is constructed and validated by a given model as well as coal water-filled area location, which shows that the constructed method is feasible.

Keywords Central-loop · Modified central-loop · Circle loop · Rectangular loop · Apparent resistivity

---

Y. Lu (✉) · G. Xue
Institute of Geology and Geophysics, Chinese Academy of Sciences, Beijing, China

X. Li · Z. Qi
College of Geology Engineering and Geomatics, Chang'an University, Xi'an, China

Q. Di et al. (eds.), *Technology and Application of Environmental and Engineering Geophysics*, Springer Geophysics,
DOI 10.1007/978-981-10-3244-8_26

1 Introduction

Transient electromagnetic method (TEM) is sensitive to anomalies of geological structures with low resistivity, and is relatively easy to implement in complex working conditions [1], and therefore commonly used to probe water-rich geological bodies.

In practice, it is neither convenient nor efficient for central-loop TEM to constantly move the transmitting loop from one place to another so as to observe the central TEM signal. To overcome such problems and also to decrease the effect of local lateral heterogeneity on the soundings, one can exploit the fact that there is no sizable difference in the signals for receiver stations located within a fixed distance around the central position of the loop. As a result, one may measure the TEM values around the central position within a fixed range inside the loop and deploy an improved central-loop source design. The apparent resistivity at every receiving point is usually calculated by the formula appropriate to a central-loop during the data interpretation.

Actually, for the large square-loop transmitter the response field may be computed by stacking the individual electromagnetic fields of many magnetic dipoles located all along the loop using some form of numerical integration. Xue [2] provide the idea that calculating apparent resistivity of modified central loop TEM of non-central point with the formula of large-fixed loop system. However, apparent resistivity at non-center points which hided in the formula and result in not convenient in practical applications.

Because there existing analytical solution for circle central-loop TEM even at non-central point in half-space. And it is relatively easy to search simple formula for apparent resistivity calculation. Many of the early papers on TEM modeling [3] used a circular transmitting loop to simulate the effect of the polygonal loops that are used in field practice. Singh and Mogi [3] simplified the Bessel function formulation in the electromagnetic field expression for the circular transmitter loop by using a hyper-geometrical distribution function, and hence obtained a frequency-domain electromagnetic field expression of the circular-loop for any point receiver. Raiche [4] finished Transient electromagnetic field computations for polygonal loops on layered earth. Xue et al. [2] obtained electromagnetic expressions for the inner and outside fields of the circular emitting loop by using the double Bessel function under some approximate conditions.

The in-circle-loop magnetic field response of homogeneous half-space conductivity is given by Hohmann and Ward [5], and also there have been many researches on the topics of resistivity or conductivity. However, the simple calculation formula of the apparent resistivity for non-central point has not yet appeared so far.

2 Apprarent Resistivity Expressions at Non-centre of Circle Loop

TEM formulas for the central point of the circle loop

For a transmitter loop with radius a and harmonic current $I = I_0 e^{-j\omega t}$, which is on the surface of a homogeneous conducting half-space, the received electromagnetic response in the center of the loop can be written as [6]

$$\mathrm{H_z}(\omega) = \frac{I_0}{k_1^2 a^3}[3 - (3 + 3k_1 a + k_1^2 a^2)e^{-k_1 a}] \tag{1}$$

where ω is the angular frequency of harmonic current, $H_z(\omega)$ is the vertical magnetic field response, I_0 is the amplitude of the harmonic current, where k_1 is called wave number, ω is the angular frequency of harmonic current.

Inverse Fourier transformation of $H_Z(\omega)$, the magnetic field step response $H_Z(t)$ in the time domain is

$$H_z(t) = \frac{1}{2\pi}\int_{-\infty}^{\infty} \frac{F(\omega)}{-i\omega} e^{-i\omega t} d\omega \tag{2}$$

The vertical magnetic induction response $B_Z(\omega)$ and $B_Z(t)$, in frequency and time domain respectively, are given via

$$B_Z(\omega) = \mu_0 H_Z(\omega), \quad B_Z(t) = \mu_0 H_Z(t) \tag{3}$$

Late-stage apparent resistivity is

$$\rho(t) = \frac{\mu_0}{4\pi t}\left(\frac{2\pi I_0 a^2 \mu_0}{5t\frac{\partial B_z(t)}{\partial t}}\right)^{2/3} \tag{4}$$

where the partial derivative of the electromagnetic induction response is

$$\frac{\partial B_z(t)}{\partial t} = \frac{I_0 \rho_1}{a^3}[3erf(u) - \sqrt{\frac{2}{\pi}}u(3 + u^2)e^{-\frac{u^2}{2}}] \tag{5}$$

where the $erf(u)$ is error function, and $u(t)$ is the non-dimension parameter, and

$$u(t) = a\sqrt{\frac{\mu_0}{2\rho_1 t}}, \quad erf(u) = \sqrt{\frac{2}{\pi}}\int_0^{u(t)} e^{-\frac{t^2}{2}} dt \tag{6}$$

Kaufman and Keller [6] gave the calculation form of the apparent resistivity $\rho_\tau(t)$ from $V(t)$ as follow

$$\rho_\tau(\mathrm{t}) = \frac{\mu_0}{4\pi \mathrm{t}}\left(\frac{2\mu_0 \mathrm{Mq}}{5\mathrm{tV(t)}}\right)^{2/3} \tag{7}$$

where M presents transmit magnetic moment and q presents the receiving area.

3 The TEM Formulas for None-central Point of the Circle Loop

Kaufman and Keller [6] also gave the electromagnetic response at any point in a circle-loop on the surface of a homogeneous half-space

$$H_z(\omega) = I_0 a \int\limits_0^\infty \frac{\lambda^2}{\lambda + u_1} J_1(\lambda a) J_0(\lambda r) d\lambda \tag{8}$$

where r is the distance from the center point to the field point, and where J_0 and J_1 are Bessel functions. Due to the product of Bessel functions, the integration in Eq. (8) is very complex, it can neither be transformed into a polynomial as Eq. (1), nor be subject to Fourier transformation. So far, a solution of Eq. (8) is still a difficult problem in electromagnetic field calculation.

In order to analyze the complex relation of $G(\lambda)$ and λ, The integrand function in Eq. (8) can be written as

$$G(\lambda) = \frac{\lambda^2}{\lambda + u_1} J_1(\lambda a) J_0(\lambda r) \tag{9}$$

$G(\lambda)$ is a function of a, r and λ.

Fixing the value of a and r, the variety of the real part and imaginary part of the integrand function $G(\lambda)$ with integral variants λ are calculated and shown in Fig. 1, in which $a = 50$ m, $r = 5$ m, $\rho = 100\ \Omega$ m, and $\omega = 400$ rad/s, u1 = 0.047.

As shown in Fig. 1, the real part of the integrand contains high frequency oscillations and is un-attenuated, and this will lead to the mathematical difficulty in solving the integral in interval $[0, \infty)$. However, the imaginary part of the integrand is quickly attenuated, and its integral is easy. Therefore, according to the numerical integration method of related Hankel transforms by Quadrature and continued fraction expansion [7], an approximate method for the integral of $G(\lambda)$ has been proposed. First, one can search for a λ_0 which corresponds to the zero point of the imaginary part of the integrand, and then do Gauss Quadrature between interval $[0, \lambda_0]$. This can well improve the efficiency of the integral calculation.

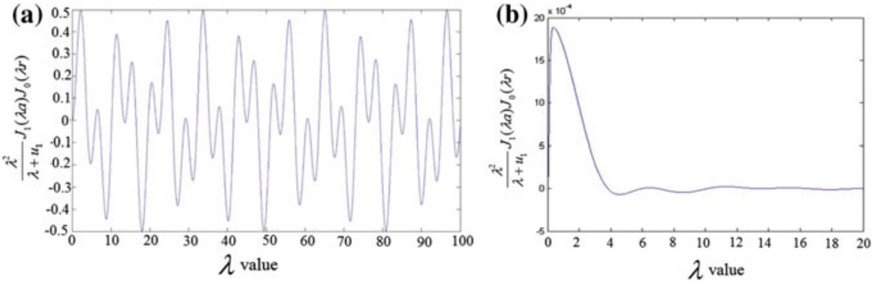

Fig. 1 Dynamic characteristic of the integrand *G*(λ). **a** Real part of the integrand, **b** imaginary part of the i

In order to compare the shape of the imaginary part of the electromagnetic response $H_Z(\omega)$ in the center point with that at different non-center points, an example with $a = 50$ m and $\rho = 1\ \Omega$ m is completed. The electromagnetic response $H_Z(\omega)$ in the center point is calculated according to Eq. (1), and those at different non-center points (r = 0, 10, 20, 45 m) are calculated using the numerical integration scheme proposed in this study. The results are shown in Fig. 2.

From Fig. 2, one can see that the imaginary parts of the electromagnetic response $H_Z(\omega)$, at the center point and at different non-center points, have similar characteristics, only the amplitudes are different. Inspired by this, we assume that the formula of the electromagnetic response at non-center points has a similar polynomial form such as the formula Eq. (1) of center points if fixing the value of offset, resistivity and current. Thus, the electromagnetic response at non-center points can be written as

$$\mathrm{H_z}(\omega) = \frac{I_0}{k_1^2 a^3}\left[Z_0(r) - (Z_1(r) + Z_2(r)k_1 a + Z_3(r)k_1^2 a^2)e^{-k_1 a}\right] \tag{10}$$

where r is the distance from the center point to the non-center point, $Z_0(r)$, $Z_1(r)$, $Z_2(r)$ and $Z_3(r)$ are the undetermined coefficient functions.

Fig. 2 Electromagnetic responses at different non-center points

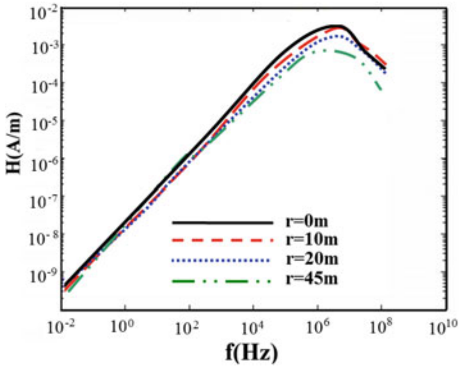

4 Determination of the Coefficient Functions

For different offsets r, the values of the coefficient functions in Eq. (12) are different. Once these coefficient functions are determined, one can build the functional relationship between the apparent resistivity and electromagnetic response at a given offset-distance.

With known current I_0, loop radius a and given r_m, one can calculate $H_Z(r_m, \omega_i)$ according to the theoretical formula Eq. 8 at non-center point using the numerical integration scheme between interval [0, λ_0] for different $\omega_i(\mathrm{k}_{1i} = \sqrt{-j\omega_i\sigma\mu_0})$. When ω_i, r_m and $H_Z(r_m, \omega_i)$ are known, one can then determine the values of $Z_0(r_m)$, $Z_1(r_m)$, $Z_2(r_m)$ and $Z_3(r_m)$ by solving Eq. (10).

Substitute ω_i, r_m and $H_Z(r_m, \omega_i)$ into Eq. (10), one gets

$$H_Z(\omega_i, r_m) = \sum_{s=0}^{3} a_{is} Z_s(r_m)_i, \quad i = 1, 2, \ldots, N; \;\; m = 1, 2, \ldots \tag{11}$$

where

$$\begin{array}{cc} a_{i0} = \frac{I_0}{(k_{1i})^2 a^3} & a_{i1} = \frac{I_0}{(k_{1i})^2 a^3} e^{-k_{1i}a} \\ a_{i2} = \frac{I_0}{(k_{1i})^2 a^3} \mathrm{k}_{1i} a e^{-k_{1i}a} & a_{i3} = \frac{I_0}{(k_{1i})^2 a^3} \mathrm{k}_{1i} a^2 e^{-k_{1i}a} \end{array} \tag{12}$$

One can solve the $Z_0(r_m)$, $Z_1(r_m)$, $Z_2(r_m)$ and $Z_3(r_m)$ according to Eq. (13) using the least square method (LSM).

As soon as many groups $Z_0(r_m)$, $Z_1(r_m)$, $Z_2(r_m)$ and $Z_3(r_m)$ corresponding to r_m, (m = 1, 2, …) are obtained, one can determine the coefficient functions $Z_0(r)$, $Z_1(r)$, $Z_2(r)$ and $Z_3(r)$ using the curve fitting method.

Using above-mentioned method, the obtained coefficient functions $Z_0(r)$, $Z_1(r)$, $Z_2(r)$ and $Z_3(r)$ are shown in Fig. 3 and Table 1, in which a/r can be regarded as a normalized parameter, resistivity $\rho = 100\ \Omega$ m. For $r/a = 0$ (means central point) the values of the four coefficient functions are, respectively, 2.989677401, −2.989677395, −2.98967875 and −0.995519472; whereas the true values are 3, −3, −3 and −1 (Eq. 3), so that the maximum error does not exceed 0.5%.

In order to calculate the apparent resistivity, one must know the variation rate $\partial B_Z(t)/\partial t$ of the electromagnetic induction response. One gets [6]

$$\frac{\partial B_z(t)}{\partial t} = \frac{I_0\rho_1}{a^3}[Z_0 + Z_1(1 - erf(u)) + Z_2\sqrt{\frac{2}{\pi}}ue^{-\frac{u^2}{2}} + Z_3\sqrt{\frac{2}{\pi}}u^3e^{-u^2/2}] \tag{13}$$

When the $\partial B_Z(t)/\partial t$ is known, based on the formula shape of Eq. (6), one can guess the expression for the apparent resistivity as follow

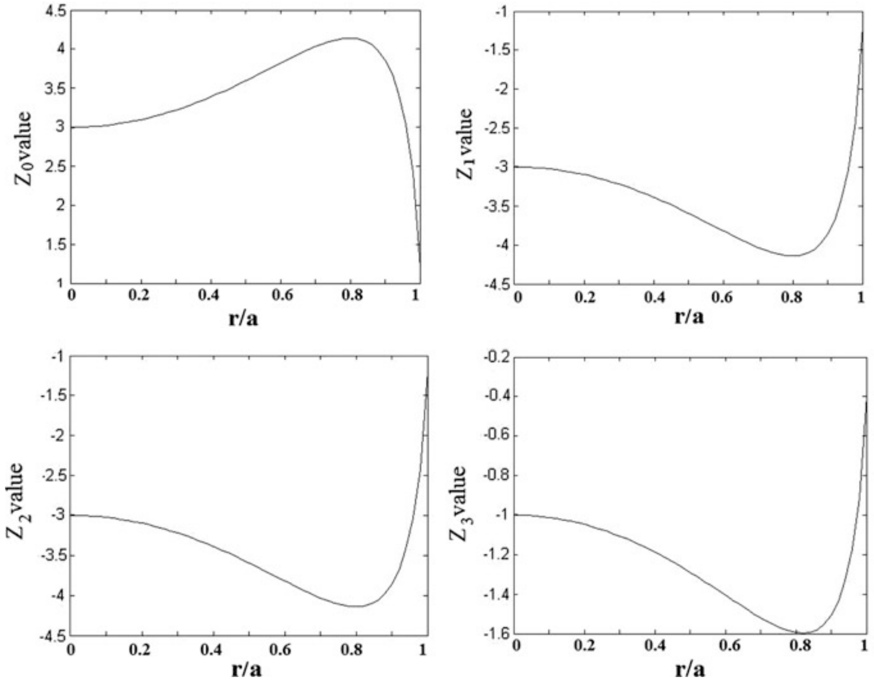

Fig. 3 Calculated values for coefficient functions Z_0(r), Z_1(r), Z_2(r), and Z_3(r)

Table 1 Coefficients of Z

r/a(m)	Z_0	Z_1	Z_2	Z_3
0	2.989677401	−2.989677395	−2.98967875	−0.995519472
0.2	3.097729509	−3.097729589	−3.097711215	−1.04713085
0.4	3.387237568	−3.387237894	−3.387163057	−1.188124213
0.6	3.819810265	−3.819810997	−3.819642952	−1.405320361
0.8	4.141052855	−4.14105405	−4.140779567	−1.594674478
1	1.1949062	−1.194906211	−1.194903999	−0.393408592

$$\rho\left(\frac{\partial B_z(t)}{\partial t}\right) = \frac{\mu_0}{4\pi t}\left(Z\frac{2\pi I_0 a^2\mu_0}{5t\frac{\partial B_z(t)}{\partial t}}\right)^{2/3} \tag{14}$$

where Z is the function of $Z_0(r)$, $Z_1(r)$, $Z_2(r)$ and $Z_3(r)$ which will be determined.

In the case of very late time, $u(t)$ will be very small so that $erf(u)$ and $e^{-u^2/2}$ may be expanded as a Taylor series, therefore

$$erf(u) = \sqrt{\frac{2}{\pi}}(u - \frac{u^3}{3!} + \frac{3u^5}{5!} - \cdots) \tag{15}$$

$$e^{-u^2/2} = 1 - \frac{u^2}{2} + \frac{u^4}{8} - \cdots \tag{16}$$

Considering that $u(t)$ is very small at late times, one can ignore the higher order terms of $erf(u)$ and $e^{-u^2/2}$. Substituting Eqs. (15) and (16) into Eqs. (13) and (14), one gets

$$Z = \frac{Z_2(r)}{8} - \frac{Z_1(r)}{40} - \frac{Z_3(r)}{2} \tag{17}$$

The Eq. (14) is checked using a half-space model. The resistivity ρ_1 of the model is 100 Ω m and its transmitter loop radius a is 50 m. The decays curves of secondary magnetic field at 0 m away from the center point are calculated according to Eqs. (5) and (13), respectively (Fig. 4a). The apparent resistivity have been calculated by formulas (4) and (14), respectively (Fig. 4b) it shows clear that the calculated result which from theoretical and constructed formula agree with each other. This indicates that the obtained result by constructed formula is more consistent with the real case.

Fig. 4 Half-space model calculated result according to theoretical and constructed formula, **a** decay curves derived by theoretical and constructed formula, **b** apparent resistivity curves derived by theoretical and constructed formula

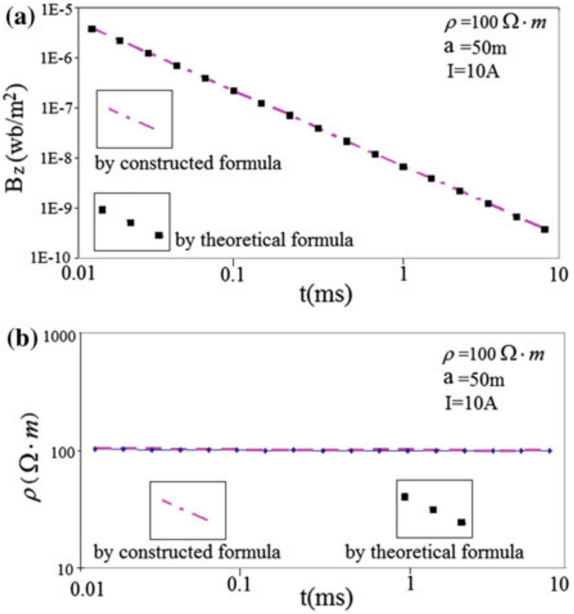

5 Comparison of Circle and Rectangular Loop in the Modified Central-Point TEM System

Figure 5 show the comparison of response due to circle and square loop where Fig. 5a shown of circle and equivalent square loop, Fig. 5b is the distribution due to square loop, Fig. 5c is the distribution due to circle loop, Fig. 5d show the distribution of errors between circle and square loop. Based on Fig. 5d, One can see that the error between circle and rectangular loop is small around the central of loop, which indicate that one can use the formula derived from circle loop to calculate the apparent resistivity of modified square-central-loop system.

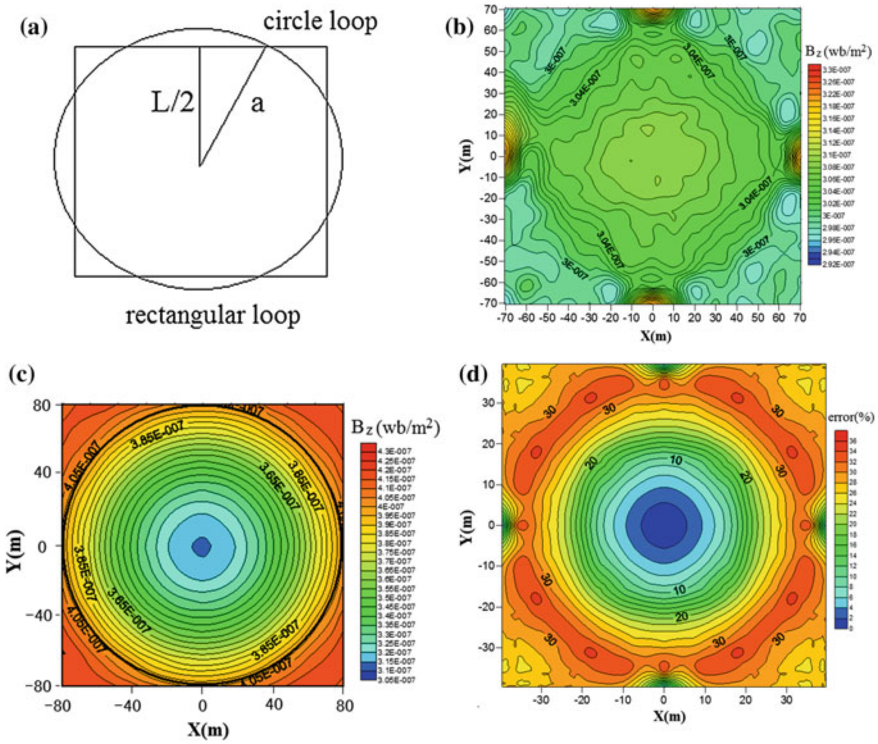

Fig. 5 Comparison the response due to *circle* and *square* loop, **a** shown of *circle* and equivalent *square* loop (L = 140 m, a = 80), **b** distribution due to *square* loop (L = 80), **c** distribution due to *circle* loop (a = 80), **d** the distribution of errors between *circle* and *square* loop

6 Practical Survey Examples of Mined-Out Areas Filled with Water

The TEM exploration procedures of example are the TEM response data of multiple measure points in the 1/3 range of the transmitting loop are collected when the loop is in a given location. Then moving the transmitting loop from northwest to southeast to a new position, the mentioned-above measures are repeated. Last, all measure points compose a measure area such as Fig. 6. The exploration example is a region located in east 35 km in Yuzhou City of Henan province. In the survey area, there are several abandoned coal mines which caused many cracks in the resident houses. This kind of geological disaster has brought serious threat to the living conditions of the local residents. The geological hazards of this exploration area are shown in Fig. 6.

The thickness of the loess layer in the survey area is about 5 m, and the thickness of Quaternary Stratum is about 30 m which is mainly composed of gravel and clay. The lithology is mainly fine-grained sandstone, and the thickness of this stratum is about 90 m. There is a 1.4 m coal layer thick at 134 m depth. The main purpose of this survey study is to identify the distribution of mined-out areas and water-filled areas.

The measure system mainly includes a transmitting circle loop who's the length is 200 m and transmitting frequency 25 Hz. Terra TEM instrument is used to acquire the field data. The number of time gates is 40 in the range of time windows from 0.087 ms to 8 ms, and the size of measure grid is 100 m × 40 m.

The plane distribution of apparent resistivity at underground 130 m for this survey area is obtained using the proposed method in this study. The plane apparent resistivity is shown in Fig. 7a, where the red colors indicate high resistivity regions, and the blue colors low-resistivity areas. It can be found that the distribution of apparent resistivity in the overall area is very inconsistent. Furthermore, many small

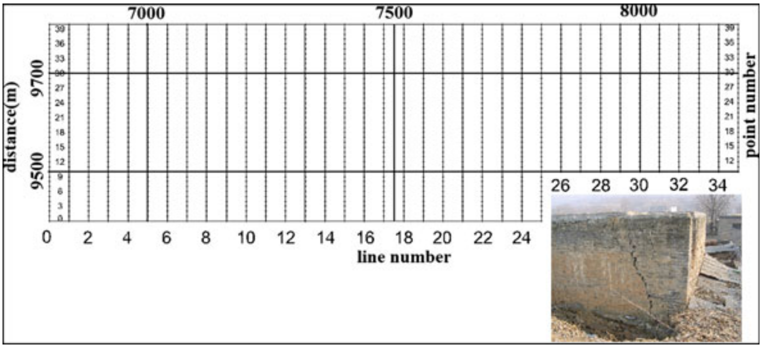

Fig. 6 Geographical position and geological hazards in the second exploration area geographical position of the second survey area (The grid size is 100 m × 40 m), geological hazards picture caused by mine-out area located in the around the position of (38427400, 3779700)

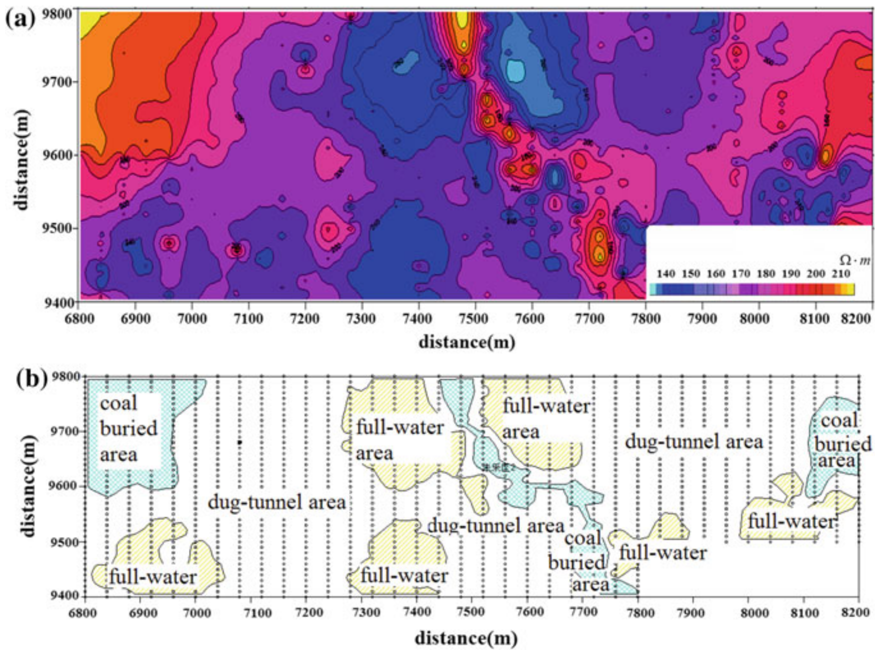

Fig. 7 Plan contour of apparent resistivity and explained geological structure at underground. **a** Horizontal section of interpolated apparent resistivity in 130 m depth. **b** Horizontal section of interpreted geological structure

regions with the lower resistivity are also found, which may be the mined-out areas filled with water. The plane distribution map of this geological structure can be inferred from the apparent resistivity, and it is shown in Fig. 7b. It shows that there are three water-rich areas and multiple un-mined coal areas. What makes us most proud is that the above-mentioned geological explanations are accord to the geological survey results using successively geological digging exploration in this area, and two digging areas are shown by two blue areas in Fig. 7b.

7 Conclusion

This study presents a new expression to evaluate the apparent resistivity of non-center points of a transmitting loop. The applicability of the new expression was validated by a given reliable model. Two practical examples of the underground geophysical explorations in Shanxi and Henan provinces of China indicated that, the proposed method of calculating the apparent resistivity can give clear explanations to complex geological structures and correctly delineate the water–filled areas in coal mines.

References

1. Danielsen, J. E, Auken E., and Jorgensen F., 2003, The application of The transient electromagnetic method in hydro-geophysical surveys: Journal of applied geophysics, **53**, no. 4, 181–198. doi:10.1016/j.jappgeo.2003.08.004.
2. Xue, G.Q. Bai C.Y. and Yan S. 2012 Deep sounding TEM investigation method based on a modified fixed central-loop system, Journal of Applied Geophysics 76(2012)23–32.
3. Singh, N.P., and Mogi, T., 2005, Electromagnetic response of a large circular loop source on a layered earth: a new computation method. Pure and Applied Geophysics, **162**, no. 1, 181–200. doi:10.1007/s00024-004-2586-2.
4. Raiche, A.P., 1987, Transient electromagnetic field computations for polygonal loops on layered earth: Geophysics, **52**, no. 6, 785–793. doi:10.1190/1.1442345.
5. Hohmann, G. W., and Ward, S. H., 1986, Electromagnetic theory for geophysical applications, 1, Theory, *in* M. Nabighian, Eds., Soc. Exploration. Geophys.
6. Kaufman, A. A., and Keller, G. V., 1987, Frequency and Transient Soundings, Beijing, Geological Publishing House, 145–148.
7. Chave, A. D., 1983, Numerical integration of related Hankel transforms by quadrature and continued fraction expansion: Geophysics, **48**, no. 12, 1671–1686. doi:10.1190/1.1441448.

The Response of In-loop Transient Electromagnetic Configuration

Wen Chen, Guoqiang Xue and Dongyang Hou

Abstract For the aim to assess the large loop transient electromagnetic method (TEM), an important method in engineering exploration, we study the distribution of vertical and horizontal magnetic component by calculating the 1-D response corresponding to in-loop and out-loop field point. A new algorithm for Dual Bessel integral has been developed. We divided the integral range $(0, \infty)$ into $(0, \lambda_0]$ and $[\lambda_0, \infty)$. In the integral range of $(0, \lambda_0]$, based on the derivative relationship of Bessel integral, transforming the integral into the form of easily calculation. In the range of integral of $[\lambda_0, \infty)$, Linear sine and cosine transformation algorithm can be used for the computation. We design models for numerical simulation and give the result. Based on the results, we draw a conclusion that vertical magnetic field component can be surveyed in the range of 50% inside of the loop and horizontal magnetic field component is so smaller than vertical component that it can not be well surveyed inside large loop.

Keywords Large loop transient electromagnetic method · None-zero offset

1 Introduction

Transient Electromagnetic Method (TEM) is commonly used in hydrogeology [1], oil surface data study, ocean investigation [3], and other exploration. But for the underground cave response, the studies is not sufficient. For China is developing rapidly, to find applied engineering geological exploration method is significant.

There are a lot of different TEM configurations which have been used in engineering exploration. For example long-offset transient electromagnetic method (LOTEM), grounded-source TEM which is more suitable for deep oil field exploration; surface-borehole TEM [4] which is seldom used in China because of the complex of theory; center loop TEM and coincident loop TEM [5].

W. Chen (✉) · G. Xue · D. Hou
Key Laboratory of Mineral Resources, Institute of Geology and Geophysics, CAS,
Beijing, China

Q. Di et al. (eds.), *Technology and Application of Environmental and Engineering Geophysics*, Springer Geophysics,
DOI 10.1007/978-981-10-3244-8_27

In-loop survey is a popular TEM configuration in China [2]. The transmitter loop is kept fixed, so the field near the center of the loop is even and stable. Reliable results can be got. But how to define the range inside-loop where TEM vertical component can be surveyed is seldom reported.

In this paper, we show the magnetic field distribution of large loop TEM by calculating the decay curve of field point with different offset, and we get the conclusion that vertical magnetic field component can be surveyed in the range of 50% inside of the loop and horizontal magnetic field component is so small than vertical component that it can not be survey inside loop. We also give the two dimensional numerical calculation results of caves.

2 Theoretical Analyses of Large Loop Tem Response

Figure 1 is the large loop configuration, where large loop laid on the earth surface, there are some survey points inside square loop where the field can be regard as even-field.

In order to numerically show the feature, exactly define the range, we analyses the electromagnetic response of large-loop, finish numerical calculation of vertical magnetic field corresponding to different in-loop situation. The electromagnetic field fundamental law in frequency domain obey the Maxwell equations

$$\nabla \times E = -\frac{\partial B}{\partial \mathrm{t}} \tag{1}$$

$$\nabla \times H = j + \frac{\partial D}{\partial \mathrm{t}} \tag{2}$$

$$\nabla \cdot B = 0 \tag{3}$$

$$\nabla \cdot \mathbf{D} = \rho \tag{4}$$

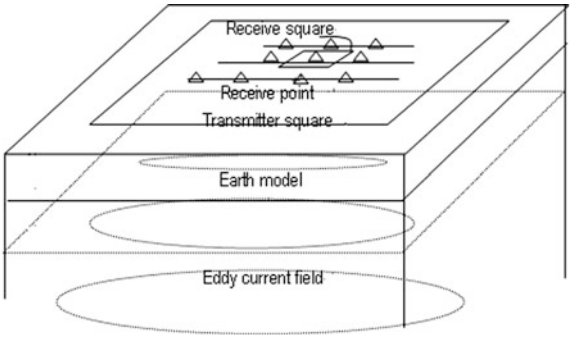

Fig. 1 The configuration of large loop TEM

where **E** denotes the electrical intensity (V/m), **B** denotes the magnetic induction, **H** denotes the intensity of the magnetic field ($\mathrm{Wb/m^2}$), **D** denotes the electric displacement vector ($\mathrm{C/m^2}$), **j** denotes the electric current density ($\mathrm{A/m^2}$) and ρ is the free-electric density ($\mathrm{C/m^3}$).

In layered earth, the response in frequency domain is:

In the center of loop,

$$H_r(\omega) = E_\phi(\omega) = 0 \tag{5}$$

$$Hz(\omega) = I_0 a \int\limits_0^\infty \frac{\lambda Z^{(1)}}{Z^{(1)} + Z_0} J_1(\lambda a) d\lambda \tag{6}$$

where a is the length of loop, I_0 is current, $H_r(\omega), E_\phi(\omega)$ is horizontal magnetic and electric field component. $Hz(\omega)$ is vertical magnetic component, λ is integral invariants, $J_1(\lambda)$ is Bessel function. Z_0 is wave-impedance of first layer medium, $Z^{(1)}$ is the total impedance.

In the other location of in-loop with none-zero offset, the response is

$$\mathrm{H}_r(\omega) = -I_0 a \int\limits_0^\infty \frac{\lambda \mathrm{Z}^{(1)}}{\mathrm{Z}^{(1)} + \mathrm{Z}_0} J_1(\lambda a) J_1(\lambda r) d\lambda, \tag{7}$$

$$\mathrm{E}_\phi(\omega) = i\omega\mu_0 I_0 a \int\limits_0^\infty \frac{\mathrm{Z}^{(1)}}{\mathrm{Z}^{(1)} + \mathrm{Z}_0} J_1(\lambda a) J_1(\lambda r) d\lambda \tag{8}$$

$$\mathrm{H_z}(\omega) = I_0 a \int_0^\infty \frac{\lambda Z^{(1)}}{Z^{(1)} + Z_0} J_1(\lambda a) J_0(\lambda r) \mathrm{d}\lambda \tag{9}$$

where r is the distance from the center of loop to field point.

3 Numerical Calculation of Large-Loop TEM Response

The TEM response can be transformed from Eqs. (7) to (9) by Fourier calculator:

$$\mathbf{H}(t) = \frac{1}{2\pi i} \int\limits_{-\infty}^{\infty} \frac{\mathbf{H}(\omega)}{\omega} e^{-i\omega t} d\omega \tag{10}$$

$$\mathbf{E}(t) = \frac{1}{2\pi}\int_{-\infty}^{\infty} \frac{\mathbf{E}(\omega)}{-i\omega} e^{-i\omega t} d\omega \tag{11}$$

TEM response in loop center with zero offset is:

$$H_z(t) = \frac{2}{\pi}\int_{0}^{\infty} \operatorname{Im}\left[I_0 a \int_{0}^{\infty} \frac{\lambda Z^{(1)}}{Z^{(1)} + Z_0} J_1(\lambda a) d\lambda\right] \frac{\cos\omega t}{\omega} d\omega \tag{12}$$

For Eq. (6) of the condition in zero-offset, Hankel transformation linear filter technology is used to get the stable solution (Fig. 2).

For the condition of none-zero offset, the Eqs. (7), (8), (9) are double Bessel function, because of the high oscillation and slow decay of integral kernel, we divide the integral range $(0, \infty)$ into two parts $(0, \lambda_0]$ and $[\lambda_0, \infty)$. Where λ_0 is selected parameter which best fit for λa, λr to satisfy the argument modified Bessel function approximate condition.

$$\mathrm{H_z} = I_0 a \int_{0}^{\lambda_0} \frac{\lambda Z^{(1)}}{Z^{(1)} + Z_0} J_1(\lambda a) J_0(\lambda r) + I_0 a \int_{\lambda_0}^{\infty -} \frac{\lambda Z^{(1)}}{z^{(1)} + Z_0} J_1(\lambda a) J_0(\lambda r) \tag{13}$$

we define Eq. (13) as

$$\mathrm{H_z} = H_{z1} + H_{z2} \tag{14}$$

where,

$$H_{z1} = I_0 a \int_{0}^{\lambda_0} \frac{\lambda Z^{(1)}}{z^{(1)} + Z_0} J_1(\lambda a) J_0(\lambda r) d\lambda \tag{15}$$

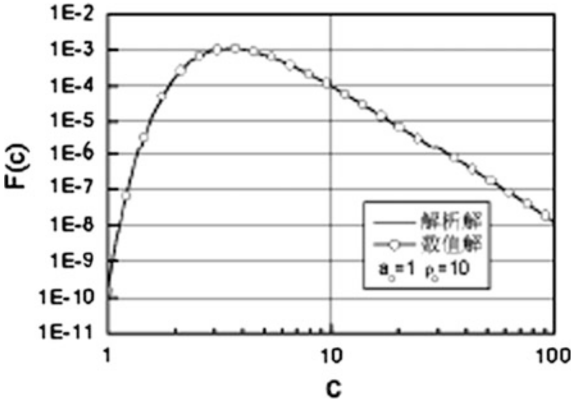

Fig. 2 The calculated results

$$H_{z2} = I_0 a \int_{\lambda_0}^{\infty -} \frac{\lambda Z^{(1)}}{z^{(1)} + Z_0} J_1(\lambda a) J_0(\lambda r) d\lambda \tag{16}$$

let $J_1(\lambda a) = \frac{d}{d\lambda}[-\frac{J_0(\lambda a)}{a}]$, we transform Eq. (15) as (Caufman 1983)

$$H_{z1} = -\frac{J_0(\lambda r) J_0(\lambda a)}{a} \lambda \frac{Z^{(1)}}{Z^{(1)} + Z_0}\Big|_0^{\lambda_0} + \frac{1}{a} \int_0^{\lambda_0} \left[\lambda \frac{Z^{(1)}}{Z^{(1)} + Z_0} J_0(\lambda a) J_0(\lambda r)' \right] d\lambda \tag{17}$$

$$H_{z1} = -\frac{J_0(\lambda r) J_0(\lambda a)}{a} \lambda \frac{Z^{(1)}}{Z^{(1)} + Z_0}\Big|_0^{\lambda_0} + \frac{1}{a} \sum_{i=0}^{n} g_i \int_{\lambda_i}^{\lambda_{i+1}} [J_0(\lambda a)] d\lambda \tag{18}$$

where $g_i = \frac{\lambda_{j+1} F(\lambda_{j+1}) J_1(\lambda_{j+1} a) - \lambda_j F(\lambda_j) J_1(\lambda_j a)}{\lambda_{j+1} - \lambda_j}$.

For the condition of $\lambda_0 \cdot a \gg 1$, Eq. (16) can be approximately written as,

$$H_{z2} \approx \frac{1}{\pi \sqrt{ar}} \int_{\lambda_0}^{\infty -} \frac{\lambda Z^{(1)}}{z^{(1)} + Z_0} \left\{ \cos[\lambda(a + r) - \pi] + \cos\left[\lambda(a - r) - \frac{\pi}{2} \right] \right\} d\lambda \tag{19}$$

Equation can be solved by using linear Cosine algorithm.

In order to test the calculation method, we consider the special Bessel equation

$$F(c) = \int_{\lambda_0}^{\infty} \frac{\lambda}{\lambda^2 + c^2} J_1(\lambda a) J_1(\lambda \rho) d\lambda = \frac{1}{2c^2} \exp(-\frac{a^2 + \rho^2}{4c^2}) I_1(\frac{a\rho}{2c^2}) \tag{20}$$

where I_1 is the first order first type Bessel function.

We get the analytic solution and numerical calculated result, It shows that the method is valid.

4 Analyses of the Calculated Result

We calculate vertical field component with the configuration, the parameter which we adopted is loop length L = 300 m, transmitter current 10 A, sending frequency 30 Hz, number of receiving channel of 20, time range of 0.087–7.015 ms. the recorder range of survey point of 0–280 m (Fig. 3a), where square line means large loop which L = 300 m, the geo-electric model:

$$\rho_1 = 1000\ \Omega \cdot \mathrm{m}, \rho_2 = 10\ \Omega \cdot \mathrm{m}, h_1 = 100\ \mathrm{m}.$$

The calculated decay curve with different offset is shown in Fig. 3b, where horizontal coordinate present offset field point, vertical coordinate present time derivate of magnetic field component.

It shows clear that in the zero offset, the values of vertical magnetic field reach max, in the center range of loop, the offset is small, the values of magnetic filed is big. The values decrease with the increase of offset.

We calculate the response of inside and outside loop field point, and draw the plane figure of time derivate of magnetic field component, including vertical (Fig. 4) and horizontal component (Fig. 5). In Fig. 4, it shows clear that in the center of loop, vertical magnetic field component reaches the biggest, in the edge of loop, the value is small. In the outside loop situation, the value is smaller. Whereas the distribution of horizontal magnetic component (Fig. 5) is opposite to those of Fig. 4, where the value of center loop is the smallest, in the four corners outside of loop, the value is bigger than the value of inside loop.

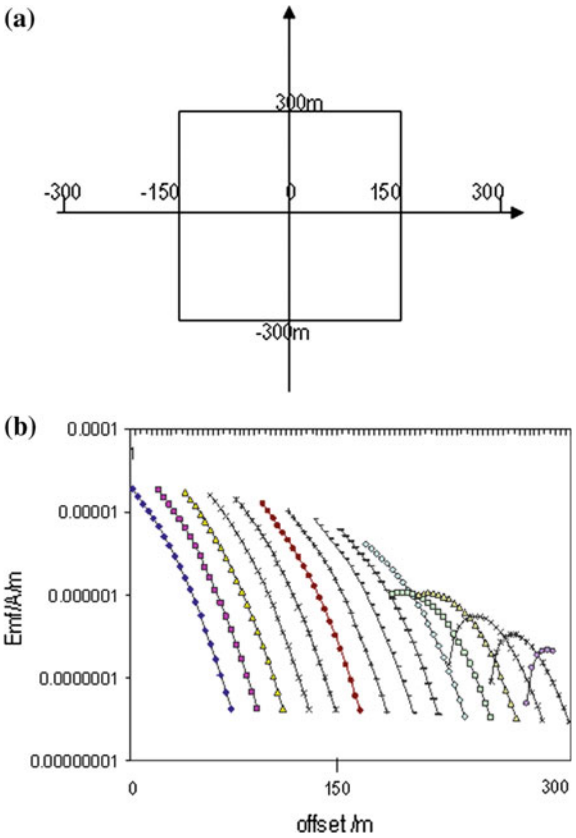

Fig. 3 **a** The system of calculation (L = 300 m). **b** *Vertical* magnetic component time derivative data with different offset (L = 300 m, F = 30 Hz)

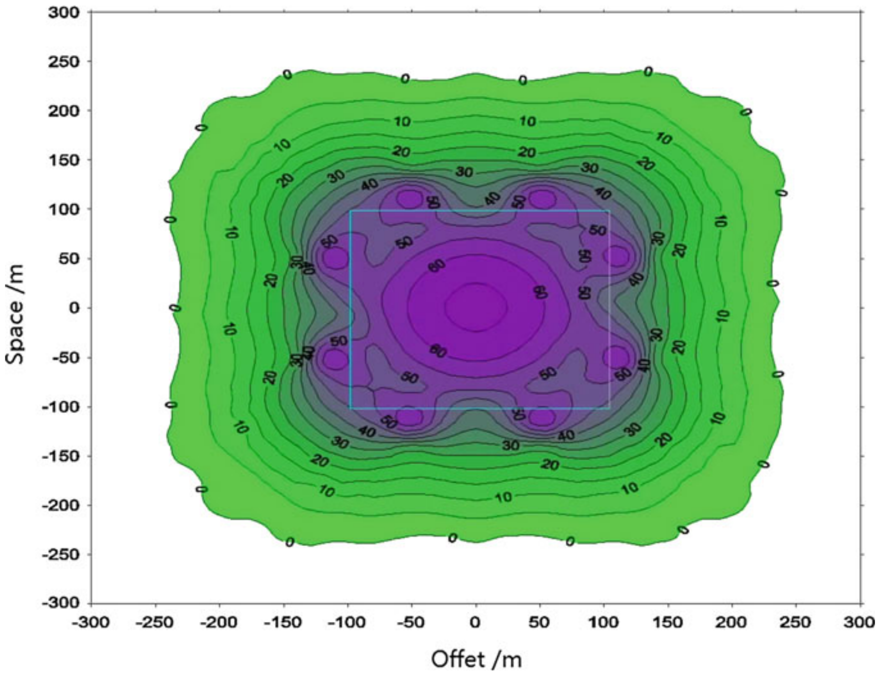

Fig. 4 The distribution of *vertical* magnetic field component

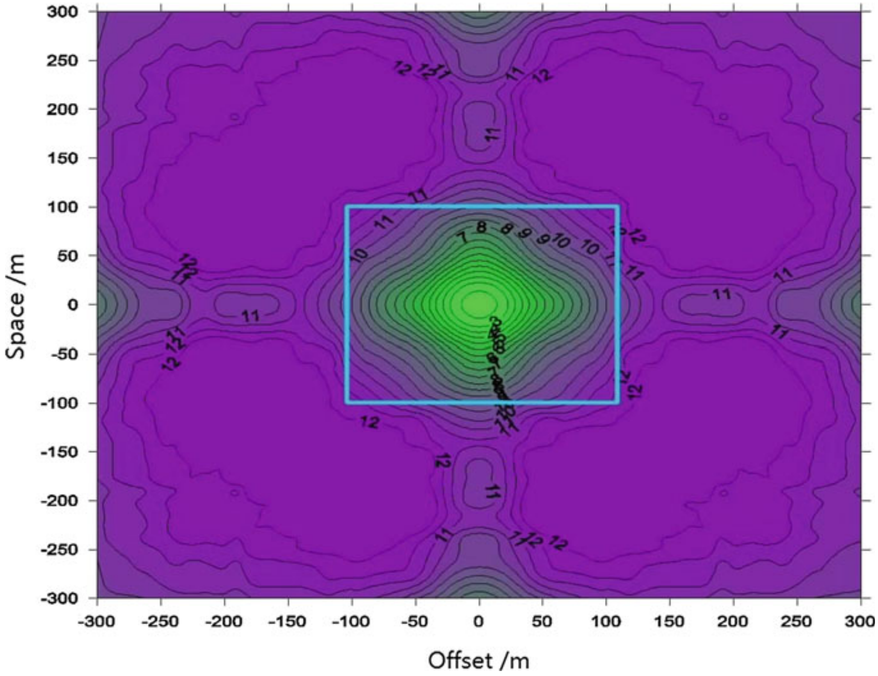

Fig. 5 The distribution of *horizontal* magnetic field component

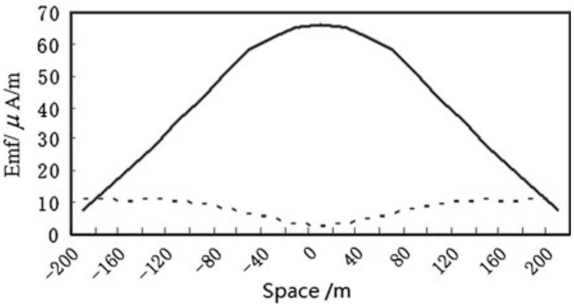

Fig. 6 The percent decay curve of *vertical* and *horizontal* magnetic with different field point. *Solid line* is time derivate of *vertical* magnetic field component. *Dashed line* is time derivate of *horizontal* magnetic field component

Table 1 Percent energy decay with different offset (L = 200 m, 300 m, 500 m)

Length of loop (m)	Offset (m)								
	0	20	40	80	100	120	140	180	200
L = 200	0	1.5	6.0	21	34	45	57	78	87
L = 300	0	2.5	5.2	15	24	34	46	78	94
L = 500	0	0.2	0.6	3.9	6.8	10	16	31	39

According to Figs. 4 and 5, we draw the percent decay curve of vertical and horizontal magnetic with different field points (Fig. 6), where solid line is vertical magnetic field component, dash line is horizontal magnetic field component. It shows clear that: (1) in some range around the center of loop, the values of vertical field almost agree with each other; (2) vertical magnetic field component is bigger than horizontal magnetic field component around loop. When the offset distance reaches 180 m, the two field values equal each other.

Table 1 gives the list of percent energy decay with different offset distance. We can draw the conclusion: (1) in the situation of zero offset, the energy of magnetic reaches biggest value; (2) outside the loop, energy decays fast; (3) if we regard 10% as the limitation of energy decay, we can define the range of 50% in-loop, even-magnetic field can be surveyed. The larger loop it is, the greater range percent it is.

5 Conclusion

There are three main reasons that we apply large loop TEM to detect underground cavity: (1) the configuration can realize fast exploration; (2) this method has the best lateral and vertical resolution with regard to underground target among the EM technique; and (3) the method is less influenced by the near-surface inhomogeneity.

We analyzed the response feature of loop-source, present the distribution both of vertical and horizontal magnetic field component, and gave the numerical result of TEM response in the underground cavity. Furthermore, we checked the method's detection ability in the case of cavities detection. We considered both high resistive and conductive caves. With the help of model analysis, we got a realistic theoretical model and this has fount a successful application on a coal mine.

We draw the conclusions as:

(1) Because of the low cost and fast exploration, large loop TEM configuration can be employed to detecting underground target. During field working, vertical magnetic field component can only be surveyed in the range of 60% inside loop to ensure the field value being regarded as agreement.
(2) Inside of loop, horizontal magnetic field component is so smaller than vertical component that it can not be surveyed well.

References

1. Taylor, K., Widmer, M. and Chesley, M., (1992) Use of transient electromagnetics to define local hydrogeology in an arid alluvial environment. Geophysics, 57, 343–352.
2. Zhang, Z. and Xiao, J. (2001) Inversions of surface and borehole data from large-loop transient electromagnetic system over a 1-D earth. Geophysics, 66, 1090–1096.
3. Edwards, R. N. (1997) On the resource evaluation of marine gas hydrate deposits using sea-floor transient electric dipole-dipole methods. Geophysics, 62, 63–74.
4. Eaton P. A. and Hohmann, G. W. (1984) The influence of a conductive host on two-dimensional borehole transient electromagnetic response. Geophysics, 49, 861–869.
5. Yang, C. H. et al. (1999) Combined application of dc and TEM to sea-water intrusion mapping. Geophysics, 64, 417–425.

Application of Multiple Geophysical Methods to Prospect Concealed Ores Beneath Quaternary Cover: A Case Study from a Copper-Polymetallic Deposit

Yinsheng Meng, Ruizhong Zhang, Ruide Liu, Tianliang Lin and Wenguo Wang

Abstract The magmatic hydrothermal vein-type copper-polymetallic deposits in Weilasituo are strictly controlled by NE-trending fault zones. Whether the concealed orebody exists in the north of Weilasituo ore district is an urgent problem to be solved. The northern of Weilasituo ore district was covered by Quaternary sediments, possessing similar metallogenetic conditions to Weilasituo ore district. In order to investigate the concealed oresbodies, the authors build the multiple geophysical procedures to prospect concealed orebodies in coverage area, including gravity, magnetic induced polarization in median gradient array and controlled source audio-frequency magnetotelluric measurements. Based on the results obtained above, it has been demonstrated that there exists a concealed orebody in the north of Weilasituo ore district. Multiple geophysical procedures constructed in this paper to prospect blind orebodies beneath coverage area, can meet the demand of prospecting ores in covered areas.

Keywords Multiple geophysical methods · Ore-controlling fault · Concealed deposit

1 Introduction

The challenges encountered in prospecting deep ores beneath covered region include large depth, strong interference, low precision and difficulty in understanding the deep metallogenic regularity [1, 2]. Therefore, it is difficult to obtain geological and geochemical information in most cases, especially for hydrothermal

---

Y. Meng (✉) · R. Zhang
State Key Laboratory of Geological Processes and Mineral Resources,
China University of Geosciences, Beijing, China
e-mail: josemeng@163.com

R. Liu · T. Lin · W. Wang
Institute of Geophysical and Geochemical Exploration, Chinese Academy
of Geological Sciences, Langfang, China

Q. Di et al. (eds.), *Technology and Application of Environmental and Engineering Geophysics*, Springer Geophysics,
DOI 10.1007/978-981-10-3244-8_28

vein-type orebody. In order to promote the effectiveness of exploring blind deposits or orebody, it is necessary to apply multiple geophysical methods that can penetrated rocks during locating and predicting blind hydrothermal vein-type orebody beneath covered region. This article takes the north area of Weilasituo copper polymetallic deposit as an example, which is a magmatic hydrothermal vein-type deposit beneath Quaternary cover. In this case, the exploration processes to locate concealed magmatic hydrothermal vein-type orebodies beneath coverage area were constructed. Based on gravitational, magnetic and electrical methods, combined with the geological data, this paper studies the distribution of deep structures, determines relationship between deep structure and blind orebodies, speculates channels in which the hydrothermal migrated, and locates blind deposits beneath the coverage.

2 Metallogenic Characteristics

2.1 Regional Geological Setting

Folds and faults are well developed in west slope of Daxinganling's southern section. Main structures are the NE-trending extrusive tectonic belts, which control the distribution of magmatic rocks in the area.

Besides the wide-distributed Quaternary [3, 4] alluvial and aeolian sand, the area mainly exposes Proterozoic Buyant group (mainly Xilinguole diamictite), Upper Carboniferous, Permian and Jurassic stratum. Magmatic intrusions distributed in the southern section of Daxinganling metallogenic belt mainly occurred in Hercynian and Yanshanian.

2.2 Ore Deposit Geology

The study area is mainly covered by Quaternary sediments. The exposed faults are rare and most of them are NW- and NEE-trending. The NW-trending fault, namely Zhulike-river fault, is a blind tensile fault, crossing the southwest part of the mining area, and is considered to be the migration channel of ore-bearing hydrothermal fluids; The S-shape NEE-trending compression fault is the main ore-controlling structure. Its scale is variable along strike and inclination, and the thickness changes greatly. The fault surface incline to north and the dip angle is about 30°, The intersection of NEE- and NW-trending faults controls the occurrence of orebodies.

The intrusive rocks in the study area could be divided into the Hercynian quartz diorite and the Early Yanshanian granite. The metamorphism in the area include regional metamorphism, dynamic metamorphism and hydrothermal metamorphism. Hercynian dikes mainly developed in biotitic plagioclase gneiss. The physical properties of gangue rock are shown in Table 1.

Table 1 Statistical table of the physical properties of copper-polymetallic ore at Weilasituo

Name	Den. g/cm^3	Mag./10-6SI	Res. Ω·M	C-rate ms
	Avg	Avg	Avg	Avg
Diorite	2.655	664.5	4832.4	0.4
Gneiss	2.712	658.1	2690.1	2.7
Mafic dike mineralized	3.500	46599.8	773.3	52.1
Diorite mineralized	3.728	4076.3	147.4	56.0
Sphalerite	4.289	58987.0	90.3	71.6
Cu-Zn deposit	3.992	10874.1	41.4	80.8
Chalcopyrite	4.227	39632.9	40.8	90.5

3 Method

The properties of rock and ore were obtained by MOLSPIN magnetic survey system, Made in UK, and RP-1 electrical meter. The analyzed results are shown in Table 1. The charging rate and density of wall rock is low, but the resistivity is higher; The charging rate of oxidized ore is low, but the resistivity value is higher; Sulfide ore and pyritization rock are the main geological bodies that caused high charging rate and low resistivity geophysical abnormalities, shown in Table 1.

Based on the physical characteristics of geological bodies mentioned above, and the regional gravitational, magnetic and electric field, we tend to combine geophysical abnormal with ore, to speculate structures and rocks, to define the relationship between rocks, structures and orebodies, and then to select target areas to carry out detailed survey, finally, to predict the position of blind orebodies (Fig. 1a).

4 Example

According to geological analyses mentioned above, we proposed the solution to prospect orebodies beneath Quaternary coverage and summarized the solution as three steps: discover the fault, enclose rock and define orebody. In this paper, we use multiple geophysical methods, including gravity measurement to predict structure, magnetic measurement and induced polarization (IP) to predict rock and mineralization, controlled source audio-frequency magnetotelluric method (CSAMT) to locate orebodies. The multiple geophysical prospecting flow charts to explore blind orebodies beneath coverage area are shown in Fig. 1a.

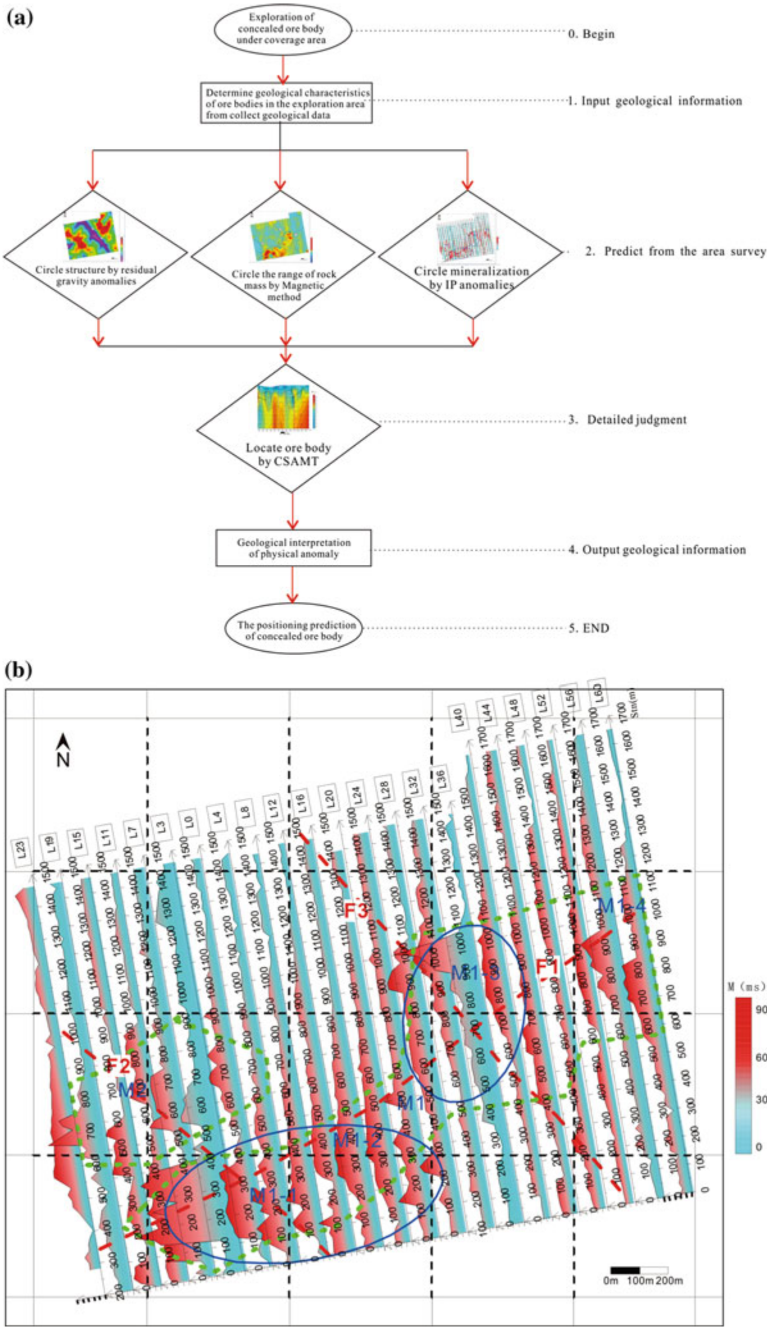

Fig. 1 The multiple-geophysical process to prospect the concealed ore-bodies in coverage areas. **a** The *upper* one, fig shows process; **b** the *down* of the fig, shows geophysical interpretation. The *red dotted line* shown in down of the fig means inferred fractures by geophysical methods, *blue ovals* means inferred ore-bearing locations, *green dotted line* means IP abnomal areas

4.1 Analysis and Inference by Gravity Anomalies

This paper collects gravitational field data by CG-5 gravimeter. According to residual gravity values of study area, there are three lower residual gravity anomalies. This paper infers that there maybe three faults, namely F1, F2 and F3, in the area. Their geometric parameters are as follow, the strike of fault F2 and F3 are NW30°, while F1 is a NEE–trending fault. The F2 fault ranges from line 10 to line 48; the scope of F3 is from line 23 to line 8; fracture F1 runs through all survey lines in the area and trends to NE60°. The intersections, F1 across F2 and F3, are detailed survey targets by magnetic method, induced polarization and CSAMT.

4.2 Analysis and Inference by Magnetic Anomaies

In this paper, acquisition of high precision magnetic data was done by GSM-19T proton precession magnetometer. After magnetically polarization and 500 m upward continuation, the study area is in the gradient belt where magnetic anomalies switch from positive to negative. There are two anomalies with high magnetic values connected with each other forming crescent-shape area, with six smaller magnetic anomalies in it, namely C1 to C6. The locations of six anomalies perfectly correspond to intersections of faults delineated by gravity method. Referring to geological and physical properties, shown in Table 1, in the study area, we speculate crescent-shape magnetic anomaly corresponding to two ore-bearing/mineralized rock, and there exist deep blind orebodies.

4.3 Analysis and Inference from IP Anomalies

We get induced polarization in median gradient array and CSAMT data by GDP-32II, a multiple electromagnetic receiver. According to planar contour map of apparent charging rate calculated from induced polarization in median gradient array, there are two anomaly areas with lower apparent resistivity and higher apparent charging rate in the study area corresponding to fractures delineated by residual gravity anomalies and rocks predicted by magnetic method. Based on research of gravity, magnetic method and induced polarization, the paper infers fractures F1, F2 and F3 are the main ore-controlling fractures, they strictly control distribution of orebodies in the study area, we put forward that the fracture intersection is good location for deep blind orebodies occurrences. Red dotted line means fractures, blue oval means ores, green dotted line means C-rate abnomals, shown in Fig. 1b.

4.4 Analysis and Inference from CSAMT Anomalies

According to research of gravity, magnetic and IP in median gradient array, we define good mutual verification lines including line 0, 36, 44 and 48; consequently, we carry out CSAMT survey on them. Taking line 36, across F1 and F3, moreover, the geological and mineralized information is good, as an example in this paper. By comprehensive analysis and research on relationship between structures and deep blind orebodies, we locate one-site of ore whose altitude range is from 1250 to 820 m, station range is from point 870 to 1100, NW-trending 15°, 40° inclination; One mineralized ore, namely B, which altitude range is from 1250 to 820 m, station range is from point 310 to 520, NW15°, 30° inclination.

5 Discussions and Conclusions

The multiple geophysical exploration procedures shown in this paper can be applied to prospect blind orebodies beneath the coverage area, by using geophysical area measurements, including gravity, magnetic and IP method to enclose the ore-controlling fault structures and mineralized rocks in the study area, define the relationship between structures, rocks and orebodies occurrence, and determine areas needing further fine measurements.

Further, CSAMT has predicted the embedded depth of blind vein orebodies, two-site blind orebodies have been predicted. Distribution of deposit is strictly controlled by faults, and the deep NW-trending faults in the study area are the main ore-controlling structures. The interaction of two sets of faults is the favorable location for mineralization, meanwhile, there may be much more large-scale blind orebodies in deeper intersections of deep faults. As a result, the multiple geophysical procedures to prospect blind orebodies beneath the coverage area constructed in this paper can meet the demand of prospecting deep blind ores in covered areas, and have promotion value.

Acknowledgments This article was funded by Project 111 (No. B07011), Chinese national NSF Project (No. 41504063), Geological survey project of China Geological Survey (No. 1212011120202).

References

1. CHEG Qiu-ming, “Ideas and Methods for Mineral Resources Integrated Prediction in Covered Areas,” Earth Science-Journal of China of China University of Geosciences, 2012, 37(1), pp. 1109–1125. (In Chinese with English Abstract)
2. GUO Ling-jun, ZHAO Zhi-jun, CUI Lai-wang, YANG Bo, LIAN Shi-en, “Geological and Mineral Resource Characteristics and Oreprospect of Cu-polymetallic Deposits in the Northern Part of Abag Banner, Inner Mongolia,” Acta Geoscientica Sinica, 2011, 32(1), pp. 57–63. (In Chinese with English Abstract)

3. HUANG Zong-li, YAN Jia-yong, "The Relationship between the Residual Gravity Anomaly and the Distribution of Metallic Deposits in China," Acta Geoscientica Sinica, 2011, 32(6), pp. 652–658. (In Chinese with English Abstract)
4. LIU Jian-meng, ZHANG Rui, ZHANG Qing-zhou, "The regional metallogeny of Da Hinggan Ling, China," Earth Science Frontiers, 2004, 11(01), pp. 269–277. (In Chinese with English Abstract)

Accurate Recognition of Underwater Riprap of Rivers and Lakes Based on the Seismic Imaging

Fuyu Jiang, Wenkai Chang and Leilei Xie

Abstract During the operation of rivers and lakes dam, due to the reasons for engineering measures, deposition or geological disaster, bank collapse and the river changes still occur. To enhance slope stability and anti-erosion ability, reducing the incidence of bank collapse, the riprap method is widely used in revetment dam engineering. In general, such as riprap stacked body is stable when dry, but with the water level rise and changes in natural conditions, loosely stacked body will slip to the bottom of collapse, leading to reservoir sedimentation, even a threat to the dam safety. Therefore, we should track and monitor the range, chemical speciation of these stacked body periodically, on the one hand is the need for the project to evaluate the quality of underwater riprap, the other is an indispensable work for the management to ensure the flood discharge section and the capacity of the reservoir. However enrockment has loose characteristics, the body full of water and sediment, it can no longer be regarded as a single block. Furthermore earthquake method is limited by the epicenter equipment frequency band, energy size and bubble effect, it is difficult to achieve seismic wave signal by artificial excitation penetrating the underwater gravel, riprap and other discrete body, so it is difficult to collect enough seismic wave that has high signal to noise ratio to reflect the occurrence status of enrockment. Combined with the exploration of Longhekou serveoir, using a new type of source equipment called 'a light pressure type automatic trigger device which could be used in shallow water'. The practice results showed that the distribution and thickness of riprap which seismic imaging identified was coincided to the physical truth. This provided important theories and practical basis for accurate identification of underwater target in shallow water by using the seismic imaging method.

This work is supported by National Natural Science Foundation of China (No. 41504081) and Natural Science Foundation of Jiangsu Province, China (No. BK20140844).

F. Jiang (✉) · W. Chang · L. Xie
School of Earth Sciences and Engineering, Hohai University, Nanjing, China
e-mail: jiangfy@hhu.edu.cn

Q. Di et al. (eds.), *Technology and Application of Environmental and Engineering Geophysics*, Springer Geophysics,
DOI 10.1007/978-981-10-3244-8_29

Keywords Underwater riprap · Tesseral 2D software · Forward calculation · Elastic wave equation · 'Light pressure type automatic trigger device used in shallow water

1 Introduction

At present, the major detection method of stacked body underwater are drilling and geophysical exploration. It has many limits about drilling which are water depth, surface width, drilling depth, wind, flow rate, season, tidal current and navigation conditions. Moreover, the construction of operation platform is time-consuming and dangerous, and the measuring points are less, so it is difficult to determine the distribution range of the target body [1]. In recent years, the rapid development of water geophysical techniques contain electromagnetic method, resistivity method, seismic wave method and so on. And they has become important means of obtaining target body [2–9]. However, the ripraps has different physical properties with surrounding rock and its environment, which has decided these methods are generally difficult to determine the bottom position of the underwater ripraps. For example, GPR method affected by the frequency and water depth, it is difficult to penetrate water depth more than 15 m, and the thickness of riprap layer more than 4 m; In resistivity method, because of the characteristics of loose riprap body, we can not regard the riprap as a single body, the stone riprap saturates water and sediment, so that there is no significant resistivity difference between riprap and surrounding rock, this does not satisfy the properties premise; The seismic exploration is restricted by the band width of the device, the amount of energy and bubble effect, it is difficult to collect high signal to noise ratio. We have developed a new type of source equipment called 'a light pressure type automatic trigger device which could be used in shallow water', it resolve this problem well.

2 Seismic Exploration the Riprap of Longhekou Serveroir

Longhekou serveroir is located in the Hangbu River, and its east bank is located in the main river, in order to reduce flood damage to the bank, during the reservoir reinforcement design, using underwater riprap to increase cover weight, design section in Fig. 1.

To overcome the traditional source more clutter, bubble effect, impact energy and frequency is not adjustable, not fixed and other shortcomings, in seismic data acquisition process, we use a new type of source equipment which calls 'a light pressure type automatic trigger device which could be used in shallow water' [10]. By the hammer that weight adjustable to impact the bottom with special metal, such that the resulting seismic wave propagation in a certain direction. The hammer is pulled by air pump, and through the time of the air pump discharge and fill to adjust

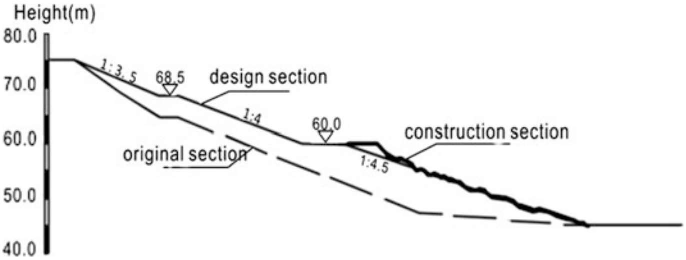

Fig. 1 Design section map

the impact frequency, the compressor and generator for air pump must be a distance from the source vessel to eliminate clutter. The device produce seismic waves with energy and band moderate, low noise, energy and impact frequency can be adjustable and fixed. Meanwhile, the device is portable, the total weight is less 60 kg, it is suitable for shallow waters and the use of the site without lifting equipment. Structure is shown in Fig. 2.

The Fig. 3 shows the seismic imaging waveform of the Longhekou serveroir. The color curve is automatic recourse alignments, the results reflect the distribution of various rock layers basically. Compare with Fig. 1, the seismic phase axis is appeared at about 5 m underwater, it descripts that surface elevation of the water is about 73 m; In 0–25 m, a horizontal high-amplitude phase axis of seismic wave is appeared, with the corresponding Fig. 1, there has a high impedance and horizontal

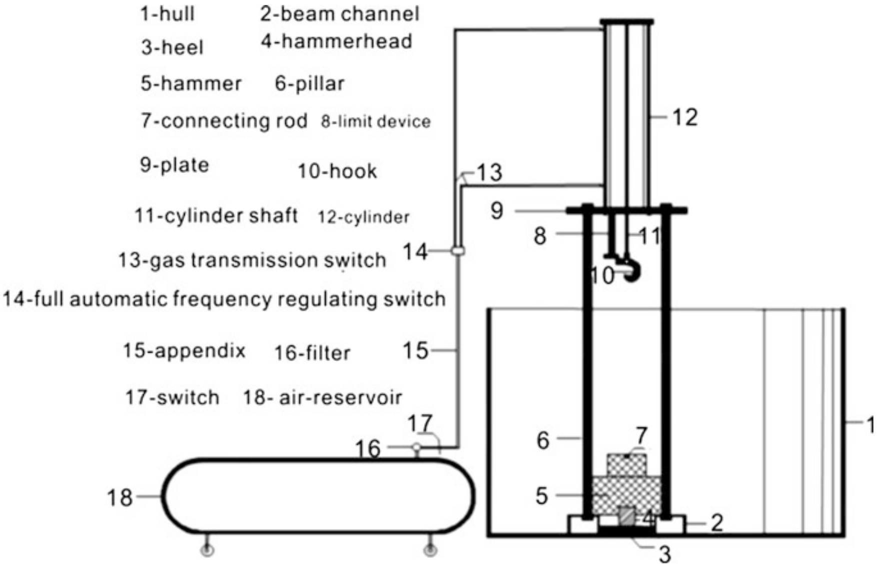

Fig. 2 The map of the source device

stone pitching at the elevation of 68.5 m; At 25–75 m, there is a gravel layer with a relatively large slope, and its wave impedance is less than dry stone, but with the clear phase axis, continuously; The riprap level distribution in 75–150 m, thickness in the range between 1 and 6 m, because the riprap was thrown down random, its top boundary is irregular pile, so that the top interface of the riprap seismic image is a irregular shape, which coincide with the actual; Riprap bottom interface and artificial backfill has obvious difference in wave impedance, so the amplitude of the reflected wave group is obviously different(red curve), the top interface due to the existence of two seimic wave reflection and diffraction occurs in the process of speed down, the top interface of the fill soil is irregular; The blue curve is inferred to be the bedrock surface, according to the exposed rock at two sides of the Longhekou reservoir, mainly for granite, gneiss and neutral volcano rock, bedrock surface depth is about 18 m, the drilling data in the survey and design stage of the Longhekou dam is basically consistent with the data. Because the original river bed was badly washed, the bottom of the river bed is not or contained less sediment, this is consistent with no sand in seismic map.

The ripraps are in discrete state, small thickness and deep water, these factors make it difficult to drill on the water, we use sounding method to measure the top interface of the riprap layer, to verify the accuracy of seismic imaging test. Detailed analysis and comparison of results are shown in Table 1. Visible from the table, the absolute error is less than 2.1 m and the relative error is no more than 11.2%; With the increase of the exploration depth, absolute error and relative error increases gradually, this is because the result of seismic image is effected by exploration depth. Overall, the method has high precision for detecting the bottom and top interface of the riprap.

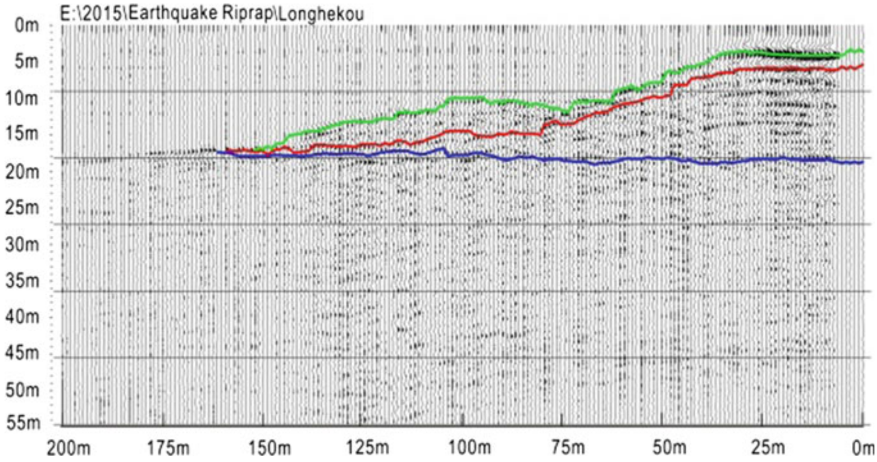

Fig. 3 Seismic reflection waveform of Longhekou serveroir

Table 1 Comparison of seismic results and sounder results

Horizontal position (m)		150	140	130	120	110	100	90	80	70
Top interface	Seismic (m)	14.8	13.7	12.9	12.1	11.8	10.2	10.2	10.9	11.3
	Sounding (m)	15.1	14.2	13.4	12.8	11.4	9.7	10	10.3	10.7
	Absolute error	0.3	0.5	0.5	0.7	−0.4	−0.5	−0.2	−0.6	−0.6
	Relative error	−2.0	−3.5	−3.7	−5.5	3.5	5.2	2.0	5.8	5.6
Bottom interface	Seismic (m)	18.3	17.7	16.9	15.5	15	14.2	13.8	14	14.3
	Sounding (m)	20.4	16.2	15.4	16.7	16.9	15.7	14.5	13.1	13.4
	Absolute error	2.1	−1.5	−1.5	1.2	1.9	1.5	0.7	−0.9	−0.9
	Relative error	−10.3	9.3	9.7	−7.2	−11.2	−9.6	−4.8	6.9	6.7

3 Conclusions

Riprap has loose characteristics, the body full of water and sediment, it can no longer be regarded as a single block. Furthermore earthquake method is limited by the epicenter equipment frequency band, energy size and bubble effect, it is difficult to achieve seismic wave signal by artificial excitation penetrating the underwater gravel, riprap and other discrete body, so it is difficult to collect enough seismic wave that has high signal to noise ratio to reflect the occurrence status of enrockment. Combined with the exploration of Longhekou serveroir, we develop a new type of source equipment called ‘a light pressure type automatic trigger device which could be used in shallow water’, we also use sounding method to verify the accuracy of seismic imaging test, the method has high precision for detecting the bottom and top interface of the riprap.

Acknowledgments We are grateful to the anonymous reviewers for their comments and thoughtful suggestions. At the same time, we would like to express our warmest gratitude to Jinhuang Yu, Ao Yang and Zongwen Zheng, without their invaluable help and generous encouragement, the article would not been accomplished.

References

1. Gao Jianbo. Brief discussion on the method selection and application of water geological drilling [J]. Railway Investigation and Surveying, 2012, 3:51–54.
2. Ma Hongjiao, Liyu, Cai Hui, et al. The application of geological radar detection technology to enclose tideland for cultivation to throwfill [J]. Journal of Nanjing Forestry University(Natural Sciences Edition), 2004, 28(2):51–53.
3. Wang Chuanlei. The magnetic detection of sunken ships in the madang section of the Yangtze River [J]. Journal of Environmental & Engineering Geophysics, 2006, 11(2):123–131.
4. Yu Jinhuang, Tao Yuezan. Research on high density resistivity method’s forward and inversion simulation of underwater enrockment [J]. Journal of Heifei University of Technology, 2014, 37(3):333–337.

5. Wang Jian, Zhang Saimin, Ma Xiaocheng. Application of water multi-electrode resistivity method in oil-gas pipeline projects [J]. Jilin Geology, 2012, 31(2):76–79.
6. Cheng Q, Tuo XG, GE B, et al. The application of the high-density electrical method to the survey of Chayuangou landslide in Gaochuan, Sichuan province [J]. Geophysical and Geochemical Exploration, 2012, 36: 69–72.
7. Vladimir Shtiveman. Shallow water seismic surveys for site investigation in the Haifa Port Extension area, Israel [J]. Journal of Applied Geophysics, 2001, 46(2):143–158.
8. T. Hussein, A.G. Mula, H. SCHNEIDER. Geological and seismic investigations with regard to shallow ground water exploration in Eastern Sudan Republic [J]. Journal of African Earth Sciences, 1989, 8(1):75–78.
9. Willianm P, Anderson JR, David G, et al. The effects of Holocene barrier-island evolution on water-table elevations, Hatteras Island, North Carolina, USA [J], Hydrogeology Journal, 2000 (8):390–404.
10. Yu Jinhuang. Light pressure type automatic trigger device used in shallow water [P]. China: ZL 2013 1 0010619.6.

Application of Seismic Imaging Method in Detecting the Complex Geological Hazards

Hua Zhang, Hui Yang and Luoyi Zhang

Abstract In recent years, geological hazards happened frequently, for example goaf, karst, ground fissure, landslide threatening engineering construction and human life severely. How to take some measures effectively and find out the space character of geological hazards are very important to control geological hazards. In this paper, we firstly explain the principle of seismic imaging method. Then analyze the character of geophysical abnormity in the different geological hazards, and discuss the effect of seismic imaging method in detecting the geological hazards. Meanwhile combining with some engineering examples, we have detected these geological hazards accurately and we can get some proofs from the borehole. It indicates that this method has lots of advantages in detecting geological hazards. For example high resolution, low cost, high efficiency and it can make up for disadvantages of other detecting methods.

Keywords Seismic imaging method · Geological hazards · Abnormity · Reflected wave

1 Introduction

During the process of all kinds of engineering construction. There are some different geological hazards, such as coal goaf, karst, landslide, ground subsidence, ground fissure and so on. These geological hazards not only seriously hinder the

---

This research work was sponsored by the National Natural Science Foundation of China (No. 41304097), the Natural Science Foundation of Jiangxi Province (20151BAB203044) and the China Scholarship Council (No: 201508360061).

H. Zhang (✉) · H. Yang · L. Zhang
Fundamental Science on Radioactive Geology and Exploration Technology Laboratory,
East China University of Technology, Nanchang 330013, Jiangxi, China
e-mail: zhhua1979@163.com

Q. Di et al. (eds.), *Technology and Application of Environmental and Engineering Geophysics*, Springer Geophysics,
DOI 10.1007/978-981-10-3244-8_30

engineering progress and cause huge economic losses, but also threaten the safety of human life and property, so we must find out the scope and scale of these geological hazards, and analyze its causes. Of course, we also need to predict its developing tendency and harmfulness, which can provide some relevant technical parameters for the prevention engineering design and different construction. For the geological hazard investigation, the conventional exploration method is drilling, but drilling is a point exploration method, which has a long exploration cycle and high cost, and most of time, it is hard to find out the overall spatial distribution characteristics of geological hazards, that make great uncertainty in the geological hazard governance design. The occurrence of geological hazard often show many geophysical anomaly characteristics, such as resistivity, impedance, dielectric constant, speed and so on, which provide a premise condition for taking corresponding geophysical methods to detect the spatial distribution and slope of the geological hazards, and the geophysical methods have some advantages of low cost, high effect, direct effect and fast detecting, which are widely used in different geological hazards investigation. So in this paper we introduce the application effect of seismic image method in geological hazard survey combining some cases that the seismic image method detects the geological hazards such as goaf, karst, ground fissure, landslide and so on [1, 2].

2 Theory of Seismic Image Method

Shallow seismic exploration method which uses the many seismic wave information to detect the underground medium through the continuous scanning the targets on the ground or under the water, and its exploration depth is more larger than the depth of the ground penetrating radar(GPR). In the measurement process of seismic image method, we shot with a single point, and receive the signal with a single detector. After a shot, the shot point and receive point move forward a certain distance (trace distance) at the same time, after repeating the process above, we can obtain a seismic reflection time profile, and its schematic diagram is shown in Fig. 1. Because we adopt a single shot to fire and a single detector to receive it, we don’t need to do the NMO and stacking in the process of data processing, which can save the time of data processing and also avoid the stretching and distortion effect that is caused by NMO in shallow reflection wave. At last we can retain all the dynamic characteristics of reflection wave and reduce the processing error, so this method has been widely used in the engineering area [3, 4].

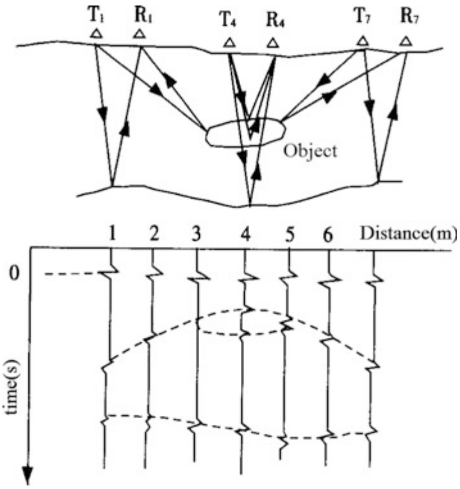

Fig. 1 The theory of exploration of seismic imaging method

3 Engineering Examples

3.1 Goaf Investigation

Some highway appear different subsidence and dislocation to some extent in Shandong province, after investigation we find it is a large number of unknown goaf which is formed by the local small mines that is cross-border mining, and this causes different degrees ground fissures and sinking in the highway. Because the depth of coal seam is relatively shallow from 20 to 30 m, but the goaf formed by it has strong destructive power, that causes a very large damage to the highway operation. In order to determine the sinking details and mark out the scope and scale of the goaf, and provide detailed geological data for the next step maintenance and management of the road, we take an exploration for this area using the seismic image method. Coal goaf mainly represents interruption of coal seam reflected wave and discontinuous of phase axis, or appears some low frequency and messy weak reflection in the seismic image profile. So we design four seismic measuring lines that are vertical to the road trend, the offset distance is 8 m and the point distance is 1 m, then we use the hammer to shot. From the seismic image profile, we know that there are several goaf in this area. The depth profile of second line is shown in Fig. 2, we can find a one abnormal phenomenon of phase axis interruption and discontinuous that is from 57 to 70 m in horizontal distance and from 20 to 23 m in depth. We can infer that it is a coal goaf and there is also a proof from borehole. The result can provides accurate location for the grouting treatment for the highway, at last we can get a good results.

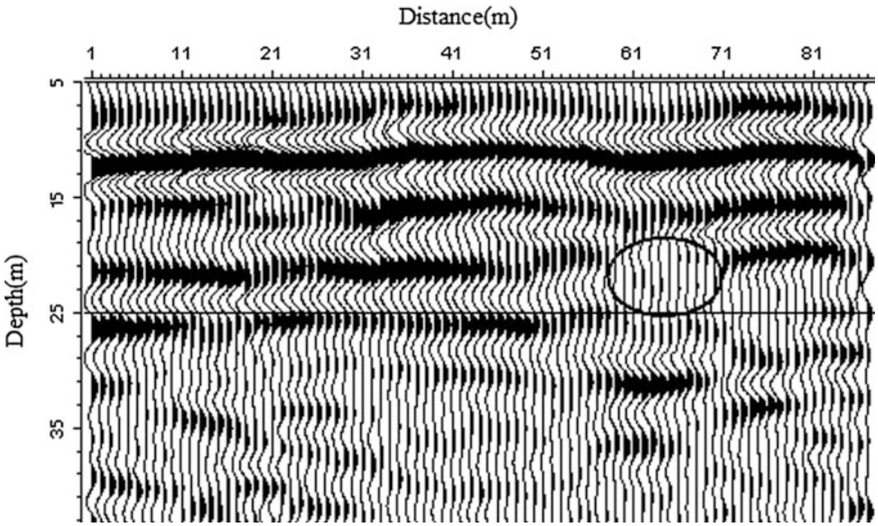

Fig. 2 Seismic imaging depth profile of the goaf

3.2 Karst Investigation

Some company want to build high buildings that is more than 30 layers at a site, in order to ensure the big building's safety, we must make a geological hazard evaluation before its construction. The terrain of this area is flat, and the exposed bedrock is limestone, but its karst fissure is abundant, and its fillings materials are mainly water and clay, so there is a potential threat to the construction in this area. In order to take corresponding methods to deal with the karst, we must detect the distribution range and the depth of the karst. Because we need to detect the developed karst in the limestone, as we know, the reflection coefficients are large in the interface formed by up and down surrounding rocks, which is very easy to form two or more groups reflection wave signal, and it has a strong amplitude, low frequency. But in no karst areas, the rock mass is full dense and the amplitude of signal is relatively weak or there is no reflection interface. So we design six seismic measuring lines, and the distance between each line is 20 m, the offset distance and point distance is 8 and 1 m respectively. At last we can detect the location of the karst development accurately, As shown in Fig. 3, the karst development location is from 17 to 26 m in the horizontal distance and from 18 to 33 m in depth. From the follow-up grouting amount in this position, the amount of cement and mortar are larger, and it indicates the effect of the grouting is very good. In other words, it can also indicates that it is feasible to use the seismic image method to detect the karst.

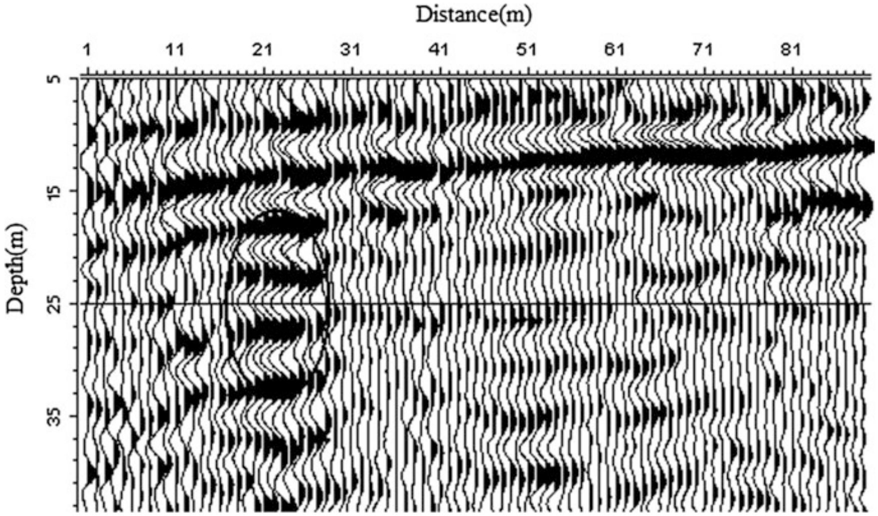

Fig. 3 Seismic imaging depth profile of the karst

3.3 Ground Fissure Investigation

We are going to build a highway in some loess area in Shanxi province, but there develop lots of ground fissures. We can see some ground fissure on the surface of the earth, some horizontal shift of the ground fissures nearly reach 1 m. So we must take the seismic image method to detect the ground fissures in this area. We design some measuring line that are vertical to the ground fissure's trend, and its offset distance of the measuring line is 6 m, and it strides across the known ground fissures. We plan to survey the ground fissure hazard according to the thinking that is from known to unknown. It can be seen from the Fig. 4, there is an obvious reflection wave abnormal area which is from 18 to 24 m in its horizontal distance, and its phase axis is interrupted, furthermore the position of top and bottom layer also appears the dislocation and distortion. It is interpreted as the reflection of the ground fissures, and its depth is about 18 m. Finally it can be verified from the manual excavation, and the shape and scale of ground fissure are matched well with the inference using the geophysical prospecting method.

3.4 Landslide Hazard Investigation

Some new town was constructed at the foot of the mountain in Guizhou province, but behind it, there is a steep hillside, and its angel is about 25° to 60°, Besides the local rainfall is abundant, so it is easy to form landslide, we must carry out the special geological hazard exploration evaluation and other researches in this area,

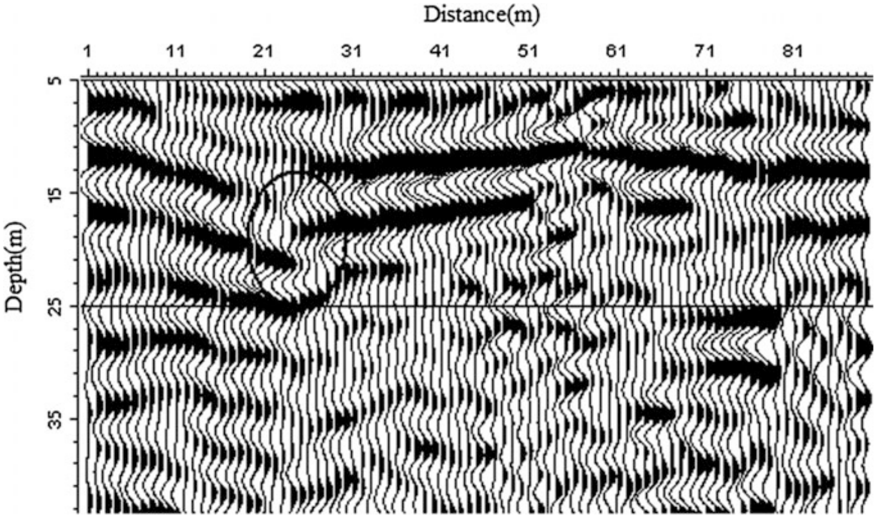

Fig. 4 Seismic imaging depth profile of the ground fissure

and one of the methods is the geological hazard exploration. The surface is covered with residual soil and clay that belong to the Quaternary period in this area, but the bedrock is composed of Triassic limestone, due to the continuous rain, some local position have appeared a tiny ground fissure under the effect of gravity and pulling, so we must govern it as soon as possible. We can ensure that the landslide surface is top limestone interface through the field investigation. Our main task is to detect the buried depth of the landslide and determine the shape of sliding surface, and provide a reference for the comprehensive treatment. Because there is a larger different wave impedance between the top and bottom medium which can forms strong reflection interfaces, and it can satisfy the premise of geophysical detection, so we also choose the seismic image method. We design five longitudinal line, eight traverse line, and the offset distance is 8 meters, the point distance is also 1 m. At last we find out buried depth and shape of landslide surface in this area basically. Figure 5 is a depth profile of one vertical line. We can see from the Fig. 5 that the buried depth of landslide surface is about from 5 to 25 m, and the western thickness is shallower than the eastern. From the 1 to 46 m in horizontal distance, the reflected wave of limestone surface is uniform, so we can infer that the landslide body doesn’t occur in this area. However, from the 47 m, because of the effect of shear stress, the rock mass begins to change its shape, and the ground fissures are abundant, damaging the internal connection of rock badly, forming a larger tension ground fissures, resulting in reflected wave phase axis distortion. So the landslide surface is more development from this location and have a tendency to slide down. The position of landslide surface is showed as the black line in the Fig. 5, which has a great harm to the village below. So we can make effective governance for this landslide from the seismic image data and try to avoid the occurrence of landslide geological hazards.

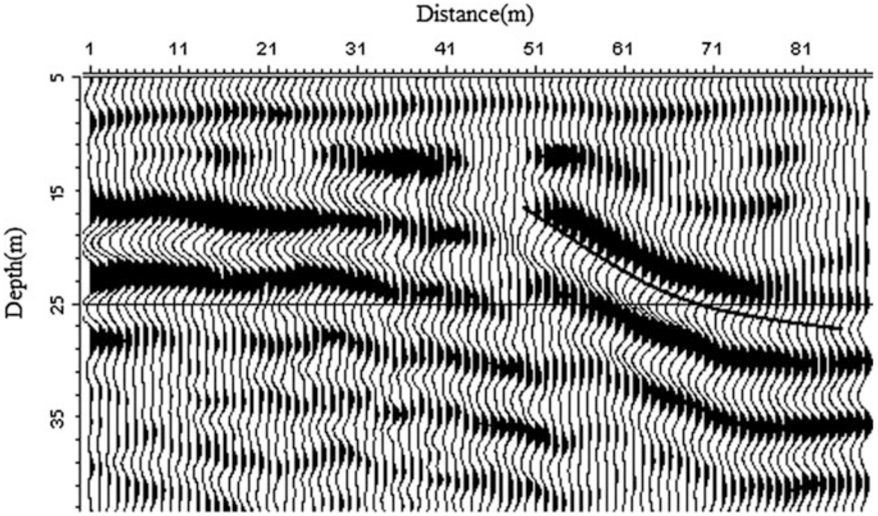

Fig. 5 Seismic imaging depth profile of the landslide

4 Conclusions

It is more intuitive and vivid to reflect the morphology and occurrence of the target body using seismic image method, and it is also more economical to detect the planar and space distribution of the harmful geological phenomenon, such as goaf, karst, ground fissure, and landslide and so on, moreover, this method has a better effect than other geophysical methods. At the same time, this method can provide a more comprehensive and a reliable geophysical result for formulating optimal strategies of governing the geological hazard, so it can make up the deficiency of drilling method effectively. On the other hand, we should also recognize that this method is influenced by some field conditions, for example site, ground conditions and so on, and its offset distance is not sure sometimes. So for detecting the more complex geological hazard body, we should combined with the other survey methods, such as geophysical method, drilling method, geotechnical test method and so on, and enrich its exploration effects. At last we can provide more abundant fundamental data for geological hazard governance.

Acknowledgments I thank Dr. D. M. Pan at China University of Mining and Technology for his valuable instruction and suggestion, and provide the real data. Finally, the authors would also like to thank the anonymous reviewers whose constructive comments helped improve this paper.

References

1. P. T. He, B. Z. Xiao, and X. C. Wu, “Application of Seismic Prospecting in Yuqian Freeway,” Chinese Journal of Underground Space and Engineering, vol. 4, pp. 1011–1015, April 2008.
2. G. Y. Lu, Z. Q. Zhu, and X. L. Hang, “Application of ground penetrating radar to control of geological hazards of road tunnel,” Journal of Natural Hazard, vol.6, pp. 118–122, Feburary 2008.
3. W. H. Wang, X. L. Wang, and J. P. Liu, “The Application of Seismic Imaging Method in Exploring Karst Caves of a Superhighway,” Chinese Journal of Engineering Geophysics, vol. 4. pp. 141–145, May 2007.
4. X. J. Feng, Z. S. Li, and L. S. Song, “Seismic exploration of Boqishan landslide in Baoji,” Hydrogeology and Engineering Geology, vol. 1, pp. 55–58, December 2003.

Theoretical Study on Tensor Controllable Source Electromagnetic Field Distribution Law

Ruodi Yang

Abstract Tensor controllable source electromagnetic method was put forward long; however, since controllable source launching system satisfying tensor electrical impedance observation is quite complex and hard to manufacture, it was difficult to be applied. In 2010 Germany Metronix Company developed successfully the first controllable source magnetotelluric instrument that satisfied tensor electronic impedance observation, whose rotating dipole launcher could launch magnetic fields with different directions of polarization, different tensions and different frequencies. Now optimal electromagnetic field signals at all points within the testing area could be observed. That is why theoretical study was conducted on such launching device in this essay.

Keywords Tensor · Controllable source · Electromagnetic field distribution

1 Introduction

Controllable source audiomagnetotelluric method was put forward in the 1970s and used in the field of physical geography, exerting enormous functions in mineral deposit surveys, oil-gas exploration and hydrological environment. The greatest feature of this method was adopting artificial field source, which could enhance greatly the intensity of electromagnetic signal and making up the defects of natural field source signal being weak and difficult to measure. Moreover, it is with high working efficiency. With a dipole source emission, it could explore within large sector area at both sides; it is with large detecting depth; it is with high horizontal and vertical resolution; however, though scalar measurement could determine correctly simple layered medium, it requires multi-component measurement including electric field and magnetic field, i.e. tensor measurement for some more complex two-dimensional and three-dimensional media. In 1991, Xiao boLi,

---

R. Yang (✉)
School of Resource and Geoscience, CUMT, Xuzhou, China
e-mail: cumtyrd@163.com

Q. Di et al. (eds.), *Technology and Application of Environmental and Engineering Geophysics*, Springer Geophysics,
DOI 10.1007/978-981-10-3244-8_31

Laust B. Pedersen published an essay entitled Controllable Source Tensor Magnetotelluric Method in Geophysics, illustrating tensor CSAMT theories; however, due to manufacturing difficulties of tensor controllable source launching devices, scalar measurement is still the major method adopted at home and abroad. In 2011, Germany Metronix Company manufactured TXM-22 controllable source launching system, which was designed especially aiming at the above problems to meet the requirements of tensor detection. Since the detectable area it covered was increased, the observation efficiency was also enhanced greatly, which has opened new situation for tensor CSAMT application.

In 1960, Cantwell, T. put forward that underground media electric property was tensor impedance [1] and in 1972, Vozoff, K. summarized systematically the method of tensor impedance [2]. The relation between tensor impedance and electromagnetic field is:

$$\begin{bmatrix} E_x \\ E_y \\ E_z \end{bmatrix} = \begin{bmatrix} Z_{xx} & Z_{xy} & Z_{xz} \\ Z_{yx} & Z_{yy} & Z_{yz} \\ Z_{zx} & Z_{zy} & Z_{zz} \end{bmatrix} \begin{bmatrix} H_x \\ H_y \\ H_z \end{bmatrix} \tag{1}$$

It is known as relational expression of tensor impedance.

Besides super-high frequency, E_z component is very tiny, which is hard to be observed; therefore, relation of tensor impedance could be summed up as:

$$\begin{aligned} E_y &= Z_{yx}H_x + Z_{yy}H_y \\ E_x &= Z_{xx}H_x + Z_{xy}H_y \end{aligned} \tag{2}$$

Thus, under the conditions of two-dimensional or three-dimensional construction, electric field E_x is induced not only by H_y but also by H_x. E_x induced by H_y depends on tensor impedance Z_{xy} while E_x induced by H_x depends on tensor impedance Z_{xx}. Meanwhile, tensor impedance values Z_{yx} and Z_{yy} also have such dependency.

It is not hard to find out that to solve tensor impedance, at least two groups of electromagnetic fields with different directions of polarization:

$$\begin{aligned} Z_{xx} &= \frac{E_{1x}H_{2y} - E_{2x}H_{1y}}{H_{1x}H_{2y} - H_{2x}H_{1y}} \quad & Z_{yy} &= \frac{E_{1y}H_{2x} - E_{2y}H_{1x}}{H_{2x}H_{1y} - H_{1y}H_{2y}} \\ Z_{\mathrm{yx}} &= \frac{E_{2y}H_{1y} - E_{1y}H_{2y}}{H_{2x}H_{1y} - H_{1x}H_{2y}} \quad & Z_{xy} &= \frac{E_{2x}H_{1y} - E_{1x}H_{2x}}{H_{1x}H_{2y} - H_{2x}H_{1y}} \end{aligned} \tag{3}$$

Rotating dipole launching device could transmit changing magnetic fields at different directions of polarization and with different frequencies so as to solve various groups of tensor impedance elements, which is known as rotating dipole launching device; so, in terms of such launching device, it becomes more and more important to study electromagnetic field distribution law of electric dipole at

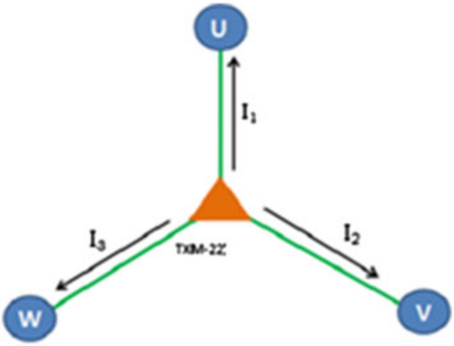

Fig. 1 Schematic diagram of rotating dipole launching device

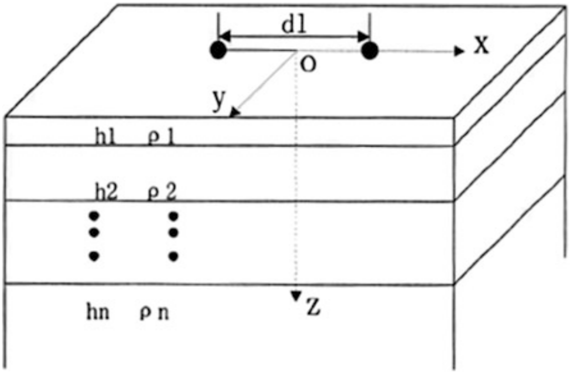

Fig. 2 Schematic diagram of layered earth-electricity model

different directions of polarization. In the following, this essay would deduce the electromagnetic field distribution (Fig. 1) of electric dipole at different directions of polarization with tensor detection method (Fig. 2).

2 Theoretical Formula Derivation

As is shown above, the electrical resistivity and layer thickness at n layer in N-layer leveling course medium are labeled respectively sum. One level electric dipole (earth conductor) is at the surface of the layered medium, with the dipole moment P=IdL. Choose the dipole moment center as the common origin of coordinate of cylindrical coordinate system and rectangular coordinate system. Set X direction points to the direction of dipole moment, z-axis downward vertically, then the expressions of electromagnetic field components in cylindrical coordinate system at quasi-static limit are:

$$E_r = \frac{IdL}{2\pi}\cos\varphi\left[\frac{i\omega\mu}{r}\int_0^\infty \frac{1}{m+\frac{m_1}{R^*}}J_1(mr)dm - \rho_1\int_0^\infty \frac{mm_1}{R}J_0(mr)dm + \frac{\rho_1}{r}\int_0^\infty \frac{m_1}{R}J_1(mr)dm\right] \tag{4}$$

$$E_\varphi = \frac{IdL}{2\pi}\sin\varphi\left[\frac{\rho_1}{r}\int_0^\infty \frac{m_1}{R}J_1(mr)dm - i\omega\mu\int_0^\infty \frac{m}{m+\frac{\mathrm{m}_1}{R^*}}J_0(mr)dm + \frac{i\omega\mu}{r}\int_0^\infty \frac{1}{m+\frac{m_1}{R^*}}J_1(mr)dm\right] \tag{5}$$

$$H_r = -\frac{IdL}{2\pi}\sin\varphi\left[\int_0^\infty \frac{m}{m+\frac{m_1}{R^*}}\cdot J_1(mr)dm + r\int_0^\infty \frac{m_1}{R^*\cdot\frac{m}{m+\frac{m_1}{R^*}}}\cdot J_0(mr)dm\right] \tag{6}$$

$$H_\varphi = \frac{IdL}{2\pi}\cos\varphi\int_0^\infty \frac{m}{m+\frac{m_1}{R^*}}J_1(mr)dm \tag{7}$$

$$H_z = \frac{IdL}{2\pi}\sin\varphi\int_0^\infty \frac{m^2}{m+\frac{m_1}{R^*}}J_1(mr)dm \tag{8}$$

In the type:

$$R^* = \coth\left[m_1h_1 + \coth^{-1}\frac{m_1}{m_2}\coth(m_2h_2 + \cdots + \coth^{-1}\frac{m_{N-1}}{m_N})\right]$$

$$\mathrm{R} = \coth\left[m_1h_1 + \coth^{-1}\frac{m_1\rho_1}{m_2\rho_2}\coth(m_2h_2 + \cdots + \coth^{-1}\frac{m_{N-1}\rho_{N-1}}{m_N\rho_N})\right]$$

$$m_j = \sqrt{m^2 - k_j^2},\ k_j^2 = \frac{i\omega\mu}{\rho_j}$$

In the formula, The expressions of the components of electromagnetic field at rectangular coordinate system are (considering the field measuring factors, only expressions of horizontal components are written out here):

$$E_x = E_r\cos\varphi - E_\varphi\sin\varphi \tag{9}$$

$$E_y = E_r\sin\varphi + E_\varphi\cos\varphi \tag{10}$$

$$H_x = H_r\cos\varphi - H_\varphi\sin\varphi \tag{11}$$

$$H_y = H_r\sin\varphi + H_\varphi\cos\varphi \tag{12}$$

When dipole rotates surrounding the center to certain angle, even if, since the centre origin of cylindrical coordinate system does not change, the electromagnetic field components of dipole of new direction of polarization at the same point at the same cylindrical coordinate system could be deducted, which are:

$$E_r' = \frac{IdL}{2\pi}\cos\theta\left[\frac{i\omega\mu}{r}\int_0^\infty \frac{1}{m+\frac{m_1}{R^*}}J_1(mr)dm - \rho_1\int_0^\infty \frac{mm_1}{R}J_0(mr)dm + \frac{\rho_1}{r}\int_0^\infty \frac{m_1}{R}J_1(mr)dm\right] \tag{13}$$

$$E_\varphi' = \frac{IdL}{2\pi}\sin\theta\left[\frac{\rho_1}{r}\int_0^\infty \frac{m_1}{R}J_1(mr)dm - i\omega\mu\int_0^\infty \frac{m}{m+\frac{m_1}{R^*}}J_0(mr)dm + \frac{i\omega\mu}{r}\int_0^\infty \frac{1}{m+\frac{m_1}{R^*}}J_1(mr)dm\right] \tag{14}$$

$$H_r' = -\frac{IdL}{2\pi}\sin\theta\left[\int_0^\infty \frac{m}{m+\frac{m_1}{R^*}}\cdot J_1(mr)dm + r\int_0^\infty \frac{m_1}{R^*\cdot\frac{m}{m+\frac{m_1}{R^*}}}\cdot J_0(mr)dm\right] \tag{15}$$

$$\mathrm{H}_\varphi' = \frac{\mathrm{IdL}}{2\pi}\cos\theta\int_0^\infty \frac{\mathrm{m}}{\mathrm{m}+\frac{\mathrm{m}_1}{\mathrm{R}^*}}\mathrm{J}_1(\mathrm{mr})\mathrm{dm} \tag{16}$$

$$\mathrm{H}_z' = \frac{\mathrm{IdL}}{2\pi}\sin\theta\int_0^\infty \frac{\mathrm{m}^2}{\mathrm{m}+\frac{\mathrm{m}_1}{\mathrm{R}^*}}\mathrm{J}_1(\mathrm{mr})\mathrm{dm} \tag{17}$$

Convert the components of electromagnetic field at cylindrical coordinate system to the same rectangular coordinate system, the expressions of the components of all electromagnetic field could be obtained, which are:

$$E_x' = E_r'\cos\varphi - E_\varphi'\sin\varphi \tag{18}$$

$$E_y' = E_r'\sin\varphi + E_\varphi'\cos\varphi \tag{19}$$

$$H_x' = H_r'\cos\varphi - H_\varphi'\sin\varphi \tag{20}$$

$$H_y' = H_r'\sin\varphi + H_\varphi'\cos\varphi \tag{21}$$

Thus, we could obtain the electric field components and magnetic field components of dipole electromagnetic field at new direction of polarization on the ground. According to the above method, electromagnetic field distribution of electric dipole at random directions of polarization at the same coordinate could be obtained. Take formulas 6–9 and 15–18 into formula 3, and the forward modeling of tensor impedance could then be realized.

3 Conclusion

Coordinate rotation method is adopted to solve the mathematical expressions of all electromagnetic field components of electric dipole at different polar directions at the same rectangular coordinate system so as to set theoretical basis for later one-dimensional and two-dimensional forward modeling. Thus, matlab or comosol software could be used to simulate electromagnetic field distribution of electric dipole at different directions of polarization to solve further tensor impedance and realize forward modeling of tensor impedance.

References

1. Cantwell, T., Detection and analysis of low frequency magnetotelluric signals, Ph.D. Thesis [M], M.I.T., 1960.
2. Vozoff, K., The magnetotelluric method in the exploration of Sedimentary basins, Geophysics [J], Vol. 37, No. 1, PP 98–141, 1972.

An Optimization Method for Interpreting ERT Data Based on Groundwater Numerical Modeling (Which Data Polarization Mode Should Be Used in 2D Inversion)

Xuelan Li, Diquan Li, Bo Yuan and Yanhui Dong

Abstract Aiming at choice of data polarization mode in magnetotelluric 2D inversion, trying to assist the geophysical inversion with the hydraulic characteristics of the water level and water quality information contained in the geological body. Based on this idea, a method for interpreting ERT data based on groundwater numerical modeling which data polarization mode should be used in 2D inversion is provided in this article. In this article, Magneto-telluric method as a way to accomplish numerical simulation of geophysical forward and inversion. Firstly, by studying the known geological model and multiple geological models with different choice of data polarization mode interpreted from ERT data, a set of groundwater numerical models can be set up. Then numerical simulation of groundwater flow and solute transport were conducted. Lastly, the optimal data polarization mode can be obtained by comparing the result of numerical simulation of groundwater. Sensitivity analysis were also conducted to verify the method. And the result show that the inversion model using only TE mode data is more valid, next is TE + TM, TM mode only is not proposed by comparing the numerical value of Standard of the Estimate, Root Mean Squared, Normalized RMS and Correlation Coefficient.

Keywords Magneto-telluric · Inversion · Geological model · Numerical simulation of groundwater flow · Solute transport

---

X. Li (✉) · D. Li · B. Yuan
School of Geosciences and Info-Physics, Central South University, Changsha 410083, China
e-mail: lixuelan@csu.edu.cn

Y. Dong
Institute of Geology and Geophysics, Chinese Academy of Sciences, Beijing 100029, China

Q. Di et al. (eds.), *Technology and Application of Environmental and Engineering Geophysics*, Springer Geophysics,
DOI 10.1007/978-981-10-3244-8_32

1 Introduction

In the prospecting of electromagnetic method, the TE and TM polarization modes have different advantages and disadvantages. According to the geological environment and the requirements of exploration, different devices models often produce different results. Geoelectric structure is generally three-dimensional in actually, so a three-dimensional inversion should be used to gain electrical property of structure underground, but the interpretation of three-dimensional inversion didn't used widely. Therefore, the real data for interpretation depends on the two-dimensional inversion techniques at present. However, It will encounter some issues if the two-dimensional inversion is used, such as: the inversion result has great difference due to the choice of data polarization mode are different when the observed data need to rotate on structural trends to accomplish 2D inversion in [1]. Faced with this problem, to obtain the main features of underground structures which data polarization mode should be chose?

This is a very important issue, because a subsequent electrical structure analysis and geological interpretations are based on the inversion results.

At present, researchers have noticed this problem, a series of relevant research are carried out, but it's remained a great divergence at the choice of the data polarization mode. So far, that divergence has not been completely resolved. Especially in the country, it's not using one data polarization mode solely but choosing TE and TM mode joint inversion.

Since the hydraulic characteristics of the geological bodies, such as permeability, has a direct correlation with lithology. Aiming to make a more thorough study of this problem, trying to assist the choice of data polarization mode for the geophysical inversion with the hydraulic characteristics of the water level and water quality information contained in the geological body. Based on this idea, a method for interpreting ERT data based on groundwater numerical modeling which data polarization mode should be used in 2D inversion is researched, and Magneto-telluric method as a way to accomplish numerical simulation of geophysical forward and inversion.

2 Research Methods

Geophysical forward is a way that gives the distribution of the field source, calculating the values about the field source. It equals calculating abnormal effect by the existing state (shape, occurrence, spatial position) geological and physical parameters (density, magnetic properties, electrical properties, flexibility, speed, et al.). The known geological and physical properties can be referred to as a model. Inversion is the reverse process of forward. If a point of the model space is defined as m, the data space is defined as d, according to the laws of physics, the relationship between m and d can be written as,

$$d = Gm \tag{1}$$

$$m = G^{-1}d \tag{2}$$

where G is a mapping between model space m and data space d.

3 Numerical Simulation

3.1 MT Forward Modeling and Inversion Calculation

Firstly, building a known geological model, name of Model i, shown as Fig. 1. Based on the distribution curves for the resistivity of several rock, Fig. 1 is converted into construction geoelectric model (the resistivity of clay, sandstone, granite were taken as 10, 500, 10,000 Ω m). Measuring point spacing is 50 m, the number of frequency is 40, and forward simulation used *MTSoft2D* which is developed by Chengdu University of Technology.

Inverse calculation using *GME_3DI* (*V4.1*) system which developed by Central South University, and gained different inversion results by selecting three different data polarization mode (TE, TM, TE + TM). After that, the resistivity was less than 50 Ω m divided into the clay; 50–1000 Ω m divided into sandstone; greater than 1000 Ω m was divided into granite, so the geological interpretation of MT method inversion was obtained (shown in Fig. 2).

Model i1–i3, Model i4–i6, Model i7–i9 were TE, TM, TE + TM data polarization mode with the interpolation spacing was 25, 50, 25 m, the number of interpolation frequency was 40, 40, 50.

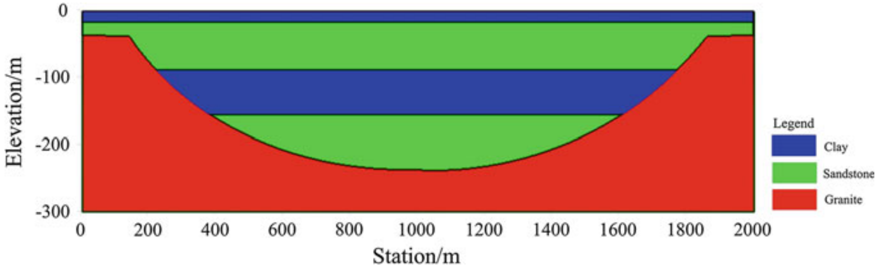

Fig. 1 The known geological Model i

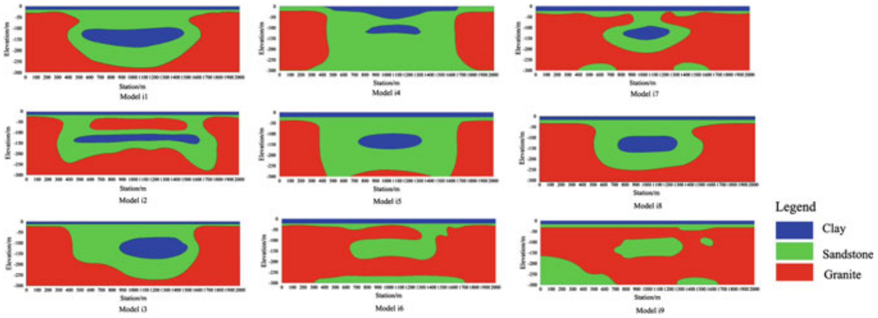

Fig. 2 The geological interpretation of MT method inversion

3.2 An Optimization Method for Interpreting ERT Data Based on Groundwater Numerical Modeling

Numerical simulation of groundwater used *Visual MODFLOW 2011.1*, Model i and Model i1–i9 were converted into groundwater numerical modeling. Ten groundwater numerical modeling used the same space subdivision, boundary conditions, and the excitation of source term with rainfall, pumping and injection wells (including point sources). According to [2] determined the value of permeability for different lithological. The numerical simulation use Transient flow, lasting 2000 days. 22 Observation wells was set up to monitor the response which generated by excitation source at the whole profile, and calculating the errors between Observation (Model i) and Calculation (Model i1–i9) Water level of groundwater numerical modeling, the results shown in Table 1. The results of Solute transport are consistent with the water level (table is omitted).

According to the results of Table 1, when the interpolation frequency and spacing are 40 and 25 m, the error of TE mode is minimal, and the Correlation Coefficient is greater than TM, TE + TM mode; Then, when the interpolation frequency and spacing are changing which the value are 40 and 50 m, Standard error of the estimate, Root Mean Squared, Normalized RMS between TE and TM mode are relatively close, TE + TM mode is slightly smaller than TE and TM, but the Correlation Coefficient of TE is the maximum; Lastly, the interpolation frequency and spacing are 50 and 25 m is simulated, the results is similar to the interpolation frequency and spacing are 40 and 25 m.

Only one scenario is analysed, in order to exclude the contingency, Sensitivity analysis were also conducted to verify the method. The second scenarios is established by adding an injection wells, and the errors are also calculated, the results is similar to the first scenario from Table 2. So the results show that TE mode is more valid than TE + TM mode, and TE + TM mode superior TM mode.

Table 1 The errors between observation and calculation water level of multiple geological models (the scenario one)

Frequency, spacing	Polarization mode	Model	Num. of data point	Standard error of the estimate (m)	Root mean squared (m)	Normalized RMS (%)	Correlation coefficient
40, 25	TE	Model i1	440	0.103	2.632	14.964	0.886
	TM	Model i4	440	0.258	10.229	58.154	−0.03
	TE + TM	Model i7	440	0.367	9.831	55.893	0.054
40, 50	TE	Model i2	440	0.143	3.729	21.201	0.738
	TM	Model i5	440	0.148	3.762	21.386	0.659
	TE + TM	Model i8	440	0.137	3.313	18.836	0.716
50, 25	TE	Model i3	440	0.118	2.926	16.635	0.84
	TM	Model i6	440	0.401	11.139	63.326	−0.143
	TE + TM	Model i9	440	0.281	6.673	37.936	0.244

Table 2 The errors between observation and calculation water level of multiple geological models (the scenario two)

Frequency, spacing	Polarization mode	Model	Num. of data point	Standard error of the estimate (m)	Root mean squared (m)	Normalized RMS (%)	Correlation coefficient
40, 25	TE	Model i1	440	0.121	3.288	18.145	0.936
	TM	Model i4	440	0.851	45.528	251.208	−0.417
	TE + TM	Model i7	440	0.46	10.127	55.878	0.245
40, 50	TE	Model i2	440	0.173	4.281	23.624	0.643
	TM	Model i5	440	0.302	14.063	77.598	−0.026
	TE + TM	Model i8	440	0.147	3.313	21.068	0.867
50, 25	TE	Model i3	440	0.149	3.968	21.892	0.853
	TM	Model i6	440	1.081	33.738	186.155	0.007
	TE + TM	Model i9	440	0.229	7.246	39.981	0.544

4 Conclusions

Groundwater numerical modeling and Sensitivity analysis were conducted to verify the feasibility to determine the optimal polarization. And the result show that the inversion model using only TE mode data is more valid, next is TE + TM, TM mode only is not proposed by comparing the numerical value of Standard of the Estimate, Root Mean Squared, Normalized RMS and Correlation Coefficient. A method for interpreting ERT data based on groundwater numerical modeling which data polarization mode should be used in 2D inversion mentioned in this article is provided a new way of thinking and method.

References

1. Chen, X. B, Zhao, G. Z, and Ma, X, “A preliminary study on the selection of the rotation direction of the data in the MT 2D inversion,” Oil geophysical prospecting (in Chinese), 43, no.1, pp. 113–118. February, 2008.
2. China Geological Survey, Hydrogeological manual. Geology Publishing House, 2012.

Surveying Karst Caves Under 14 Tunnels Bottom on Gui-Guang High-Speed Railway

Shihang Zhong, Rong Wang and Zefeng Wang

Abstract In order to prompt the development in west China, it is necessary to construct high-speed railway. However, there are many limestone and dolostone, as well as karst caves in west China, especially in GuiLin city, which make it difficult to dig tunnel or build bridge. A new method, (named Landsonar by authors), which use an extremely small source-geophone distance single-channel was introduced and applied for surveying karst caves in 14 tunnels among 179 km railway. Landsonar result and boreholes recorder agree with each other.

Keywords Karst caves · Tunnel · Landsonar · Predication

1 Introduction

There are many parts pass through limestone or dolostone zone in Gui-Guang high-speed railway, and several karst caves under tunnel bottom was uncovered at construction stage, but never was surveyed. Considering the hide dangerous, Railway administration decided to survey at the debugging stage. Author's company surveyed 14 tunnels among 179 km railway and total survey line's length was 23 km. The main purpose was to locate the karst caves of which diameter are bigger than 1 and 13 m depth under tunnel foundation bed bottom.

Landsonar method with hammer source is the good method for surveying karst caves and was used to survey on the three Survey line (left, middle, right) in every tunnel, source-geophone distance = station distance = 1 m.

S. Zhong (✉) · R. Wang · Z. Wang
H.E.M.E. New-Tech Development Co., Ltd, Beijing, China

Q. Di et al. (eds.), *Technology and Application of Environmental and Engineering Geophysics*, Springer Geophysics,
DOI 10.1007/978-981-10-3244-8_33

2 Landsonar

Landsonar, the abbreviation of a extremely small source-geophone distance with high frequency wide-band and high–fidelity elastic wave reflection continuous holographic profiling. Its main characters are as follows.

- An extremely small source-geophone distance single-channel was introduced that can avoid the noise from direct wave, ground wave, refracted wave, and was suitable to explore the cave. The topographic effect was very limited. The strength of reflections was excited by hammer sources with very high efficiency.
- The frequency band was 10–4000 Hz wide. The receiving system would not attenuate any reflections within this frequency band that can fully utilize the specific property about frequency spectrum of refraction wave. The authors have discover from practice works that 1500–3000 Hz frequency of reflection wave are best frequency band for exploring cave.

For these characters Landsonar got high success rate, especially at the surveying the single karst caves and Landsonar have applied in 140 projects successfully.

3 Data Acquisition

In this exploration works it was used that hammer source with two Vertical Stack, source-geophone distance = station distance = 1 m. Geophone was laid at two side of exciting point which bond with surface of concrete by vaseline and was hold by hand. For high efficient of data acquisition, 3 Landsonar instruments were used to acquire data at the same time. For the characters of Landsonar, it can work around

Fig. 1 Three instruments working at the same time

Fig. 2 The way to work of Landsonar

each other. The fastest velocity of data acquisition was 3100 points per group and per day which was equal to 1.5 km/group day (Figs. 1 and 2).

4 Surveying Result

4.1 The Important Parameters and Achievements Show

- Wave Velocity: All the velocity was actual site measurement with the common midpoint and refraction method. The velocity of concrete was 3250 m/s and the velocity of weathered limestone and dolomite was different in each tunnel, which is from 3250 to 3700 m/s;
- To suppose the caves were spheroid. The karst cave was defined by event of reflection wave with hyperbola type. There were three Survey lines (Left, Middle, Right) in each tunnel. In the first the caves of every survey line were marked by reflection events of hyperbola, and then distribution map with different depth was drawn for analyzing if there was the same karst cave reflection in two survey line and two or three connected karst caves in one survey line, which also was a hide dangerous.

On the basis of result about data interpretation all the tunnels was classified, and in the same tunnel different parts were marked base on the amount of caves.

Class of tunnel—
A: karst developed (more than 25 caves/100 m or most caves whose diameter >3 m)
A1—Dense part; A2—The other part of A;
B: karst not much developed (less than 25 caves/100 m)
B1—Dense part; B2—The other part of B;
C: karst developed weakly

Karst developed tunnel basically came through limestone, which was not coincidence but was regular, because the corrosion of limestone was heavier than dolomite. The total karst caves reflection with diameter bigger than 1 m were 4491 from 0 to 13 m depth, and there were 402 karst caves with diameter bigger than 2 m and 20 karst caves with diameter bigger than 3 m.

And every karst caves was classified to I, II, III base on the depth and diameter.

Diameter (m)	Depth (m)	Class
≧5 m	0–13 m	**I**
3–5 m	<5 m	**I**
1–3 m	<3 m	**I**
3–5 m	5–10 m	**II**
1–3 m	3–5 m	**II**
≦1 m		**III**

From the landsonar time-section (Fig. 3), it can be seen that many reflection events of hyperbola which indicate karst cave and underground river. The most exploration depth is about 13 m (Figs. 4 and 5).

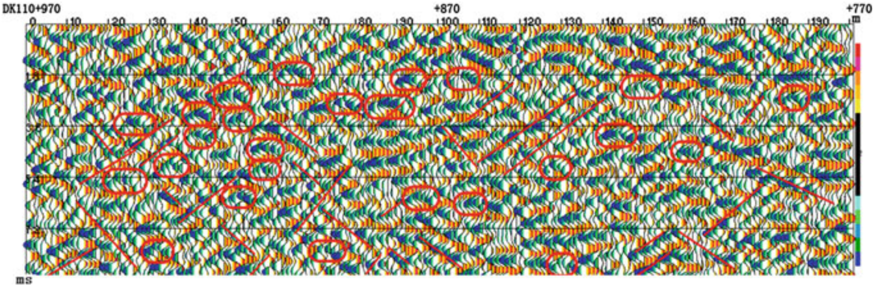

Fig. 3 One part of Landsonar time-section

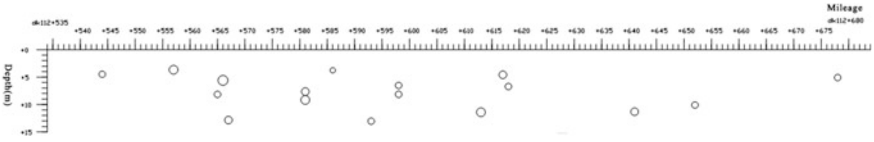

Fig. 4 The profile of karst caves

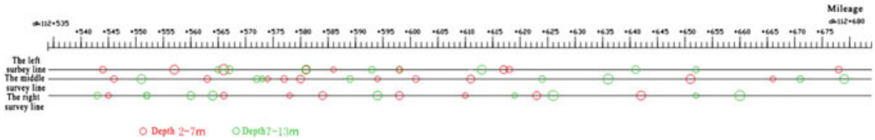

Fig. 5 The plant distributed of karst caves

5 Testing and Verifying by Boreholes

The surveying job was on the surface foundation bed, and the bed and the invert which is arched was connected together. It was an angel of 12 degree between perpendicular direction and incident wave, reflected wave of Landsonar which basically were vertical to the reflected surface. So the different between the Landsonar data and the real karst caves' position may arrive 1.5 m when the depth was 10 m, which must be considered when testing and verifying.

There were 8 boreholes used to test and verify the data of geophysical prospecting and 7 boreholes among them accorded well.

References

1. Zhong Shihang. The New Method Suited to Survey in Busy Streets of City And on Water Surface And Survey the Single Karst Cave. Proceeding of 2012 Forum on Urban Geo-environment and Sustainable Development (3–7 December 2012, Hong Kong, China), 2012, P 101
2. Zhong Shihang, Sun Hongzhi, Wang Rong. Landsonar. Beijing: China Science and Technology Press, 2012
3. Zhong Shihang, Sun Hongzhi, Wang Rong, et al. Detection and Forecasting for Hidden Danger of Karst Fissure Water and other Geological Disasters during Construction of Tunnels and Underground Projects. Chinese Journal of Rock Mechanics and Engineering, 2012, 31 (S1):3298–3327